Optical properties of GaN quantum dots and nanowires

Julien Renard

To cite this version:

Julien Renard. Optical properties of GaN quantum dots and nanowires. Condensed Matter [cond-mat]. Université Joseph-Fourier - Grenoble I, 2009. English. NNT : . tel-00475438

HAL Id: tel-00475438

https://theses.hal.science/tel-00475438v1

Submitted on 22 Apr 2010

Université Joseph Fourier – Grenoble 1

THÈSE

présentée par

Julien RENARD

pour obtenir le titre de

Docteur de l'Université Joseph Fourier

Specialité : Physique de la matière condensée et du rayonnement

Optical properties of GaN quantum dots and nanowires

soutenue publiquement le 28 Septembre 2009

Composition du jury :

Président :	L. Saminadayar
Rapporteurs :	M. Leroux
	C. Lienau
Examinateur :	N. Grandjean
Codirecteurs de thèse :	H. Mariette
	B. Gayral

Équipe mixte CEA-CNRS-UJF *"Nanophysique et Semiconducteurs"*
CEA Grenoble

Remerciements

J'ai eu la chance de réaliser ma thèse au sein de l'équipe mixte CEA-CNRS-UJF 'Nanophysique et Semiconducteurs'. Je tiens à remercier Henri Mariette et Jean-Michel Gérard, respectivement directeur de l'équipe et du service de m'avoir accueilli dans leur laboratoire.

Je remercie Laurent Saminadayar d'avoir accepté de présider mon jury de soutenance. J'ai également beaucoup apprecié le travail effectué par Mathieu Leroux et Christoph Lienau, rapporteurs de ce manuscrit. En particulier, merci à Christoph d'avoir consenti à venir depuis Oldenburg pour participer à mon jury. Ce fût un plaisir de croiser à nouveau son chemin et je le remercie pour ses nombreux conseils avisés. Je suis reconnaissant envers Nicolas Grandjean d'avoir participé à mon jury de thèse en tant qu'examinateur.

Mes plus sincères remerciements s'adressent à Bruno Gayral, qui m'a supervisé pendant ces trois années. Etre encadré par Bruno signifie à la fois une grande liberté pour conduire ses recherches mais sutout la possibilité de bénéficier des ses grandes compétences tant sur le plan expérimental que sur sa compréhension plus générale des phénomènes que nous étudiions. On peut difficilement réver meilleur encadrement. Je tiens également à souligner que j'ai beaucoup apprécié les efforts de Bruno pour que je puisse me rendre dans diverses conférences afin d'y présenter mes résultats. Le fait qu'il prenne soin de toujours valoriser mon travail a également beaucoup joué dans la confiance que j'ai pu acquérir durant ces trois années. A côté de cela, j'ai eu, d'une manière plus générale, beaucoup de plaisir à côtoyer Bruno et à travailler avec lui.

Je tiens à remercier vivement Henri Mariette, mon directeur de thèse. Henri a toujours répondu présent à mes diverses sollicitations et s'est montré enthousiaste vis à vis de mes travaux, ce que j'ai beaucoup apprécié. Il a également joué un rôle très important à divers moment de ma thèse, en particulier lors de ma recherche de postdoc. Je tiens à souligner les qualités humaines d'Henri qui font que j'ai eu beaucoup de plaisir à le cotoyer pendant ces trois années.

L'interaction avec les épitaxieurs a eu une place capitale dans mes travaux.

J'en viens donc tout naturellement à souligner l'importance qu'à eu Bruno Daudin aux cours de ces trois années. Il s'est toujours montré très réactif vis à vis des diverses idées que nous lui avons proposées et une grande partie de mes travaux s'est réalisée en proche collaboration avec Bruno D. Bien evidemment, je tiens à remercier les doctorants qui ont réalisés la croissance des échantillons et avec qui j'ai pu travailler : Benoit Amstatt pour le plan m, Sebastien Founta pour le plan a, Gabriel Tourbot et Olivier Landré pour les nanofils. Egalement un merci particulier à Rudeesun Songmuang pour la croissance des nanofils et qui a grandement participé au démarrage du sujet dans l'équipe. Grâce à Bruno D., j'ai eu la chance de pouvoir collaborer avec Rafa Mata et Ana Cros de l'Université de Valencia, chez qui j'ai eu l'opportunité d'aller réaliser quelques manips Raman fin 2008. Mon séjour s'est révélé fort productif et instructif, en plus d'être très sympathique.

Eva Monroy, en charge de l'autre MBE nitrure du groupe, a toujours répondu positivement aux diverses idées que nous avons eues avec Bruno G. Elle a toujours accepté de réaliser, avec son doctorant Prem Kumar, de nombreux échantillons à notre demande, malgré le temps requis pour mener de telles études. De plus, la qualité des échantillons a toujours été au rendez vous, ce qui est très agréable pour un opticien!

Je tiens a remercier Catherine Bougerol pour toutes les études TEM qu'elle a menées. Egalement merci à Edith Bellet pour les mesures effectuées par rayons X, à la MOCVD team (Joël Eymery, Christophe Durand , Robert Koster et Mohamed Azize) pour les divers projets menés ensemble. J'ai eu le plaisir de pouvoir effectuer des manips avec Maxime Richard et Aurélien Trichet, qui seront je l'espère continuées par Diane Sam Giao, qui prend la suite de ce travail et à qui je souhaite bonne chance. Merci aussi à Fabian Rol, qui m'a précédé et qui a mis en place beaucoup de choses qui m'ont été très utiles pendant cette thèse.

Nous avons la chance d'avoir pu intéragir efficacement avec nos collègues du LSIM, Yann-Michel Niquet et Dulce Camacho en ce qui concerne la thématique nanofils.

Durant cette thèse, j'ai pu travailler en collaboration avec différentes équipes en dehors de Grenoble. Je souhaiterais ici mentionner le groupe de Nicolas Grandjean, pour les travaux sur les microdisques présentés au chapitre 5. Dans le cadre de l'ANR Sinphoni, nous avons plus recemment eu le plaisir de travailler avec le Crhea (Sylvain Sergent, Fabrice Semond et Mathieu Leroux), toujours sur la thématique microdisque. Les résultats présentés dans le chapitre 6, sur la dynamique de spin, ont été obtenus en proche collaboration avec Andrea Ballochi et Xavier Marie de l'INSA Toulouse. J'ai eu en particulier la chance de faire une semaine de manip avec Andrea. Je tiens également à remercier nos collègues de l'IPCMS à

Strasbourg pour les manips de dynamique de spin dans les nanofils de GaN.

Un très grand merci à Joël Bleuse, qui s'est toujours montré disponible pour m'assister sur la manip de TRPL et qui n'a jamais rechigné à modifier la configuration de la manip. Sans lui, bon nombre des manips de TRPL n'auraient tout simplement pas vu le jour.

Un merci spécial à Le Si Dang, qui au delà des quelques manips de CL que j'ai pu réaliser avec lui, a toujours été de bon conseil. Egalement merci à Régis, qui entre autre choses, a toujours trouvé le temps de venir assister à mes diverses répétitions de talks/soutenance...

Les simulations Monte Carlo présentées dans le chapitre quatre de ce manuscrit ont pu être réalisées grâce à Guillaume Tarel. Merci beaucoup à Guillaume pour cela et également pour m'avoir supporté dans les divers conférences que nous avons faites ensemble ! Il m'a également bien aidé pour divers problèmes, en particulier sous Matlab et est au final un bien meilleur geek que Manu, que ce soit dit ! Une partie de ce manuscrit (cherchez laquelle !) est écrite dans un anglais quasi parfait (!!): merci à Myriam pour cela.

L'ambiance qui régne dans une équipe est pour moi très importante. J'ai été servi pendant ces trois années ! Mes divers acolytes de la pause café matinale y ont grandement participé : Yann, Jean, Maëla, Rita, Yoanna, Hervé, Regis, Serge, Julien, Lise, Momo, Périne (j'ai bon pour l'orthographe là?), à Bruno, Henri, Vincent, Gabriel, Olivier, Joël, Marlène, Kuntheak et Yoann. En particulier merci à Henri pour ses blagues (si si!), à Bruno pour le point culture du jour(!), à Joël grâce à qui on n'a plus besoin de lire le canard et Yoann et Hervé (à qui il reste à faire des progrès au squash!!) pour les débats politiques enflammés! J'ai été très heureux de partager mon bureau une partie de ma thèse avec Yoanna Nowicki, qui a ensuite succombé aux sirènes de l'industrie (!). Ma new cobureau, avec qui j'ai eu la chance de partager bien plus qu'un bureau, se reconnaitra. Merci à toi, qui a contribué a ce que trois années soient pour moi une foultitude de bon moments.

J'en viens donc naturellement aux personnes avec qui j'ai partagé des choses en dehors du labo pendant ces trois années. Dans le désordre : Lise, Nico, Marion, Louis, Manu, Constance, Sirona, Fabien, Jean , Caro, Guillaume, Delphine, Julien (merci d'être venu à ma soutenance qui a certainement du être totalement incompréhensible!), Marie, Benji (le roi de la frite)... mais également tous les anciens de PG et tous les autres qui ne rentrent pas dans cette catégorie (!) (en particulier Claire et Thom pour vos muscles fort utiles en ce mois d'Octobre 2009).

Je remercie bien entendu ma famille, entre autre pour l'organisation parfaite de mon pôt, mais surtout pour m'avoir soutenu tout au long de mes études sans forcément trop comprendre où cela me mènerait. Enfin, merci à Maud, qui m'a supporté pendant ces trois années !

Contents

Introduction

Semiconductor heterostructures have proved to be very interesting for both applications and fundamental purposes. For instance, since their first optical characterizations in the 80's [1–4], quantum dots have been continuously investigated and have revealed very interesting physical phenomena. Among other effects due to the energy levels quantization we can mention the observation, by means of optical or electronic probing, of single photon emission [5], Coulomb blockade and single electron charging [6], spin robustness and its manipulation [7–9]. On the other hand, the introduction of semiconductor heterostructures in devices allowed to dramatically increase the performances, for instance the reduction of the threshold current in a laser with embedded quantum wells as the gain medium [10].

III-N semiconductors have attracted attention later than other semiconductors in terms of applications, especially arsenides, but since the development of the first III-N based semiconductor optoelectronic devices [11, 12] the interest never went down. On the device point of view, they are supposed to bring new possibilities for instance in terms of achievable wavelengths for optical devices and in terms of achievable frequencies for electronic devices. The peculiarities of III-N compounds, namely a large band gap and a wurtzite structure have also led to new physical phenomena. For instance, the large band offsets enhance the thermal stability of the emission in quantum dots and eventually allowed the demonstration of single photon emission up to 200 K [13]. Also, the strong electric field which appears when growing heterostructures along the polar axis has for consequence an electron-hole separation which results in a strong red shift of the luminescence and a reduction of the oscillator strength. Radiative lifetimes reaching the microsecond have thus been measured [14].

Nanowires are another kind of semiconductor structures that has recently attracted much attention. Their expected advantages come in part from the free surface offered by this new geometry which should allow an easy strain relaxation and eventually lead to heterostructures with reduced defect densities. For nitrides, which do present a very high density of defects in traditional two dimensional structures, the potential improvements are very acute.

In this context, the aim of this thesis was to study the optical properties of various kind of nitride based heterostructures and to demonstrate new behaviors. The manuscript will be organized as follows : we will begin by presenting general considerations about III-N semiconductors and heterostructures in chapter 1. Then we will focus on the optical properties of non-polar nitride nanostructures in chapter 2. We will see that, besides the reduction of the electric field which is very interesting for potential applications, these structures have an original behavior in terms of polarization of the luminescence.

In chapter 3 we will show that the study of GaN nanowires and heterostructures embedded in GaN nanowires offers new possibility compared to two dimensional structures. These structures present indeed a strong optical polarization anisotropy due to the anisotropy of the refractive index. Also we will present evidences for a reduction of the electric field for heterostructures embedded in nanowires compared to two dimensional heterostructures. We attribute this reduction to a decrease of the piezoelectric contribution.

The study of single quantum dots embedded in nanowires will be presented in chapter 4. We will in particular show the emissions of both exciton and biexciton. Eventually, we will show that these structures are indeed quantum dots, i.e. that the energy levels are fully discretized, thanks to a photon correlation experiment.

In chapter 5, we will study structures in which one uses the coupling of a light emitter to a confined light mode, namely microcavities. More specifically, we will present results obtained in GaN microdisks with embedded InGaN quantum wells. We will show photoluminescence spectra in which quality factors up to 11000 appear. These are the best quality factors ever measured for a nitride microcavity.

The dynamics of both spins and carriers in GaN/AlN heterostructures will be studied in chapter 6. Time resolved experiments will show that when they are trapped in quantum dots, the excitons are insensitive to non radiative recombinations and spin relaxation. We will indeed evidence that the non radiative decays are longer than a few μs at room temperature. On the other hand, spin relaxation has been probed on the exciton lifetime and is longer than the ns up to room temperature.

Chapter 1

General properties of nitride materials

III-N semiconductors have several peculiarities compared to other semiconductors, like III-As for instance. The aim of this chapter is thus to introduce these semiconductors and especially GaN. After dealing with the structural properties and focusing on the built-in polarization, we will give informations about the electronic structure and its consequences on the optical properties. We will then present general considerations about experimental methods in optics. Finally we will focus on heterostructures and discuss in details the consequences of the polarization and the topic of non polar heterostructures.

Contents

1.1 Structural properties

III-N materials can crystallize in either the zinc-blende (cubic system) or the wurtzite (hexagonal system) structure. The most stable one is the wurtzite and apart from the band gap, this is what gives III-N materials their peculiarities. During this dissertation we will mainly focus on the wurtzite structure because we did not study samples with the zinc-blende structure.

1.1.1 The wurtzite structure

The symmetry properties of the structure are the one of the space group it belongs to, namely $P6_3mc$ in the Hermann-Mauguin notation (or C_{6v}^4 in the Schoenflies notation). It means that the Bravais lattice is primitive, that there is a six fold screw rotation (i.e. of angle 60°) of vector $\frac{1}{2}\mathbf{c}$. There is also a mirror symmetry perpendicular to $\mathbf{a}$ and a glide mirror perpendicular to $\mathbf{m}$ with the translation vector $\frac{1}{2}\mathbf{c}$. The structure with the directions is represented in figure 1.1. As one can see, the basis has two III atoms (one at (0,0,0) and one at $(\frac{2}{3},\frac{1}{3},\frac{1}{2})$) and two N atoms (one at $(0,0,\zeta)$ and one at $(\frac{2}{3},\frac{1}{3},\frac{1}{2}+\zeta)$). In all semiconducting compounds $\zeta \cong \frac{3}{8}$, the value for tetrahedral coordination of the atoms. In other words the wurtzite structure can actually be seen as two hexagonal compact lattices of III and N atoms shifted by $\frac{3}{8}\mathbf{c}$. In the ideal wurtzite structure, the four nearest neighbors of an atom are sited at the corners of an *undeformed* tetrahedron. For the realistic wurtzite structure, the tetrahedron is slightly stretched or compressed in the $\mathbf{c}$ direction depending on the $\frac{c}{a}$ ratio [15]. Then in the ideal wurtzite structure $\frac{c}{a} = \sqrt{\frac{8}{3}} = 1.633$. The values of the lattices parameters for the III-N compounds are given in table 1.1.

As one can see in figure 1.1 (and also in the notation of the space group), the wurtzite structure is non-centrosymmetric. One consequence is that the [0001] and [000$\bar{1}$] directions are not equivalent (for the correspondence between three and four indexes notation, see appendix A) and one can define the polarity of the material. The [0001] axis is oriented from the III compound towards the N. The structures grown along the [0001] axis are called "metal polarity" and the ones grown along [000$\bar{1}$] are called "nitrogen polarity". The two situations are illustrated in figure 1.2.

1.1.2 Spontaneous and piezoelectric polarizations

Like many semiconductors, apart from the ones having the diamond structure which is centrosymmetric, III-N materials are piezoelectric. It

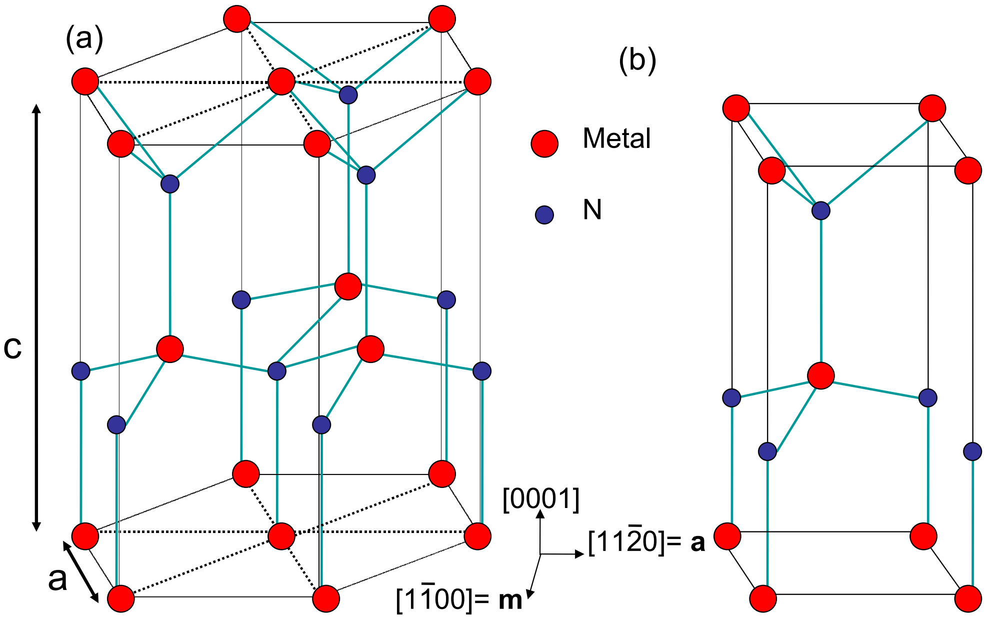

Figure 1.1: The wurtzite crystal structure (a) and its primitive cell (b)

means that when a stress is applied to them, they respond by developing a polarization. In addition to piezoelectricity, III-N materials, due to their low symmetry, present a polarization even in the absence of external stress. This polarization is thus called "spontaneous". Like every macroscopic physical properties, the symmetries that are relevant to explain the effect are the ones of the crystal point group, which is $6mm$ in Hermann-Mauguin notation (C_{6v} in the Schoenflies notation) for the wurtzite structure.

	GaN	AlN	InN
a(Å)	3.189	3.112	3.545
c(Å)	5.185	4.982	5.703
$\frac{c}{a}$	1.626	1.601	1.609

Table 1.1: Measured lattice parameters of nitride semiconductors in the wurtzite crystal structure [16]. $\frac{c}{a}$=1.633 for the ideal wurtzite structure.

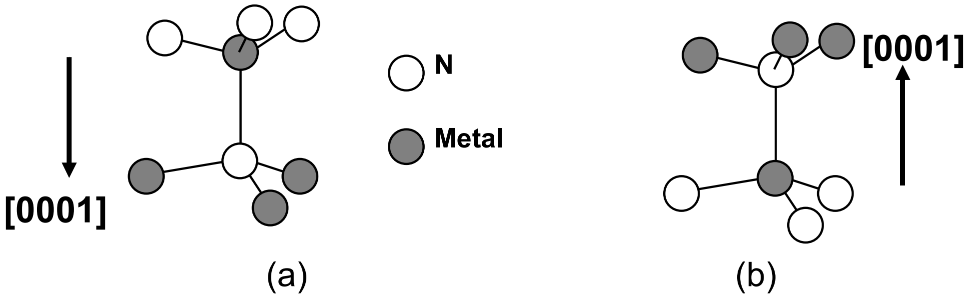

Figure 1.2: Illustration of the “nitrogen” (a) and “metal” (b) polarities for structures grown along the c-axis of the wurtzite structure

Spontaneous polarization

The wurtzite structure is the one of highest symmetry compatible with the existence of spontaneous polarization. Furthermore, the symmetry of the crystal ($6mm$ point group) implies that this polarization should be parallel to the c-axis [17], i. e. $\mathbf{P}^{sp} = P_3^{sp}\mathbf{u}_z$. Two elements are responsible for the spontaneous polarization.

First of all, one has to take into account that metal and nitrogen present a difference in electronegativity, which is larger for nitrogen. This means that the electron cloud along the III-N binding is somewhat shifted towards the nitrogen. This together with the low symmetry of the wurtzite structure make the barycenter of the positive and negative charge to be at different positions, even in an ideal wurtzite structure ($\frac{c}{a} = \sqrt{\frac{8}{3}}$). It creates microscopic dipoles in the primitive cell which give rise to a macroscopic polarization. This would be the only cause of spontaneous polarization for an ideal wurtzite crystal.

Secondly, as we already mention, the crystal structure of III-N materials is not ideal ($\frac{c}{a} \neq \sqrt{\frac{8}{3}}$) and the tetrahedron is slightly deformed making the III-N binding shorter along the [0001] direction than the three other bindings. This is another reason which makes the barycenters of the positive and negative charges to be different giving rise to a macroscopic polarization. Ab initio calculations have been performed in order to estimate the value of this spontaneous polarization [18]. The values are reported in table 1.2. It changes from one material to another due to both the electronegativity differences of the metals and differences in the $\frac{c}{a}$ ratio. One has to mention that the spontaneous polarization for a ternary alloy cannot be obtained by a simple linear interpolation [19, 20].

	GaN	AlN	InN
P$_{sp}$ (Cm^{-2})	-0.029	-0.081	-0.032

Table 1.2: Calculated values of the spontaneous polarization [18]

Piezoelectric polarization

This polarization appears when a material which is non centrosymmetric is subject to a stress. The cause is actually an additional deformation of the tetrahedron with respect to the unstressed material. The general treatment of the polarization created by an applied stress is done by using the piezoelectric tensor d(of rank 3). It links the component of the polarization P_i (i=x,y,z) to the components of the stress tensor σ_{ij} :

$$P_i = \sum_{j=1}^{3}\sum_{k=1}^{3} d_{ijk}\sigma_{jk} = d_{ijk}\sigma_{jk} \tag{1.1}$$

The 27 coefficients d_{ijk} are called the piezoelectric moduli. Due to tensor symmetries, there are actually 18 independent d_{ijk} .This makes possible the use of the matrix notation by defining new symbols [17] for the d_{ijk}, by replacing jk by only one suffix. We have to follow the rules :

Tensor notation	11	22	33	23,32	31,13	12,21
Matrix notation	1	2	3	4	5	6

For the non diagonal terms there is a factor 2 to take into account arising from this definition. For instance $d_{16} = 2d_{112}$.

The same rules apply to replace the two suffixes of σ_{ij} by only one. In the new notation we have then :

$$P_i = \sum_{j=1}^{3} d_{ij}\sigma_j = d_{ij}\sigma_j \tag{1.2}$$

or in the matrix form :

$$\begin{pmatrix} P_1 \\ P_2 \\ P_3 \end{pmatrix} = \begin{pmatrix} d_{11} & d_{12} & d_{13} & d_{14} & d_{15} & d_{16} \\ d_{21} & d_{22} & d_{23} & d_{24} & d_{25} & d_{26} \\ d_{31} & d_{32} & d_{33} & d_{34} & d_{35} & d_{36} \end{pmatrix} \begin{pmatrix} \sigma_1 \\ \sigma_2 \\ \sigma_3 \\ \sigma_4 \\ \sigma_5 \\ \sigma_6 \end{pmatrix} \tag{1.3}$$

Symmetry arguments based on the operations of the point group $6mm$ reduce the non vanishing components d_{ij} to 5 with only 3 being independent [17]. The matrix becomes :

$$\begin{pmatrix} 0 & 0 & 0 & 0 & d_{15} & 0 \\ 0 & 0 & 0 & d_{15} & 0 & 0 \\ d_{31} & d_{31} & d_{33} & 0 & 0 & 0 \end{pmatrix}$$

Experimentally, one generally has access to the strain ϵ which is related to the stress by the Hooke's law :

$$\sigma_{ij} = c_{ijkl}\epsilon_{kl} \tag{1.4}$$

where the 81 components c_{ijkl} form a rank 4 tensor called the stiffness tensor. By using once again general properties of tensors, one can use a matrix notation. If we take into account the symmetry of the relevant point group, $6mm$, there are actually 12 non vanishing components, with only 5 being independent [17] :

$$\begin{pmatrix} \sigma_1 \\ \sigma_2 \\ \sigma_3 \\ \sigma_4 \\ \sigma_5 \\ \sigma_6 \end{pmatrix} = \begin{pmatrix} c_{11} & c_{12} & c_{13} & 0 & 0 & 0 \\ c_{12} & c_{11} & c_{13} & 0 & 0 & 0 \\ c_{13} & c_{13} & c_{33} & 0 & 0 & 0 \\ 0 & 0 & 0 & c_{44} & 0 & 0 \\ 0 & 0 & 0 & 0 & c_{44} & 0 \\ 0 & 0 & 0 & 0 & 0 & \frac{1}{2}(c_{11} - c_{12}) \end{pmatrix} \begin{pmatrix} \epsilon_1 \\ \epsilon_2 \\ \epsilon_3 \\ \epsilon_4 \\ \epsilon_5 \\ \epsilon_6 \end{pmatrix} \tag{1.5}$$

Using equation 1.3 and 1.5, one gets the relationship between the piezoelectric polarization and the strain, which is expressed by the matrix of the e_{ij} coefficients. The values of the piezoelectric coefficients reported in the literature are presented in the table 1.3. The values are somehow scattered (especially the shear strain related ones for which there is even an uncertainty about the sign) but the important fact is that these constants are at least 5 times larger than for other usual semiconductors (see for instance [21] for III-V semiconductors other than III-N).

If one neglects the shear strain, which is usually a good approximation in the case of epitaxial growth, one can see that the only non vanishing component of the piezoelectric polarization will be along the c-axis, i.e. $\mathbf{P}^{pz} = P_3^{pz}\mathbf{u}_z$. For instance, for a [0001] growth, provided $\sigma_3 = 0$ (free surface which gives the biaxial approximation: $\epsilon_3 = \frac{-2C_{13}}{C_{33}}\epsilon_1 = -0.53\epsilon_1$) and isotropic in-plane strain ($\epsilon_1 = \epsilon_2$) one can easily show that :

$$P_3^{pz} = 2d_{31}\epsilon_1(c_{11} + c_{12} - 2\frac{c_{13}^2}{c_{33}}) \tag{1.6}$$

	d$_{31}$ (pmV^{-1})	e$_{31}$ (Cm^{-2})	d$_{33}$ (pmV^{-1})	e$_{33}$ (Cm^{-2})	d$_{15}$ (pmV^{-1})	e$_{15}$ (Cm^{-2})	References
GaN	-1.6	(-0.55)	3.1	(0.90)	3.1	(0.28)	[16]
	-1.4	(-0.49)	2.7	(0.78)	1.8	(0.16)	[22]
	-1.9	-0.55	3.7	1.12	6.4	0.61	[23]
	(-1.38)	-0.49	(2.57)	0.73	-	-	[18]
	(-0.68)	-0.22	(1.47)	0.43	(2.41)	0.22	[24]
AlN	-2.1	(-0.44)	5.4	(1.53)	3.6	(0.42)	[16]
	-2.1	(-0.44)	5.4	(1.53)	2.9	(0.34)	[22]
	-2.8	-0.6	5.6	1.5	9.7	1.13	[23]
	(-2.39)	-0.60	(5.41)	1.46	-	-	[18]
	-1.88 +/-0.57	-0.58 +/-0.23	4.53 +/-0.86	1.39 +/-0.22	-2.42 +/-0.50	-0.29 +/-0.06	[25]
InN	-3.5	(-0.67)	7.6	(0.86)	5.5	(0.25)	[16]

Table 1.3: Values of the piezoelectric coefficients in III-N wurtzite compounds. When only one set of parameters (d_{ij} or e_{ij}) is given in a reference, the other set is extracted with the values of the elastic coefficients of [26].

With the numerical values of the c_{ij} and d_{31}, one sees that for a crystal in compression (resp. extension) the contribution of the piezoelectric polarization will be opposite (resp. added) to the one of the spontaneous polarization. The effect of a polarization **P** will be to create charge sheets σ_{surf} when a variation of the polarization occurs :

$$\sigma_{surf} = \Delta\mathbf{P}.\mathbf{n} \tag{1.7}$$

with **n** being the normal to the interface. These charge sheets will then create an electric field, to which we are sensitive to. In theory, one should be able to see this effect in a bulk crystal (i.e. pyroelectricity), but the sheet charges are compensated by either surface states or residual doping providing free carriers. Nevertheless, in heterostructures the presence of an electric field is clearly established and the effects are spectacular, as we will discuss later in 1.4.1.

1.2 Electronic properties

In this part we will present general considerations concerning the electronic properties of semiconductors with a wurtzite crystal structure. We will focus on the region of the $\boldsymbol{k}$-space located at $\boldsymbol{k} = 0$, which is the relevant

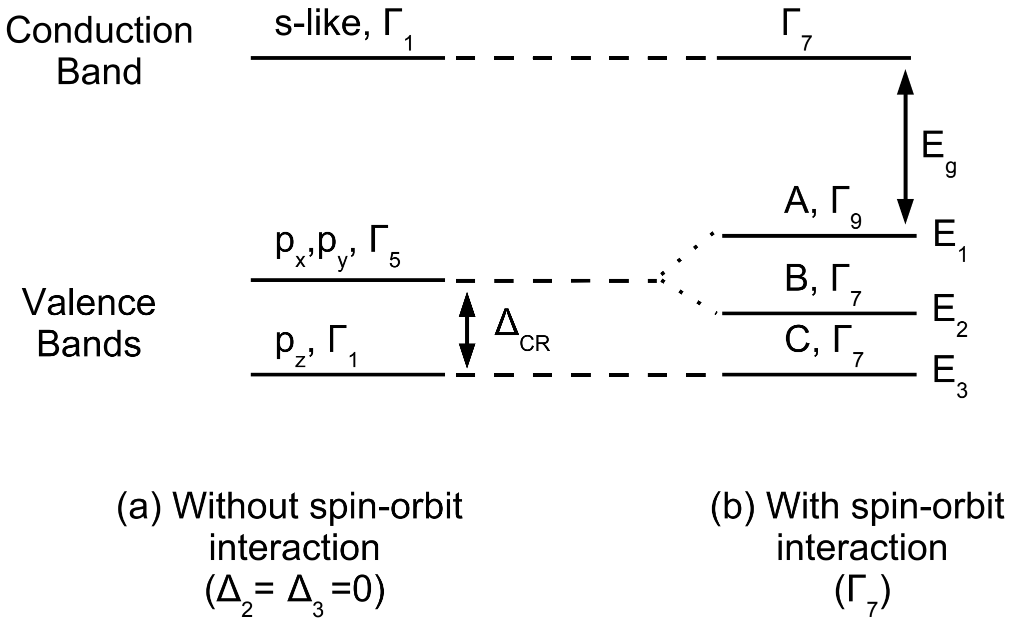

Figure 1.3: The construction of the band structure of GaN at the $\mathbf{\Gamma}$ point of the Brillouin zone (C_{6v} symmetry) from the situation without spin-orbit (i.e. with only the crystal field) (a) and adding the spin-orbit interaction (b).

one for the optical properties, at least for semiconductors with a direct band gap. The symmetries of the eigenstates (Bloch states) for $\boldsymbol{k} = 0$ (the $\mathbf{\Gamma}$ point) are described by the point group [27], namely C_{6v}.

1.2.1 Bulk band structure

Like many semiconductors compounds, the symmetry of the orbital part of the wavefunction is inherited from the s-orbitals (resp. p-orbitals) for the conduction band (resp. valence band). Thus, with the use of the character table of the point group [27–29], one can see that, neglecting spin, the first level of the conduction band transforms like $\mathbf{\Gamma}_1$. For the valence band, the situation is more tricky, due to the fact that there are three states originating from a p-orbital. The basis functions are p_x, p_y, p_z. Using once again the character table, one sees that p_x and p_y transform like $\mathbf{\Gamma}_5$ and p_z like $\mathbf{\Gamma}_1$. It gives then two levels (the one with a $\mathbf{\Gamma}_5$ symmetry being degenerate). The splitting of the two levels is given by the strength of the crystal field. In the major part of the wurtzite compounds (except AlN), the $\mathbf{\Gamma}_1$ level lies below the $\mathbf{\Gamma}_5$ one. The situation is illustrated in figure 1.3. For electronic eigenstates, we have to include the spin (i.e. to include the spin-orbit coupling). We have then to use the representations of the double group which take the spin into account. In the group C_{6v}, the spin-$\frac{1}{2}$ transforms like $\mathbf{\Gamma}_7$ [27–30]. Thus the symmetry of the electronic wave function including spin is simply given by the product of representation of the orbital and spin parts. We have to use the multiplication table of the double group [27, 28] and we obtain for the conduction band:

$$\mathbf{\Gamma}_1 \otimes \mathbf{\Gamma}_7 = \mathbf{\Gamma}_7 \tag{1.8}$$

It means that including spin, the conduction band in a crystal with a wurtzite structure transforms like $\mathbf{\Gamma}_7$.

For the valence band, we have to consider separately $\mathbf{\Gamma}_1$ and $\mathbf{\Gamma}_5$. For $\mathbf{\Gamma}_1$, the situation is formally the same as for the conduction band and we obtain one band of symmetry $\mathbf{\Gamma}_7$. For $\mathbf{\Gamma}_5$ we have to look at the multiplication table :

$$\mathbf{\Gamma}_5 \otimes \mathbf{\Gamma}_7 = \mathbf{\Gamma}_7 \oplus \mathbf{\Gamma}_9 \tag{1.9}$$

We thus obtain two bands of different symmetry. The position and the separation is set by the strength and sign of the spin-orbit coupling. Generally the uppermost valence (labeled A) band has a $\mathbf{\Gamma}_9$ symmetry and the two $\mathbf{\Gamma}_7$ bands (labeled B and C) lie below. The complete picture is illustrated in figure 1.3. The eigenfunctions and eigenenergies are obtained by taking into account the mixing of the bands with a symmetry $\mathbf{\Gamma}_7$. Let us define the eigenfunctions of the projection of the orbital moment along z, l_z [31] :

$$\begin{aligned}
\mid 1\rangle &= -\frac{(x+iy)}{\sqrt{2}} \quad , \\
\mid 0\rangle &= z \quad , \\
\mid -1\rangle &= \frac{(x-iy)}{\sqrt{2}}
\end{aligned} \tag{1.10}$$

Following the notations of Chuang et al. [32], the three eigenenergies and the six eigenfunctions are then given by:

$$\begin{aligned}
\mathbf{\Gamma}_9(A) : & E_1 = \Delta_1 + \Delta_2 \\
& u_1 =\mid 1, \uparrow\rangle \ \ , \\
& u_4 =\mid -1, \downarrow\rangle \ \ ; \\
\mathbf{\Gamma}_7(B) : & E_2 = \frac{\Delta_1 - \Delta_2}{2} + \sqrt{(\frac{\Delta_1 - \Delta_2}{2})^2 + 2\Delta_3^2} \\
& au_2 + bu_6 = a \mid -1, \uparrow\rangle + b \mid 0, \downarrow\rangle \ \ , \\
& bu_3 + au_5 = b \mid 0, \uparrow\rangle + a \mid 1, \downarrow\rangle \ \ ; \\
\mathbf{\Gamma}_7(C) : & E_3 = \frac{\Delta_1 - \Delta_2}{2} - \sqrt{(\frac{\Delta_1 - \Delta_2}{2})^2 + 2\Delta_3^2} \\
& bu_2 - au_6 = b \mid -1, \uparrow\rangle - a \mid 0, \downarrow\rangle \ \ , \\
& - au_3 + bu_5 = a \mid 0, \uparrow\rangle + b \mid 1, \downarrow\rangle
\end{aligned} \tag{1.11}$$

where :

$$\Delta_1 = \Delta_{CR} \ , \ \Delta_2 = \Delta_3 = \frac{1}{3}\Delta_{SO} \ , \ a = \frac{E_2}{\sqrt{E_2^2 + 2\Delta_3^2}} \ , \ b = \frac{\sqrt{2}\Delta_3}{\sqrt{E_2^2 + 2\Delta_3^2}} \tag{1.12}$$

with Δ_{CR} (resp. Δ_{SO}) being the crystal field split energy (resp. spin-orbit split-off energy). Some values of these parameters (including band gap) are reported in table 1.4 together with the effective masses, the exciton Bohr radius and binding energies. If we want to focus on the optical properties, we have to build the electronic excitations, namely the excitons, from the conduction and valence bands. The exciton wave functions (for a Wannier exciton [27]) are a product of the electron and hole wavefunctions and of the envelope wavefunction (in the sense of the relative motion of the electron and hole) [27] :

$$\mathbf{\Gamma}_{exciton} = \mathbf{\Gamma}_{el} \otimes \mathbf{\Gamma}_h \otimes \mathbf{\Gamma}_{env} \tag{1.13}$$

thus we have to consider separately the A and B, C excitons. For the ground state, which we will consider, $\mathbf{\Gamma}_{env} = \mathbf{\Gamma}_1$. The excitons symmetries are given by :

$$\begin{aligned}
A \quad & \text{excitons} : \mathbf{\Gamma}_7^c \otimes \mathbf{\Gamma}_9^v \otimes \mathbf{\Gamma}_1^{env} = \mathbf{\Gamma}_5 \oplus \mathbf{\Gamma}_6 \\
B, C \quad & \text{excitons} : \mathbf{\Gamma}_7^c \otimes \mathbf{\Gamma}_7^v \otimes \mathbf{\Gamma}_1^{env} = \mathbf{\Gamma}_1 \oplus \mathbf{\Gamma}_2 \oplus \mathbf{\Gamma}_5
\end{aligned} \tag{1.14}$$

We will use these symmetries to determine the polarization selection rules.

	GaN	AlN	InN
E_g(eV)	3.510	6.25	0.78
Δ_{CR}(meV)	10	-169	40
Δ_{SO}(meV)	17	19	5
$m^*_{el}(m_0)$	0.2	0.3	0.07
$m^*_h(m_0)$	1	-	-
E^X_b(meV)	27	48	-
a^X_B(nm)	2.8	1.2	-

Table 1.4: Values of the band gap (at 0 K), the crystal field splitting and the spin orbit splitting in GaN, AlN and InN[16]. We have also reported the effective masses of the conduction band and of the uppermost valence band (only for GaN) [16, 33] at the center of the Brillouin zone as well as the value of exciton binding energies and Bohr radius [34, 35].

1.2.2 Optical polarization properties

The polarization selection rules can be established very easily using group-theoretical considerations. We have to know the symmetry of the initial and final states as well as the symmetry of the Hamiltonian. In our case, the dipolar Hamiltonian H_{em} (em stems for electromagnetic) describing the coupling to the electromagnetic field has the symmetry $\mathbf{\Gamma}_1$ for $\mathbf{E}||\mathbf{c}$ and $\mathbf{\Gamma}_5$ for $\mathbf{E}\perp\mathbf{c}$[27]. One transition will be allowed if the matrix element :

$$\langle u_h \mid H_{em} \mid u_{el} \rangle \tag{1.15}$$

is non vanishing. u_h (resp. u_{el}) is the wavefunction of the hole (resp. electron). In the language of group theory this is equivalent to :

$$\mathbf{\Gamma}_1 \subset (\mathbf{\Gamma}_h \otimes \mathbf{\Gamma}_{em} \otimes \mathbf{\Gamma}_{el}) \quad (= \mathbf{\Gamma}_{exciton} \otimes \mathbf{\Gamma}_{em}) \tag{1.16}$$

because we have seen that $\mathbf{\Gamma}_h \otimes \mathbf{\Gamma}_{el} = \mathbf{\Gamma}_{exciton}$. Starting from the symmetry of the exciton we get the complete picture as illustrated in table 1.5.

We conclude that the A exciton is allowed only for $\mathbf{E}\perp\mathbf{c}$ but the B and C excitons are allowed whatever the polarization.

1.2.3 Effect of the strain

Both the energy and the selection rules of the transitions are very sensitive to the strain which is present in the material. In the case of heteroepitaxy, the strain in the layers can be large (for instance the difference in lattice

Exciton	Representation	**E**⊥**c**	**E**||**c**
A	$\boldsymbol{\Gamma_5}$	✓	×
	$\boldsymbol{\Gamma_6}$	×	×
B and C	$\boldsymbol{\Gamma_1}$	×	✓
	$\boldsymbol{\Gamma_2}$	×	×
	$\boldsymbol{\Gamma_5}$	✓	×

Table 1.5: Polarization selection rules for the electronic transitions in the dipolar approximation

parameter a for GaN and AlN is 2.4 %) and gives rise to important effects. To quantitatively address this problem, one has to take into account the strain Hamiltonian in the Wurtzite structure (the so called Rashba-Sheka-Pikus (RSP) Hamiltonian). It was first studied by Pikus and Bir [36, 37]. They obtained the most general form of the Hamiltonian, taking into account symmetry considerations, and studied it in different cases. To treat the conduction band at the Γ point, one needs two parameters in the Hamiltonian, describing the influence of a strain along the c-axis (ϵ_{zz}) or perpendicular to the c-axis (ϵ_{xx},ϵ_{yy}):

$$H_c^{strain} = \alpha_{||}\epsilon_{zz} + \alpha_{\perp}(\epsilon_{xx} + \epsilon_{yy}) \tag{1.17}$$

following the notation of [38] for the conduction band deformation potentials α. The case of the valence bands is more complicated and it involves six deformations potentials labeled $D_1 - D_6$ (or $C_1 - C_6$ depending on the authors). We will not give the full strain Hamiltonian for the valence bands but it can be found, together with its study in different cases in the literature [32, 36–41]. One striking feature is that depending on the strain, the repartition of the ground state oscillator strengths on the 3 axes can change dramatically. In particular the selection rules for the fundamental transition can be very different from the ones of the A exciton of an unstrained layer and for instance the major part of the oscillator strength can be along the c-axis [38, 39, 41–44], which is a forbidden transition at vanishing strain (for an illustration see e.g. the figure 4 of reference [38]). In table 1.6, we report some values of the deformation potentials found in the literature. The quasicubic approximation [37], which treats the wurtzite structure like the closest cubic zinc-blende structure (these structures differ only from the third nearest neighbors) gives additional relations between the deformation potentials :

$\alpha_{\|\|}$	$\alpha_{\perp}$	D_1	D_2	D_3	D_4	D_5	D_6	a$_1$	a$_2$	References
-44.5	-44.5	-41.4	-33.3	8.2	-4.1	-4.7	-	-3.1	-11.2	[38]
-	-	0.7	2.1	1.4	-0.7	-	-	-	-	[32]
-	-	-	-	-	-	-	-	-8.16	-8.16	[45]
-	-	-	-	-	-	-	-	-4.09	-8.87	[46]
-	-	-	-	-	-	-	-	-6.5	-11.8	[47]
-	-	-15.35	12.32	3.03	-1.52	-	-	-	-	[48]
-	-	-	-	1.9	-1.0	-	-	-9.6	-8.2	[49]
-	-	-3.7	4.5	8.2	-4.1	-4	-5.5	-4.9	-11.3	[16]

Table 1.6: Deformation potentials (in eV) in wurtzite GaN for the conduction and valence bands. The hydrostatic deformations potentials a$_1$ and a$_2$ are defined by : a$_1$=$\alpha_{||}$-D_1 and a$_2$=$\alpha_{\perp}$-D_2

$$\begin{aligned} 2D_4 &= -D_3 \ , \\ D_1 - D_2 &= -D_3 \ , \\ \alpha_{||} &= \alpha_{\perp} = \alpha \end{aligned} \tag{1.18}$$

We will get back in details on the influence of the strains on the repartition of oscillator strengths along the 3 directions in part 2.4.3.

In the next part, we will focus on the optical properties which are a consequence of the electronic structure of the material.

1.3 Optical properties of bulk GaN

Keeping in mind the electronic properties of GaN, one can now address the issue of the optical properties which are our main concern. We will begin by general considerations concerning optical characterization methods and the informations they can give access to. Then we will focus on one original structure : thick semipolar 2D layers.

1.3.1 Experimental methods : what are we sensitive to?

The easiest way to characterize a material is to perform photoluminescence (PL). Generally, one performs this kind of experiment with a continuous wave (CW) laser and excite the material well above the band gap (244 nm = 5.1 eV in our case, see appendix B for the complete setup). Then the created carriers will relax by emitting phonons (thermalization), in a time short compared to the radiative recombination time. The thermalized electrons and holes may at this step recombine radiatively (for details about nonradiative recombination processes , see e.g. [50]). Considering that the luminescence comes from a population of thermalized carriers, the PL is a very sensitive probe of the low energy levels. At this point, we have to stress that the emissions that will actually be observed depends strongly on the quality of the sample.

Starting with an ideal sample (i.e. no chemical and structural defect), one should observe the luminescence of polaritons. An exciton formed by the binding of an electron and a hole in a semiconductor with a dipole allowed transition is indeed strongly coupled to the electromagnetic field. It implies that in very high quality samples, intrinsic optical properties have to be described in the strong coupling (polariton) picture [27, 51, 52]. Concerning GaN, some results on thick, high quality samples have been interpreted in this picture [53–55].

If one adds some disorder, the polariton effects are not relevant anymore but the dominant excitations can still be described in terms of free excitons FX (bound electron-hole pair). These free excitons can eventually recombine radiatively.

Adding some additional disorder, for instance some chemical impurities, the free excitons will then bind to these shallow defects (binding energy of typically a few meV) which create small potential traps. One thus sees the luminescence from bound exciton, for instance a donor bound exciton D^0X when the exciton is bound to a neutral donor (the most common ones are Si and O in GaN). The energy difference between the FX and D^0X transition is the donor binding energy and is related to the donor ionization energy [56]. To have a spectrum dominated by the D^0X emission at low temperature is typical for GaN bulk layers.

If one adds some more disorder, one can then create enough deep states in the band gap so that they will appear in a luminescence spectrum. The related transitions will then appear at much lower energy than the band gap. An example of such a transition is a donor acceptor-pair (DAP) [27]. The electron (resp. hole) is bound to the donor (resp. acceptor) and the dominant interaction is not the electron-hole one. But if they are close enough (i.e. the wave-functions overlap) they can recombine radiatively.

In PL, a way to discriminate excitonic and defect related luminescence can be to vary parameters such as temperature and excitation power or perform a polarization sensitive detection of the luminescence (see appendix B concerning this setup). For instance when rising the temperature, excitons bound

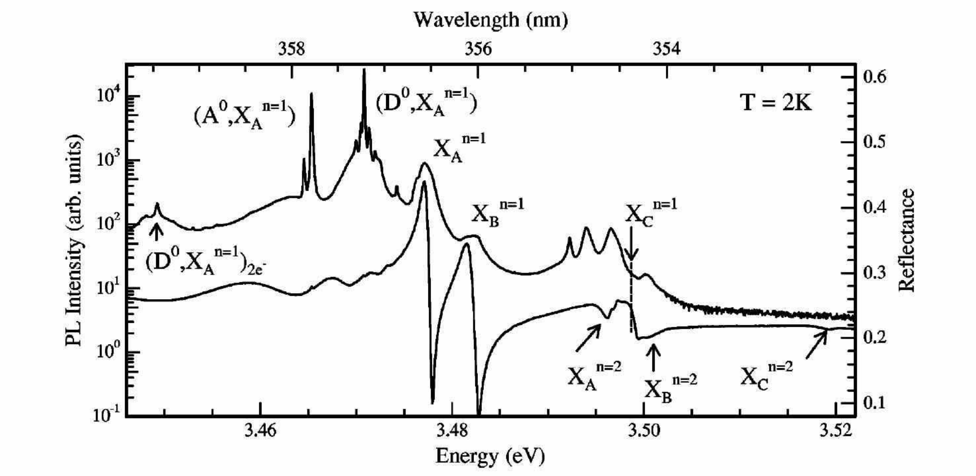

FIG. 1. Low-temperature PL and RF spectra of the homoepitaxial GaN layer in the band-edge region. The resolution is 0.12 meV

Figure 1.4: Comparison of PL and reflectivity spectra on a very high quality GaN layer at low temperature [57].

to shallow impurities (D^0X or A^0X for instance) will thermalize towards the free excitons and these luminescences of bound excitons will quench. Another kind of luminescence that will quench when rising the temperature is a free to bound luminescence (free electron with a hole bound on an acceptor for instance) because the neutral impurity can be ionized. An increase of the excitation power can produce a saturation of defects luminescence or blue shift a DAP luminescence [27, 52]. Polarization resolved PL can also give access to the selection rules and by this way discriminate between intrinsic and extrinsic luminescence. In fact, due to the change in the symmetry around the centers involved in extrinsic luminescence in comparison to the bulk material, the selection rules are relaxed.

Using a pulsed laser for the excitation and a time sensitive detection system (see appendix C for details about the setup), one can also perform time resolved photoluminescence (TRPL). Especially at low temperatures, when nonradiative processes can be frozen, this gives informations about radiative decay times. These decay times can help to determine the recombination mechanism involved because they carry informations about the electron-hole overlap. For instance a DAP recombination, involving different localization centers for the hole and the electron, will have a much longer decay time than a bound exciton recombination.

A very powerful experiment to gain insight into the band structure with-

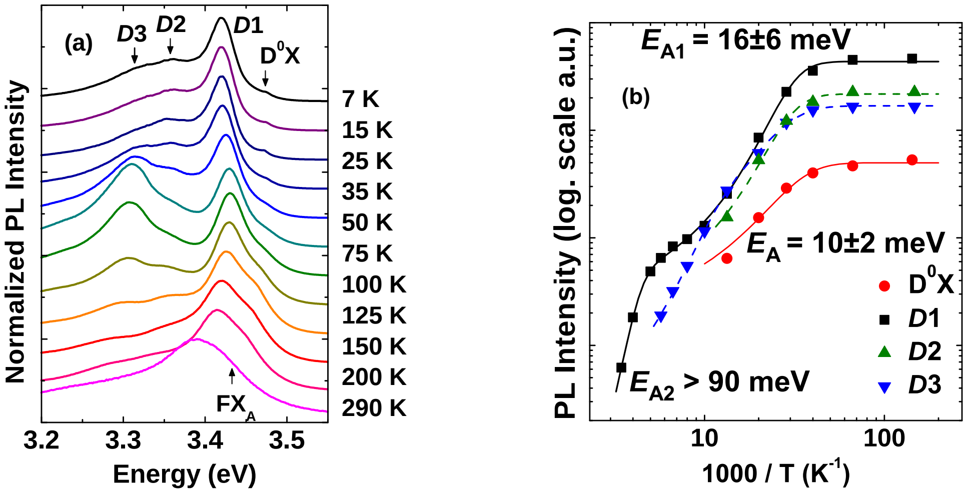

Figure 1.5: Temperature dependent PL of a 670 nm thick (11$\bar{2}$2) GaN layer (a) grown on m-sapphire and integrated intensity (b).

out being masked by the effects of the defects is reflectivity (or transmission which gives pretty much the same informations but is often more difficult to realize). In this kind of experiment one is sensitive to the dielectric function and consequently to both the density of states and the oscillator strength. Thus the spectra are dominated by intrinsic features (i.e. exciton or even polariton) even for typical samples with impurities concentration such that defects related features (especially D^{0}X or DAP) dominate the PL.

To summarize this part and illustrate the difference in PL and reflectivity, we present in figure 1.4 the reflectivity and PL spectra measured in ref. [57] at 4K on a bulk GaN substrate of high crystalline quality and purity (1.5 μm of GaN grown by metal-organic vapour-phase epitaxy on a GaN bulk single crystal prepared by the high-pressure high-temperature method [58]). The PL spectrum is dominated by the D^{0}X transitions (width around 100 μeV) and many other peaks are resolved thanks to the very high quality of the sample. On the other hand, the reflectivity spectrum is dominated by the free exciton transitions, which appear much weakly in PL.

1.3.2 Semipolar GaN

In this part, we will present an in depth optical characterization of semipolar (11$\bar{2}$2) GaN grown on m-plane sapphire. In recent years, this orientation has attracted much interest due to the fact that it is supposed to present the advantages of non polar directions (see 2.1), especially in terms of reduction of the internal electric field. But on the other hand the drawbacks of the non polar orientations, such as a strong in-plane anisotropy, are hoped to be reduced in the semipolar orientation. The molecular beam epitaxy (MBE) growth is described elsewhere (see appendix F and [59, 60]). Let us stress that the study of a semipolar layer is not equivalent to the study of a tilted c-plane layer even for a bulk layer with no heterostructure. The growth and substrates are indeed different and the improvement of semipolar heteroepitaxial GaN is still under progress. In figure 1.5 we present the evolution of the PL with the temperature together with the dependence of the intensity with temperature for the different lines. PL at low temperatures is dominated by a peak at 3.42 eV (D1). The donor bound exciton D^0X appears as a shoulder at higher energy (3.473 eV) and the activation energy of its thermal quenching around 10 meV (see figure 1.5(b)) tends to support this interpretation. The position of this peak confirms the x-rays which indicated that the layer is fully relaxed [60]. Two other contributions appear at 3.30 eV (D3) and 3.35 eV (D2). The position of the free exciton at room temperature (provided the band gap follows a Varshni law [16]) is indicated by an arrow. It allows us to conclude that the room temperature PL spectrum is dominated by the D1 emission. We tentatively attribute this line to the recombination of excitons bound to stacking faults because it presents the same temperature behavior than what was seen in GaN with other orientations [61–65]. As seen in figure 1.5(b), where the intensity is plotted as function of temperature for each peak, one needs two activation energies to fit the thermal quenching of this peak. One is rather small around 16 meV and the other one is much larger, more than 90 meV. On the other hand, the lines D2 and D3 were attributed to transitions involving deeper states, related to structural defects [64–66]. Their thermal quenching are rather fast, with activations energies similar to the D1 line.

TRPL measurements (see appendix C for the setup description) at low temperatures on these lines give additional informations confirming our assumptions as exemplified in figure 1.6. On the one hand, the D^0X and D1 lines have short decay times between 50 and 80 ps. On the other hand, the D2 and D3 lines, in addition to a rapid decay around 140ps (1/e decay time), have an important part of their luminescence decaying much slower. In the experiment presented in figure 1.6(a), performed with pulses every 13 ns, one sees that the luminescence of these lines decays only by slightly more than one order of magnitude between two pulses. We thus performed experiments with a delay of 1.1 μs between two pulses. The figure 1.6(b) shows that a decay of two orders of magnitude of the luminescence of D2 and D3 is only

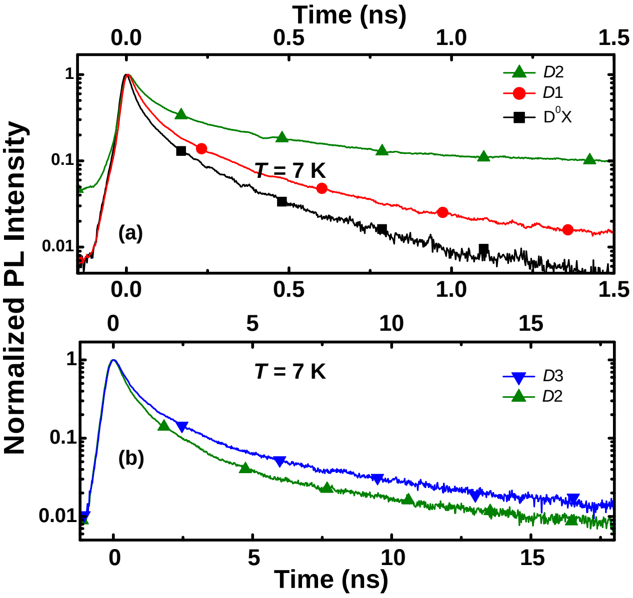

Figure 1.6: TRPL of a $(11\bar{2}2)$ GaN layer at low temperature. In (a) the repetition rate is 76 MHz (13ns) and 0.9MHz (1.1μs) in (b).

obtained after almost 20 ns as a consequence of a broad distribution of decay times. The presence of a rapid decay suggests nevertheless that electron and holes are not separated [66]. On the other hand DAP recombinations, where electron and hole wavefunctions do not overlap well, do not usually present such short 1/e decay times. Together with the small activation energies [61], it seems that DAP can be ruled out as the origin of this luminescence. So far it is difficult to be more conclusive than attributing these lines to electron and holes bound to structural defects.

1.4 Heterostructures

In this part we will describe how the electronic properties evolve when one confines the carriers in an heterostructure made of wurtzite crystals. The consequences on the optical properties and the strong differences between polar and non polar heterostructures will be discussed. We will not present general considerations concerning the electronic properties of het-

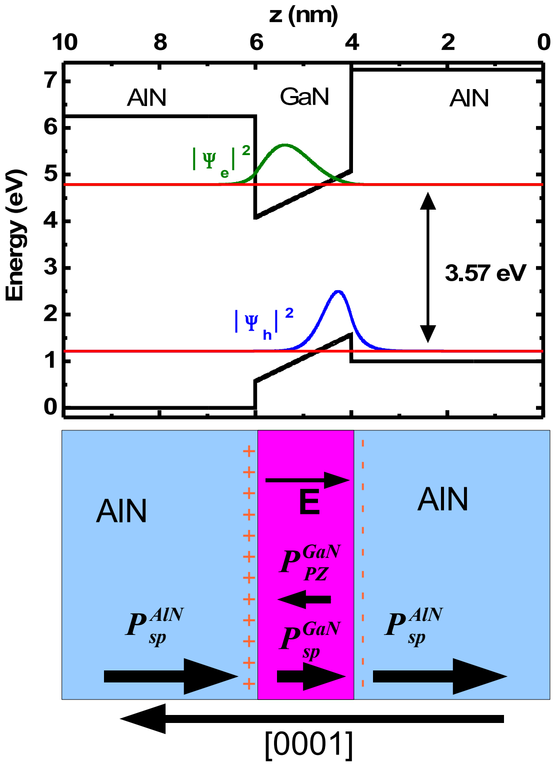

Figure 1.7: Polar QW: illustration of the effect of the electric field. We considered a 2 nm thick GaN/AlN QW with a field of 5MV/cm (for simplicity, the electric field is assumed to be screened in the barriers). The bottom part shows the structure with the different contribution to the polarization. The upper part presents the calculated band structure , with the electron (resp. hole) probability density distribution $|\Psi_e|^2$ (resp. $|\Psi_h|^2$).

erostructures, nevertheless one can refer to textbooks treating this topic in details [27, 52, 67].

1.4.1 Polarization and its consequences

In part 1.1.2, we saw that any discontinuity of polarization will create a charge sheet according to equation 1.7. For instance, for a [0001] oriented GaN quantum well (QW) inserted in AlN barriers, each interface will carry a charge sheet of opposite sign. It will result in the presence of an electric field inside the QW. Using the simple capacitance model for this structure or writing the conservation of the electric displacement **D** (here we consider only the normal component of **D** for our one dimensional problem) one obtains the electric field **E** inside the QW, provided the doping is negligible, the barrier is much thicker than the well (thickness L) and the two materials have the same dielectric constant ϵ_r (ϵ_0 is the vacuum permittivity) :

$$\mathbf{F_{QW}} = \frac{\mathbf{\Delta P}}{\epsilon_0 \epsilon_r} \tag{1.19}$$

The presence of this electric field has two main consequences. It bends the conduction and valence bands inside the QW and spatially separates the electron and hole wave function [68]. This effect is named the quantum confined Stark effect (QCSE). It thus lowers the energy of the optical transitions and reduces their oscillator strength. The energy of the fundamental transition is now given by [69]:

$$E = E_g(\mathrm{GaN}) + E_c^e + E_c^h + E_b^{eh} - e.F_{QW}.L \tag{1.20}$$

where E_g(GaN) is the gap of GaN, E_c^e and E_c^h are the confinement energies of the electron and the hole in the triangular potential of the QW, E_b^{eh} is the electron-hole binding energy and e the charge of the electron. The situation is illustrated in figure 1.7. One should pay attention to the direction of the electric field. For a structure grown along the $+\mathbf{c}$ direction, the electric field is positive along the $-\mathbf{c}$ direction and the electrons (resp. holes) tend to be in the upper (resp. lower) part of the well. The ways to show the QCSE in PL experiments is to study both the energies and decay times of the luminescence as a function of the well thickness. The energies decrease much faster than what is expected from the confinement effect and eventually the structure luminesces below the band gap of the bulk material. The decay times increase dramatically with the thickness as a consequence of the reduced electron hole overlap (see figure 1.8) [14, 70].

1.4.2 Non polar versus polar heterostructures : Quantum wells

The QCSE in polar heterostructures is an important drawback for the realization of GaN based devices light emitting in the UV or for the realization of InGaN based devices with a high In content. The reduction of the oscillator strength limits output power of the devices. Furthermore, the strong electric field makes the output wavelength very sensitive to variation of the input current that can screen the field. Consequently people have tried to get rid of the electric field by growing structures along other directions than [0001]. In fact, we will see that the QCSE can be strongly reduced or even suppressed in heterostructures grown along other orientations.

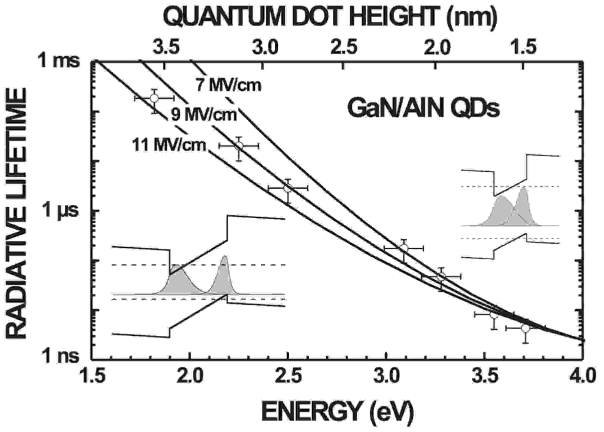

FIG. 3. Measured radiative lifetime (circles) versus measured energy of PL peak for the different QD samples. Solid lines show the calculated value of lifetime as a function of energy of the fundamental transition for an effective electric field of respectively 7, 9, and 11 MV/cm and $A=90$ (see text). The calculated QD height corresponding to the transition energies for a 9 MV/cm electric field is reported on the top axis. The electron and hole energy levels and wave functions are sketched in the regimes dominated by Stark effect (left) and quantum confinement (right).

Figure 1.8: Illustration of the QCSE in polar GaN/AlN quantum dots. One sees the red shift of the luminescence together with a strong reduction of the oscillator strength as the thickness of the dots increases [14]. The GaN bulk band gap is around 3.5 eV.

We have seen in 1.1.2, that in order to create a charge sheet at an interface, there must be a discontinuity of the normal component of the polarization. Thus for a QW, one has to consider only the polarization along the growth axis. For a growth along [0001], due to the difference of polarization (sum of spontaneous and piezoelectric polarization) between the barrier and the well along [0001], an electric field is present, as detailed in 1.4.1. In certain situations, the spontaneous and piezoelectric polarization differences can be compensated so that the total polarization is equal in the well and barrier materials. Let us check under which conditions this would be fulfilled for a polar GaN/AlN quantum well. Using equation 1.6 one can write that one needs $P_{sp}^{GaN} + P_{pz}^{GaN} = P_{sp}^{AlN} + P_{pz}^{AlN}$. Assuming a pseudomorphic structure, one can calculate the in-plane lattice parameter a :

$$a = \frac{a_{Al}.a_{Ga}(\frac{P_{sp}^{Ga}-P_{sp}^{Al}}{2} + d_{31}^{Al}(c_{11}^{Al} + c_{12}^{Al} - \frac{(c_{13}^{Al})^2}{c_{33}^{Al}}) - d_{31}^{Ga}(c_{11}^{Ga} + c_{12}^{Ga} - \frac{(c_{13}^{Ga})^2}{c_{33}^{Ga}}))}{a_{Ga}(d_{31}^{Al}(c_{11}^{Al} + c_{12}^{Al} - \frac{(c_{13}^{Al})^2}{c_{33}^{Al}})) - a_{Al}(d_{31}^{Ga}(c_{11}^{Ga} + c_{12}^{Ga} - \frac{(c_{13}^{Ga})^2}{c_{33}^{Ga}}))} \tag{1.21}$$

where Ga (resp. Al) stems for the parameters of GaN (resp AlN). This gives an in-plane lattice parameter of 2.548 Å. It means a strain of -20.1 % for GaN and -18.1 % for AlN. It is totally unrealistic to grow such a structure because such a strain will be relaxed immediately. Thus one can conclude that there will be an important electric field in any (0001) GaN/AlN QWs. Let us stress that for ternary or quaternary alloys, the electric field can be significantly reduced thanks to a decrease of the polarization discontinuities [71].

For non polar QWs, the situation is very different. For instance for a $(1\bar{1}00)$ GaN/AlN QW (m-plane), we have to study whether there is a discontinuity of polarization along $[1\bar{1}00]$. There is no spontaneous polarization along this axis thus we should look carefully to the effect of the piezoelectric polarization. A piezoelectric polarization along a non polar axis arises only from a shear strain, as seen in 1.3. For instance for P_1 :

$$P_1 = d_{15}c_{44}\epsilon_{13} \tag{1.22}$$

A non vanishing value of ϵ_{13} means a shear strain in the growth plane. For a QW, due to the in-plane invariance, the in-plane shear strain must vanish and thus $P_1 = 0$. One concludes that, regarding the out-of-plane component, both spontaneous and piezoelectric polarizations vanish. Eventually it leads to the absence of electric field and consequently no QCSE in any non polar QW. This was first demonstrated in ref. [72] for m-plane QWs.

1.4.3 Non polar versus polar heterostructures : Quantum dots

For quantum dots, the situation is more complicated because we have no in-plane invariance any more. Thus, because of the facets of the QDs, we have to take into account the discontinuity of the polarization along the 3 axis. Considering that we only want to get qualitative results in this discussion, we will consider that we still can use the point group of the bulk material (C_{6v}) in the description of the polarization. This is not rigorously true [73, 74] but this has been used even for detailed calculations [75–77].

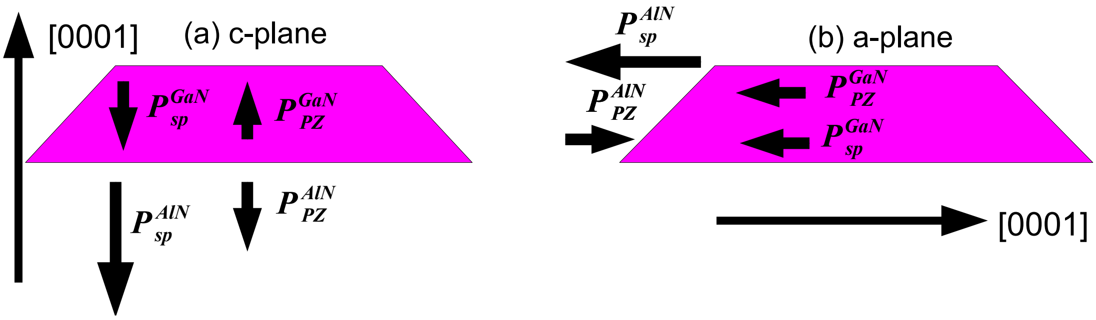

Figure 1.9: The different contributions to the polarization difference in c-plane (a) and a-plane QDs (b) grown on SiC [78]

Using the piezoelectric coefficients e_{ij} (see 1.1.2), one can write the expression of the piezoelectric polarization [76] :

$$\mathbf{P_{pz}} = \begin{pmatrix} 2e_{15}\epsilon_{13} \\ 2e_{15}\epsilon_{23} \\ e_{31}(\epsilon_{11} + \epsilon_{22}) + e_{33}\epsilon_{33} \end{pmatrix} = \begin{pmatrix} P_{shear,1} \\ P_{shear,2} \\ P_{axial} \end{pmatrix} \tag{1.23}$$

This polarization should be added to the spontaneous one, namely (we recall that z is the $\mathbf{c}$ direction) :

$$\mathbf{P_{sp}} = P_{sp}.\mathbf{e_z}$$

The strain inhomogeneity can create a polarization gradient inside the quantum dot but for the sake of simplicity we will consider a mean value of the strain in our discussion. In principle, one should take into account the polarizations arising from shear strain in QDs : $P_{shear,1}$, $P_{shear,2}$. Nevertheless, the shear is highly inhomogeneous in QDs and one cannot reasonably assume an average strain in order to get an estimation of the electric field. Also, due to symmetry, the electric field cannot be constant along the non polar directions in a QD. Thus more realistic calculations are required. For this reason we will only consider the component of the polarization along [0001] in our discussion and present general tendencies shown by detailed results concerning the effect of the other components [75–77, 79]. We will now first address polar QDs and then focus on non polar QDs. The corresponding situations with the different contributions are illustrated in figure 1.9.

Polar QDs

In this case, as illustrated in figure 1.9, there are two differences to take into account : the difference ΔP_z along the growth axis [0001] will create charge sheets at the top and bottom interfaces. But this difference will also create charge sheets on the facets because in real QDs the c-axis does not lie in the facet planes (this would be the case for cuboid QDs). We can write $\Delta P_z = \Delta P_{sp} + \Delta P_{pz}$ where ΔP_{sp} =0.052 Cm^{-2} and ΔP_{pz} will depend on the strain state. Although a rigorous calculation should consider the inhomogeneity of the strain state in the QDs [76], we will consider it homogeneous. For a growth on a relaxed AlN buffer (thick AlN on sapphire for instance) we thus have $\Delta P_{pz} = P_{pz}^{GaN} = e_{31}(\epsilon_{11} + \epsilon_{22}) + e_{33}\epsilon_{33}$. Considering a biaxial strain and that $\epsilon_{11} = \epsilon_{22} = \frac{a_{AlN} - a_{GaN}}{a_{GaN}} = -0.024$ one gets ΔP_{pz}=0.038 Cm^{-2} [77]. The total polarization difference is thus ΔP_z =0.09 Cm^{-2}. For a growth on 6H-SiC, the situation is different because we have to take into account the strain in the AlN. Following Cros et al. [78] one gets ΔP_z=0.073 Cm^{-2}.

Regarding the facets, the angle ϕ with respect to the c-axis is important. It is around 60° [80] and thus $\sin\phi = \frac{\sqrt{3}}{2}$. The density of charges on the facets given by this contribution is thus reduced compared to the density on the top and bottom interfaces.

We have now to estimate the electric field along [0001] and in the QD plane with the polarization discontinuities we have calculated. For the [0001] direction, one can use the expression of the electric field inside a capacitance of finite dimensions as illustrated in 1.10(a):

$$F(z) = \frac{\sigma}{\pi\epsilon_0\epsilon_r}\Bigg[\arctan\left(\frac{a.b}{(\frac{h}{2} - z)\sqrt{a^2 + b^2 + (\frac{h}{2} - z)^2}}\right) + \arctan\left(\frac{a.b}{(\frac{h}{2} + z)\sqrt{a^2 + b^2 + (\frac{h}{2} + z)^2}}\right)\Bigg] \tag{1.24}$$

where a and b are the dimensions of the sheet and h the distance between them. For square sheets of size 20 nm with a distance of 2 nm, it gives a value of around 9.6MV/cm (resp. 7.8 MV/cm) if the QD is strained on AlN (resp. grown on SiC) and the dependence on the vertical dimension and position is negligible (see figure 1.10(a)).

Concerning the in-plane field, the facets both carry charges of the same sign. The resulting electric field is plotted in figure 1.10(b). One sees that the electric field depends strongly on the lateral position. Nevertheless the value

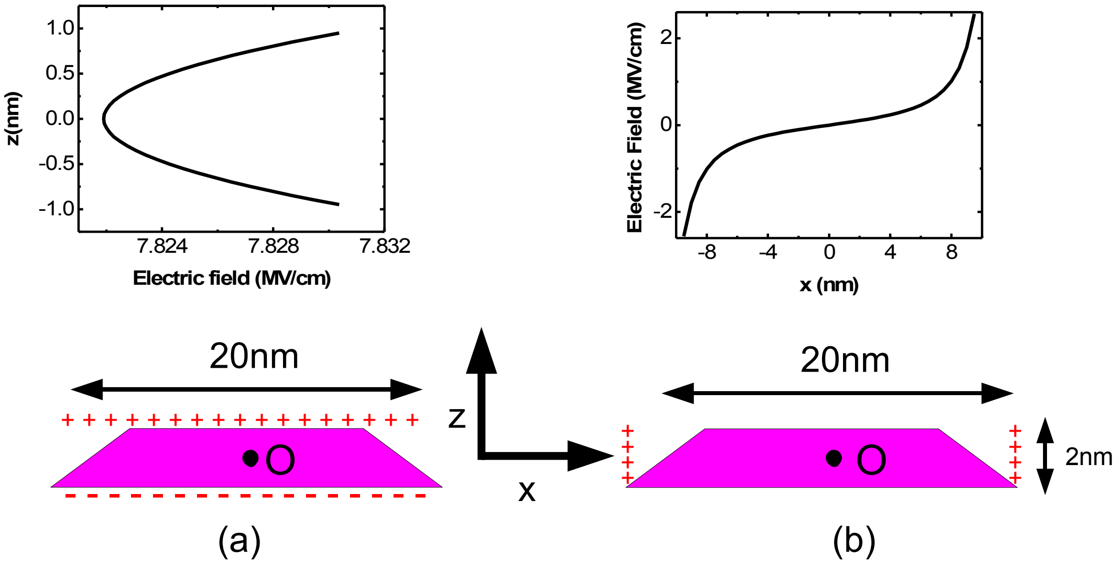

Figure 1.10: Model for the calculation of the electric field inside a polar QD. In (a), the field along the c-axis and in (b), the in-plane field. The size of the sheet is 20x20 nm (distance h =2 nm) in (a) and 20x2 nm (distance 20 nm) in (b). The center of the dot is the point x=y=z=0 for the plots. Let us note that for (b), the area where the electric field becomes significant are only the sides. Here the electric field is likely to be screened by the bottom facet charges that are not taken into account in this calculation. Anyway the exciton is localized in the center of the dot, thus the exact profile of the electric field in this area has few consequences on the exciton.

is below 1MV/cm in more than 80% of the QD (for the case of ΔP_z=0.073 Cm^{-2}). It certainly creates an additional in-plane confinement as suggested in [76] . In this article, they performed more sophisticated calculations of this in-plane field, including shear strain (but with the uncertainty about the value of e_{15}), and they extracted values reaching 1 MV/cm [76]. Concerning the additional lateral confinement, one should mention that due to the fact that we do not take the wetting layer into account in our simple model, our calculated electric field is certainly more realistic in the upper part of the dots, where the electron is localized. Our model does indeed suggest the additional lateral confinement for the electron in this part. The lateral confinement of the hole at the bottom of the dot necessitates more realistic calculations and should take into account the strain not only for the built-in potential determination but also for the conduction and valence band egdes

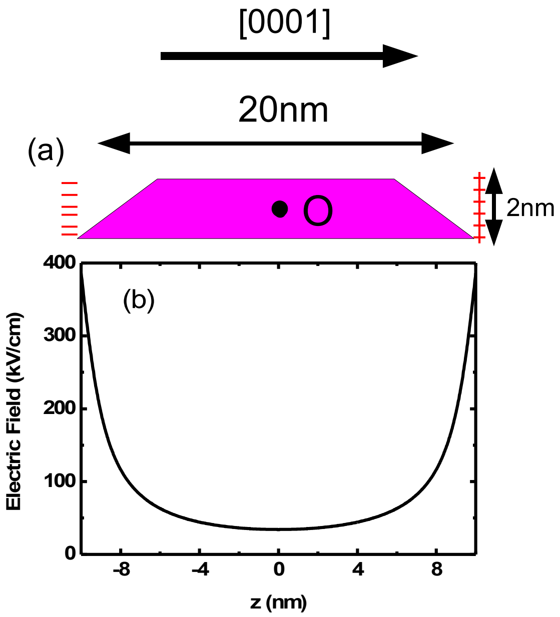

Figure 1.11: Electric field in a-plane QDs grown on SiC. The model is depicted in (a). In (b), we present the variation of the in-plane electric field along the c-axis.

calculations [75, 76].

From the simple discussion made in this part, one can conclude that for polar QDs, there will be a huge electric field along the growth direction in the order of 7-10 MV/cm. Furthermore, the effect of an in-plane electric can be neglected in first approximation.

Non polar QDs

In this case we have to consider the charges on the facets which will create an in-plane electric field. These facets form an angle ϕ of roughly 30° with respect to the c-axis [81]. The electric field will be proportional to $\Delta P \sin\phi$. Following Cros et al. [78] for (11-20) QDs on a SiC substrate, one gets $\Delta P = -0.012$ C.m^{-2}. The important point in this case is that the piezoelectric contribution tends to decrease the spontaneous one resulting thus in a much smaller polarization difference. One can make the calculation for a relaxed AlN in the biaxial approximation (although it is supposed to fail in QDs [82]). We thus have : $\epsilon_{33} = \frac{c_{AlN}-c_{GaN}}{c_{GaN}} = -0.039$, $\epsilon_{22} = \frac{a_{AlN}-a_{GaN}}{a_{GaN}} = -0.024$.

The strain along the growth axis is given by the biaxial approximation :

$$\epsilon_{11} = \frac{-C_{12}\epsilon_{22} - C_{13}\epsilon_{33}}{C_{11}} = 0.019$$

And the piezoelectric polarization in GaN is $P_{PZ} = -0.032$ C.m^{-2}. The total polarization difference is then $\Delta P = -0.020$ C.m^{-2}. Let us now turn to the electric field. We use the simple model described in figure 1.11(a). In contrast to the polar case, the dependence when moving along the c-axis is not negligible. This is illustrated in figure 1.11(b). Nevertheless at the center of the dot, the electric field is reduced to 32 kV/cm. To summarize this discussion, we have plotted in figure 1.12 the electrostatic potential along the [0001] direction in the case of the polar and non polar QDs studied in this part. This clearly illustrates the expected strong reduction of the effects of the electric field in non polar QDs. Furthermore, due to the small area of the facets, the total charge carried will be much smaller than on the other interfaces and this can be screened by residual doping. This effect would again reduce the electric field in non polar QDs.

The effect of shear strains and inhomogeneity

In the previous discussion we neglected the effects of the shear strain and considered an homogeneous strain in a QD. The first one is responsible for polarization variations along the non polar axis, see equation 1.23. The strain inhomogeneity is responsible for polarization variation inside (and also outside) the QD creating a charge density in the material : $\rho = -\nabla \mathbf{P}$. This density of charges ρ will influence the built-in potential inside the dot in addition to the contribution of the interfaces. Besides, for transition energies and wave functions calculations, one should take into account the strain inhomogeneity. The strain inhomogeneity, with a more relaxed GaN at the center of the dot [82], at least for c-plane QDs, suggests an additional lateral localization mechanism in addition to any built-in field induced lateral localization [75, 76].

In [77], the authors studied in details the various contributions to the electrostatic potential for both a-plane and c-plane QDs. One has to point out that they considered GaN embedded in relaxed AlN. This assumption , especially for a-plane QDs, has certainly an effect on the conclusions drawn. Thus one should be careful in extrapolating some conclusions to the case of GaN/AlN QDs grown on SiC. Nevertheless they show that for polar QDs, whatever the sign of e_{15}, the effect of the shear strain is negligible along the c-direction. The main contributions come (with roughly the same magnitude) from the spontaneous polarization and the axial part of the piezoelectric

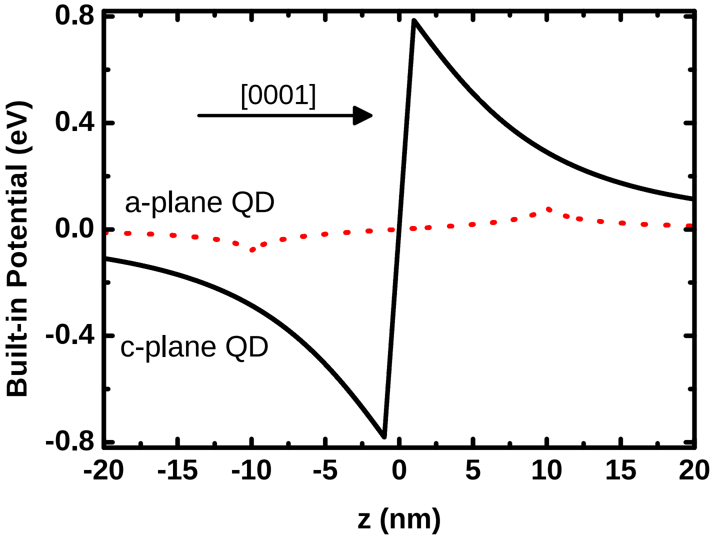

Figure 1.12: Comparison of the built-in potential along the c-axis (going through the center of the dot) in polar (thick line) and non polar QDs (dotted line). The QDs have the same shape, namely 20x20 nm in the growth plane and are 2 nm thick.

polarization. For polar QDs, the shape of the quantum dot has also very few effects on the electrostatic potential. The situation is very different for a-plane QDs. To have reduced potential variations inside the QDs, the authors show that one needs a negative value of e_{15} which will then give an opposite contribution to the spontaneous and axial parts. The shape of the QDs has been studied by varying the angle of the facets in a truncated pyramid. The peak electrostatic potential is strongly affected, decreasing when slopping the facets.

To conclude, we would like once again to mention that realistic calculations require a good knowledge of the strain in the QD and its surrounding as well as accurate values of the piezoelectric constants. That is why so far, it is difficult to have reliable quantitative conclusions.

In this chapter, we have presented the peculiarities of III-N semiconductors that are required to understand their optical properties. Their wurtzite structure gives them a unique behavior and we have seen that due to both the internal and piezoelectric polarization, heterostructures grown along the c-axis present a strong quantum confined Stark effect. The electric field can indeed reach 10 MV/cm. We dealt with non-polar heterostructures and showed that the electric field should be suppressed in quantum wells. For quantum dots, the situation is not so obvious but a simple modelization allowed us to conclude that it should be strongly reduced.

Chapter 2

Peculiarities of non polar GaN nanostructures : polarization and time resolved studies of the luminescence

In chapter 1, we presented general considerations about the band structure (see 1.2) and the effect of the growth orientation on the electronic properties (see 1.4). In this part, we will focus on the optical spectroscopy of non polar nanostructures, both m and a-plane, and show some peculiarities : the strong reduction of the QCSE and the in-plane polarization anisotropy.

Contents

2.1 Why study non polar GaN nanostructures?

2.1.1 On the interest of non polar nanostructures

As already pointed out in 1.4.2, when grown along the c-axis, GaN/AlN nanostructures present a huge electric field. One “usable” consequence is that it allows to tune the emission wavelength on a very broad range (typically 300-650 nm) [83, 84] but the drawback for the realization of light emitting devices is that the oscillator strengths considerably decrease when the wavelength increases. This can limit the efficiency for quantum wells based devices in which nonradiative processes are important. If one wants to have a radiative lifetime below a few ns, one thus needs to restrict oneself to wavelengths below 350 nm for GaN/AlN nanostructures [70, 85] and below 450 nm for InGaN/GaN nanostructures [86]. Also, the sensitivity of the wavelength emission to the carrier injection density (due to the screening of the electric field [87]) is a problem for reliable devices. Thus it has been tried to grow structures in the Zinc Blende phase [88–91] or along non polar (and semipolar) orientations of the wurtzite structure [72, 92–97]. The main problem for these structures is, like c-plane nitride 15 years ago, the very high density of defects resulting partly from the lack of adapted substrate. Nevertheless, recent progress in the fabrication of very low dislocation density GaN (as low as 10^6 cm^{-2}) and high quality bulk GaN substrate [98–101] that can then be sliced in a non polar plane [102] have lead to substantial breakthroughs [93].

From the optical point of view, non polar heterostructures present many interesting properties. First of all, the QCSE is supposed to be strongly reduced. Concerning QWs, this has been demonstrated for GaN/AlGaN grown along the m-plane [72, 103] and a-plane [104–107]. Concerning QDs, this has been demonstrated by our group for the a-plane [78, 108–110] and during this work for m-plane [111, 112]. Another interesting point of non polar samples is that one can study the optical anisotropy between the c-axis and a non polar axis much more conveniently than for polar samples (for which one should work on the side of the sample). The optical anisotropy has been studied in various structures and orientations [104, 106, 109, 113–115]. During this work we specifically addressed the issue of m-plane QDs and the impact of the strain in a-plane QWs.

2.1.2 Evidence for QCSE reduction in m-plane QDs

The m-plane QDs samples were grown by B. Amstatt during his thesis [116]. The MBE growth on m-plane 6H-SiC has been studied extensively and

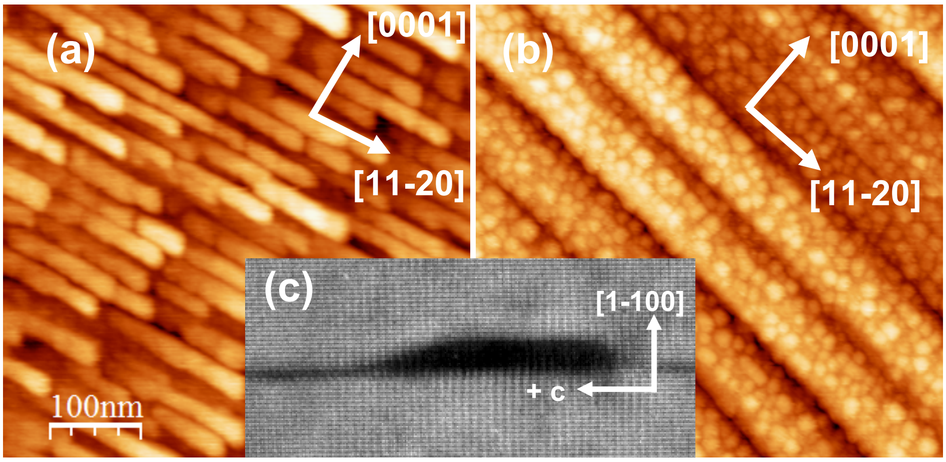

Figure 2.1: Illustration of the wires (a) and dots (b) geometry (AFM image: B. Amstatt). The structures are aligned along the [11$\bar{2}$0] direction. The inset (c) shows a TEM image (C. Bougerol) of a quantum dot viewed along the [11$\bar{2}$0] zone axis (scale is given by the spacing in the c-plane : 0.25 nm).

it has been shown that under Ga rich conditions two key parameters govern the structures obtained : the strain state of the AlN buffer and the quantity of deposited GaN [111, 117, 118]. From the structural point of view, one can obtain two kinds of nanostructures, namely QDs and QWires (see the atomic force microscope (AFM) and transmission electron microscope (TEM) images in figure 2.1). From the optical point of view (apart from the sensitivity to nonradiative processes, as we will see later), these structures have similar properties. We have performed several studies in order to demonstrate the strong reduction of the QCSE.

First of all, we measured the CW PL as a function of the size of the nanostructures (i.e. the deposited GaN). The results are presented in figure 2.2 for both dots (thick AlN buffer) and wires (thin AlN buffer). One sees that even for large amounts of deposited GaN, the luminescence is still above the GaN band gap. This is one first evidence of the strong reduction of QCSE in comparison with c-plane nanostructures. In this latter case, the QDs luminesce indeed below the GaN band gap for thicknesses above ≈2 nm.

Another indication was obtained in PL experiments as a function of the excitation power. In fact, for polar structures a blue shift of the PL with the density of injected carriers is observed, as a consequence of the screening of

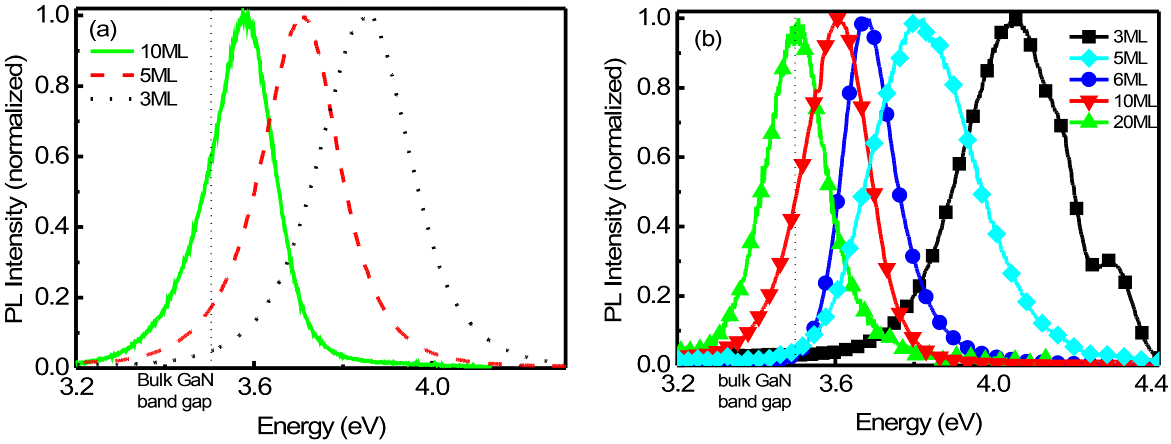

Figure 2.2: Low temperature PL of m-plane GaN wires (a) and dots (b) as a function of the amount of deposited GaN.

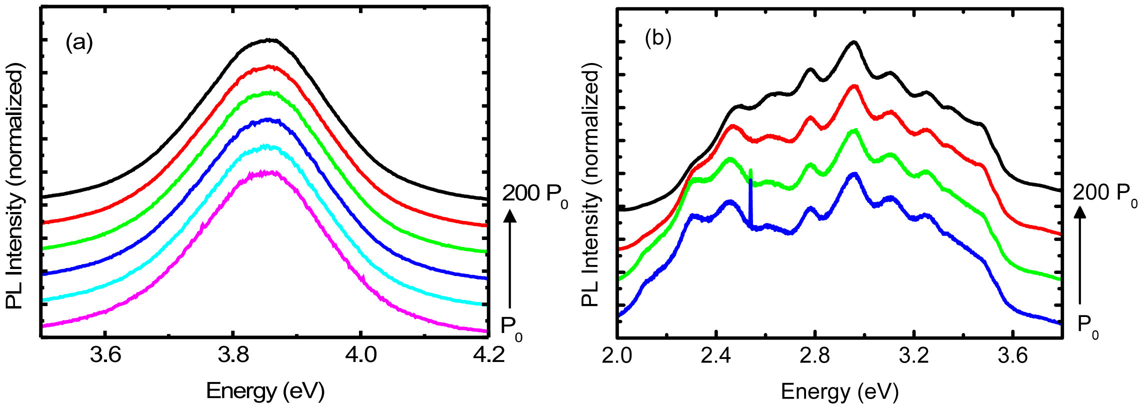

Figure 2.3: Comparison of the power dependence of the PL for m-plane (a) and c-plane (b) QDs. In both cases $P_0 \approx 100$ mW.cm^{-2}. The measurements are performed at low temperature. The excitation energy is 5.1 eV. The curves have been vertically shifted for clarity. No change is seen for m-plane (a) but the situation is different for c-plane (b), especially on the low energy part, where screening occurs above 10 P_0.

the internal electric field [119]. We present the study on m-plane nanostructures in figure 2.3(a). The PL presents no shift over more than two orders of magnitude of excitation power and the situation is very different in c-plane QDs as illustrated in figure 2.3(b). One has to emphasize that the powers used in the two experiments (m-plane / c-plane) are comparable. Thus it means that for c-plane QDs, considering that no screening occurs below 500 mW.cm^{-2}, one can say that the injection is below 1 e-h pair per dot (let us stress that these densities are in accordance with what has been reported in the litterature [119]). Above this limit, additional e-h pairs start to screen the electric field and one sees the shift of the PL. One can conclude that 10 μW correspond roughly to 1 e-h pair per dot. Provided the absorption in m-plane QDs is comparable (the exciting laser is at 5.1 eV and should for both c-plane and m-plane QDs be absorbed in WL states), one can compare the excitation powers. Thus one can conclude that in m-plane QDs, even for an injection rate above 1 e-h pair per dot, no shift is seen which means that no "measurable" electric field has to be screened. To rule out the presence of QCSE, the best evidences come from TRPL. The radiative decay times are indeed very good probes of the e-h overlap and any electric field should separate the carriers, even slightly, and increase the decay times. In figure 2.4, we present TRPL at low temperature on m-plane nanostructures of different sizes. One can see that whatever the size of the nanostructures, the decay times (1/e decay) remain short, below 300 ps. Furthermore, no increase with size is measured. It means that the electron hole overlap does not change significantly when the size of the dots increases. This is very different from what is observed in c-plane nanostructures as already mentionned (see for instance figure 1.8 in chapter 1). The influence of the size of the nanostructures on the decay time is in this latter case impressive. Let us note that even a small electric field should significantly increase the decay time in large nanostructures. These experiments confirm the strong reduction of QCSE in m-planes nanostructures.

2.2 m-plane Quantum Dots : polarization anisotropy and study of the nonradiative processes

2.2.1 Polarization studies

We explained at the beginning of this chapter that due to the in-plane anisotropy of a plane containing the c-axis, these kinds of samples are well suited to study the anisotropy of the optical properties. We saw in part 1.2.2 that we can expect a strong anisotropy of the optical properties, particularly

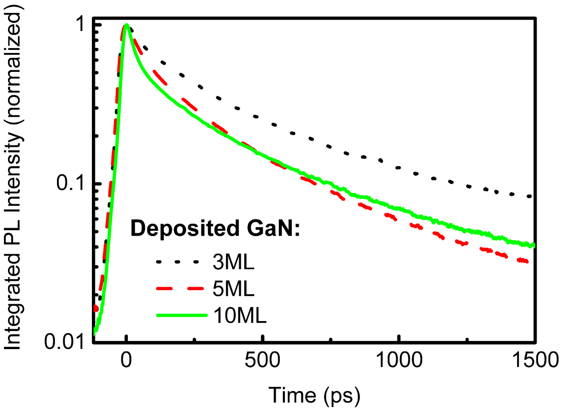

Figure 2.4: TRPL at low temperature on m-plane nanostructures for different amount of GaN deposited on a 50 nm AlN buffer (i.e the structures are wires).

for the ground state (hole of symmetry $\mathbf{\Gamma}_9$, i.e. the A valence band) which is forbidden for $\mathbf{E}||\mathbf{c}$ in an unstrained material. Recently, a complete in-plane anisotropy of the A-exciton was measured by reflectivity on a-plane unstrained bulk GaN [120] and a value above 90 % was measured for the D_0X_A exciton in PL for an unstrained m-plane layer [121]. In figure 2.5, we present a 3D plot of the PL intensity as a function of both energy and polarization on m-plane QDs (3 MLs on a 320 nm AlN buffer) and QWires (5 GaN MLs on a 50 nm AlN buffer). Let us first note that the 400 meV shift between the two samples is likely due to a small height difference (1 ML difference would lead to a shift of 200 meV) that could be expected from the amount of deposited GaN (3 MLs versus 5MLs). A 400 meV shift induced by the QCSE in the wires would also imply that the electron and the hole are seperated. This would have for consequence a vanishing oscillator strength, which is not the case, as we will see later (see figure 2.8(a)). Focusing on the polarization of the luminescence of figure 2.5, one can see that the intensity strongly depends on the angle with respect to the c-axis for both samples. The angle dependant integrated intensity is fitted by the function

$$I(\theta) = \cos^2\theta + P\sin^2\theta \tag{2.1}$$

where P is the fitting parameter and θ the angle with respect to the $[11\bar{2}0]$ axis. The resulting fits are presented in the inset of figure 2.5. One can also

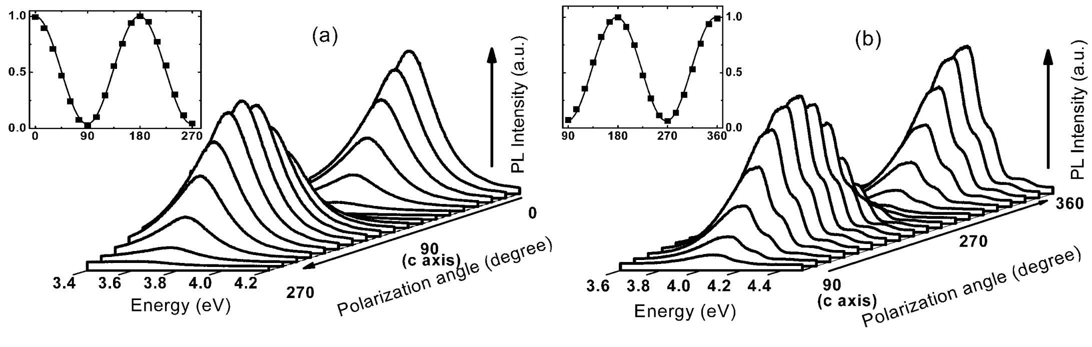

Figure 2.5: 3D plot of the PL intensity as a function of the energy and polarization angle for m-plane QWires (a) and QDots (b). The measurements are performed at low temperature. The insets shows the integrated PL intensity dependence on the polarization angle and a fit by function 2.1.

define the degree of polarization (DOP) ρ :

$$\rho = \frac{I_{[11\bar{2}0]} - I_{[0001]}}{I_{[11\bar{2}0]} + I_{[0001]}} = \frac{1-P}{1+P} \tag{2.2}$$

One obtains an energy averaged DOP as high 92%±2% for the wires and 88%±2% for the dots. In figure 2.6, we illustrate the energy dependance of the DOP. The situation looks at first sight different for dots and wires. On the one hand, for the dots both polarizations have a well defined maximum and the DOP is almost constant over the entire energy range. On the other hand, for wires the PL does not have a clear maximum for $\mathbf{E}||\mathbf{c}$ and the DOP strongly decreases at low energies. We think that this effect is actually not intrinsic to the GaN wires but that the low energy unpolarized luminescence could come from defects of the AlN buffer (or from the SiC substrate itself). Several indications tend to support this assumption : first of all, when we measure a sample consisting of an AlN buffer grown on m-plane SiC, we typically observe luminescence below 3.7 eV, as illustrated in figure 2.7(a). Moreover, we measured the polarization dependant PL on many m-plane nanostructures and when the luminescence extended below 3.7 eV, we always had a strong reduction of the DOP. Two other indications come from TRPL measurements and temperature dependance of the PL. These will be detailled in the next part discussing nonradiative processes.

We interpret the strong DOP in m-plane GaN nanostructures by considering that although their electronic structure should be different from the one

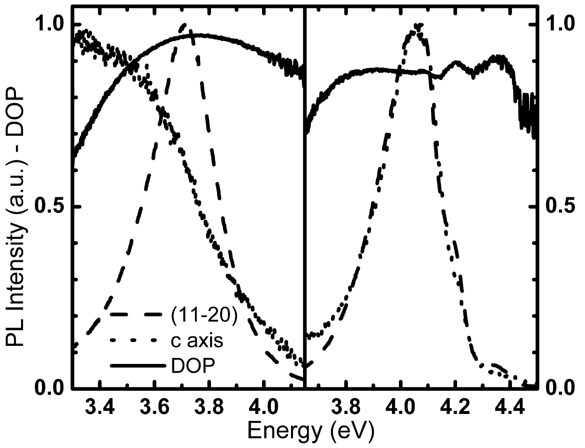

Figure 2.6: PL intensity for the c and $[11\bar{2}0]$ direction for wires (left) and dots (right). The solid lines show the energy dependence of the DOP.

of the bulk, both the effect of the strains and the confinement do not modify effectively the selection rules of the ground state, which is still strongly polarized like the A-exciton of the bulk GaN. We will discuss in details the influence of strain and confinement on the DOP in the case of a-plane quantum wells in section 2.4.

To conclude this part, we want to emphasize that even at room temperature, a strong DOP is still present : around 70 % for the wires and 65 % for the dots (see figure 2.7(b)). It suggests that even at 300K, a weak thermalization occurs towards excited states with other selection rules.

2.2.2 Nonradiative processes : dots versus wires

In the precedent part, we have shown that at low temperature, dots and wires have essentially the same behavior. In this part, we will study the influence of the temperature on the luminescence, in both CW and time resolved experiments. The aim is to have a consistent description of the evolution of the integrated intensity and the decay time with the temperature in order to get some insight into nonradiative processes [122, 123]. Concerning the intensity, one can write it as a product of elementary mechanisms :

$$I(T) = I_{exc}.\eta_{abs}.\eta_{relax}.\eta_{rad}.\eta_{collec} \tag{2.3}$$

where I_{exc} is the intensity of the excitation, and $\eta_{abs}, \eta_{relax}, \eta_{rad}, \eta_{collec}$ are the efficiency of respectively the absorption, the relaxation, the radiation and the collection. At this point, we have to make some assumptions. I_{exc}

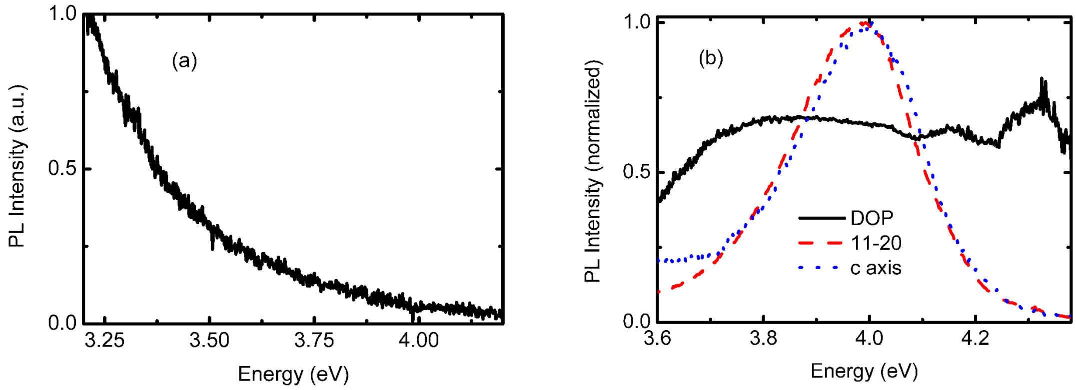

Figure 2.7: Illustration of the contribution of an AlN buffer layer to the PL signal (a). Room temperature polarization of the PL in m-plane QDs (b).

and η_{collec} can be considered constant, as we do not change the experimental settings. From the data we have (namely intensity and decay time as a function of the temperature), one can only describe the variations of two independent parameters of the model. For instance η_{rad} can be written :

$$\eta_{rad} = \frac{\tau_{nrad}(T)}{\tau_{nrad}(T) + \tau_{rad}(T)} \tag{2.4}$$

where $\tau_{rad}(T)$ (resp. $\tau_{nrad}(T)$) is the radiative (resp. nonradiative) recombination time. Then it already contains two independent parameters which evolve with the temperature. Consequently, one has to consider that η_{abs}, η_{relax} do not depend on the temperature. Considering that the excitation occurs in the wetting layer (WL) (it also means more than 1 eV above the luminescence) , this assumption is questionable, especially for η_{relax}. One thus writes :

$$I(T) = I_0 \; \frac{\tau_{nrad}(T)}{\tau_{nrad}(T) + \tau_{rad}(T)} \tag{2.5}$$

Provided the relaxation time is much shorter than the recombination time one can write the PL decay time τ :

$$\tau_{PL}(T) = \frac{\tau_{nrad}(T).\tau_{rad}(T)}{\tau_{nrad}(T) + \tau_{rad}(T)} \tag{2.6}$$

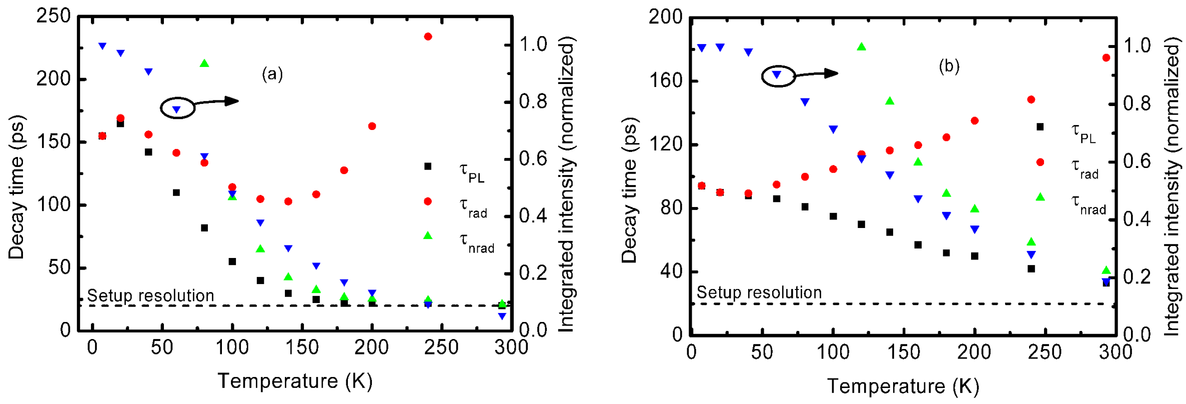

Figure 2.8: Temperature dependence of the PL intensity (downside triangles) as well as the radiative and nonradiative decay times extracted from the simple model presented in the text. (a): wires and (b): dots.

To get rid of I_0 and extract the variation of τ_{rad} and τ_{nrad}, one can reasonably assume that $\eta_{rad}(5K) = 1$, which means that $\tau_{rad} << \tau_{nrad}$ at low temperatures. Finally one gets:

$$\begin{aligned} \tau_{rad}(T) &= \frac{\tau_{PL}(T).I(4K)}{I(T)} \quad , \\ \tau_{nrad}(T) &= \frac{\tau_{PL}(T)}{1-\frac{I(T)}{I(4K)}} \end{aligned} \tag{2.7}$$

The results of this simple modelization are presented in figure 2.8 with the experimental data. The first observation that one can make is about the quenching of the luminescence. The PL intensity of the dots decreases by a factor 5 from 5K to room temperature, to be compared with the factor 20 for the wires. Here one needs to emphasize that even if from the experimental point of view the quenching of the luminescence with the temperature can be different for two samples made in the same conditions, especially for samples with a single layer of nanostructures, we do think that this difference is relevant. Furthermore, we measured a superlattice (which from our experience tend to have a better temperature behavior than single layer sample) of wires and this sample presented a quenching similar to the single layer of wires, i.e. a drop by about a factor 20 of the intensity from 5K to room temperature.

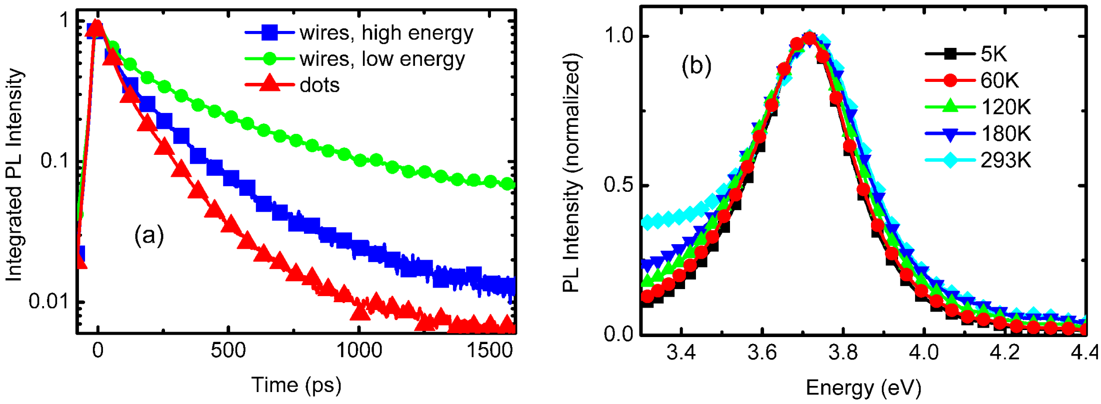

Figure 2.9: Energy dependence of the TRPL at low temperature (a), where the difference appears clearly for the wires. The evolution of the shape of the PL with the temperature for the wires is illustrated in (b).

The other striking feature of figure 2.8 is that already at low temperatures, the decay times of the PL is less influenced by the nonradiative decay in the dots than in the wires. For instance in our simple model, the crossing between radiative and nonradiative decay times occurs at less than 100 K in the wires and around 160 K in the dots.

Some features of figure 2.8 deserve comments. For instance, above 200 K our results are not reliable anymore for the wires because we reach the time resolution of our TRPL setup. Thus in the model, the decrease of the intensity is artificially taken into account by a strong increase of the radiative decay time. One should also comment on the variation of the radiative decay time in both sample. In QDs, if there is no thermally induced population of excited states, the radiative decay time should not depend on the temperature. In QWs, the radiative decay time of a 2D exciton should increase with the temperature. Our case is likely to be in between concerning the confinement but in nitride nanostructures, the relative position of the confined levels is not well known, thus it is difficult to draw a conclusion about the fact that we do see a variation of the radiative decay time in our model. Let us just note that a variation of the *calculated* radiative decay time could be explained by a variation of the actual absorption and relaxation efficiency.

Nevertheless, this simple model allow us to say that an exciton is less sensitive to nonradiative processes in dots than wires. We assume that at low temperature, an exciton does not extend over the entire wire but is rather localized in potential fluctuations. Low temperature localization is indeed well known to occur in AlGaN/GaN [124] and AlN/GaN [110]. But when one raises the temperature, excitons are more easily delocalized in wires than in dots. They are at this point more sensitive to nonradiative centers.

Let us now comment on the variation of the decay time with the energy (figure 2.9(a)) and the evolution of the PL shape of the wires with the temperature (figure 2.9(b)). It appears clearly that the low energy side of the wire luminescence has longer decay times than the high energy side. This is not the case for the dots. At similar energies (3.9 eV) dots and wires present similar decay times, which confirms that excitons are not delocalized in the wires because it would result in a much shorter decay. Focusing on the long lived luminescence on the low energy side of the wires luminescence, two mechanisms can be considered :

i) this luminescence comes from defects of the AlN buffer or the SiC substrate

ii) this luminescence stems from the large wires in which a non-negligible QCSE takes place.

The explanation i) can deal with all the features we observe. We noted indeed previously (see part 2.2.1) that the low energy side of the wires is strongly depolarized and it is not obvious why the QCSE could lead to such a depolarization (explanation ii)), while the luminescence of defects is expected to be weakly polarized. Furthermore such defects should be long lived, as we did observe in TRPL. The presence of QCSE (explanation ii)) can nevertheless not be totally ruled out. The largest wires have indeed large facets perpendicular to the c-axis compared to both dots and small wires. Thus more charges are potentially carried on these facets creating a larger electric field. Qualitatively the QCSE, by separating the e-h pairs, could possibly explain some changes in the exciton selection rules and thus result in a less polarized emission, although the details of this mechanism are not clear and would necessitate in depth calculations. It seems to us that a slight change in the wires diameter is not very likely to explain the dramatic feature of the TRPL (see figure 2.9(a)) that is why we tend to prefer the explanation i). Furthermore, the evolution of the shape of the PL of the wires with the temperature (see figure 2.9(b)) indicates that the low energy side quenches slower than the high energy one. While a mechanism that could explain why the wires with a larger QCSE are less subject to nonradiative processes than the small ones is not obvious, a luminescence from deep defects of the AlN easily explains this feature.

Let us now summarize this study on the difference between wires and dots. We have seen that at low temperature they have essentially the same behavior, namely a strongly polarized luminescence and short decay times as a consequence of a strongly reduced QCSE. We do think that in wires, the excitons are localized at low temperature but they are more easily sensitive to nonradiative processes when one increases the temperature, due to an easier delocalization. Even at room temperature, the emission is still strongly polarized and suggests that the ground state exciton preserves his heavy hole character (A exciton) up to room temperature, with a weak thermalization.

2.3 m-plane Quantum Dots : single nanostructure luminescence

In this section, we will focus on the luminescence of single m-plane nanostructures. To study single nanostructures one needs to have samples with a reasonable density (not much higher than 10^{10}cm^{-2}) and have access to a process in order to isolate single nanostructures. One possibility is to use the combination of polystyrene balls and a metallic mask in order to end with small holes into the mask [125]. This method is relatively easy to realize but one problem is that one cannot control the position of the holes and localize them. Thus it is not experimentally possible to get back to the same aperture. This is a strong limitation of this method. The other possibility, that we have used, is to perform e-beam lithography (realized by M. Terrier) and induced coupled plasma etching (realized in the LTM) in order to create a pattern of mesas with different sizes. In figure 2.10, we present scanning electron microscope (SEM) images at different magnification realized right after the etching. At low magnification, one sees the pattern (see figure 2.10(a)) and one can also notice that the etching produces a deposition that has to be removed afterwards. At high magnification, one can see that the shape of the small mesas is not well defined (they are supposed to be squares) due to both the e-beam (+ lift off) and etching steps. Furthermore the majority of the small mesas (below 300 nm) do not even exist after the whole process.

Despite these technological limitations, we have managed to process two m-plane samples : one of wires and one of dots. The problem of the dots sample for microphotoluminescence (μPL) is that they have a too high density (see figure 2.1), typically 10^{11}cm^{-2}. Thus even on the smallest mesas we could achieve, the number of dots is still to high. That is why we eventually managed to lead an in-depth study only on wires. All the measurements presented in this part are performed at liquid helium temperature.

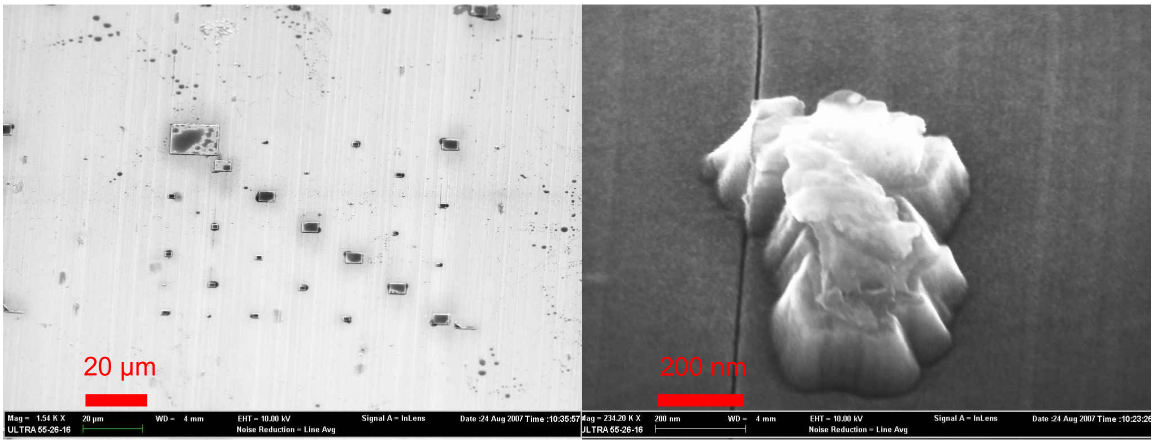

Figure 2.10: SEM images of a sample of m-plane QDs after e-beam lithography and ICP etching. The left picture is recorded at low magnification in order to show the pattern and the right picture is a zoom on a small mesa which shows that the edges are not well defined on such small structures. The picture are tilted and the scale is given for the horizontal axis.

2.3.1 Observation of the emission from a single m-plane nanostructure

Cathodoluminescence

Before realizing the complicated process of mesas etching in order to perform μPL, we tried to isolate the luminescence of single m-plane nanostructure in cathodoluminescence (CL). In CL, one can tune both the acceleration voltage (typically between 1 and 30 kV) and the spot size which acts on the total current and the penetration into the sample. The effect of the accelerating voltage on the penetration depth is clearly illustrated in figure 2.11(a). In this experiment we scan an area of 5x5 μm with the electron spot. The signal around 3 eV stems from the SiC substrate. Its contribution to the signal increases with the field because the penetration depth increases as well [125].

The broad luminescence around 3.7 eV comes from the wires, the position being comparable with the one we measured in PL on the same sample (see part 2.2.1). At higher energy, one sees two additional contributions. The one around 5.1 eV is likely due to the 2 MLs WL [116] but the origin of the one around 4.7 eV is not clear so far. It could come from fluctuations of the

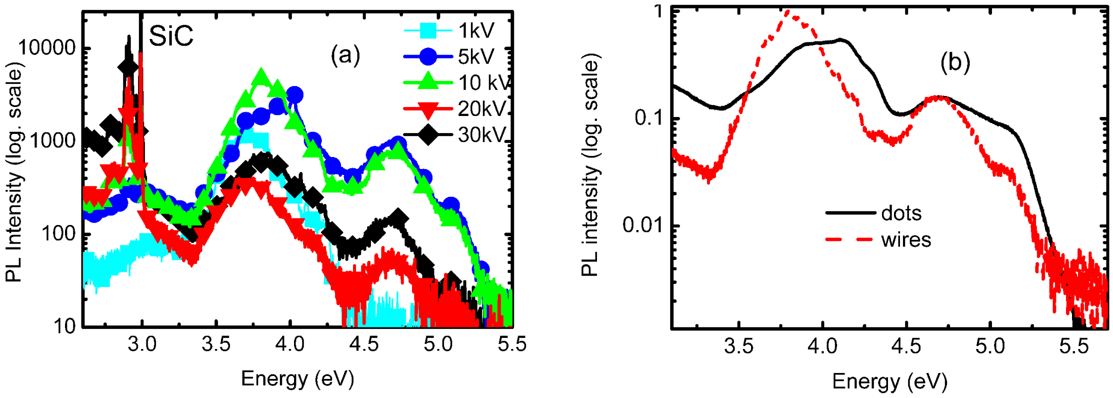

Figure 2.11: Dependence of the CL on the acceleration voltage (a) performed on a sample of m-plane wires at low temperature and comparison of the spectrum of wires and dots (b).

WL size, reaching 3 MLs in some areas. As illustrated in figure 2.11(b), we do indeed also observe this contribution in samples of dots thus it leads us to the conclusion that it is not related to the wires/dots morphology. It is more likely related to the morphology of the AlN buffer which does present strong waves along the c-axis [116] and its influence on the WL. Such a signal around 4.7 eV was also observed in a-plane QDs. It was attributed to thicker parts of the WL [125].

We turn now to measures performed on unprocessed samples with a voltage of 30 kV in such a configuration that the spot size reaches about 500 nm (intensity around 5.4 nA). Working at smaller intensity (smaller spot size) leads to an important decrease of the signal and does not allow to record spectra with a reasonable signal to noise ratio. As a general trend, we were only able to isolate lines in the high energy part of the spectrum. The best spectrum we could record (on a sample of wires) is presented in figure 2.12. The sharpest line has a linewidth of 2 meV. But one has to mention that the lines were generally much larger (certainly due to strong fluctuation in the environment [125] created by the many carriers created in CL) and not well isolated. Combined with a low signal this prevented us to perform in depth study of the luminescence in CL.

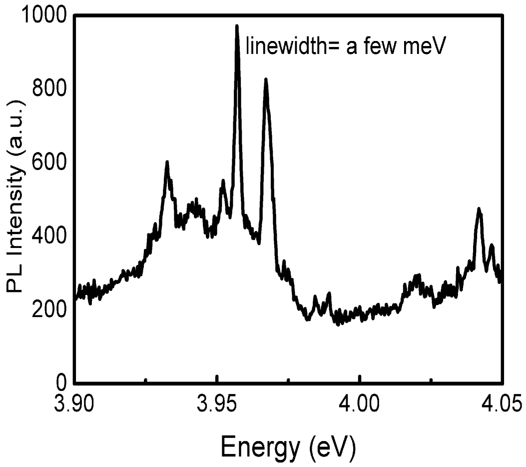

Figure 2.12: CL at low temperature on an unprocessed sample of wires. The linewidths are as narrow as 2 meV.

Microphotoluminescence

We will now present the experiments we performed in μPL on processed samples. We will see that the luminescence of single m-plane nanostructures have many similarities with a-planes QDs. First of all, we are only able to isolate sharp lines in the high energy part of the spectrum, like we already noticed in CL. Secondly, we often measure a doublet or a multiplet of lines (see figure 2.14) and sometimes single lines. Finally, one other feature of this lines is that they are often broad (more than 1 meV, i.e. not limited by the radiative decay time) and that their position (as well as their intensity) evolves in time (see figure 2.13). These features are gathered in the term of spectral diffusion. This behavior has been extensively studied in a-plane GaN QDs [125], in c-plane GaN and InGaN QDs [126, 127] but also in other system like arsenide QDs [128, 129], II-VI QDs [130–133] or nanocrystals [134–136], where a link with the blinking [137] has been put into evidence [135, 138, 139] . The underlying mechanism is the modification of the local surrounding of the nanostructure which is induced by carriers nearby. These trappings and detrappings of carriers in the vicinity of the nanostructure change the energy of its transitions. Depending on the position of the traps, the energy shifts will be small or large compared to our spectral resolution (around 400 μeV) and will appear to us as a broadening or a multiplet. Also depending on the time constant of the trappings, these changes will be resolved or not in our experiments which have typical integration times of the order of 1 second. From figure 2.13 (see also [125]), it is clear that there

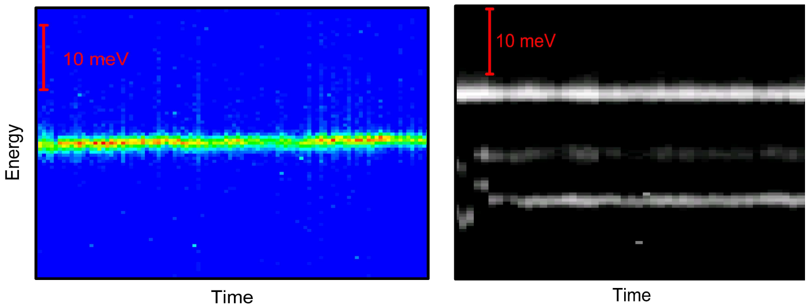

Figure 2.13: The left and right figure illustrate the diffusion spectral (at low temperature) in μPL on a single dot. Left : the 100 spectra of 0.5 second taken successively illustrate the intensity fluctuations. Left : the 50 spectra of 3 seconds taken successively put into evidence a discrete jump of the lines by about 5 meV.

is a distribution of time constant in these mechanisms, some of them around 1 sec being measurable in our experiments. But some of them are certainly much faster and the high frequency cutoff, if any, is difficult to determine.

Before focusing on the polarization properties of single nanostructures, we would like to enlighten the features observed as a function of the excitation power. The goal of such measurements is to get some insight into the energy level structure of a single nanostructure. Most often, no special features appear when increasing the power. When some features appear, this apparition is often not reversible as reported in a-plane QDs [125]. This is certainly due to a non reversible modification of the local environment of the nanostructure. In figure 2.15(a), we present one of the reversible sweep we could measure. Besides the low power line at 3.745 eV (5 meV broad), we see the apparition of a line at higher energy (18 meV above) when rising the power. Qualitatively, one could think of an excited state, for instance a biexciton. But in order to be more quantitative one needs to monitor the integrated intensity as a function of the excitation power. This is presented in figure 2.15(b), where we see that although a clear tendency appears, i.e. the high energy line increases faster than the low energy one, too much scattering in the data prevent us to draw a definitive conclusion about the exponents of these dependences. The scattering in the data is due to fluctuations in the intensity that can have many origins. One intrinsic reason is that in link with spectral diffusion, the intensity of a line evolves in time (see figure 2.13). Extrinsic reasons comes from the fact that one slightly moves the exciting beam when changing the power and thus the ratio between the measured power and the actual power exciting the sample can change. Even by taking special

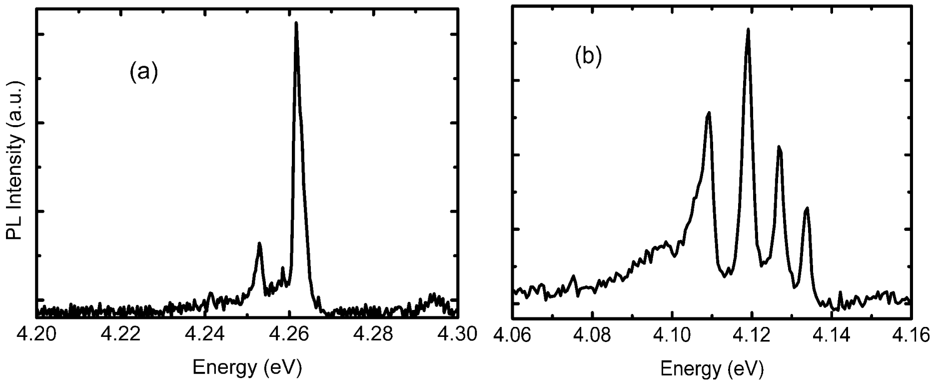

Figure 2.14: Doublet (a) or multiplet (a) often show up in the PL spectra of a single wire. In both case the linewidths are between 2 and 4 meV.

care to optimize the signal after changing the power, this effect is important, especially at low signals where the optimization is less precise. These two effects result thus in very scattered data. Thus an attribution of these lines based on the power dependence would be too conclusive. Nevertheless, if the excited state is a biexciton, it would have a negative binding energy. We will get back to power dependence measurements on single QDs in chapter 4 and explain in more details the issue of the biexciton binding energy.

2.3.2 Polarization measurement on a single nanostructure

We have seen in part 2.2.1 that the PL on an ensemble of m-plane wires is strongly polarized. We will now present the same kind of measurements on single wires. We first want to emphasize, that the fact that the intensity of a single line evolves complicates dramatically this kind of experiments. In figure 2.16(a), we present a study carried in μPL on a 1 μm mesa. We see that the whole spectrum is strongly polarized. In particular the two dominant lines, even if they are not well spectrally separated from the other contributions, have a DOP higher than 90 % (see the inset of figure 2.16(a)), in close agreement with the measure on the ensemble (see figure 2.6). Considering the measure presented in figure 2.16(b) on a well isolated single line (400 nm mesa), we see that in this case the DOP reaches only 73+/- 2%. This is smaller than the DOP measured on the ensemble (around 85 %) and together with the measurements of figure 2.16(a), show that there is some

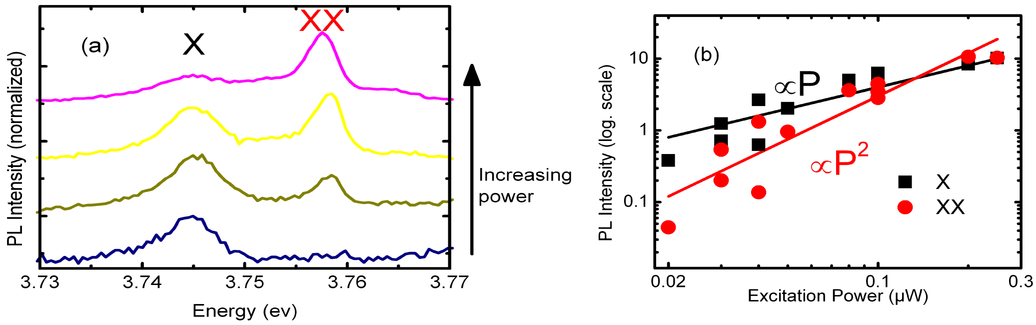

Figure 2.15: (a) : Power dependence of the PL recorded on a Qwire. (b) shows the integrated intensity of both lines as a function of the excitation power on a log-log scale. The solid lines represent a linear and quadratic dependence. X is tentatively attributed to an exciton and XX to a biexciton recombination (see the discussion in the text).

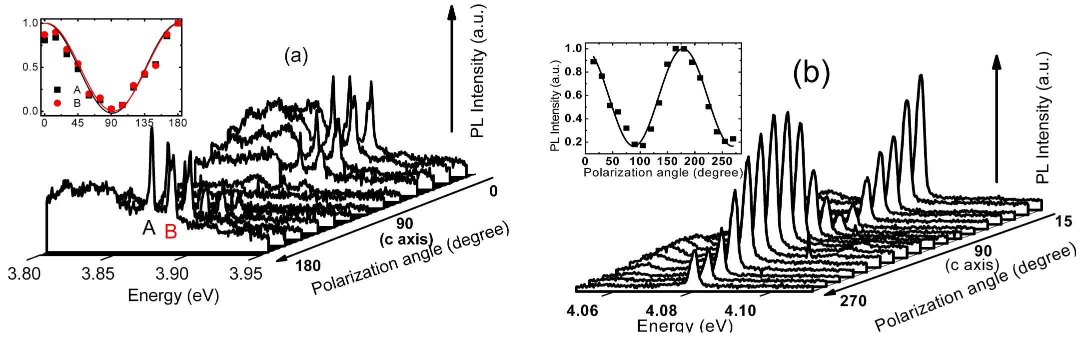

Figure 2.16: (a): polarization resolved study on a 1 μm mesa showing several contributions. The whole signal is strongly polarized. The inset illustrates this by plotting the intensity (normalized to its maximum) of the two dominant lines (labeled A and B) as a function of the polarization angle. The solid lines represent fits by equation 2.1. (b): 3D plot of the PL intensity at low temperature for an isolated single nanostructure (wire) as function of energy an polarization angle. The inset shows the dependence of the integrated intensity with the polarization angle. The solid line is a fit with equation 2.1.

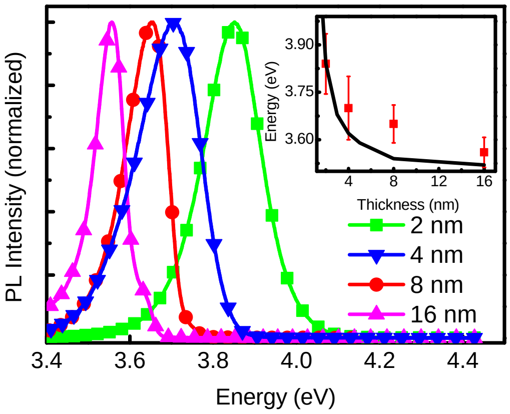

Figure 2.17: The low temperature PL of the set of a-plane GaN/AlN QWs studied in part 2.4 is presented in figure. The inset show the the thickness dependence of the PL emission energy. The error bars are the FWHM of the emission. The solid line respresent the theoretical values for an unstrained GaN/AlN non polar QW, neglecting the excitonic effects.

dispersion of the DOP on single wires. We attribute this dispersion to the inhomogeneity in size and strain from one wire to another.

2.4 a-plane Quantum wells : effect of the strain on the polarization anisotropy

In the last two parts we have presented the optical properties of m-plane nanostructures. In this part, we will focus on the other non polar orientation, namely a-plane. We will in particular show the phenomenon of polarization switching in a-plane GaN/AlN QWs grown on SiC. As we will detail, this is mainly due to the effect of a strongly non biaxial strain on the valence band structure. This phenomenon was reported in the case of AlGaN/AlN and InGaN/GaN c-plane QWs [115, 140] but in these cases this was closely related to the fact that the well is constituted of a ternary alloy. This study was performed in collaboration with our colleagues of the university of Valencia. PL was performed in Grenoble and Valencia. Raman was performed in Valencia during a visit I had the opportunity to make in their group. X-Rays and TEM were done in Grenoble. Finally the calculations were realized in Valencia.

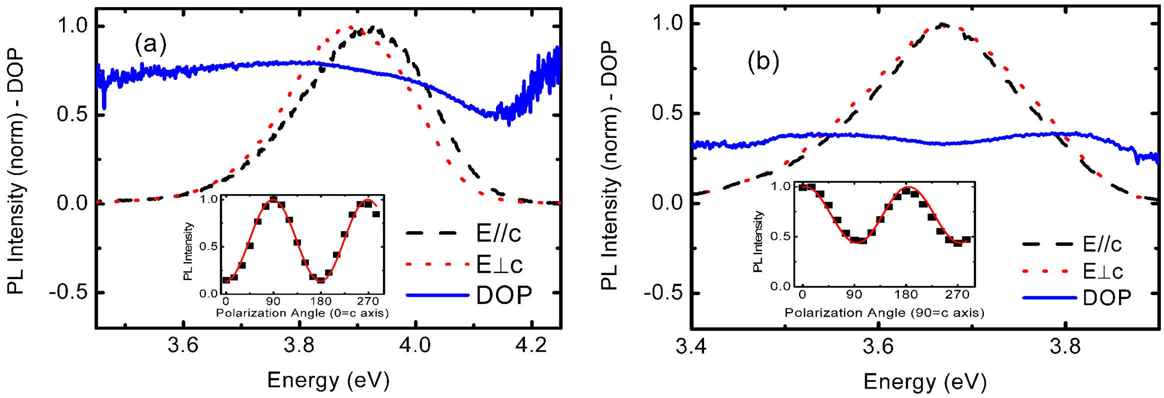

Figure 2.18: Polarization of the PL (low temperature) of the 2 nm (a) and 4 nm (b) QWs. Both emission are polarized perpendicular to the c-axis (positive DOP). The insets show the integrated intensity as a function of the polarization and the solid lines are fits with equation 2.1.

2.4.1 Description of the set of samples

The growth substrate is a-plane SiC (see appendix F for details about the growth conditions). The growth , which was done by S. Founta, begins by a 50 nm AlN buffer (in which sacrificial GaN/AlN wells are grown in order to improve the optical properties [141]) which is followed by the 5 QWs. The sizes of the QWs are : 2,4,8 and 16 nm. The AlN spacers are 10 nm thick. In figure 2.17, we present the PL of the 4 samples. The inset shows the energy of the luminescence as a function of the well size. One clearly sees the effect of the quantum confinement and the fact that the PL does not go below the GaN band gap is a consequence of the vanishing QCSE in non-polar QWs.

2.4.2 Evidence for polarization "switching"

Let us now present the experimental evidence of polarization switching based on polarization resolved PL. In figure 2.18 and 2.19, we present the measurements on the 4 samples. The inset of each figure shows the dependence of the integrated intensity with the polarization angle and a fit by the function 2.1, used to extract the DOP. One sees that the DOP is positive for wells up to 8 nm (apart from a feature in the high energy part of the 8 nm wells), meaning $I_{[1\bar{1}00]} > I_{[0001]}$, but for the 16 nm wells, this is the contrary. The energy averaged DOP for all the samples is presented in fig-

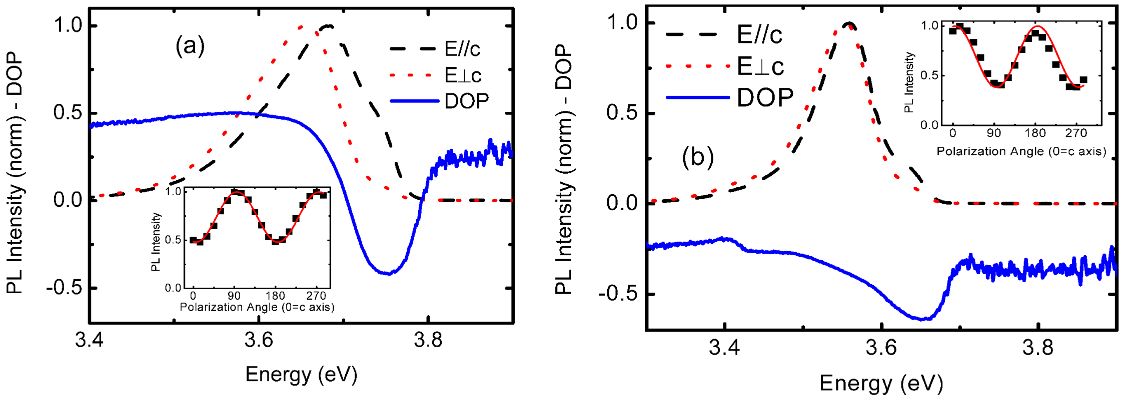

Figure 2.19: Polarization of the PL (low temperature) of the 8 nm (a) and 16 nm (b) QWs. The 8 nm sample is mainly polarized perpendicular to the c-axis (positive DOP), apart from a contribution at high energy which is polarized along the c-axis. In contrast all the PL of the 16 nm sample is polarized along the c-axis. The insets show the integrated intensity as a function of the polarization and the solid lines are fits with equation 2.1.

ure 2.20(a) where the switching appears clearly. Let us stress that the DOP weakly depends on the temperature. This is an indication that it is not significantly affected by localization that is likely to occur in such structures at low temperature [110, 124]. One can thus conclude that the polarization switching is related to intrinsic properties of these quantum wells, i.e. their band structure.

2.4.3 Theoretical description : effect of the strain

In this part, we will show that the dependence of the DOP with the well size can be explained taking into account the strain variation. As we saw in part 1.2.3, the strain can have an important influence on the polarization selection rules of the ground state. After detailing the experimental determination of the strains, we will present the theoretical model, developed by our collaborators of the university of Valencia, which can describe the results.

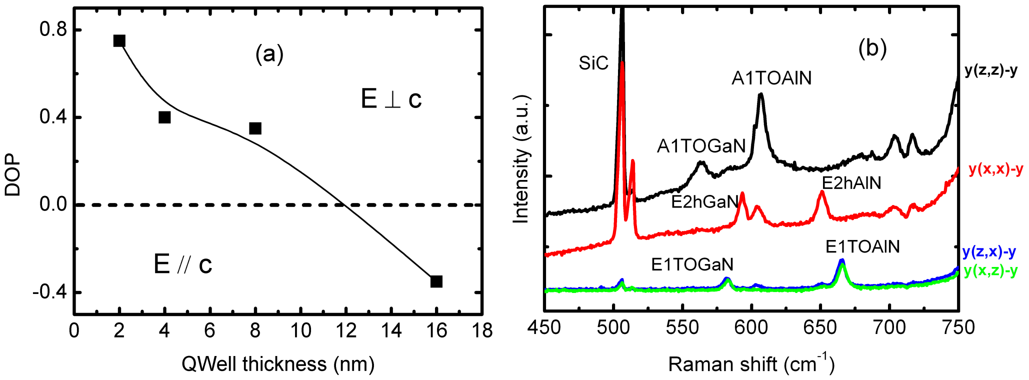

Figure 2.20: (a) : Variation of the DOP with the well thickness. Note the switching from **E**||**c** to **E**⊥**c** when reducing the well thickness as detailled in the text. The solid line is a guide for the eyes. (b) : Raman spectra recorded with the 514.2 nm line of an argon laser on the 8 nm thick quantum wells. The different curves are for various configurations (see the right of the figure). For instance y(zx)-y means : excitation with **k**||**y** (the growth axis in our case) and a polarization **E**||**z** (we recall that z is the c-axis). Collection with **k**||**y** and a polarization **E**||**x**.

Qualitative explanation

Neglecting the shear strains, the strain Hamiltonian for the valence band reads [32, 37]:

$$\mathbf{H}_\epsilon = (D_1 + D_3 J_z^2)\epsilon_{zz} + (D_2 + D_4 J_z^2)\epsilon_\perp - D_5 \epsilon_+ (J_+^2 + J_-^2) \tag{2.8}$$

where D$_1$-D$_5$ are the deformations potentials (see 1.2.3), $\epsilon_\perp = \epsilon_{xx} + \epsilon_{yy}$, $J_\pm = \frac{1}{\sqrt{2}}(J_x \pm J_y)$ and $\epsilon_+ = \epsilon_{xx} - \epsilon_{yy}$. Due to the fact that some terms are dependent of the total momentum J, the influence of the strain on a state will depend on its momentum. Combined to this change in the eigenvalues of the Hamiltonian (energy of the states), there is a change in the eigenstates. Thus the oscillator strengths along the 3 directions, given by the momentum matrix elements [32, 38] will evolve as well. This evolution clearly shows up in the figure 4 of ref.[38], where the authors present calculations of the oscillator strengths along the 3 directions depending on the strain (in m-plane GaN in their case). We now have access to a mechanism that could explain why a-plane GaN/AlN QW samples presenting significant differences of strains could have different polarization of their emission.

In the next part we will thus present experimental results about the determination of the strain that we will use in the theoretical model.

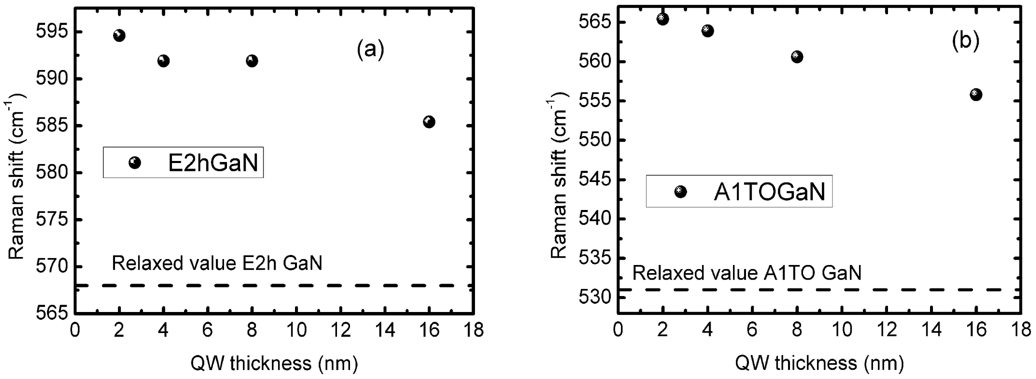

Figure 2.21: Variation of the Raman shifts with the quantum wells thickness : mode E2h (a) and A1TO (b).

Determination of the strains in the QWs : Raman, TEM and X-Rays measurements

We have used the combination of three experimental methods in order to determine the strain in the QWs. In Raman, one needs at least to identify two peaks in order to extract the strain. The relationship between strain and Raman shift of one mode indeed reads [46, 143, 144]:

$$\Delta\omega_i = a_i(\epsilon_{xx} + e_{yy}) + b_i\epsilon_{zz} \tag{2.9}$$

where the a_i are the deformations potential for the mode i considered [143, 144]. The identification of the peaks is done thanks to polarization resolved experiments (although the energy position is a first indication), in which one can access the selection rules. These selection rules are indeed fingerprints of the Raman peaks [143]. The Raman spectra recorded on the 8 nm thick quantum well are presented in figure 2.20(b). These measurements were performed in Valencia, where I add the opportunity to realize them with Ana Cros and Rafa Mata. One sees that 3 modes are observed for GaN, depending on the configuration : A1TO, E2h, E1TO. In figure 2.21, we plot the evolution of the Raman peaks with the GaN wells thicknesses for the two modes we will use : A1TO, E2h. The first observation that we can make is that all samples are strongly stressed (the dotted line shows the position for a relaxed GaN 2.21). Furthermore the relaxation is very slow when the quantum wells size is increased. Using the two modes and the Poisson law which provides an additional equation, the extracted strains are

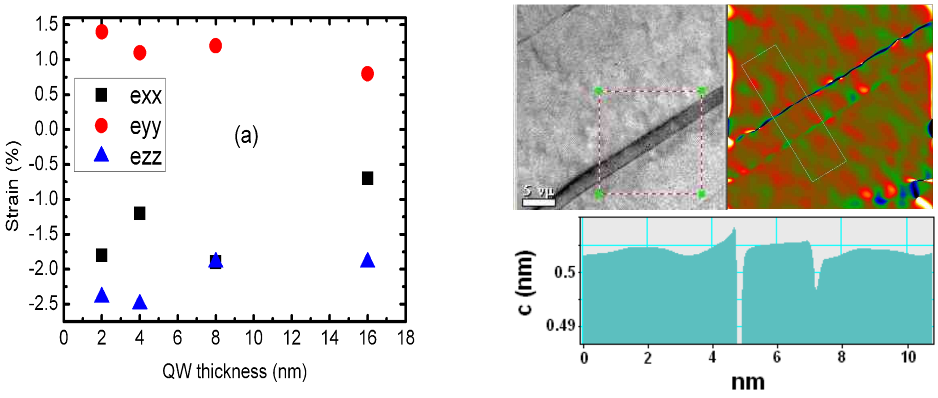

Figure 2.22: (a) : strain extracted from the Raman measurements. We recall that y is the growth axis and z the c-axis. (b) : TEM analysis (area in the dotted square of (a)) of the lattice parameter along the c-axis on the thinner quantum wells (2 nm). One sees that GaN is matched on AlN along this direction. The color plot represents the local lattice parameter and the graph its variation along the growth axis (Note that the sharp features at the interfaces are artifacts [142]). No variation is observed at the GaN/AlN interface.

presented in figure 2.22(a).

To confirm this data, we performed TEM on the thinner quantum well. The image (realized by C. Bougerol) is presented in figure 2.22(b). The main information is that the GaN lattice parameter along the c-direction matches the AlN. Thanks to the X-rays (E. Bellet-Amalric), we could determine the strain in the AlN buffer : for the lattice parameter c, the AlN buffer is fully matched onto the SiC substrate. We thus conclude that the entire structure has the same lattice parameter c : the one of SiC (0.504 nm). For GaN, it gives a strain of -2.8% which is in accordance with the Raman measurements. For the [1-100] direction, we used the same procedure (i.e. we used as a reference for TEM the lattice parameter of the AlN buffer extracted from the X-rays). In this case, there is a relaxation and the structure is not matched on the SiC. The strain in the GaN quantum well is : e_{xx}= -2.2 %. Once again, the value is larger than the one measured in Raman but the agreement is reasonable. Using the Poisson's law, we can then determine the out-of-plane lattice parameter and calculate the strain : e_{yy}= 1.6 %.

For the other samples, we did not have TEM informations and we thus have only Raman and X-rays measurements. We tried to use both in the best way and we finally converged on the values of the strain presented in

QW thickness (nm)	ϵ_{xx} (%)	ϵ_{zz} (%)	ϵ_{yy}(%)
2	-2.2	-2.8	1.6
4	-2.1	-2.6	1.5
8	-2.1	-2.5	1.5
16	-0.9	-2.3	1

Table 2.1: Strain in the GaN quantum wells extracted from the combination of Raman, TEM and X-rays.

table 2.1.

Theoretical model : 8 bands k.p formalism

In this part, we will present the calculations made in order to study the influence of the strain on the electronic properties of the quantum wells. They were done by our colleagues of the University of Valencia (A. Cros, J. A. Budagosky and A. García-Cristóbal).

The model to calculate the electronic structure of the quantum wells is a 8 bands k.p model, including confinement. The strain is taken into account in the same way as in ref. [32, 38]. The confinement is taken into account following [145]. Once the eigenstates of the complete Hamiltonian are computed, one can calculate the relative oscillator strengths of the ground state along and perpendicular to the c-axis. The first important information that was extracted from this study is that the parameters used in the litterature (especially the deformation potentials) can lead to fairly different results.

Let us illustrate this with the calculated degree of polarization for a-plane bulk GaN, i.e. disregrading the effect of the confinement. In figure 2.23, we present the DOP as a function of the in-plane strain using either the parameters of [75] (the parameters of [32] lead to similar results) or [38]. Let us stress that the influence of the out of plane strain is very weak. One sees that the boundary between the two area, namely the one with a positive DOP (i.e. more emission with **E**$\perp$**c**) and the one with a negative DOP, is strongly shifted. For instance, having $\epsilon_{zz} = -2\%$ and $\epsilon_{xx} = -1\%$ would lead to a strongly positive DOP in the case of [75] but a strongly negative one in the case of [38]. The experimental strains are reported in the same graphs. One sees that they are close from the boundary. Furthermore, the trend is good, as the 16 nm quantum well is the one having the negative experimental DOP. Let us stress that at first sight this result can be very surprising : the thickest quantum well, i.e. the more relaxed one, is the one that presents a negative DOP. Nevertheless, the results of figure 2.23 suggest the following

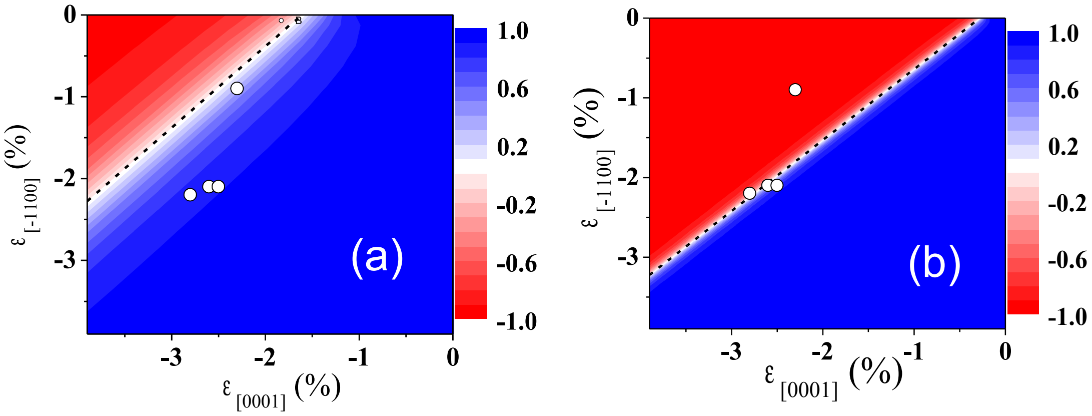

Figure 2.23: (a) : degree of polarization of bulk a-plane GaN as a function of the in-plane strain using the parameters of [75]. (b) : same figure as (a) but using the parameters of [38]. In both figures, the dots are the values of the strain in the quantum wells determined experimentally.

interpretation : the key point is that the ϵ_{zz} component does relax much slowly than the ϵ_{xx} one. That is why the thickest quantum well sample ends up in the area where the DOP is negative, different from both the other samples and an unstrained GaN layer. It seems to us, at this point, that trying to be more quantitative than that would be too conclusive due to the uncertainity in the deformation potentials. It is now clear that a reasonable set of deformation potentials can describded our experimental results. Other interesting effects, such as the influence of a small in plane localization are currently under investigation.

In this chapter, we have seen that non polar GaN/AlN heterostructures have several peculiarities compared to c-plane heterostructures. The strong reduction of the quantum confined Stark effect in m-plane quantum dots has been shown. We have presented a detailled study of the nonradiative processes in the two types of structures that can be grown on a m-plane SiC substrate : quantum wires and quantum dots. We have evidenced that despite the strain and the confinement, the polarization of the luminescence of m-plane nanostructures is similar to the bulk : a maximum perpendicular to the c-axis. We managed to perform such a study down to the single nanostructure level. This polarization of the luminescence has been studied for a-plane quantum wells as well. We have shown that in this case there is a strong effect of the strain which results in an original phenomenon. For the thickest quantum well sample the ground state is polarized along c-axis. But with a different strain, as it is the case for the thinner quan wells, the optical polarization gets back to a bulk-like one with a maximum perpendicular to the c-axis.

Chapter 3

Optical properties of GaN nanowire heterostructures

This chapter is devoted to the characterization of the optical properties of ensemble of nanowires. The first section will present general considerations on the nanowire topic. Then we will expose our present understanding concerning the nanowire growth. The next section will focus on the properties of ensemble of nanowires made of pure GaN. After presenting the influence of an AlN capping, we will study the properties of ensemble of nanowires containing heterostructures. We will conclude this chapter by the optical properties of pure GaN nanowires on the single wire level. The growth of the GaN nanowires (resp. AlN) was performed by R. Songmuang and G. Tourbot (resp. O. Landré).

Contents

3.1 On the interest of semiconductor nanowires

It is now widely admitted that mastering structures at the nanoscale level is a prerequisite for future devices with reduced dimensions. Nanowires made with a bottom up approach seem very promising for the the realization of these nanoscale devices. One of their advantages is that they can be grown on strongly mismatched substrates (for instance Silicon) where a traditional two dimensional growth would have resulted in a material of very poor crystalline quality. This comes from the fact that surface relaxation of strains is allowed by the large surface/volume ratio. This is true for nanowires made of pure material, for instance GaN, where very good crystalline and optical qualities are obtained on strongly mismatched substrates [146, 147].

For nanowire heterostructures, the situation is not that simple. For axial heterostructures, in the case of a material grown on the top of a nanowire made of another material, there is a relationship between the thickness of the material deposited and the radius of the nanowire before the apparition of misfit dislocations [148]. If the radius is small enough, one can theoretically grow an infinite wire without any dislocation at the interface [148]. Concerning radial core-shell heterostructures, the critical radius and shell thickness have been theoretically investigated, for instance as a function of Al composition for a GaN/AlGaN core-shell nanowire [149]. For a GaN nanowire with a diameter of 30 nm, the critical thickness for an AlN shell would be only a few nm [149] before the apparition of dislocations. One can indeed feel that the nanowire geometry does not help a lot for the strain relaxation in this case unlike in the case of axial heterostructures.

Regarding optoelectronic devices, nanowires are supposed to be interesting in order to increase the light extraction. A straightforward effect comes from the reduced mean optical index which tends to decrease the total internal reflections although what really happens at the subwavelength scale is not obvious. Thanks to the possibility to tailor the positions and dimensions of the nanowires (using patterned substrates for instance), one could also think to enhance the light extraction by designing a photonic crystal [150].

To conclude this part, we would like to emphasize that although the possibility to use nanowires as a building block of devices with improved performances compared to two dimensional devices is widely recognized, a clear demonstration of device improvement (for instance a light emitting device with a better efficiency) based on nanowires is still to be demonstrated.

3.2 Growth of GaN nanowires

In this section we will give an overview of our present understanding concerning the growth of GaN nanowires (the growth direction being the c-axis) by plasma assisted molecular beam epitaxy (PAMBE) without catalyst, a topic which is still not clearly understood. More on the topic can be found in the thesis of Olivier Landré [151]. We will not discuss the selective growth on patterned substrate where the mechanisms are likely to be very different [152–154]. It is now admitted that one can separate the growth in two distinct phases : the nucleation (which actually seems to contain different parts as we will see later) and the steady state growth phase. Let us first note that concerning the growth phase, a simple geometrical model can explain a different growth rate for the lateral and axial directions [155]. Nevertheless it does not contain all the physics especially in terms of difference between species (i.e. between Ga and Al).

What is somehow puzzling in the path towards a model for the growth and nucleation is that numerous parameters (substrate, III-V ratio, growth temperature...) seem to influence the growth and drawing a general picture that would gather all the observations is very challenging. The only common growth conditions appear to be a high growth temperature and a N-rich regime. We will begin by discussing the steady state growth phase for which more agreement seems to exist. Several experiments led to identify some of the key parameters to take into account in order to describe this phase. Especially the importance of the diffusion of Ga during the growth phase seems now established [156–158] but the exact mechanism by which the adatoms reach the top of the nanowire for the incorporation is not totally clear yet. The nanowires indeed present m-plane facets [159] and in this plane the Ga diffusion along the c-axis is not favorable. First principles calculations show indeed that there is a barrier to the diffusion in this direction [160].

But before this steady-state growth regime occurs a complex nucleation mechanism. In [161], the authors have performed a detailled analysis of the first stages of the growth of GaN on a thin (a few nm) AlN buffer on Si (111). The study combined real time in situ grazing incidence X-rays diffraction, anomalous diffraction experiments and high resolution transmission electron (HRTEM) microscope experiments. One key point is that the nucleation of nanowires is essentially different from the formation of SK quantum dots although they both take place above a given critical thickness. The difference comes from the relaxation mechanism : elastic in the case of quantum dots, plastic in the case of nanowires. This appears clearly in HRTEM images where the presence of dislocations at the AlN/GaN interface is shown. The difference also shows up unambiguously in real time X-rays experiments. As

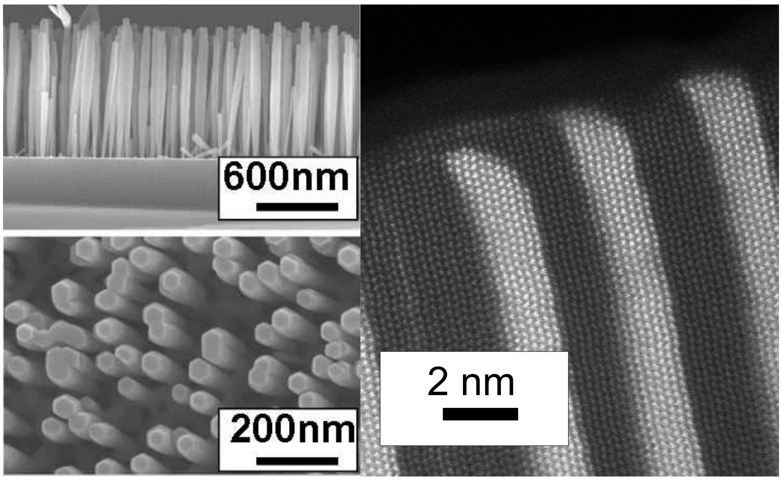

Figure 3.1: SEM images illustrating the growth of GaN nanowires. One sees that the wires are well separated and that their density is around 10^{10}cm^{-2}. The HRTEM image (C. Bougerol) of the right shows an heterostructure and put into evidence the lateral growth of AlN (in dark).

a consequence of elastic relaxation, GaN appears as a shoulder of AlN in the case of self organized quantum dots but in the case of nanowires, no diffraction intensity appears in between the AlN and GaN relaxed value. The GaN is indeed fully relaxed in the case of nanowires. The reason for the difference in relaxation between the two systems can be found when studying the influence of the thickness of the AlN buffer layer. The possibility to grow nanowires or quantum dots depends indeed on this thickness. For thin AlN buffer with a granular structure, the growth of nanowires occurs, for thick AlN buffer with larger grains the growth of quantum dots occurs. More than the thickness of the buffer, it is actually its quality, meaning the size of the grains that sets the structures which will be grown. The growth of nanowires requires thus a granular buffer with size around the typical nanowire diameter, i.e. 50 nm. This will result in an easy plastic relaxation.

To conclude on this topic one can mention that this requirement of an easy relaxation could explain the possibility to grow GaN nanowires on Si without AlN buffer or even on SiO_2 [162]. In [163] the authors show indeed that between the Si and the GaN, an intermediate Si_3N_4 is observed. It could like SiO_2 make easier the relaxation of the GaN island.

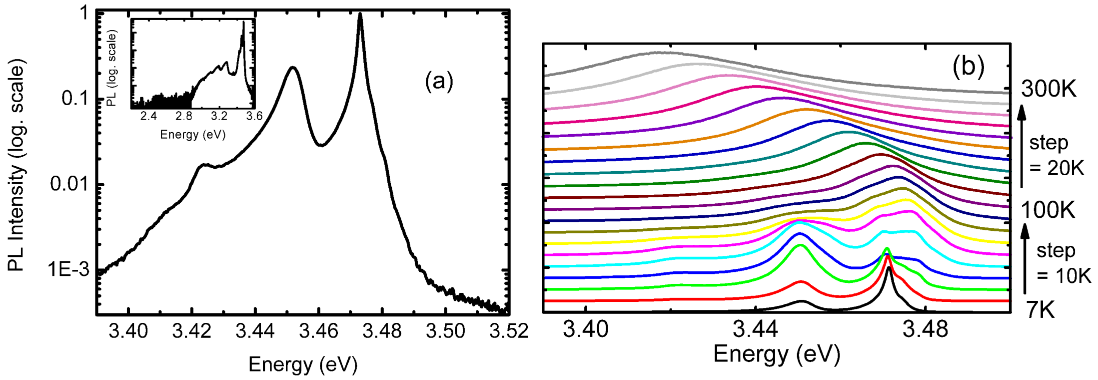

Figure 3.2: (a): low temperature luminescence in the band edge region of an ensemble of GaN nanowires excited at 244 nm. The inset shows the PL on a larger range to illustrate the absence of yellow band emission. (b): temperature dependence of the luminescence.

3.3 Optical properties of ensemble of GaN nanowires

In this section we will focus on the optical properties of nanowires made of pure GaN. We will begin with photoluminescence experiments and present the temperature dependence as well as the temporal dependence. Then we will give evidence for the positions of the free exciton resonances by both reflectivity and photoluminescence excitation experiments. We will conclude this section by polarization resolved experiments made in a plane containing the c-axis.

3.3.1 Standard characterizations

The standard growth conditions for GaN nanowires are a high substrate temperature, above 750°C and nitrogen rich conditions with a III/V ratio around 0.3. It results in well separated wires with a typical diameter around 40 nm, as seen in figure 3.1. With this diameter, we do not expect any noticeable effects of the lateral confinement and thus characteristics comparable to a bulk layer should be observed. The length of the nanowires depends on the growth time, substrate temperature and Ga flux but typically one obtains 600 nm wires after 4 hours. In figure 3.2(a) we present the spectrum of typical GaN nanowires. The dominant contribution, attributed to a donor bound exciton (D_0X_A) recombination is located at 3.472 eV and has a linewidth of 1.2 meV, which is the state of the art [147, 164–167]. The position and the linewidth are a proof that the GaN is fully relaxed and of very good structural quality. The linewidth is indeed comparable to good GaN epilayers (but larger than the state of art free standing GaN [57]). This is remarkable, considering it consists of only a few hundreds nm of GaN grown on a Si (111) substrate. At higher energies, one sees shoulders at respectively 3.478 eV and 3.483 eV that we attribute to the free A and B excitons. The second contribution is situated around 3.45 eV. It is observed by almost all groups growing GaN nanowires [147, 167] but its attribution is still subject to discussions. We will get back to this line in 3.7. The third contribution is situated around 3.41-3.42 eV and it is now widely admitted that it stems from excitons bound to stacking faults situated at the very bottom of the nanowire [147, 167, 168]. Below this emission, donor acceptors pairs (DAP) emission around 3.27 with LO phonon replicas can be detected but from our experience their intensities are strongly dependent on the chemical purity of the samples, i.e. the state of the growth chamber and particularly which samples were grown previous to the one of interest (for instance after a growth using Mg, some nanowire samples can present strong DAP). No yellow band luminescence is observed, as illustrated in the inset of figure 3.2(a).

In figure 3.2(b) we present the temperature dependence of the luminescence. The evolution presents the usual characteristics of a bulk layer. A thermally induced depopulation of the donor bound exciton and a related increase of the contributions of the free excitons emissions. The quenching of the 3.45 and 3.41 eV lines is slower due to a larger confinement. Above 100 K, the emission is dominated by free exciton recombinations and the energy shift is then related to the band gap shrinkage. At room temperature, the peak is thus situated at 3.42 eV.

The dynamics of the recombination has been studied by time resolved photoluminescence (see figure 3.3(a)). We focused on the 3.47 and 3.45 eV bands. They both present a sub-ns decay time, namely 130 ps for the 3.47 eV band and 330 ps for the 3.45 eV, values similar to the ones reported by other groups [169]. The longer decay time for the 3.45 eV band is tentatively ascribed to an enhanced localization. In ref. [170] the authors have shown that the decay time of the luminescence is not significantly altered when increasing the temperature and that the room temperature decay time is strongly related to the wire diameters. It can reach more than 2 ns in wires with a diameter of 1 μm which compares well with GaN layers with very low defects density. It confirms that GaN nanowires are of very good crystalline quality. We have so far not performed a detailed study of the temperature dependence of the decay times in order to confront our results to the ones

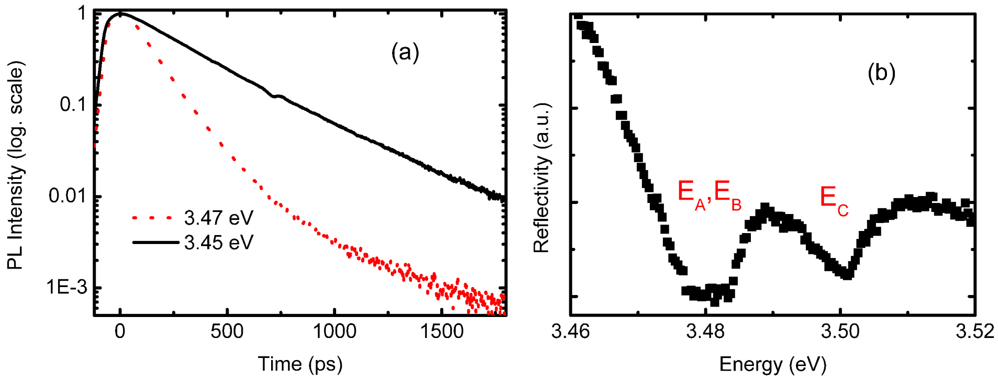

Figure 3.3: (a): comparison of the low temperature time resolved luminescence of the 3.47 and 3.45 eV lines. (b): reflectivity in the excitonic region performed at low temperature on an ensemble of GaN nanowires. We used a Xe lamp for the tunable light source.

of ref. [170]. It could indeed be interesting because our wires have a much smaller diameter than the wires studied by these authors.

3.3.2 Identification of the excitonic resonances by reflectivity and photoluminescence excitation

As we explained in part 1.3.1, photoluminescence is a limited tool in order to identify the position of the free exciton resonances. Although the data presented in the last section show two shoulders at 3.478 and 3.483 eV that we tentatively attributed to the A and B free excitons, photoluminescence excitation and reflectivity would be more convincing. We would like to emphasize that at first sight, it is not obvious that a reflectivity experiment can be performed on a nanowire ensemble due to the strong differences compared to a traditional 2D layer. It has nevertheless been shown that an ensemble of nanowires behave pretty much like a 2D layer but with a reduced index [171]. In figure 3.3(b) we present a reflectivity spectrum recorded in the excitonic region. At least two resonances appear. One is situated around 3.48 eV and is attributed to both A and B exciton. The other one is situated slightly above 3.50 eV and likely stems for the C exciton. The spectral position matches with the GaN relaxed values reported in the literature but what is striking is that the linewidths are very broad : around 6 meV for the C exciton and almost 10 meV for A-B excitons resonance, which explains why we do not separate them. This linewidths are in any case much larger than our experimental resolution (around 2 meV) and we were able to measure much sharper resonances in 2D layers. Also, together with these broad resonances, the contrast is very weak and for instance the curve presented in figure 3.3(b) required almost one hour of integration. We believe that these linewidths are intrinsic of the exciton resonances in these nanowires and it has been confirmed by experiments performed at the IPCMS (Strasbourg) with lasers instead of extended light source. To get more insight into these resonances we tried to perform a photoluminescence excitation experiment. The detection is set around 3.44 eV. In this region there is indeed some luminescence signal but it is at an energy low enough so that we can cover the excitonic region without being blinded by the scattered light. We see in figure 3.4(a) that we got informations in accordance with the reflectivity experiment : two broad resonances situated around 3.48 eV and 3.50 eV.

To conclude this part, we will try to give possible explanations for the strong difference of the linewidths measured in photoluminescence and reflectivity (or photoluminescence excitation). In photoluminescence, we see mainly the donor bound exciton, thus the linewidth is not related to the free excitons that we see in reflectivity but to localized states. The difference comes thus from the fact that we are sensitive to different states. But what can explain the linewidth seen in reflectivity, which is much broader than expected? The linewidth is obviously not limited by the decay time of the population seen in time resolved photoluminescence, which is more than 100 ps (it would thus mean less than 10 μeV), thus other mechanisms should be at the origin of this dephasing. One possibility is the spin relaxation. Our colleagues of the IPCMS have indeed measured that the spin relaxation time in these nanowires is very short, around 300 fs. It corresponds to a broadening around 4 meV which is in the range of what we measured. We thus argue that the linewidth measured by reflectivity are intrinsic of these GaN nanowires and partly due to a short spin relaxation time.

3.3.3 Polarization of the luminescence

In the last part, we have identified the position of the excitonic resonances. In this part, we will try to get more insight into the dominant contributions seen in photoluminescence thanks to polarization resolved experiments. The polarization of the luminescence comes from two contributions. The electronic properties of the material set the anisotropy of the emitting dipole. This dipole is coupled to the electromagnetic field, which does present an anisotropy due to the anisotropy of the refractive index along and perpendicular to the axis of the nanowire. These two effects are actually

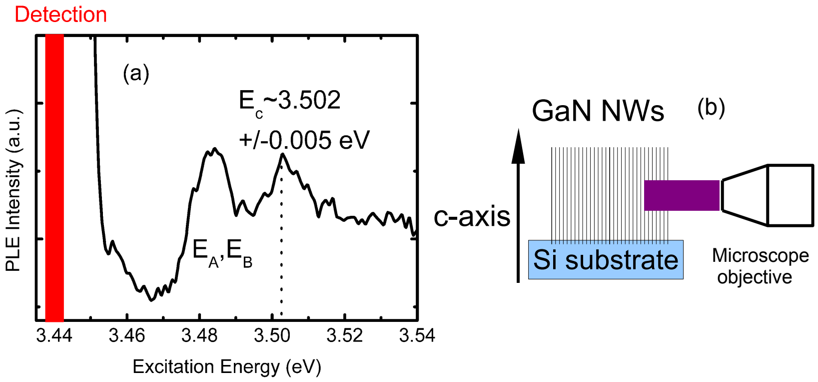

Figure 3.4: (a): photoluminescence excitation at low temperature. The detection set at 3.44 eV is indicated by the red window. (b): geometry of the polarization resolved photoluminescence experiment performed in microphotoluminescence at 90°. We thus have access to a plane containing the c-axis. The schematic is not to scale.

expected to give a polarization of the luminescence in orthognal directions. The dipole of the A exciton (ground state) couples indeed only to $\mathbf{E}\perp\mathbf{c}$. But on the other hand, the electromagnetic anisotropy should favor a luminescence with $\mathbf{E}||\mathbf{c}$.

These experiments were performed on an as-grown sample of nanowires made of pure GaN. Due to the length of the nanowires (around 1 μm), the experiment was performed in microphotoluminescence in order to have the possibility of fine tuning the excitation and collect more photons. The geometry of the experiment is indicated in figure 3.4(b) and is chosen in order to probe the anisotropy in a plane containing the c-axis. The electromagnetic anisotropy should indeed result in a maximum for $\mathbf{E}||\mathbf{c}$ (although for an ensemble of nanowires the index contrast should be reduced compared to the case of a single nanowire) but the selection rules of the A-exciton imply that the D_0X_A transition has a maximum for $\mathbf{E}\perp\mathbf{c}$. In figure 3.5(a) we present the plot of the intensity when varying the angle of polarization where clear features show up. We see that the contributions at 3.45 eV and around 3.47 eV have indeed maxima for orthogonal directions. The luminescence around 3.47 eV presents its maximum $\mathbf{E}\perp\mathbf{c}$ which confirms its attribution. The degree of polarization (see 2.2.1 for the definition) reaches 65% (see figure 3.5(b)). But on the other hand, the 3.45 eV emission is strongly polarized in the other direction, i.e. $\mathbf{E}||\mathbf{c}$. In this case the degree of polarization is

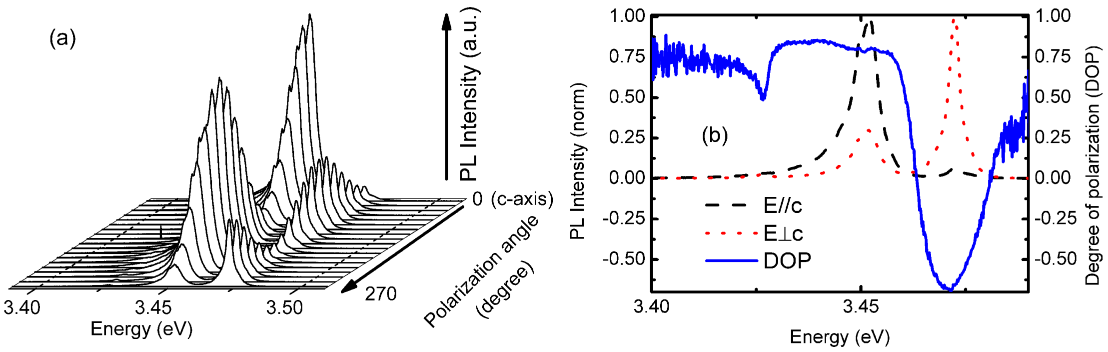

Figure 3.5: (a): photoluminescence resolved polarization at low temperature. 3D plot of the intensity as function of both energy and polarization angle. A clear counterpolarized behavior appears.(b): The normalized intensities in both configurations are compared and the solid line shows the degree of polarization as a function of the energy.

up to 80 %. If one looks at the whole spectrum, one sees that it is almost totally polarized along the c-axis except in a 20 meV window around 3.47 eV. Another interesting feature seen in the curve of the degree of polarization of figure 3.5(b) is around 3.425 eV. One sees indeed that there is a narrow feature which seems to have a maximum of its polarization for **E**⊥**c**. This emission being related to stacking faults bound excitons, it is thus very likely that the bound states are built on the A-exciton, which would explain the polarization selection rules.

At this point we have to comment on the fact that the main part of the luminescence is polarized along the c-axis and see whether or not it is reasonable to explain that in term of electromagnetic anisotropy. Given the fact that the degree of polarization is almost constant expect for sharp features, it seems reasonable to explain it qualitatively this way. Furthermore, considering our nanowire ensemble as a medium of reduced refractive index in the direction perpendicular to the c-axis, with typically $n_{eff} \approx 0.7 n_{GaN}$ [171] (which then give $\epsilon_{eff} \approx 0.5\epsilon_{GaN}$), we expect a degree of polarization given by (see part 4.1.4 for more details):

$$\rho = \frac{I_{\|} - I_{\perp}}{I_{\|} + I_{\perp}} = \frac{|\epsilon_{eff} + \epsilon_{GaN}|^2 - 4|\epsilon_{eff}|^2}{|\epsilon_{eff} + \epsilon_{GaN}|^2 + 4|\epsilon_{eff}|^2} \tag{3.1}$$

which would give a value slightly below 40% for $\epsilon_{eff} = 0.5\epsilon_{GaN}$. Let us note that this value of the degree polarization strongly depends on the effective dielectric constant (80% would require $n_{eff} = 0.45 n_{GaN}$, which is not unrealistic). It can thus qualitatively explain why the luminescence turns out to be polarized along the c-axis even if it is not for intrinsic electronic properties, i.e. due to the crystal symmetry.

A way to probe the electromagnetic anisotropy could be to vary the polarization of the excitation in order to see the anisotropy of the absorption, which should be comparable to the electromagnetically induced anisotropy of the luminescence, provided the excitation occurs at sufficiently high energy to ensure that the electronic density of state is isotropic. But our microphotoluminescence setup, where the exciting beam has a long path after the optics of polarization and has to be reflected before reaching the sample, does not allow us to perform easily a quantitative experiment. But the experiment should also be performed at a wavelentgh close of the luminescence wavelength because the electromagnetic anistropy is strongly wavelength dependent [172]. Thus combining the needs of an isotropic density of states and an exciting energy not too far from the ground state seems difficult. Another way to probe the electromagnetic anisotropy would be to get rid of the electronic anisotropy. It could be done by rising the temperature. Due to the thermalization towards excitons with other selection rules than the A-exciton, the electronic anisotropy should indeed decrease and eventually vanish. Nevertheless, quantitative values for the anisotropy of the oscillator strength of the excitons for unstrained GaN is still under discussion [32, 39, 41, 120, 173]. Thus, assuming that the internal emission is almost isotropic at room temperature, like the authors of reference [172] did, seems to us somehow too conclusive.

Let us now compare our results with what was reported in the literature. In reference [174], the authors performed measurements on a single wire. They essentially see the selection rules of the bulk material when focusing on the 3.47 region and no value for the degree of polarization is reported. In reference [172], the authors also performed polarization resolved photoluminescence on the single wire level. At room temperature they demonstrated that the luminescence is strongly polarized along the c-axis and that it is strongly dependent on the diameter of the wire. The maximum of the degree of polarization is for the small wires with values up to 90%. They developped a model following [175] to describe the electromagnetic problem and managed to fit their data assuming a quasi-isotropic internal emission and a dielectric constant around 6. Decreasing the temperature, they evidenced a strong reduction of the degree of polarization and almost no polarization is seen at low temperature. They attributed this effect to a compensation of the electromagnetic anisotropy by the internal emission.

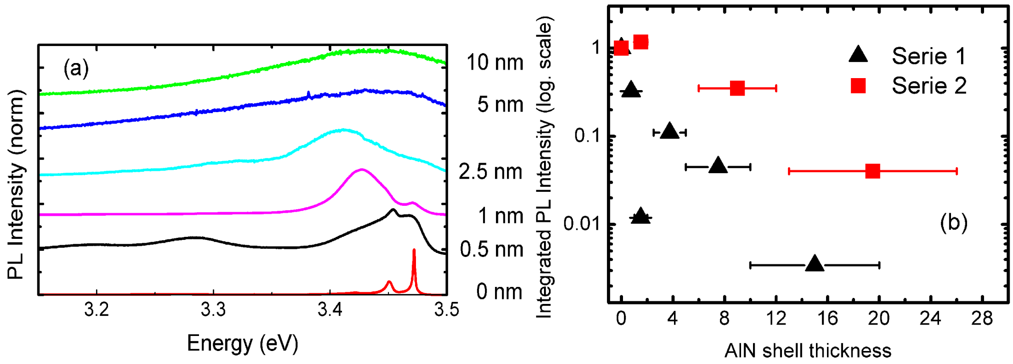

Figure 3.6: (a): low temperature PL of GaN nanowires capped with AlN. The spectra are normalized. The DAP like emission for the sample with 0.5 nm could indicate a small contamination of the growth chamber.(b): integrated intensity as a function of the AlN shell thickness. The two series studied are plotted.

3.4 Influence of AlN capping

As we recalled in 3.1, the nanowire paradigm is that they are free of strain. But as we discussed, it is not true once you start to grow heterostructures, both axial or radial. Furthermore if the strain increases, at some point dislocations appear. In our case, we noticed that when trying to grow AlN on the top of a GaN nanowire, a significant amount of material grows laterally, as illustrated in figure 3.1. This is mainly due to a strongly reduced diffusion for the Al adatoms compared to Ga adatoms. The Al adatoms are thus less likely to be preferentially incorporated at the top. The strong difference between Ga and Al is now clearly established. This is why the growth of AlN nanowires has been proved to be much more challenging than GaN. Our group recently achieved to grow AlN nanowires on SiO_2 as we will see later.

Coming back to the problem of the lateral growth of AlN, it is obvious that when AlN is grown on the side of the GaN nanowire, it will create a strain on the GaN core and eventually dislocations should appear [149]. We have thus studied GaN nanowires capped laterally by different amounts of AlN. The lateral growth rate of AlN has been calibrated : in the growth conditions used for all the samples it is around 0.25nm/min. The thicknesses will be checked by TEM in the near future. We combined optical characterizations with Raman in order to try to correlate the strain and the optical properties. The PL spectra are presented in figure 3.6(a). The most strik-

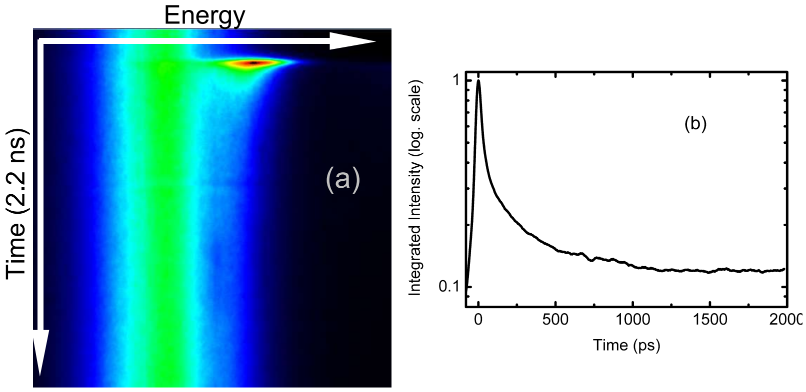

Figure 3.7: (a): low temperature time resolved PL of GaN nanowires capped with AlN (lateral thickness around 10 nm). The window is centered around 370 nm and is 85 nm wide. The vertical window is 2200 ps. (b): integrated intensity of the high energy part presenting a short decay time.

ing feature is that already for very small shell thicknesses, the PL changes significantly and the contribution around 3.47 eV quenches. Furthermore, as seen in figure 3.6(b), the integrated PL intensity decreases strongly when capping the GaN wires with AlN. Although we have large errors bars due to the uncertainty on the thickness of the AlN shell and also some discrepancy between the two sets of samples, certainly due to inhomogeneity across the samples, we attribute this quenching to the creation of nonradiative channels at the GaN/AlN interface. The fact that in the presence of AlN, most of the excitons recombine nonradiatively has been confirmed by time resolved luminescence. When we performed time resolved photoluminescence on a sample capped with AlN, we see that the broad peak around the near band edge has various contributions. At low temperatures we observe that most of the signal has a very long decay time, as seen in figure 3.7(a). This luminescence can thus be attributed to shallow defects which strongly localize the carriers. At higher energy, one sees that some part of the signal has a short decay times, around 50 ps. It is likely that this luminescence has an excitonic nature but that easy paths towards nonradiative channels exist for these excitons, which explains the short decay times, much shorter than the decay times of excitons in GaN nanowires presented in 3.3.1. This explains why in continuous wave experiments, we see mainly the broad luminescence and very weak contributions from excitonic recombinations. A detailled study of the time resolved luminescence of all the samples is in progress and should

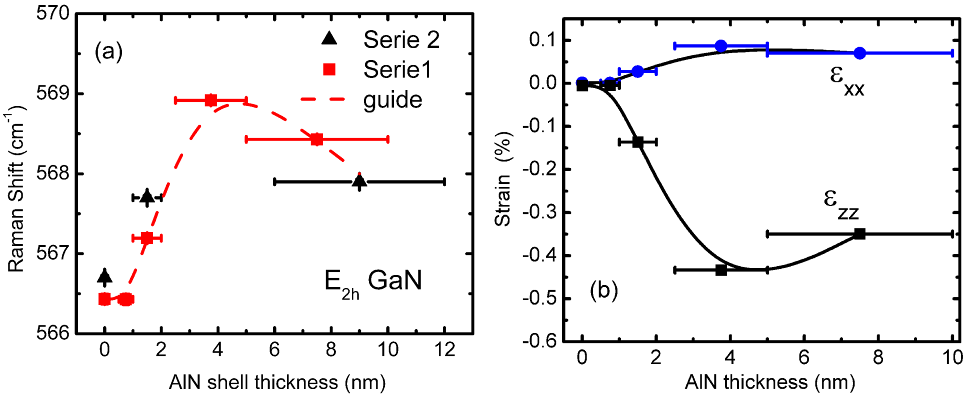

Figure 3.8: (a): Raman shift as a function of the thickness of the AlN shell. The measurements were performed with the 514.5 nm line of an argon laser. (b): values of the strain extracted from the Raman shifts in the uniaxial approximation for the first serie of samples. The solid lines are guide for the eyes.

give more insight into the importance of these nonradiative recombinations.

Another possibility to explain the features of the luminescence spectra was raised by professor N. Grandjean during the defense of this thesis. We see in figure 3.6(a), that the luminescence turns out to be dominated by a contribution around 3.4 eV when we add an AlN cap. But when growing AlN, there is of course a growth at the top of the wire. Thus we have a polar GaN/AlN interface at the top. In such interface, it is well known that a 2 dimensional electron gas (2DEG) is created. It has been reported that the luminescence of such a 2DEG is dominated by a broad luminescence around 3.4 eV [176]. It is thus possible that this 2DEG plays an important role in the luminescence of our structures. This topic is currently under investigation.

To get more informations about the electronic properties of GaN nanowires capped with AlN, one should try to have access to intrinsic properties of the GaN, like the positions of the excitonic resonances. As already mentioned in this dissertation, reflectivity or photoluminescence excitation are very powerful tool for this purpose. We hope that such experiments will be performed in a near future and that it will be possible to relate the shifts to the strains which were extracted experimentally.

The strain in the GaN has been measured by Raman spectroscopy (experiments performed by our colleagues of the university of Valencia) and we focused on the E_{2h} peak. The evolution of its position with the thickness of the AlN shell is presented in figure 3.8(a). The strain is deduced in the

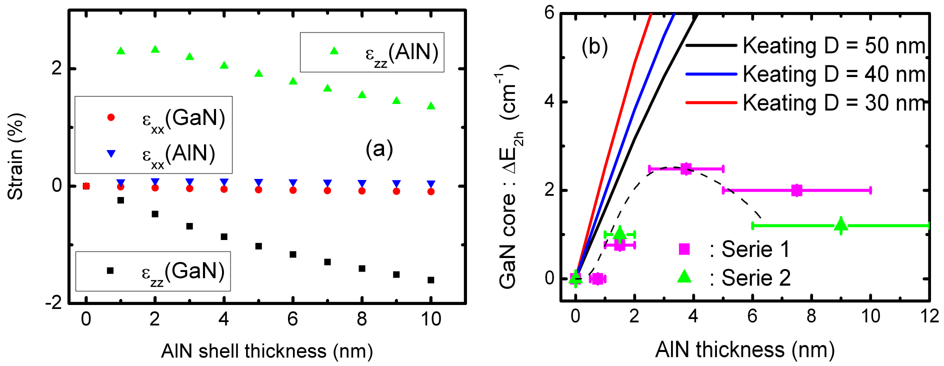

Figure 3.9: (a): Simulation of the elastic strain in GaN nanowires capped by AlN with the Keating's model. (b): comparison of Raman measurements (squares and triangles) and simulations (lines) in terms of the Raman shift of the E2h mode of the GaN core. The simulations have been performed assuming a cylindrical geometry and for various diameters (D) of the wires. The dotted line is a guide to the eyes.

uniaxial approximation ($\sigma_{xx} = \sigma_{yy} = 0 = (C_{11} + C_{12})\epsilon_{xx} + C_{33}\epsilon_{zz}$) and the results are presented in figure 3.8(b). The tendency clearly appears. For very thin AlN thicknesses, below 4 nm, the strain increases with the thickness. But adding more AlN certainly creates dislocations and this would explain why the strain decreases above 4 nm.

In order to see what is the amount of elastic strain which is expected with the thickness of AlN, calculations have been performed by our colleagues of the LSIM laboratory (D.C. Camacho and Y-M. Niquet). They use the Keating's model [177] adapted to the wurtzite structure to simulate the relaxation. The results are presented in figure 3.9(a). Let us stress that these results indicate that the uniaxial approximation used in order to extract the strains from the Raman shifts does not hold. It can be understood because due to the geometry of the epitaxy (the AlN shell is "closed"), it is actually possible to have non vanishing σ_{xx} and σ_{yy} stresses and end up with a volume shrinkage. Thus to compare the calculated strains to the experimental ones, we have to get back to the Raman shifts where no assumption is made about the strain. One can see in figure 3.9(b) that already for thin AlN shells, the agreement is not very good suggesting either that part of the relaxation is plastic from the very beginning or that some inhomogeneity in the shell could lead to a complex behavior. Further experiments are under progress, especially TEM imaging of the core/shell interface in order to show the presence of dislocations, but the fact that in such a system the relaxation is not purely elastic seems established.

3.5 Optical properties of GaN nanowires with embedded heterostructures

After having focused in details on the optical properties of ensembles of nanowires made of pure GaN, we will present our studies concerning ensembles of nanowires with embedded heterostructures. We have presented in 3.1 the potential interests of theses structures. If one wants to compare these structures, i.e. quantum dots as a slice of a nanowire, to traditional self assembled quantum dots, one can make additional remarks : one first important difference is that there is no wetting layer for quantum dots embedded in nanowires. If one think about devices working at high temperature it could prevent the thermal escape of the carriers although we will see later that even for traditional III-N quantum dots, these processes are negligible up to room temperature (see chapter 6). Furthermore, as we will see in the next chapter devoted to the study of these single quantum dots embedded in nanowires, the process to isolate a single nanowire to perform single dot spectroscopy is very easy compared to the traditional process (e-beam + etching) required for self assembled quantum dots. The possibility to study single quantum dot embedded in nanowires has now been demonstrated in various materials [178–180].

3.5.1 Evidence of quantum confined stark effect in GaN/AlN nanowire heterostructures

We have seen in chapter 1 that in 2D GaN/AlN heterostructures, a huge electric field is present and is the source of the quantum confined Stark effect (QCSE). In nanowires, the situation could actually be different. The first argument comes from the strain. It is indeed expected that the strain in a quantum dot embedded in a nanowire is different from the one of a 2D structure. Thus the piezoelectric field could be different. Furthermore due to the proximity of the surface, the presence of charges in surface states can at first sight not be ruled out. This could somehow screen the internal electric field and thus the actual field would be reduced. Also let us emphasize that the situation could be different for GaN/AlN or GaN/InGaN although we will mainly focused on GaN/AlN. In the InGaN/GaN system the polarization difference comes indeed mainly from the piezoelectric contribution,

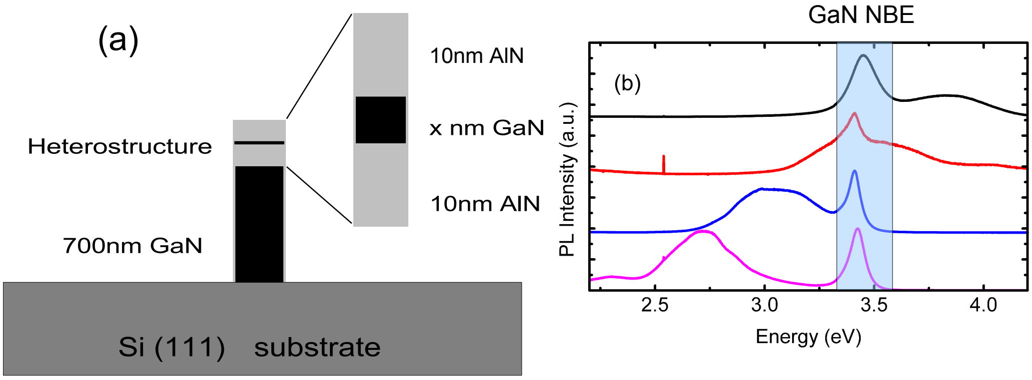

Figure 3.10: (a): schematic illustration of GaN/AlN insertions on the top of GaN nanowires. (b): photoluminescence at room temperature performed on ensembles of nanowires containing one GaN/AlN insertion. We changed the thickness (x in figure (a)) in each sample, increasing from the top.

thus if the strain is reduced in a nanowire heterostructure, the electric field could be much smaller. This is what seem to show recent studies comparing InGaN/GaN nanowires to their 2D counter part in both photoluminescence [181] and electroluminescence [182]. For GaN/AlN, the situation is not clear with very few studies [183–185] and no evidence for luminescence well below the GaN band gap. Also in these articles, the authors used GaN/AlGaN heterostructures and it is now demonstrated that the composition of Al is strongly inhomogeneous in AlGaN nanowires due to large difference for the diffusion of Al and Ga. It makes thus modelization more tricky in this system.

In this section we will separate the results obtained for GaN/AlN heterostructures grown in GaN nanowires and in AlN nanowires. Although the physical problem is almost the same, we will present them separately because the results obtained on AlN nanowires are very recent and we have less feedback, especially concerning the sizes of the insertions.

The case of GaN/AlN in GaN nanowires

The typical samples grown are as follows : a 600-700 nm long foot of GaN (diameter 30 to 50 nm) and a top with a heterostructure. The heterostructure consists of two AlN barriers (around 10 nm thick) and a GaN insertion in between. The situation is illustrated in figure 3.10(a). We studied samples with insertions ranging from 1 to 4 nm. The main problem for

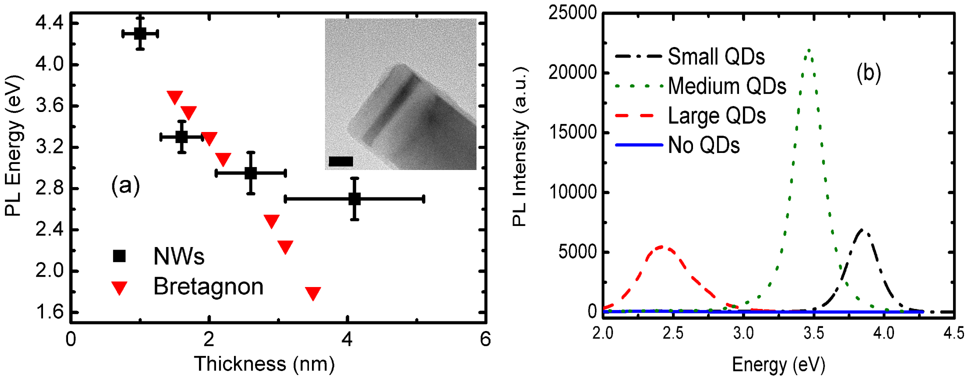

Figure 3.11: (a): position of the peak seen in photoluminescence for samples with different thickness of the insertions. The thickness has been measured by HRTEM (C. Bougerol) for the three thicker samples (see the inset for the thicker one, scale 10 nm) and is an estimation extracted from the growth time for the other. A comparison is made with data for GaN/AlN self assembled quantum dots (after Bretagnon et al.[14]).(b): photoluminescence at low temperature for GaN/AlN quantum dots of different thicknesses embedded in AlN nanowires.

these samples comes actually from the very strong signal stemming from the GaN foot, much more intense than the signal stemming from the insertions. In order to increase the relative contribution of the insertions, we performed the experiments at room temperature because we expected that the GaN insertions should be less sensitive to temperature than the GaN foot (the robustness of the luminescence of the insertion will be demonstrated in section 3.5.3). The results for the set of samples with various insertion thickness are presented in figure 3.10(b). It clearly evidences the QCSE : the very thin insertions ($\approx$ 1 nm) luminesce around 4 eV (the quantum confinement is the dominating mechanism that sets the energy) and a strong red shift is observed when this value is increased (because of the increasing effect of the electric field). We end up for a 4 nm insertion with an emission around 2.5 eV, i.e. 1 eV below the GaN band gap. In figure 3.11(a) the position of the energy of the peak is plotted versus the thickness of the insertions and compared with self assembled GaN/AlN quantum dots.

Although it is difficult to conclude at this point due to large error bars, it seems that the electric field could be reduced for the thicker insertions, the quantum dots embedded in nanowires emitting at higher energy than their self assembled counterparts of same thicknesses. One mechanism that

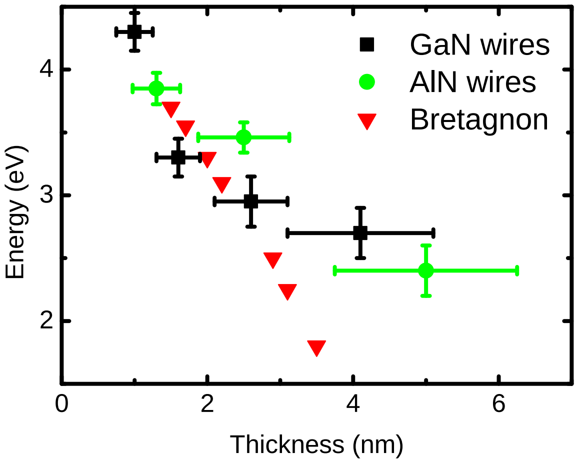

Figure 3.12: Summary of the results obtained on the dependence of the luminescence energy on the thickness of the insertion. Comparison with the data on self assembled quatum dots (after Bretagnon et al. [14]).

could potentially explain this difference would be a partial relaxation of the thicker dots in the nanowires which would reduce the piezoelectric field. For thick heterostructures which are purely radial (i.e. no lateral growth when growing the top barrier), this is expected due to the presence of the surface which allows a easy strain relaxation. In our case, a small amount of AlN grows laterally. Thus the situation is not that simple and this AlN shell has to be taken into account and should somehow prevents this relaxation. But it is possible to argue that due to a particular dot geometry, there will be a plastic relaxation in the AlN shell. This could result in a relaxation of the GaN insertions as demonstrated recently [186].

The case of GaN/AlN in AlN nanowires

We will now focus on the same kind of heterostructure than presented before but in this case the foot is made of AlN instead of GaN. This was a challenge from the growth point of view and only achieved recently in our group (O. Landre thesis [151]). We have thus not been able to measure the thickness of the insertions by HRTEM so far and they are only deduced from the growth time. But the situation looks pretty similar in this case and the strong advantage of these new structure is that we have not the problem of the emission of the GaN foot. The low temperature photoluminescence spectra are presented in figure 3.11(b) : the red shift is clearly seen and the thicker insertions luminesce far below the GaN band gap. We have plotted

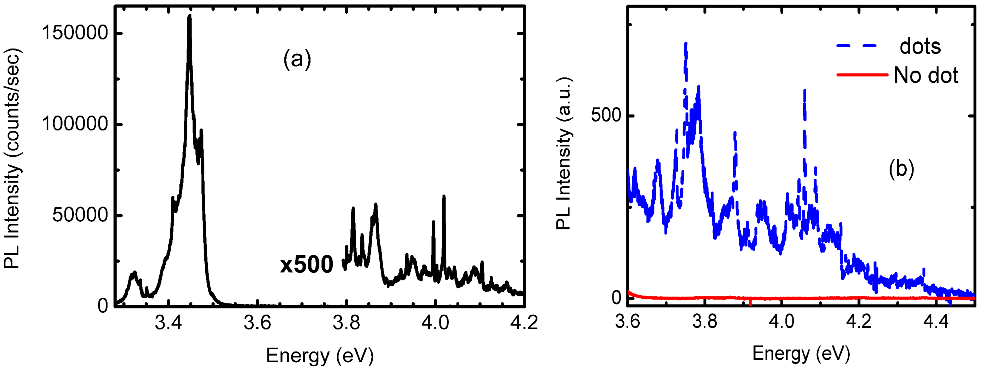

Figure 3.13: (a): microphotoluminescence at low temperature measured on a sample of undispersed (i.e. as grown) nanowires with 1 nm thick quantum dots embedded. Sharp lines appear at high energy. (b): comparison of the luminescence of a sample with small dots and one only with the AlN shell.

the luminescence energy as a function of the GaN thickness in the same graph than the one of figure 3.11(a). As illsutrated in figure 3.12, the tendency is the same and the reduction of the Stark shift for the large insertions is confirmed.

To conclude this part about the QCSE, one can say that the presence of an important electric field in GaN/AlN heterostructure embedded in nanowires is established although the measurements seem to indicate that this field is somehow reduced for the largest insertions compared to usual quantum dots. A more detailled study, including time resolved measurements is on its way in order to get precious informations on the electron-hole overlap and compare it with the situation for self-assembled quantum dots.

3.5.2 The luminescence originates indeed from the quantum dots

In this section, we will give evidences that the luminescence indeed stems from the quantum dots. Although the results about QCSE presented in the last section clearly show the effect of the confinement and thus the fact that the luminescence come from the dots, we did not have these results at the early stages of this study and we thus had to find other evidences. Especially, we will argue that this luminescence cannot stem from defects in the AlN. For instance such deep defects (4 eV is 2 eV below the AlN band gap) should have a very low oscillator strength.

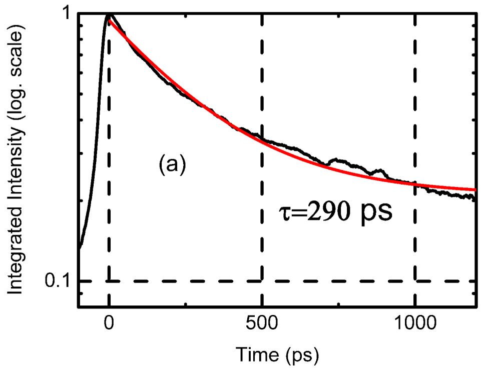

Figure 3.14: (a): time resolved photoluminescence at low temperature performed on an ensemble of small dots (luminescence around 300-310 nm) embedded in nanowires.

Dots contribution

When one says that luminescence is arising from quantum dots, one expects to see sharp lines if the dots density under the excitation spot is significantly reduced. This is what is presented in figure 3.13(a). The experiment is performed at low temperature in microphotoluminescence on an as-grown sample and one thus expects to have around 200 dots under the excitation spot. On this sample with small insertions (around 1 nm), one observes many sharp lines (linewidth down to 1 meV) at high energy, around 4 eV. Another evidence comes when comparing the luminescence of such a sample with one which only consists of a GaN nanowire capped with AlN. One could indeed argue that the sharp lines stem from localized defect states in the AlN capping. In figure 3.13(b) one can see that in the same experimental conditions no luminescence is seen in the 4 eV region for this sample compared to the sample with insertions.

Time resolved photoluminescence

We will now focus on the oscillator strength of these transitions. In figure 3.14(a) we present time resolved photoluminescence performed on an ensemble of small quantum dots embedded in nanowires. One sees that the decay time is around 290 ps which indicates that these transitions have a strong (meaning excitonic like) oscillator strength. It thus support our attribution of this emission to the quantum dots.

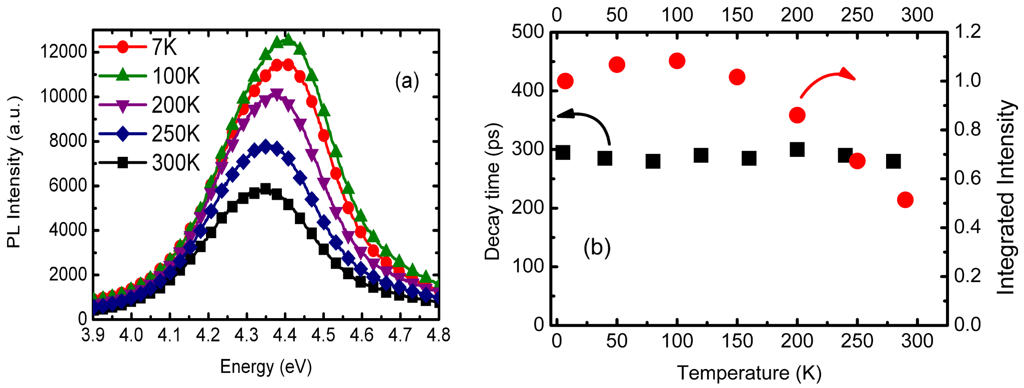

Figure 3.15: (a): temperature dependence of the luminescence of quantum dots embedded in nanowires. (b): temperature dependence of the integrated intensity, extracted from (a), and of the decay time.

3.5.3 Temperature dependence : evidence for the suppression of nonradiative recombinations

For quantum dots, the nonradiative processes are supposed to be strongly suppressed compared to bulk or even to quantum wells. A detailled study of these processes for 2D structures (quantum wells or self-assembled quantum dots) will be presented in chapter 6. In this section we will study the temperature dependence of the luminescence of quantum dots embedded in nanowires, both in continuous wave and time resolved experiments. In figure 3.15(a) one sees that the quenching of the luminescence is rather slow. More quantitatively, figure 3.15(b) shows that the integrated luminescence at room temperature is still around 50 % of its value at low temperature (we have to stress that the slight increase of the integrated intensity up to 100 K is not clearly understood so far), illustrating the very weak influence of thermally activated nonradiative recombinations (in comparison, the near band edge typically loses at least a factor 20). This is confirmed by time resolved data, which show that the decay time at room temperature, namely 290 ps, is similar to the one at low temperature. We will get back to possible explanations for the losses in the integrated intensity, which seem not to be correlated with time resolved data, in the case of self assembled quantum dots (see chapter 6). The explanations are indeed very likely to be similar. But one can anyway safely conclude about the strong reduction of thermally activated nonradiative recombinations in the case of quantum dots embedded

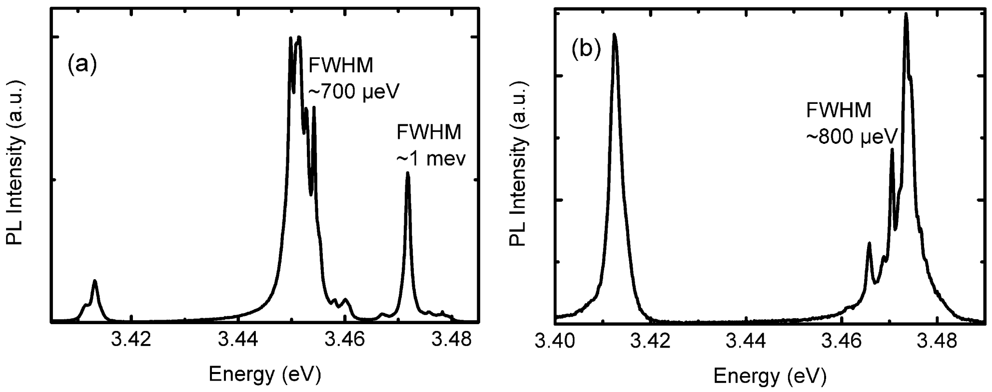

Figure 3.16: (a)and (b): low temperature microphotoluminescence measured on two different nanowires (courtesy of Diane Sam-Giao). The spectra have to be compared with the luminescence of an ensemble, see figure 3.2(a).

in nanowires compared to quantum wells for instance.

3.6 Luminescence from single nanowires : evidence for a non intrinsic behavior

In this part we will shortly discuss the optical properties of single nanowires made of pure GaN. The method to isolate single nanowires will be presented in 4.1.1. We have studied wires dispersed on various substrate, namely Si, SiO_2, Al_2O_3, metal, GaAs. The first conclusion we could draw is that the effects of the substrate are smaller than the differences one can see on different wires on the same substrate. The spectra indeed change dramatically from wire to wire. They are in particular not all similar to what is seen on an ensemble of nanowires. Two spectra are presented in figure 3.16. The common feature seems to be the presence of luminescence in the 3.47 eV area, i.e. shallowly bound excitons. Also the luminescence is usually broader compared to the ensemble but presents a structure. We sometimes see very sharp lines, less than 1 meV, out of this broader emission. It could arise from single impurity bound excitons. We do not think that the broadening is a consequence of heating, because reducing the power does not lead to significantly different spectra. The fact that the luminescence in the 3.42 eV region, attributed to stacking fault bound excitons, does not show up in all single dispersed nanowires could indicate that some nanowires are broken above the region containing the stacking faults (i.e. which is close to the Si growth substrate) during the dispersion process. At this point, that is all we can say about the optical properties of single dispersed nanowires without being too conclusive. To get more insight about this issue, we think about looking at the same nanowire in both microphotoluminescence and TEM in order to see if the optical properties can be somehow correlated to structural features. Also, as we believe that the new electrostatic environment created by the vicinity of the substrate has major consequences and could explain why the luminescence differs from wire to wire, the study of single freestanding nanowires would be of interest, as demonstrated in ref. [187].

3.7 Prospects

To conclude this chapter, we will give some directions that should guide our future researches on the topic. Concerning the issue of the 3.45 eV emission, we will perform measurements on ensemble of nanowires under magnetic field (with our colleagues of the LCMI). This emission is still under intense discussion in the community, with somehow contradictory results [147, 169]. Authors of ref. [169] attribute this emission to two electron satellites (TES) but as mentioned in [167], this is questionable for many reasons, especially the temperature dependence where different quenchings are observed for this line and the 3.47 eV one. What seems clear is that this emission is not related to the interface between the nanowires and the growth substrate. Magnetic field experiments would give further indications about the assignments to TES, similar to what has been done in 2D layers [188, 189].

One study that we only initiate is the far field imaging of the emission of nanowires (i.e. a k-space imaging). Preliminary experiments seem to show that the emission is strongly peaked around $\mathbf{k}_{||} = \mathbf{0}$. But this has to be compared with a 2D layer and also the effects of the orientation of the dipole (i.e. the polarization of the light) have to be taken into account. This kind of study is also planned to be performed on heterostructures embedded in nanowires.

We have seen that the luminescence of single GaN nanowires dispersed on a substrate is still not very well understood. We think of a more systematic study, including porous (for instance sol-gel) substrate, in order to get more informations. Also, as we already pointed out, the study of single free standing nanowires, made for instance thanks to patterned substrate is on its way.

Concerning heterostructures we have seen that thanks to the growth of

AlN nanowires we could get rid of the problem of the emission of the GaN foot, which has prevented us to study carefully dots luminescing below 3.7 eV. This should now allow us to compare the emission characteristics (for instance decay times) for dots embedded in nanowires to the self assembled ones in the whole range of energy.

In this chapter, we have presented the optical properties of ensemble of GaN nanowires. Besides photoluminescence spectra, we have shown reflectivity and photoluminescence excitation spectra. These two methods allow us to precisely identify the position of the free excitons. Polarized photoluminescence, performed in a plane containing the c-axis, shows that both the electronic (selection rules of the bulk material) and electromagnetic anisotropy are essential in order to understand the optical properties of nanowires. A peculiar behavior in the near band edge luminescence resulting from this interplay has been observed. Concerning nanowires with embedded heterostructures, the presence of the quantum confined Stark effect has been evidenced in both GaN and AlN nanowires by showing luminescence well below the GaN band gap. This quantum confined Stark effect seems to be reduced for insertions thicker than 3 nm compared to two dimensional structures. These quantum dots inserted in nanowires appear furthermore to be weakly sensitive to nonradiative defects, as evidenced by temperature dependent measurements. Finally we have shown that the optical properties of single GaN nanowires dispersed onto a substrate present a large dispersion and that extracting intrinsic characteristics would be made easier by studying free standing nanowires.

Chapter 4

Spectroscopy of single quantum dots embedded in GaN nanowires

In the last chapter, we have presented the optical properties of an ensemble of wires containing heterostructures. We have, among other things, evidenced that the electric field in nanowire heterostructures is not significantly reduced compared to 2D structures. In this chapter, we will focus on the spectroscopy of a single GaN/AlN quantum dot embedded in a nanowire. We will see that to some extent they have properties similar to SK quantum dots. We begin in the first section with the experimental procedure used in order to isolate a single nanowire containing a single quantum dot and present the low power limit of the luminescence. The next section will be devoted to power dependence measurements. We will focus in the final section on correlation experiments before giving some ideas about future work on the topic.

Contents

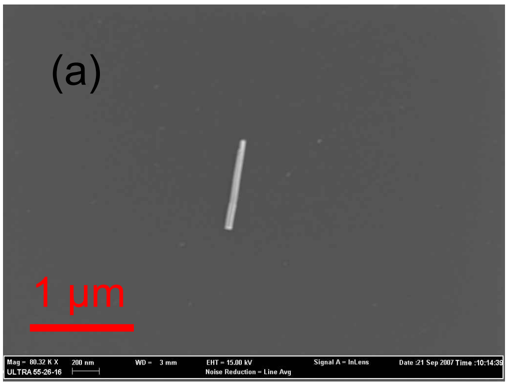

Figure 4.1: (a): SEM image of a wire dispersed on a Si substrate. The density is low enough to have only one wire excited with a 1 μm spot.

4.1 Single quantum dot emission

4.1.1 Nanowire dispersion : how to reduce the dot density?

We saw in chapter 3 that an as-grown nanowire sample has a typical density around 10^{10}cm^{-2}, i.e. 100 per μm^2. Given the size of the laser spot in μPL (diameter 1-2 μm), we therefore excite a few hundreds of wires and consequently a few hundreds of dots. This explain why we observe many lines when working on an ensemble (see figure 3.13(a)). In order to disperse the wires and reduce their density, different approaches have been tried. One of them consists in putting a sample in an ultrasonic bath (in isopropanol for instance) and after a given time (typically a couple of minutes) taking a couple of drops (typically 5) of the solution and let them dry one after another on a clean substrate (to speed up the process, the substrate is placed on a hot plate at a temperature around 80°C). In figure 4.1(a) the SEM image shows a dispersion made on a silicon substrate. Another possibility is to gently swipe an as-grown sample with a twisted piece of Texwipe (in order to make some kind of tip) and then touch the new substrate with the Texwipe. This also gives satisfactory results and the strong advantage of this technique is that it does not require the use of a solvent. We used this method for instance for the dispersion made on TEM grids because the presence of residual solvent is often a problem for TEM imaging. We also noticed that drops of solvent tend to roll off the TEM grid before they have time to dry.

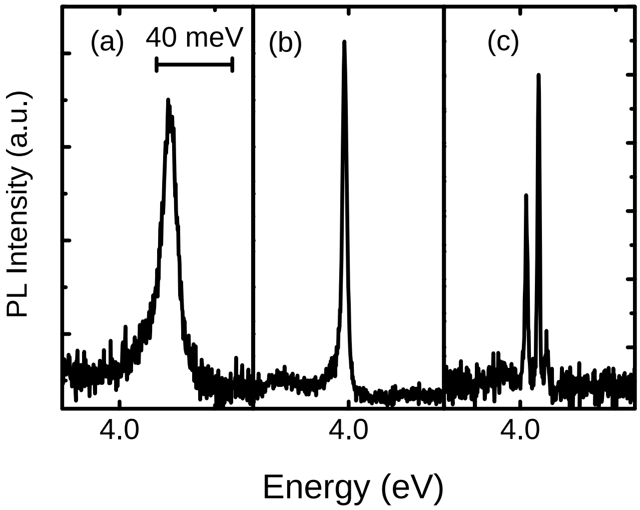

Figure 4.2: Illustration of the variation of the low power luminescence from dot to dot emitting in the same spectral region : a single broad line (a), a single narrow line (b) or a multiplet (c). The measurements are performed on a single wire.

4.1.2 Low power spectra: evidence of spectral diffusion

Using the method that we just described, we are able to probe the optical properties of single quantum dots embedded in nanowires. Unless stated otherwise, we will present studies carried out on small quantum dots luminescing in the 3.8-4.2 eV region, i.e. with a thickness (vertical dimension) around 1 nm. The lateral dimension is set by the dimension of the nanowire, typically 30 nm. The confinement is thus dominated by the vertical dimension, which sets the transition energy.

The experimental method to find the luminescence from a single quantum dot embedded in a nanowire is the following : we start by looking on a dispersed sample for an area which gives off luminescence, indicative of the presence of a nanowire (they are indeed too small to be seen in our visualization camera). This detection is made on our visualization while moving the spot across the sample and observing the luminescence. This strong luminescence (i.e. easily detectable on our visualization) comes actually from the bottom part of the nanowire made of pure GaN, which even on a single nanowire is strong enough. After this step a spatial optimization is made on the signal of the GaN foot, detected on the CCD, with piezoelectric translations stages. This steps ensures that the position is optimum onto the wire. After this second step, the monochromator moves into the region of interest, i.e. 3.8-4.2 eV, in order to observe the luminescence of the dot. We noticed that not all the dots luminesce and sometimes a wire which contains a heterostructure shows luminescence only in the range of the GaN near band edge. The reason to explain why some dots (actually the major part) do not luminesce is not clear up to now but it may be related to the dispersion process. Otherwise, the reasons are may also be intrinsic to the GaN/AlN heterostructures embedded in nanowires, possibly due to the presence of dislocations.

One striking characteristic of the low power spectra of single quantum dots is the strong differences that we observe from one dot to another. The luminescence can consist of either a single narrow line (less than 1 meV), a single broad line or a multiplet of lines. This is illustrated in figure 4.2. Once again we attribute this behavior to spectral diffusion effects, well known in nitride quantum dots, as we already explained for non polar quantum dots in 2.3.1. The effect of the trapping and untrapping of charges in the neighborhood on the luminescence is related to their position (i.e. the distance with respect to the dot) and the frequency of the phenomena. If they are close enough, it will create spectral jumps that we are able to resolve spectrally as multiplet. If not, it will appear as a broadening. If they are slow enough, we will be able to resolve the changes temporally. In figure 4.3(a), we present evidence for these temporal variations. On a time scale of around 1 sec, we can resolve changes in the spectral location of the luminescence. We also noticed some variation of the luminescence intensity with time as illustrated in figure 4.3(b)

Although we did not study this in details, we have thought about some experiments that could be useful in order to gain insight into the dynamics and the energy scales of these phenomena. The simplest one would use a single channel detector and a correlation card in TTTR mode. In this mode you label a given photon with an absolute time and you can build a correlation function for any time larger than the dead time of your detector (a few hundred ns in our case). If you select the whole luminescence you will have access to the blinking but if you select a small part of the line (by closing the slits in front of the detector), you should see a bunching in the correlation function. The bunching time will correspond to the time the quantum dot neighborhood stays in the state (or not far from it, depending on the energy scale you chose) it was in at time $t=0$.

To access a better time resolution, the idea would be to use two detectors instead of one and perform a standard correlation experiment. Again, one

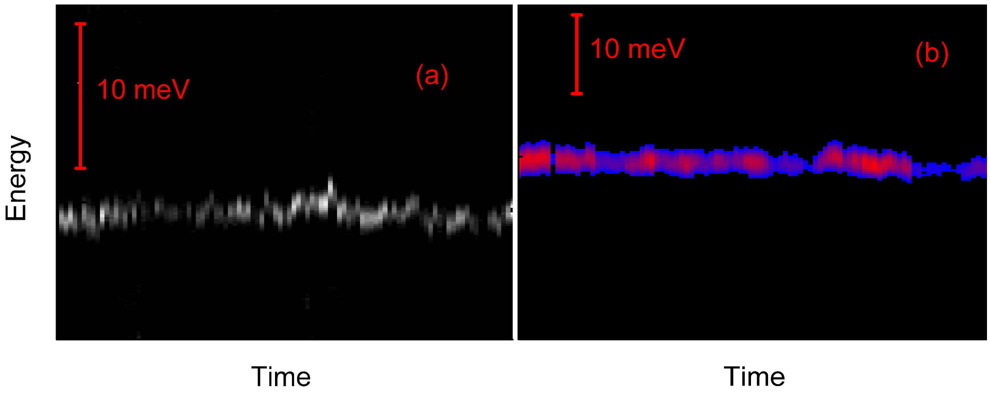

Figure 4.3: (a): Illustration of the spectral diffusion. 100 spectra are recorded successively with a 1 second integration time. (b): variation of the luminescence intensity with time. 100 spectra are recorded successively for 0.5 second

can select a given energy for each detector. If one sets both detectors to detect the same energies, one should see a bunching similar to that observed with the one detector experiment but at zero time delay, one should also see an antibunching because the emitter emits single photons (this effect is hidden in the one detector experiment due to the time resolution). If one uses two different energies for the detectors, one should only see an antibunching but in this case the characteristic time would be the spectral diffusion time. This two detectors method has been extensively used by G. Sallen [190] for the study of quantum dots embedded in II-VI nanowires. Spectral diffusion times ranging from a few ns up to a few tens of ns (at low excitation power) were reported.

One other idea to study this spectral diffusion is to use the method of Photon Correlation Fourier Spectroscopy developed by L. Coolen et al. [136, 191]. They used a Michelson interferometer before the detectors in order to obtain both a good temporal (theoretically limited by the lifetime of the emitter) and spectral (down to a few μeV) resolution.

4.1.3 Temperature dependence

We have seen in the last chapter that the luminescence of an ensemble of quantum dots embedded in nanowires does not collapse when one raises the temperature. This proves that the quantum dots have a weak sensitivity to nonradiative processes as one could expect from the 3D confinement. We thus

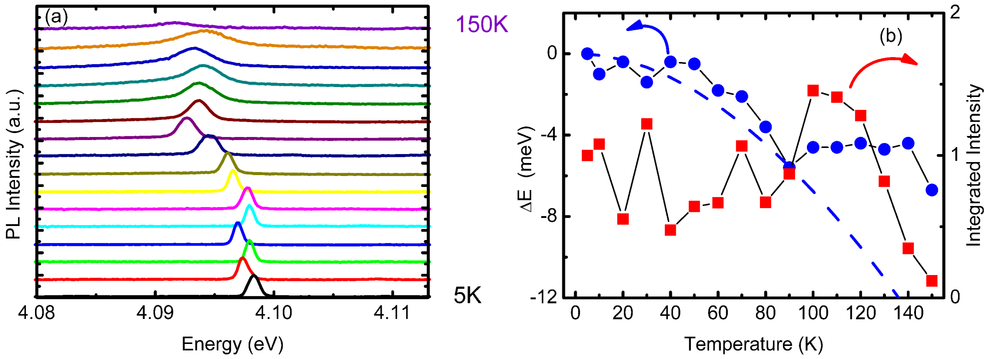

Figure 4.4: (a): luminescence of a single quantum dot as a function of temperature. The step is 10 K for the temperature variations, increasing from the bottom. (b): integrated intensity of the line (normalized to its value at low temperature) together with its shift. The dotted line follows a Varshni law with parameters $\alpha = 0.560$ meV/K and $\beta = 737$K [192].

tried to study the luminescence of a single quantum dot as a function of the temperature. Let us note that this kind of measurement is very challenging due to small thermally induced drifts in the sample position. Nevertheless, we were able to record a decent signal up to 150 K for the spectra presented in figure 4.4(a). The integrated intensity as well as the peak position variations with the temperature are represented in figure 4.4(b). At low temperatures (at least up to 60 K, yellow curve) the luminescence variations are dominated by spectral diffusion effects : the thermally induced shifts and broadening do not dominate over the spectral diffusion. Then the thermal effects are more important and not hidden by spectral diffusion. Up to 130 K for this quantum dot, no significant losses are seen in the integrated intensity but then the intensity seems to quench quickly. One difficulty of such an experiment is that a reoptimization process is required when the temperature is changed (i.e. slightly moving the excitation spot in order to maximize the signal). But due to a significant broadening of the line this step gets trickier (and not very accurate) and we believe that it does partly explain why it is difficult to record the spectrum of a single dot at higher temperature even if the total integrated intensity does not decrease significantly.

To conclude this brief study, we would like to emphasize that although the temperature dependence is a clear evidence that nonradiative processes are efficiently suppressed in these structures, a detailed study would require

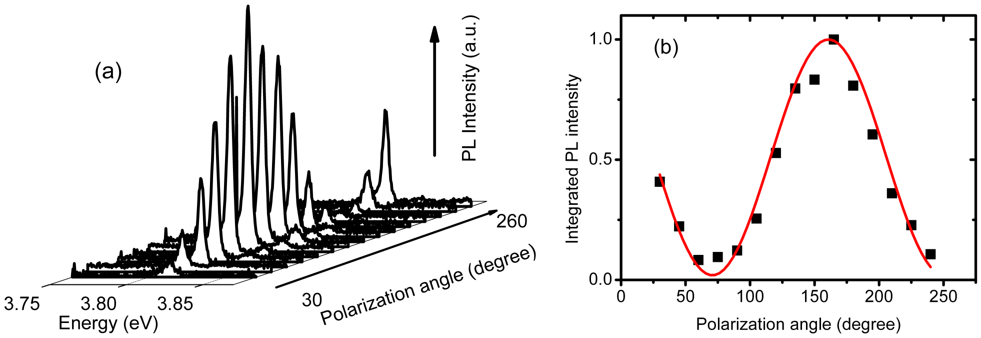

Figure 4.5: (a): 3D plot of the luminescence of a single quantum dot embedded in a nanowire as a function of the polarization angle. The absolute angle has no meaning relative to the crystallographic axis because the nanowire is dispersed onto a Si substrate and its precise orientation is not known. (b): integrated intensity as a function of the polarization angle. The solid line is fit by the function 2.1 and gives a degree of polarization of 96 %.

to couple these measurements with time resolved studies as a function of the temperature in order to extract the relative importance of both radiative and nonradiative processes in a similar fashion to what we have done in 2.2.2. We will get back to the interpretation of these kinds of measurements in the case of quantum wells and SK quantum dots in chapter 6 and show that some parameters which are difficult to access play a key role in the decrease of the luminescence.

4.1.4 Polarization of the luminescence

We have shown in 3.3.3 that the luminescence of an ensemble of GaN nanowires presents interesting polarization properties in a plane which contains the c-axis. This is a consequence of the interplay between the electronic structure of GaN and the electromagnetic anisotropy. We will now study this effect for single quantum dots embedded in nanowires.

Let us focus on single nanowires dispersed onto a substrate. The situation could in this case be different because the electromagnetic anisotropy is now much larger than for an ensemble of GaN wires. The confinement could also change the selection rules, although the ground state should stay A-like, due to the heavier mass of the A-like hole. The polarization resolved luminescence of a single dot is shown in figure 4.5(b). The luminescence is strongly polarized. The degree of polarization extracted from the fit reaches 96%. But the problem is that we do not have access in this kind of experiment to the orientation of the wire. We will thus have a qualitative discussion. In the limit of small radius for a nanowire surrounded by vacuum, the ratio of the two components of the electric field, parallel or perpendicular to the growth axis, reads [175, 193, 194] :

$$\frac{E_{||}}{E_{\perp}} = \frac{\epsilon + \epsilon_0}{2\epsilon_0} \tag{4.1}$$

where ϵ is the dielectric constant of the nanowire. This should lead to an electromagnetic induced degree of polarization in the case of intrinsically (i.e. due to the crystal symmetry) unpolarized emission :

$$\rho = \frac{I_{||} - I_{\perp}}{I_{||} + I_{\perp}} = \frac{|\epsilon + \epsilon_0|^2 - 4|\epsilon_0|^2}{|\epsilon + \epsilon_0|^2 + 4|\epsilon_0|^2} \tag{4.2}$$

To give an idea of the phenomenon, a dielectric constant of 10 should lead to a degree of polarization around 90 % with a maximum for $\mathbf{E}||\mathbf{c}$, in the case of an intrinsically unpolarized emission. So at this point it is difficult to conclude on the direction of the polarization of a single dot in a nanowire dispersed onto a substrate. Nevertheless, we can say that if the maximum is indeed for $\mathbf{E}||\mathbf{c}$, a strong relaxation of the selection rules is occuring compared to the bulk. Future experiments made on longer wires that one can see and orientate in our μPL setup (we can see wires down to 2 μm long on our visualization) should allow to draw a definitive conclusion.

4.2 Power dependence

In this part, we will focus on the power dependence of the luminescence spectra. The aim of such studies is to put into evidence the luminescence from excited states of the quantum dots, for instance biexcitons. This has been performed in various quantum dot systems and helped in the identification of several excited states [195–199]. We will begin with a simple model that describes the power dependence of the luminescence. After presenting the experimental results we will discuss the binding energy of the biexciton.

4.2.1 The two level model : what do we expect?

The simplest model to describe the luminescence emitted by a quantum dot is to consider it as a two level system : the ground state and the first

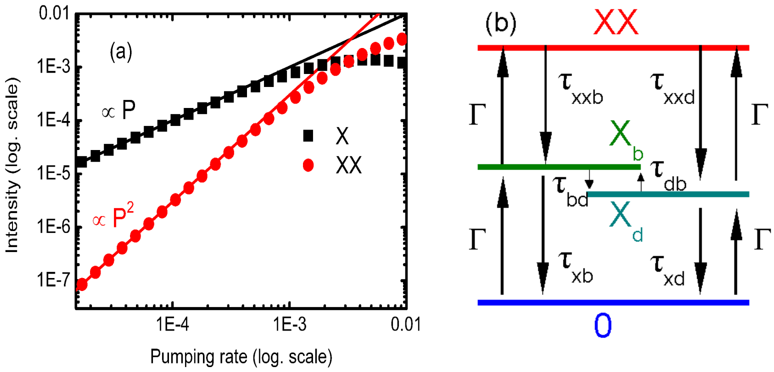

Figure 4.6: (a): plot of the intensity of the exciton (X) and biexciton (XX) from the model described in the text. We choose arbitrarily $\tau_X = 2\tau_{XX}$=300 ps for the modelization. (b): energy diagram of the levels including the dark exciton. The scattering rates for the transition are indicated.

excited state. Due to the spin degeneracy, the first state can contain up to two excitations. Three configuration are thus possible: an empty dot (labeled 0), a dot with one excitation (X) or two (XX for biexciton). The rate equations describing the transitions between the different states read :

$$\begin{aligned}
\frac{dn_{XX}}{dt} &= \Gamma n_X - \frac{n_{XX}}{\tau_{XX}} \\
\frac{dn_X}{dt} &= \Gamma n_0 - \frac{n_X}{\tau_X} + \frac{n_{XX}}{\tau_{XX}} - \Gamma n_X \\
\frac{dn_0}{dt} &= -\Gamma n_0 + \frac{n_X}{\tau_X}
\end{aligned} \tag{4.3}$$

where n_0 (resp. n_X,n_{XX}) is the probability that the dot is in the ground (resp. excitonic, biexcitonic) state, Γ is the pumping rate, τ_X (resp. τ_{XX}) is the radiative lifetime of the exciton (resp. biexciton). This model has the advantage of being analytically tractable and in the steady state it gives the intensity of the luminescence of the exciton and the biexciton :

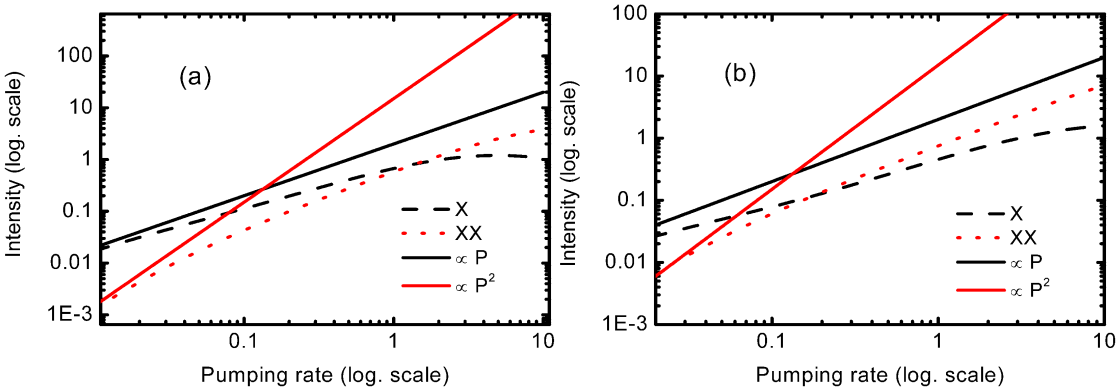

Figure 4.7: (a): plot of the intensity of the exciton (X) and biexciton (XX) obtained by solving the rate equations 4.5. The set of parameters chosen for this simulation are: $\tau_{Xb} = 2\tau_{XXb}$=300 ps; $\tau_{Xd} = 2\tau_{XXd}$=30 ns ; $\tau_{db} = 10\tau_{bd}$=30 ns. (b): simulation with modified radiative decay times: $\tau_{Xb} = 10\tau_{XXb}$=300 ps.

$$\begin{aligned} I_X \propto \frac{n_X}{\tau_X} &= \frac{1}{\tau_X + \dfrac{1}{\Gamma} + \Gamma\tau_X\tau_{XX}} \\ I_{XX} \propto \frac{n_{XX}}{\tau_{XX}} &= \frac{1}{\tau_{XX} + \dfrac{1}{\Gamma} + \dfrac{1}{\Gamma^2\tau_X}} \end{aligned} \tag{4.4}$$

In the low pumping rate limit (low excitation powers), one sees that the luminescence of the exciton will depend linearly on the pumping rate and the dependence of the biexciton will be quadratic. This is illustrated in figure 4.6(a). At high pumping rates (i.e. when the probability to have a biexciton becomes significant) a realistic model should include excited states in order to take into account other realistic channels that would contribute to the total dynamic. One other thing which is not taken into account in our simple model is the possibility to have the presence of a dark exciton into the dot (i.e. a hole and an electron with the same spin, see e.g [130, 200]). The new energy diagram to consider is illustrated in figure 4.6(b). Then the rate equations read :

$$\begin{aligned}
\frac{dn_{XX}}{dt} &= \Gamma n_{Xb} + \Gamma n_{Xd} - n_{XX}(\frac{1}{\tau_{XXb}} + \frac{1}{\tau_{XXd}}) \\
\frac{dn_{Xb}}{dt} &= \Gamma n_0 - n_{Xb}(\frac{1}{\tau_{Xb}} + \frac{1}{\tau_{bd}} + \Gamma) + \frac{n_{XX}}{\tau_{XXb}} + \frac{n_{Xd}}{\tau_{db}} \\
\frac{dn_{Xd}}{dt} &= \Gamma n_0 - n_{Xd}(\frac{1}{\tau_{Xd}} + \frac{1}{\tau_{db}} + \Gamma) + \frac{n_{XX}}{\tau_{XXd}} + \frac{n_{Xb}}{\tau_{bd}} \\
\frac{dn_0}{dt} &= -2\Gamma n_0 + \frac{n_{Xb}}{\tau_{Xb}} + + \frac{n_{Xd}}{\tau_{Xd}}
\end{aligned} \tag{4.5}$$

In this set of equations the new labels are n_{Xd} (resp. n_{Xb}), the probability to have the dot in the dark exciton state (resp. bright). We also introduced τ_{bd} (resp. τ_{db}), the spin flip time from bright to dark (resp. bright to dark). Other new parameters are the decay times of the dark (resp. bright) exciton τ_{Xd} (resp. τ_{Xb}) to the ground state. The decay channels of the biexciton are now characterized by τ_{XXb} (τ_{XXd}), the decay time to the bright (resp. dark) exciton. These equations are not easily tractable analytically, even in the steady state. A numerical resolution is presented in figure 4.7(a). One important conclusion is that the presence of the dark exciton can significantly modify the power dependences from the linear and quadratic one. This was shown for II-VI quantum dots embedded in nanowires [190], where the importance of the dark exciton has been clearly demonstrated. Actually due to the complexity of the system, many behaviors can be reproduced with realistic parameters. For instance in figure 4.7(b) we significantly reduced the lifetime of the biexciton. In this case, the saturation of the lines seems to appear much later with respect to the exciton-biexciton crossing. Another effect such as a dependence of the spin flip time on the pumping rate could also influence the global dynamic.

To conclude this part, the main point to keep in mind is that although in a simple model, a linear and quadratic dependence of the luminescence of the exciton and biexciton are expected, some realistic effects could lead to noticeable deviations from this simple behavior.

4.2.2 Experimental evidence of exciton and biexciton luminescence

We will now present the experimental data of the power dependence of the luminescence on a single quantum dot embedded in a nanowire. We have seen previously that at low excitation power the luminescence can consist of either a single line or a multiplet. We will start with the case of a single

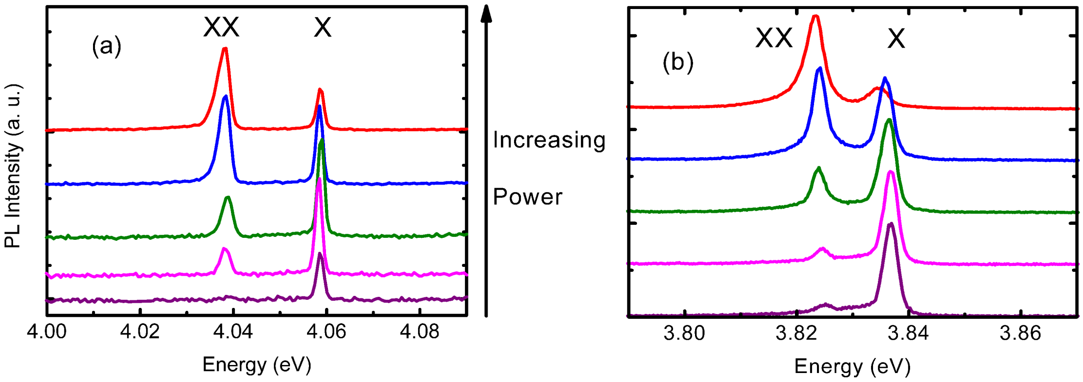

Figure 4.8: (a): Qualitative variation of the power dependence of the emission. The spectra are recorded at 4 K and they have been normalized to their maximum for clarity. The solid (resp. dotted) line shows a quadratic (resp. linear) dependence. (b): Similar spectra taken on another dot. The integrated intensities are plotted in figure 4.9.

line at low excitation power. In figure 4.8, we present the power dependence measured on two different dots. The plots of the integrated intensity as a function of the excitation power are presented in figure 4.9. The spectra of figure 4.8 look qualitatively similar, with the apparition of a line at lower energy when increasing the power. This line tends to dominate the spectrum at high excitation power. To be more quantitative, one needs to look at the plots of figure 4.9. On the one hand, one sees that the dot of figures 4.8(b) and 4.9(b) presents a behavior quite close to the one we expect from the simple model presented previously : a linear (resp. quadratic) increase of the exciton (resp. biexciton) followed by a saturation of both lines. On the other hand, the dot of figure 4.8(a) and 4.9(a) does not show such a saturation. Two effects could be invoked in order to explain this phenomenon. The first one is related to what we have seen previously in the simulations : by taking into account a complete model, including for instance dark states, the power dependences can be different from the ones of a simpler model. One could also argue that due to a difference in the wave functions of the exciton and the biexciton, the relative collection efficiency of both lines might be different. Thus one does not really measure the ratio between the number of photons emitted by the two states and so correction factor should be taken into account. For instance, if the collection efficiency is larger for the biexciton, the intensity of the biexciton should be lowered in the plot (or

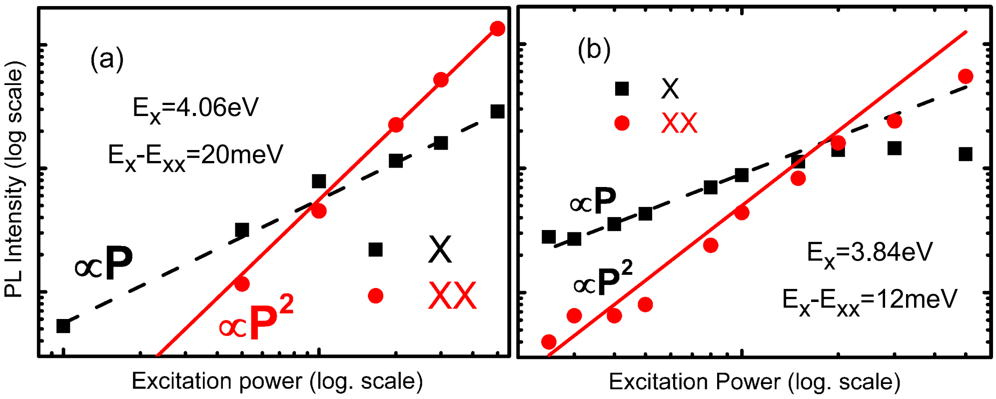

Figure 4.9: (a): Integrated intensity as a function of the excitation power for the dot of figure 4.8(a). (b): Same plot for the dot of figure 4.8(b). The energy difference between the emission energy of the exciton and the biexciton is the biexciton binding energy(see 4.2.3).

the intensity of the exciton increased) and we would end up with a situation where no saturation of the lines is expected in the range of power used.

In figure 4.10, we present the power dependence when starting with two lines at low excitation power. The possible explanations for the presence of multiplets have been discussed previously. Qualitatively, additional lines show up at lower energy when increasing the power and tend to dominate at high excitation power. The excitonic lines (resp. biexcitonic) show a linear (resp. quadratic) dependence which tends to confirm their labeling. In this case, like in figure 4.9(a) no clear saturation is seen in the range of power used.

4.2.3 Biexciton binding energy

Experimentally, what is called the binding energy of the biexciton is the difference between the energy of the two lines. This energy difference has several origins. This is illustrated in figure 4.11(a). In a single particle description, the energies of the levels read [130, 200]:

$$\begin{aligned} E(X_b) &= E_e - E_h - J_{eh} + K_{eh} \\ E(X_d) &= E_e - E_h - J_{eh} \\ E(XX) &= 2(E_e - E_h) - 4J_{eh} + J_{ee} + J_{hh} \end{aligned} \tag{4.6}$$

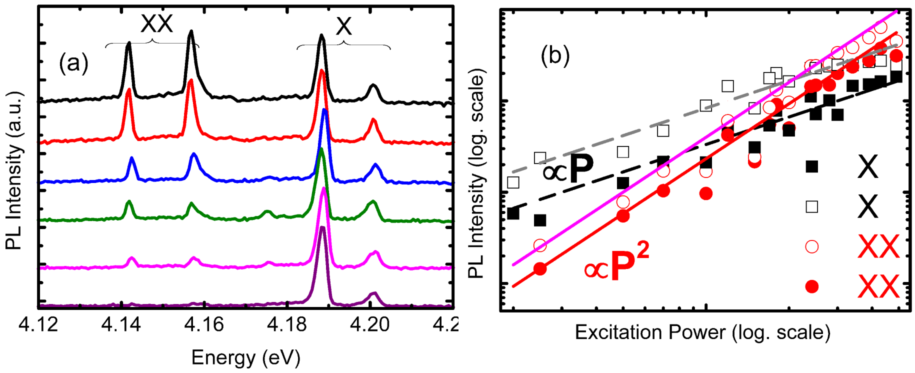

Figure 4.10: (a): Power dependence of the PL when started with two lines at low excitation power. The low energy lines appear the power is increased (from the bottom) and dominate at high excitation power. (b): Integrated intensity of the four lines as a function of the excitation power. The dotted (resp. solid) shows a linear (resp. quadratic) dependence.

In these equations, E_e (resp. E_h) is the energy of a single electron (resp. hole) confined in the dot. The term J (resp K) is the direct (resp. exchange) term of the Coulomb interaction. It leads to the dark-bright splitting $K_{eh} = \delta_0$ and often $\delta_0 > 0$, which means that the energy of the dark state is lower [130, 201–203]. Nevertheless, a transition from a bright to dark state of the ground level has been reported in II-VI nanorods as a function of the nanorod radius [204]. Coming back to the issue of the biexciton binding energy, the quantity which is experimentally measured is :

$$\begin{aligned} E(X_b) - [E(XX) - E(X_b)] &= 2E(X_b) - E(XX) \\ \Delta_{XX} &= 2J_{eh} - J_{ee} - J_{hh} + 2K_{eh} \\ &= \Delta^*_{XX} + 2\delta_0 \end{aligned} \tag{4.7}$$

The three first terms gathered in Δ^*_{XX} come from the direct Coulomb terms. One should be aware that reliable calculations of these terms should take into account the possibility to have contributions from excited states of the one particle model to the biexciton wave function, i.e. correlation effects. This will lower the energy of the biexciton and hence increase its binding energy. The importance of such corrections has been demonstrated in order to end up with bound biexciton [205–208]. This explains why in very small III-As quantum dots the biexciton is unbound as a consequence of the decrease of the number of bound states, lowering the effects of correlation

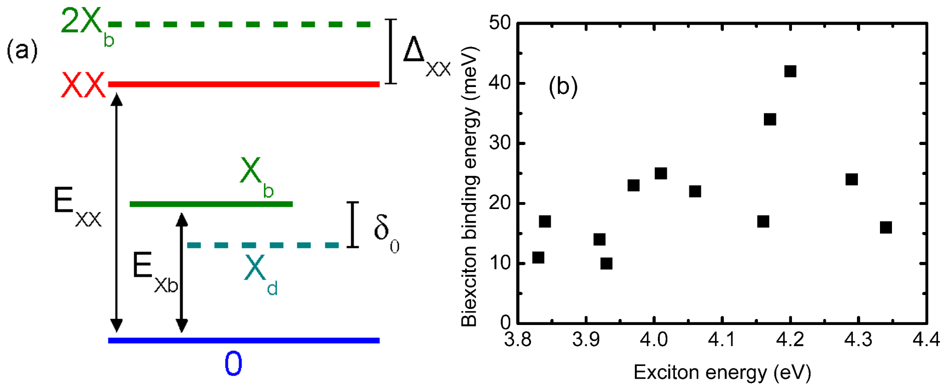

Figure 4.11: (a): Energy diagram describing the origin of the biexciton binding energy. (b): Experimental biexciton binding energies measured on 12 dots.

[206, 207].

The other contribution to the binding energy is the exchange term. It is well known that this term is enhanced in quantum dots compared with the bulk [209] (although recent calculations seems to show that a nonmonotonic behavior should be observed in very small GaAs nanocrystals [210]). For instance in II-VI materials this term is enhanced by more than one order of magnitude starting from 70 μeV in the bulk and reaching values around 1 meV in a quantum dot [130]. In GaN, the bulk value has been reported to reach almost 1 meV [54, 211]. It would thus be reasonable to think that this term is not negligible in GaN quantum dots.

The values of the binding energy of a biexciton in a quantum dot depend on the material and vary also from one dot to another. Typical values for III-As quantum dots are a few meV. For II-VI quantum dots they are generally around 10 meV but they can reach 38 meV for biexcitons localized in thickness fluctuations of very thin CdS/ZnS quantum wells [212]. For GaN an additional effect must be taken into account : the presence of a strong electric field. Separating the electron and the hole should reduce the attractive Coulomb term. Although the two effects have to be treated in a consistent way, this electron hole separation should also induce a screening of the electric field, which would increase the biexciton energy. The value of the screening energy has been estimated to reach 63 meV per e-h pair from calculations on a 4 nm dot subject to an internal field of 3.8 MV/cm [213]. This explains qualitatively why one should see unbound biexcitons in large GaN quantum dots where the effect of the electric field is important.

This has been reported by Kako et al. [199] and Simeonov et al. [214]. The group of EPFL was also able to observe a transition from positive to negative binding energy when increasing the dot size [214].

Focusing now on our measurements, one sees from the two biexcitons presented previously that we observe bound biexcitons in our quantum dots embedded in nanowires. This is true for all the biexcitons we observed and we did not measure any unbound biexciton. This was expected for the small quantum dots we studied (thickness around 1 nm) but we did not see any clear correlation between the biexciton binding energy and the emission energy as illustrated in figure 4.11(b). One sees that the data is quite scattered for the 12 biexciton we could clearly identify and the biexciton binding energies are in the 10-40 meV range. This is actually much larger than binding energies reported for SK quantum dots luminescing in the same energy range [214]. It could indicate that the electron and hole wavefunctions in quantum dots embedded in nanowires differ significantly from the wavefunctions in SK quantum dots. This would be a consequence of a modification of the confinement potential resulting from both shape and strain modifications. At this point it is nevertheless difficult to draw a definitive conclusion about these large biexciton binding energies for quantum dots embedded in nanowires.

4.3 Photon correlation experiments

In this chapter we focus on the luminescence of single quantum dots embedded in nanowires. In this part we will present strong evidences showing that the emitter are indeed 0 dimensional structures where the electronic levels are fully discretized. The experimental method is based on photon correlation spectroscopy. Details about the setup can be found in appendix E. We will start with theoretical considerations about the correlation functions and present an original method to describe them based on Monte Carlo simulations. This approach was developed by Guillaume Tarel from the EPFL (V. Savona's group) and we simply adapted his code in order to simulate our system. Our simulations were done in close collaboration with Guillaume.

4.3.1 Monte Carlo simulation of the experiments

The rate equation approach

The usual way to describe the correlation functions is to solve the rate equations of the system under consideration (see for instance equation 4.3 for the 2 level system) with a given initial condition (see for instance [215]). In the simplest case, if one wants to look at the second order correlation

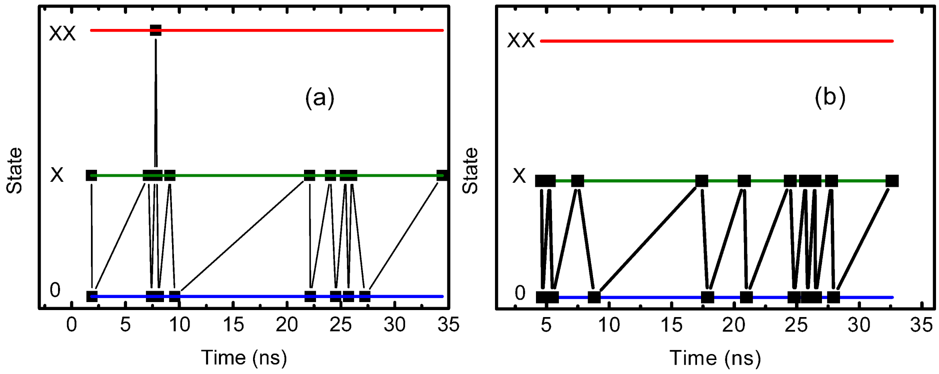

Figure 4.12: Two evolution graphs at low pumping rate. The simulation runs for 30 ns and the pumping rate corresponds to a time of 4 ns. The exciton (resp. biexciton) lifetime is set at 400 ps (resp. 200 ps).

function of the emission of the exciton at very low pump power (i.e. so that the population of the biexciton is discarded), the rate equations read:

$$\begin{aligned} \frac{dn_X}{dt} &= \Gamma n_0 - \frac{n_X}{\tau_X} \\ \frac{dn_0}{dt} &= -\Gamma n_0 + \frac{n_X}{\tau_X} \end{aligned} \tag{4.8}$$

The second order correlation function that one measures, $g_2(\xi)$ is related to the detected intensities I and is defined by :

$$g_2(\xi) = \frac{\langle I(\xi+t)I(t)\rangle}{\langle I(t)\rangle^2} \tag{4.9}$$

which is actually related to the probability to detect a photon at time $\xi + t$ provided you detected another one at time t:

$$g_2(\xi) = \frac{P(\xi+t/t)}{P(t)} \tag{4.10}$$

which does not depend on t so we will set $t = 0$. The value of $P(0+\xi/0)$ is actually the probability for the system to be in the excited state at time ξ, provided it was in the ground state at time 0 (because a photon was

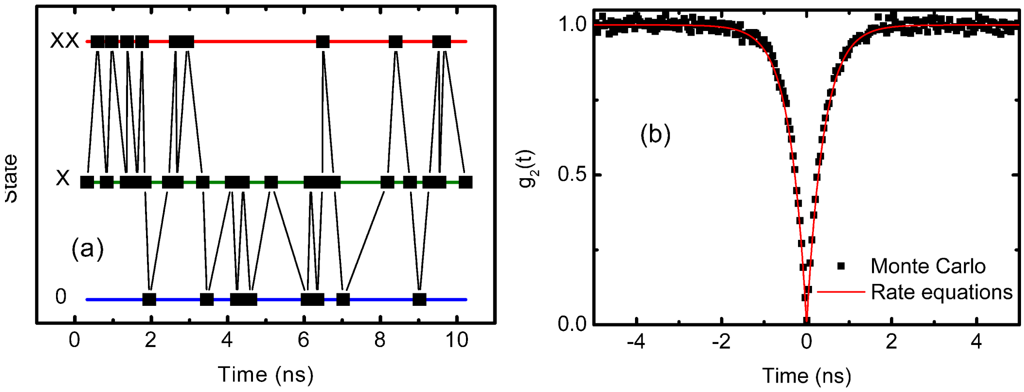

Figure 4.13: (a): Evolution graph at a pumping rate corresponding to 0.4 ns. The simulation runs for 10 ns and the lifetimes are the same than in figure 4.12 (b): Simulated (Monte Carlo) autocorrelation function on the exciton at very low pumping rate. The solid line is function 4.12 with $\Gamma = 0$ and τ_X=0.4 ns.

detected). In our notations it is then the value $n_X(\xi)$ for the solution of equation 4.8 with the initial condition $n_X(0) = 0$. It gives :

$$n_X(\xi) = \frac{\tau_X \Gamma}{\Gamma + 1} \left(1 - \exp^{-(\frac{1}{\tau_X} + \Gamma)\xi} \right) \tag{4.11}$$

The normalized correlation function is usually used and thus reads :

$$g_2(\xi) = 1 - \exp^{-(\frac{1}{\tau_X} + \Gamma)\xi} \tag{4.12}$$

It is a function which presents an exponential dip at time $\xi = 0$ and its width is given by $\dfrac{\tau_X}{1 + \Gamma\tau_X}$. It means that in the low pumping rate limit ($\Gamma\tau_X << 1$), it is possible to have access to the decay time of the exciton but the width of the dip will be reduced when the power is increased. This approach can be extended to more complicated situation and the cross-correlation between biexciton and exciton can for instance be treated [215].

The Monte Carlo approach

Another way to reproduce the correlation functions is to describe the random evolution of the system [216] with Monte Carlo simulations. The idea is that when the system is in a given state it will evolve towards another state with probabilities set in our case by the radiative decay times and the pumping rate. For instance if the two level system is in the exciton state at time $t = 0$ it will evolve towards either the biexciton or the ground state after a given time with the probability of the transition towards the biexciton depending on the pumping rate and the one of a transition towards the ground state depending on the radiative decay time. Once it has evolved towards a new state, the process starts again. This qualitative explanation describes actually what is going on physically and what has to be taken into account in the simulation. The tricky part is to translate that into a code. This step was done by Guillaume Tarel from the EPFL. His work was performed with the aim of describing the dynamics of quantum dots embedded in a microcavity and we simply used the first building block, i.e. the description of the two level system.

The parameters to be set are : exciton and biexciton lifetimes (we will take 400 ps and 200 ps for the simulations), pumping rate, experiment duration which will set the number of transitions recorded (of course in an experiment very few transitions are detected due to the collection efficiency as well as detectors dead time) and time binning for the construction of the correlation functions. In figure 4.12, we present two graphs of the evolution of the system at a low pumping rate (Γ= (4 ns)$^{-1}$) for 30 ns. From the graph we can see that the probability to have a biexciton is quite low (only one occurrence in the first simulation and no occurrence in the second one). We can notice that the initial state is arbitrarily set to be the exciton but this will have of course no influence on the correlation functions. In figure 4.13(a), we present the evolution at higher pumping rate, namely Γ= (0.4 ns)$^{-1}$ for a 10 ns experiment. A much higher probability for the biexciton shows up, as expected.

Let us now focus on the correlation functions which are easily built once the evolution of the system is known following the way a Hanburry Brown Twiss (HBT) start/stop experiment works (but in order to reduce the simulation time, all events are considered and not only the two closest ones). Of course the experiments have to be much longer than the evolution presented previously because the useful events will be the ones separated by typically less than 5 ns and many of them are needed in order to have good enough statistics. In figures 4.13(b), 4.14(a) and 4.14(b), we present the three correlation functions simulated at low pumping rate ($\Gamma = (4ns)^{-1}$): autocorrelation X-X, cross correlation X-XX and autocorrelation XX-XX . We chose an experiment duration of 10 ms in order to have enough statistics, the idea being to show that this method is able to reproduce the expected behaviors. The influence of the parameters will be presented in detail afterwards. On

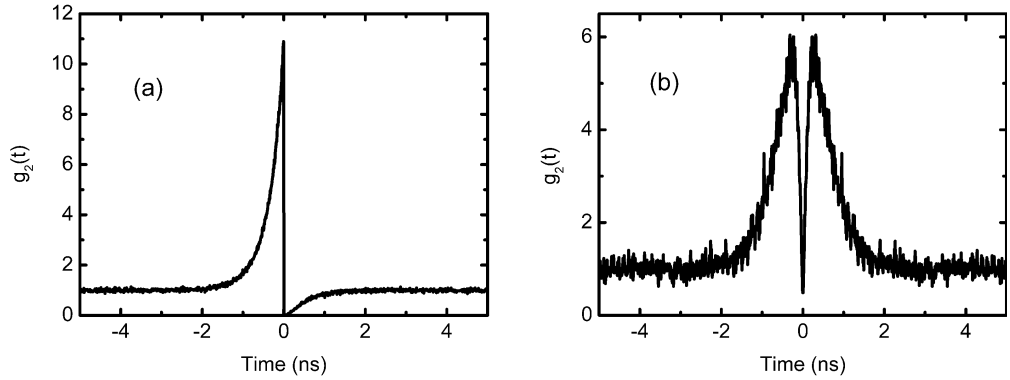

Figure 4.14: Simulated cross-correlation function of the exciton with the biexciton (a) and autocorrelation function for the biexciton (b). There is an enhanced noise in figure (b) due to the low count rate for the biexciton at very low pumping rate. In both case the bunching time is essentially set by the exciton lifetime. The antibunching time of the biexciton autocorrelation is set by the biexciton lifetime.

the one hand, figure 4.13(b) shows an antibunching at zero delay time with a width given by the lifetime of the exciton as expected from the rate equations approach. On the other hand, figure 4.14(a) shows both bunching and antibunching. The probability to emit an exciton is indeed enhanced just after the emission of a biexciton. The shape of figure 4.14(b) is actually the less intuitive one : the antibunching at zero time delay (it does not go down to zero due to the binning) is masked by a strong bunching. This bunching comes actually from the fact that when one detects a biexciton at time $t = 0$, it means that the system is in the exciton state. Thus the probability to emit another biexciton after a small delay is larger than its mean value because the more probable state at very low pumping rates is the ground state. This is what is observed experimentally [217].

Taking into account the setup resolution

Experimental setups have a finite resolution which means that if two photons are emitted with a time delay Δt, once detected they will appear as two events separated by $\Delta t \pm \delta t$. The distribution of δt, in particular its temporal width, is related to the setup resolution. A finite resolution can be nicely taken into account in our Monte Carlo simulations because we have access to the exact time of each transition when running the evolution.

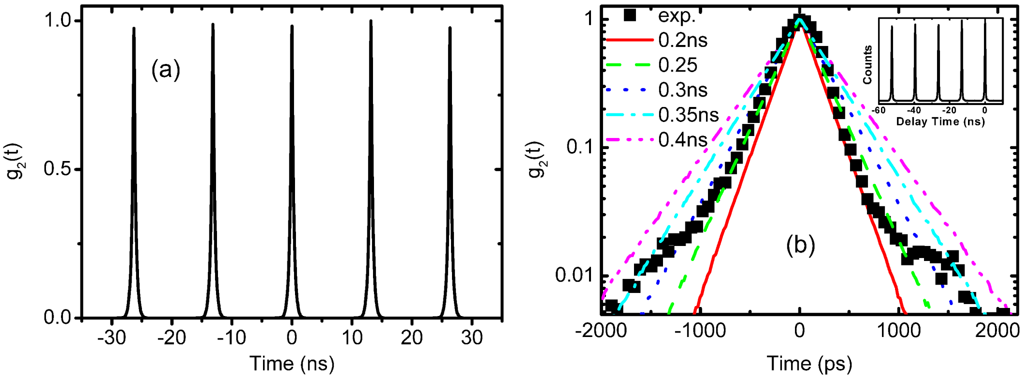

Figure 4.15: (a): autocorrelation function simulated for a pulsed laser (repetition rate 76 MHz) taking into account a 300 ps time resolution. (b): comparison of the simulated autocorrelation function with various time resolutions with the experimental one. The inset shows the experimental function on a larger scale.

Thus we just need to add a random variation to the time of each event, with a distribution given by the time resolution. In figure 4.15(a), we show the simulated autocorrelation function for a pulsed laser (76 MHz repetition rate, zero temporal width) taking into account a 300 ps time resolution. In the inset of figure 4.15(b) we show the experimental curve measured and we compare it with Monte Carlo simulations with various resolution times by focusing on one peak and showing the plot in a log scale. It appears that in order to take into account our setup resolution in the best way, we should consider a time broadening located between 250-300 ps. Coming back to the issue of the autocorrelation of the exciton, figure 4.16(a) shows that by taking a 300 ps resolution into account, the visibility of the exciton autocorrelation function is significantly reduced : $g_2(0) \approx 0.44$.

In the following simulations, we will set this resolution to be 300 ps in order to reproduce the correlation functions that we can experimentally expect.

The effect of the pumping rate

The simple model giving the autocorrelation function 4.12 predicts a variation of the temporal width of the dip with the pumping rate. This has been reported experimentally [215, 218, 219]. Our simulations reproduce this effect and are presented in figure 4.16(b). At high pumping rate the

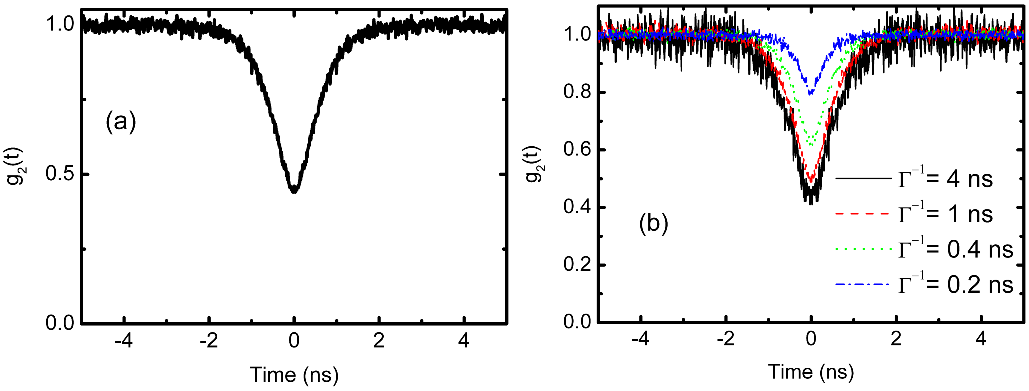

Figure 4.16: (a): simulation of the autocorrelation of the exciton (same parameters than figure 4.13(b)) taking into account a time resolution of 300 ps. (b): effect of the pumping rate on the exciton autocorrelation function.

temporal width is limited by the resolution and at low pumping rate it is a convolution of the resolution and the exciton lifetime. The value of $g_2(0)$ also increases when the power is increased as a consequence of the interplay between pumping rate and resolution. A more puzzling effect is seen in the cross-correlation between the exciton and the biexciton as illustrated in figure 4.17(a). At very low pumping rate one can clearly see the bunching with a g_2 reaching 4.3 . The antibunching is hardly visible with a g_2 going down to 0.9. This is a direct consequence of the finite resolution. With an increasing pumping rate the visibility of the bunching decreases and for $\Gamma = \frac{1}{\tau_X}$ (which would mean an equal intensity for the luminescence of both lines) one has : g_{2min}=0.7 , g_{2max}=1.07 . The conclusion is that if one wants to see the bunching one must work at very low pumping rate, but in this case the experiments is very challenging due to very low count rates. The effects on the autocorrelation of the biexciton are presented in figure 4.17(b). The best visibility is obtained at low pumping rate for the bunching and the antibunching is hardly observable. When increasing the power the bunching disappears because the mean value of the number of electron hole pairs increases. The antibunching is more visible at high pumping rate but one should note that at high pumping rate, other excited states must be taken into account in order to correctly describe the system. Otherwise, the system behaves like a dot going continuously from the exciton to the biexciton state (and never reaching its ground state) which explains why we clearly see an antibunching.

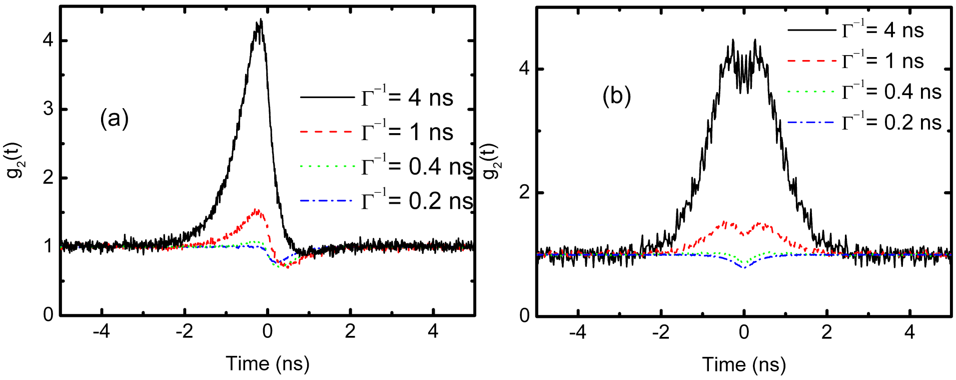

Figure 4.17: Simulation of the effect of the pumping rate on the cross-correlation (a) and on the biexciton autocorrelation (b).

The influence of the binning

Another effect to take into account is the binning in the construction of the correlation function. We will take the case of the cross correlation exciton-biexciton at a pumping rate Γ^{-1}= 1 ns where one can see both bunching and antibunching. Experimentally, our TimeHarp acquisition card of PicoQuant has bins of size 29 ps in its best resolution mode. In figure 4.18(a) we plot the simulated correlation functions for bins from 5 to 100 ps. One can see that up to about 100 ps, the binning does not alter significantly the visibility but increases dramatically the signal to noise ratio. It seems thus reasonable for our experiments to make a binning of 3 or 4 pixels.

The influence of the count rate

The key parameter that is a prerequisite to have a conceivable experiment is to have a decent count rate. In our simulations once the evolution of the system is known one has access to the number of excitons and biexcitons emitted. The number of events on each channel is proportional to the duration of the experiments but the number of coincidences scales with the products of the count rates. In figure 4.18(b) we present the evolution of the exciton-biexciton cross correlation with the total number of recorded counts. One sees that the features slowly show up as the number of counts increases. A decent curve is obtained above about 10^5 counts on the exciton channel. To translate this value in terms of experimental parameters, one should recall that the simulation takes into account all the events and not

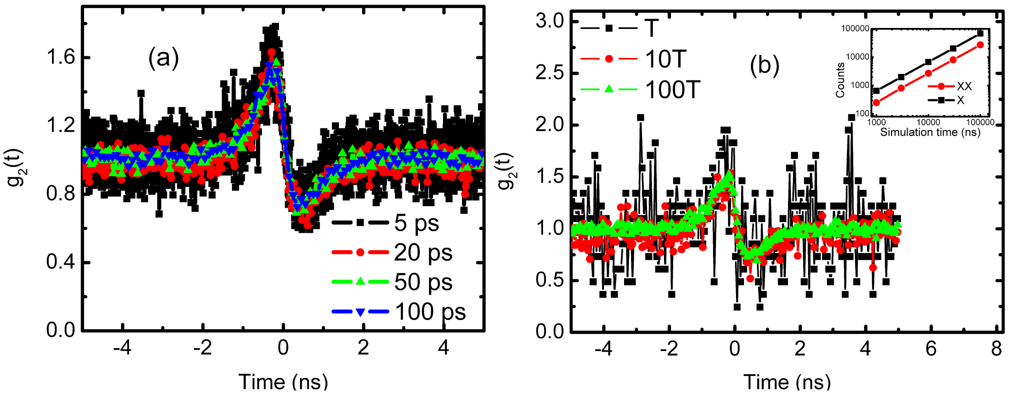

Figure 4.18: (a): Influence of the binning on the cross-correlation function. The binning increases from 5 to 100 ps and the reduction of the noise appears clearly. (b) illustrates the influence of the number of detected events on the cross-correlation function. One can change the simulation time in order to reproduce this effect. T corresponds to 1000 ns. The inset shows the linear dependence of the number of counts detected on both channels. In both figures $(\Gamma)^{-1}$= 1 ns.

only two successive ones like in the experiment. Thus if one channel has much more counts than the other one, many counts are not used in terms of coincidence. A rough approximation is found by assuming that the number of exciton counts which give a coincidence is actually equal to the number of biexciton counts. Thus in the simulated case one should multiply the number of exciton counts by a factor of 2.5 (ratio between the exciton and the biexciton intensity at a pumping rate of 1 ns, see the inset of figure 4.18(b)). Another thing to take into account is the detector dead time, which is in our case a few hundreds of ns. The simulated count rate is around 1 photon per ns thus one looses roughly a factor 100. Considering these two effects one thus needs : $10^5 \times 2.5 \times 100$=2.5 10^7 counts on the exciton channel. For a reasonable integration time of 10000 seconds it will give a count rate of 2500 photons per second. This is safely below what we typically obtained for bright quantum dots at reasonable pumping rate (i.e. when we already see clearly the biexciton). But the situation becomes quickly tricky for dots emitting less photons and in any case at very low pumping rate for any dot (when the bunching visibility is maximum).

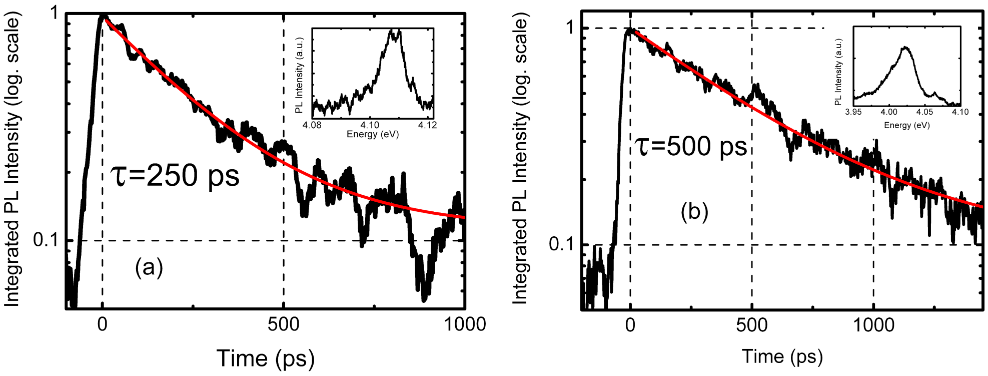

Figure 4.19: Micro TRPL at low temperature performed on two different quantum dots. The solid lines are exponential decays with the indicated decay times. The inset show the PL spectra as a function of the energy.

4.3.2 Time resolved microphotoluminescence

In the previous section, we have shown that the visibility one gets in a correlation experiment comes from the interplay between the pumping rate, the lifetimes and the resolution of the setup. We presented in chapter 3 time resolved photoluminescence for ensemble of dots embedded in nanowires. In the present chapter we focus on single quantum dots and we will thus now show similar experiments performed on the single dot level. Let us first note that this kind of experiments requires very long integration time notably due to the poor efficiency of the streak camera in the wavelength range of interest, typically between 290 and 320 nm. In figure 4.19 two decay curves recorded on two different dots are presented. It looks like the decay times vary from dot to dot but short decay times at these wavelengths where the effects of the electric field should be weak seem to be established, in accordance with measurements on ensembles.

4.3.3 Antibunching at low temperature

We will conclude this part by presenting the experimental results on correlation experiments. These kinds of experiments have been performed in 2005 on self assembled GaN/AlN quantum dots by the group of Pr. Arakawa [220]. They put into evidence a single photon emission up to 200 K [13] and managed to perform clear cross correlation experiments between the exciton

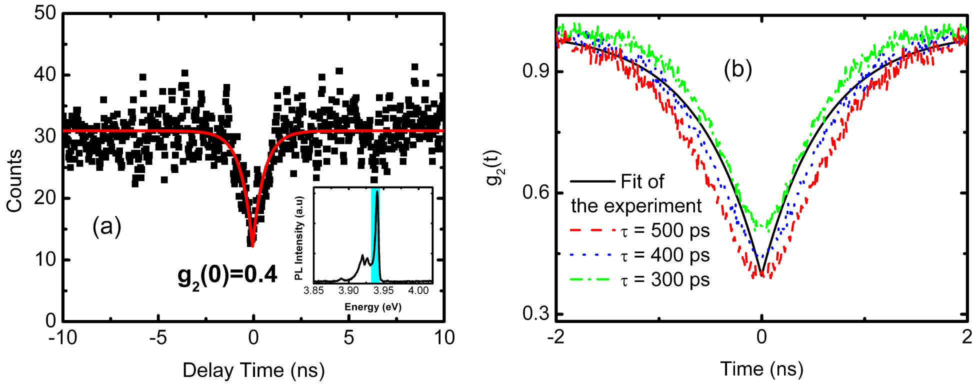

Figure 4.20: (a): experimental autocorrelation measured for the spectrum presented in the inset. The solid line is a fit by the function : $g(t) = 1 - (1 - g_2(0))\exp(-\frac{t}{\tau})$ and gives $g_2(0) = 0.4$ and τ= 620 ps. (b): adjustment of the decay time of the exciton to the experimental curve. The solid black line is the fit presented in (a). The three simulations are performed with Γ^{-1}= 4 ns and a resolution of 300 ps.

and the biexciton for dots luminescing around 360 nm [13, 220].

We have seen previously that due to our setup resolution of 300 ps, we cannot expect a $g_2(0)$ below 0.4 (for the autocorrelation of the exciton) for the dots we have studied with a lifetime below 500 ps. In figure 4.20, the best auto-correlation function we could record on the exciton is presented together with the PL spectrum. We can see that $g_2(0) \approx 0.4$ which is indeed the best value we could hope for. The fit presented gives a time of 620 ps for the dip. It means that the lifetime of this particular dot was in any case shorter than this value. Under the assumption of a low pumping rate and that the setup was in a configuration where the time resolution was 300 ps, it would give a lifetime around 400 ps for this dot (see figure 4.20(b)). It is difficult to be more conclusive given the small uncertainty on the setup resolution. This is anyway in reasonable agreement with the time resolved data for dots luminescing at the same energy.

We tried to measure the cross correlation between the exciton and the biexciton on several dots but we did not succeed so far. The main reasons were presented previously in this chapter, namely the effect of the time resolution combined with the short lifetimes and the difficulty to work at very low power.

4.4 Prospects

As we saw in this chapter, we were able to probe the optical properties of single GaN/AlN quantum dots embedded in nanowires. One additional measurement one can think of is to perform a cross correlation between the exciton and the biexciton with an improved time resolution, i.e. using other photomultiplier tubes. The observation of the bunching would then confirm the attribution of the biexciton.

Another very interesting study would be to study quantum dots emitting at lower energy than the ones we studied, where the effect of the electric field would be more important. In particular, the study of the biexciton binding energy dependence on the exciton energy would bring new insights for the comparison of SK quantum dots and dots embedded in nanowires. Also, the lifetimes should be longer at lower energy and thus the 300 ps time resolution of our current setup could then become sufficient in order to perform cross-correlation measurements. But the problem we are facing so far is the presence of the GaN nanowire below the quantum dots. The strong signal arising from the foot of the nanowire prevents us from observing single dot emission below 3.6 eV in the system we are using. A solution would be to directly grow AlN nanowires of good optical quality but this is very challenging from the growth point of view. Preliminary results obtained on a SiO_2/Si substrate seem to show that it is possible to grow AlN nanowires (as illustrated in 3.5.1) at very high substrate temperature but the optimization process of these nanowires is still under progress.

The study of InGaN quantum dots embedded in GaN nanowires would also be a direct way to get rid of the issue of the GaN foot. In this case, the dots luminesce anyway at lower energy than the GaN, whatever the thickness or composition of the dots. The literature on the topic seems to indicate that the quantum confined stark effect is significantly reduced in nanowires structures compared to 2D layers and that consequently the radiative lifetimes are shorter [181] and the biexciton binding energy turns out to be positive [221]. This subject has been started in our group at the end of 2008 but there are still some growth issues because it seems that there is a very small substrate temperature range were In can be efficiently incorporated and the control of the emission wavelength is still under progress. Nevertheless preliminary measurements performed on InGaN/GaN quantum dots embedded in nanowires luminescing at 470 nm seem to indicate a very weak influence of the electric field with decay times around 250 ps, i.e. well below the value for 2D layers.

Another idea we want to work on is to study quantum dots embedded in freestanding nanowires rather than dispersed onto a substrate. We indeed noticed that the dispersion had consequences on the optical properties of single GaN nanowires and we suspect that it could also influence the luminescence of the dots. One way would be to have access to samples with a very low density made either on patterned substrates or made by tuning the growth conditions. It would thus allow us to probe single dots on as grown samples. Furthermore, collecting the dot luminescence in a geometry where $\mathbf{k}||\mathbf{c}$ would make possible to study the in-plane polarization anisotropy, a subject that started recently to be studied in SK GaN/AlN quantum dots [222, 223].

In this chapter, the optical properties of single quantum dots embedded in nanowires were investigated. The spectral diffusion seems to be present in such structures like in self organized quantum dots. Power dependence measurements have been used to identify the exciton and biexciton recombinations. The biexciton binding energies appear to be larger in these structures than in self organized quantum dots, suggesting a difference in the confinement potential. General considerations about correlation experiments have been presented thanks to Monte Carlo random walk simulations. The oscillator strength of small quantum dots appears to be similar to self organized quantum dots, with a lifetime around 300 ps at 4 eV. The full discretization of the energy level in these structures (i.e. that they are indeed quantum dots) has been evidenced by a continuous wave autocorrelation experiment, which shows an antibunching at zero delay time. The fact that $g_2(0)$ does not reach 0 is attributed to the temporal resolution of our system, as supported by Monte-Carlo simulations.

Chapter 5

Study of the quality factors in GaN microdisks

In this chapter, we will focus on the optical properties of GaN μdisks with embedded InGaN quantum wells. Before presenting the experimental results in the second part of this chapter, we will do a short overview of the state of the art in nitride based microcavities.

Contents

5.1 Nitride based microcavities : State of the art

Broadly speaking, microcavities can be sorted in three classes : planar microcavities (in which we include micropillars, which are often obtained by etching planar microcavities), photonic crystals based microcavities or microdisks microcavities (in which can be included microspheres or microrings due to the fact that all of them are subject to whispering gallery modes). With these resonators, one often uses an emitter which is embedded in the microcavity in order to characterize the microcavity as well as to be the source of a light emitting device. Depending on the strength of the coupling between the light (the cavity) and the emitter, one can be either in the weak coupling regime, where the presence of resonator can be treated as a perturbation or in the strong coupling regime, where the two systems cannot be treated separately. In the weak coupling regime, the modification of the spontaneous emission can be observed (see [224] for the original idea , [225, 226] for the realization in atomic physics and [227] for the idea of transposing these findings in the solid state) and in the strong coupling regime the building of mixed matter-light states (polaritons) can be observed [228]. Both of these regimes can potentially be used to improve the performance of semiconductor devices to emit light. We will now focus on the state of the art concerning nitride based microcavities.

5.1.1 Planar microcavities

A planar microcavity basically consists of two mirrors separated by a distance d which is an integer number (m) of half waves :

$$d = m\frac{\lambda}{2n} \tag{5.1}$$

where n is the index of the material at the wavelength λ. When this condition is fulfilled, the transmission is then close to unity although the reflectivity of both mirror taken separately is also close to unity. The sharpness of the transmission peak versus the wavelength represents the quality factor of the cavity :

$$Q = \frac{\lambda}{\Delta\lambda} \tag{5.2}$$

The mirrors can consist simply of metallic mirrors but the difficulty to grow high quality semiconductors on a metal layer makes the use of metal, at least for the bottom mirror, not realistic (this is not the case when the emitter is an organic material). Metallic mirrors have also a non negligible absorption. Another way to realize a mirror with a good reflectivity is to grow distributed Bragg reflectors (DBR) which consist of alternating layers of two dielectrics with a contrast of refractive index. When the reflexions at each interface interfere constructively (the simplest design is to have a thickness of $\frac{\lambda}{4n}$ for each layer), one can reach a very high reflectivity, which depends on the number of pairs and the index contrast. For nitride compounds, the major problem comes from the growth. For instance if one wants to grow GaN/AlGaN DBR, one needs a relatively high Al composition in order to reach a reasonable index contrast (for instance at 400 nm : $n_{GaN} = 2.65$ and $n_{AlN} = 2.12$) to limit the number of pairs [229]. But the problem is that the layers will present a large lattice mismatch and cracks [230, 231] will appear. In ref. [232] the authors introduce a GaN/AlN superlattices every five periods in order to prevent the apparition of cracks in a GaN/AlN DBR. With 20 periods, they demonstrate a reflectivity of 97 % at 400 nm. They use this technic to realize a vertical cavity surface emitting laser by using a dielectric top DBR and an InGaN/GaN active layer [233]. The use of a top dielectric DBR has been used in various structures [230, 234, 235], because one can reach a good reflectivity with not too many pairs and get rid of the problem of cracks (some groups also managed to use them as a bottom mirror thanks to a wafer-bonding technic combined to substrate removal [236]). The dielectric material used are : SiO_2/Si_3N_4, SiN/SiO_2, Ta_2O_5/SiO_2 for the near visible and near UV. The extension to the UV would require the use of HfO_2 or Al_2O_3 together with SiO_2 [237, 238]. Another possibility to grow high quality DBR is to use AlInN which is lattice matched to GaN for a composition of 16% of Indium[239–241]. In this case, the refractive index contrast is around 7% at 450 nm.

Various physical effects were shown in nitride planar cavities. Recently, attention has been paid to the study of these structures in the strong coupling regime. The emitter can be either bulk GaN [234, 235, 242], InGaN/GaN QWs [236] or AlGaN/GaN QWs [243, 244]. The most prominent works have demonstrated polariton lasing at room temperature with bulk GaN [245] and GaN/AlGaN QWs[246]. This behavior has been interpreted in terms of a Bose Einstein condensate of exciton polaritons [247].

5.1.2 Photonic crystals

A photonic crystal (PhC) consists of a periodic arrangement of a material. Depending on the material and the pattern, the structure will have a particular photonic band structure (similar to electronic band structure in semiconductors) and for instance a photonic band gap can be created

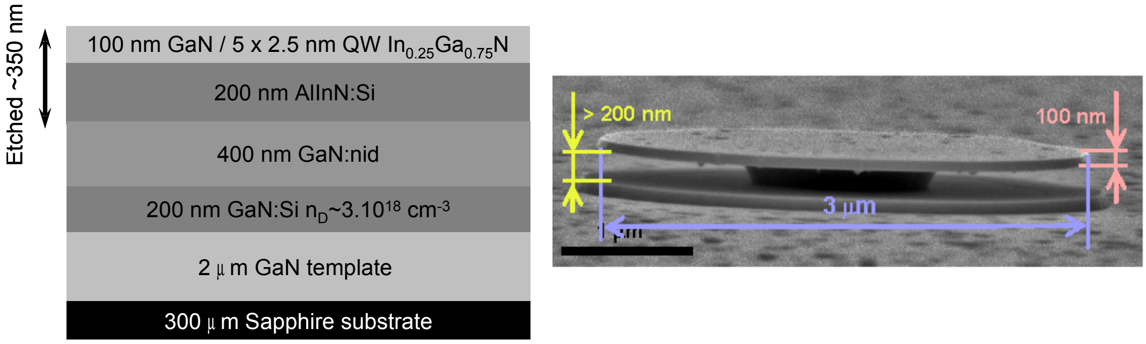

Figure 5.1: Left : the microdisk structure grown by MOVPE. The active structure consists of 5 InGaN/GaN QWs with a nominal Indium concentration around 25%. Right: SEM image of a 3 μm diameter microdisk after the whole process described in the text. Courtesy of D. Simeonov.

[227, 248]. Actually a PhC is nothing else than the extension of a planar microcavity to two or three dimensions [249]. One advantage of PhC is that they can allow a very high Q and a small modal volume at the same time. Considering that many effects (in particular the Purcell effect) require a large $\frac{Q}{V}$ ratio, these structures are very promising. In non-nitride materials, Purcell effect [250] (also for a single quantum dot [251]), strong coupling for a single quantum dot [252, 253] and 3D structures with high quality factors [254] have been demonstrated. But once again, when it comes to nitrides and nanopatterning, the situation gets tricky. Especially, the good quality of the etching which is crucial for such structures is very difficult to obtain and the fact that the characteristic dimensions have to be smaller in nitride (due to the smaller wavelength) complicates the task furthermore.

Nevertheless some effects were demonstrated : improvement of the extraction efficiency for LED using 2D PhC [255, 256], a PhC surface emitting laser injected electrically [257, 258] as well as high quality factors in AlN PhC [259].

5.1.3 Microdisks

In its simplest form, a semiconductor microdisk consists of a thin cylinder suspended in the air. The light propagates along the periphery of the disk by total internal reflexion, the so called whispering gallery modes (WGM). The light is confined vertically due to the index contrast between the semiconductor and the air. Generally, the height h of the microdisk is such that $h < \frac{\lambda}{2n}$ in order to have only the fundamental mode which overlaps well with the disk. To fully characterize one mode, one should give two numbers : the azimuthal number m and the radial number n. For a derivation of the electric field in the approximation of a vanishing field on the sides (WGM approximation), see e.g. [260, 261]. Besides an easy process, one advantage of microdisks is that they can present a small modal volume together with a high quality factor, the limiting factor being often the quality of the sidewalls. Scattering on the sidewalls indeed tends to reduce the lifetime of the photons in the cavity and thus the quality factor. In III-As compounds, quality factors as high as 3.6 10^5 have been reported [262–264]. Concerning the Purcell effect, value as high as 12 were reported for the decay time shortening, based on time resolved experiments [265]. For nitride compounds, the major problem is the selective underetching step. This step is indeed necessary in order to optically isolate the microdisk from the template and reduce the losses and its improvement has dramatic consequences in III-As microdisks [264]. Photoelectrochemical band gap selective etching was demonstrated in InGaN/GaN structures [266]. It allowed the authors to evidence quality factors as high as 4600 [266] and even lasing at room temperature under CW excitation [267]. Another approach is to use an AlInN layer, which is lattice matched to GaN. In ref. [268, 269], the authors reported the removal of a sacrificial AlInN layer based on the selective oxidation of AlInN [270] in order to reach a good optical insulation of the bottom part of the microdisk without degradation of the quality, especially in terms of roughness. Using this process, the authors reported quality factors reaching 4000 and lasing at room temperature [268, 269].

5.2 Measurements of quality factors in microdisks

In this part, we will present our experimental results on the characterization of nitride microdisks with high quality factors. We will begin by a short description of the microdisk fabrication and then evidence quality factors up to 11000 in CW microphotoluminescence. We will end this part by discussing the perspective in terms of Purcell effect in these structures.

5.2.1 Description of the samples

We had access to state of the art microdisks thanks to our collaboration with the EPFL in Lausanne [268, 269]. The microdisks were fabricated by Dobri Simeonov. The complete structure grown by MOVPE is illustrated in figure 5.1. Then the process consists of several steps :

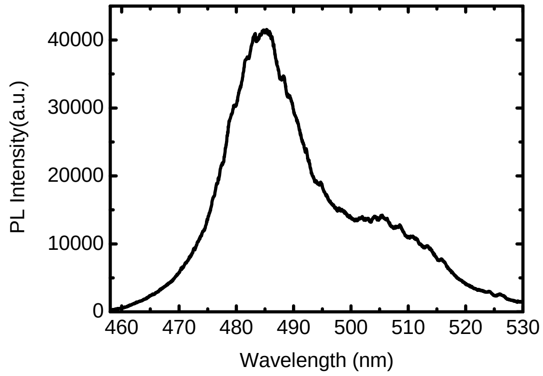

Figure 5.2: CW μPL a low temperature on a 11 μm microdisk.

- UV photolithography in order to form a pattern of 200 nm thick SiO_2 circular masks (diameters down to 3 μm)
- Reactive ion etching (Cl_2/Ar plasma) to create mesas 350 nm high (i.e. etching down to the nid GaN layer, see figure 5.1
- Oxidation of the AlInN layer in a NTA:KOH solution in a regime where no etching occurs (i.e. moderate KOH concentration and anodic current, see [268])
- Removal of the oxide in a nitric acid solution (65%)
- Removal of the SiO_2 layer in a HF solution

The structure eventually obtained is presented in the SEM image of figure 5.1.

5.2.2 CW Microphotoluminescence

To experimentally have access to the quality factors of these microdisks, we performed μPL experiments at low temperature. We used an excitation at 244 nm, well above the GaN barriers. On the largest microdisks (11 μm) , the PL basically consists of a broad emission (20 nm or 100 meV) centered around 490 nm due to the fact that too many optical modes are present, and only very weak resonances appear (see figure 5.2). In the following, we will thus focus on the smallest microdisks, which have a diameter of 3 μm.

In order to ensure that we are not overestimating the quality factor by stimulated emission we worked at very low excitation power, typically below 10 Wcm^{-2}. This can actually lead to an underestimation of the quality factors [271]. A typical spectrum obtained in a good microdisk is presented in figure 5.3(a). One sees that the spectrum is structured, with linewidths

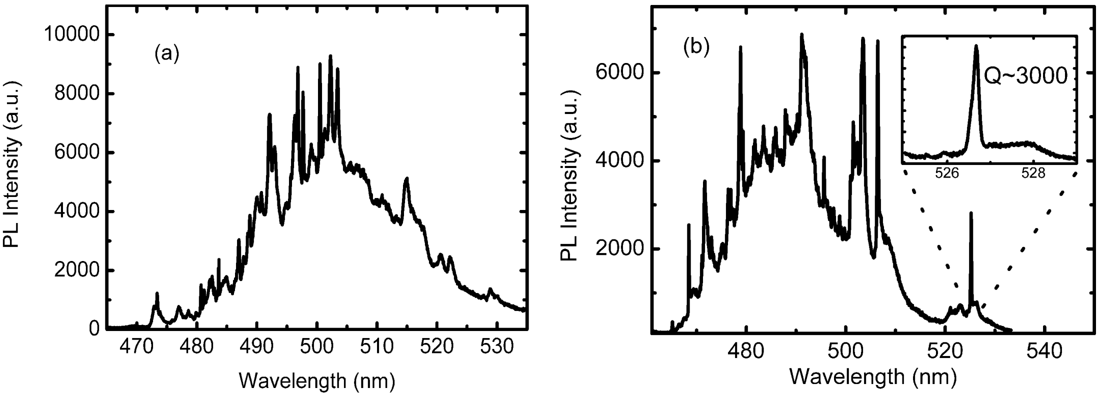

Figure 5.3: (a): Low temperature CW μPL on a good 3μm microdisk. Optical modes appear as sharp lines in the spectrum. The linewidth are down to 0.1 nm. (b): Best quality factor at low energy (525 nm) that we could measure. It reaches 3000.

down to 0.1 nm for this microdisk. This gives a quality factor of about 5000. Two key points have to be emphasized concerning the experimental spectra obtained :

- we noticed that the ratio between a given optical mode and the background (i.e. the emission which is not coupled to any optical mode) strongly depends on the position of the excitation. It can be understood because the collection mechanism for a given optical mode is rather complicated. It involves some scattering on the microdisk periphery and thus one can guess that the detected light will strongly depend on the position on the microdisk.
- we also worked in a geometry where the microdisks were tilted at 30 degrees with respect to the optical axis. Although it made the experiments quite tricky (especially in terms of imaging of the sample), it generally gives a better contrast for the optical modes. This can be understood because it is generally assumed that the WGM emit in a small angle around the disk plane [261] and the determination of the best geometry in order to enhance the contrast would require a precise knowledge of the far field emission of the microdisks [272].

Taking into account both these considerations, we present in figure 5.4, the PL of the microdisk with the best quality factor we could measure. The smallest linewidth, extracted from a Lorentzian fit is 0.043 nm (close to our spectral resolution). It gives a quality factor close to 11000. The general tendency we saw is that the quality factors tend to be better in the high

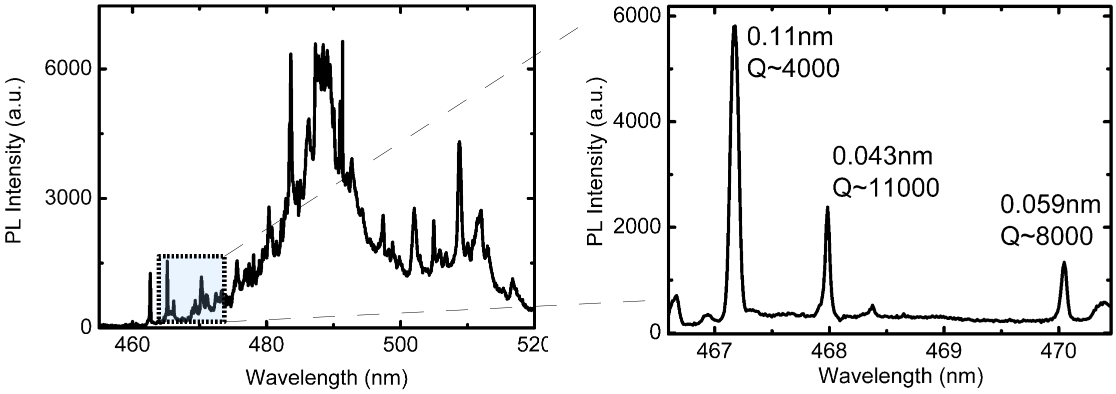

Figure 5.4: Best quality factor measured. The left part show the whole spectrum of this 3μm microdisk and the right panel is the same microdisk taken with a better resolution in the region of interest. The linewidth are extracted with Lorentzian fits (not shown).

energy part of the spectrum. For instance in figure 5.3(b), we present a WGM in the low energy part of the spectrum. Its quality factor is “only” 3000. This is in contradiction to what is generally assumed : the quality factors should be smaller in the high energy part because the absorption is larger in this part of the spectrum [261, 269, 273]. One has to mention that this was reported for samples very similar to the ones we studied [269]. The limitation by the absorption reads [273] :

$$Q_{abs} = \frac{2\pi n_{eff}}{\alpha(E)\lambda} \tag{5.3}$$

where α is absorption coefficient at the mode frequency. This is true for QWs, but in our structures (with an In composition of 25 %) , especially at low temperatures, localization cannot be neglected and the active layers have perhaps a behavior closer to QDs. In microdisks with embedded QDs, the absorption has a small effect [264]. Nevertheless, in our structures even if the emission behavior is certainly close to quantum dots, it is very likely that there is a high 2D-like density of states at high energy for the absoprtion. Thus the mechanism that could explain the higher cavity factors at high energy has still to be found.

5.2.3 Perspectives : Purcell effect

In the last part, we have presented microdisks with quality factors reaching 11000. One can thus reasonably ask ourselves whether these microdisks

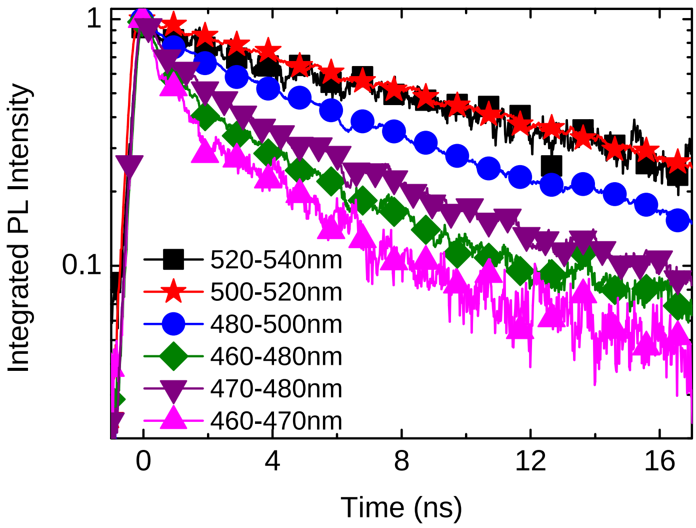

Figure 5.5: TRPL at low temperature on an unprocessed part of the sample in order to characterize the decay times distribution of the active region. The repetition rate is around 1 MHz and the spectrum is taken with a 20 ns window. In this configuration the temporal resolution is in the 400 ps range.

can present a significant Purcell effect, which could be measured experimentally by means of a shortening of the radiative decay time. The first step is to calculate the Purcell factor:

$$F_p = \frac{3}{4\pi^2} \frac{Q \left(\frac{\lambda}{n}\right)^3}{V_{eff}} \tag{5.4}$$

where V$_{eff}$ is the effective volume of the mode:

$$V_{eff} = \frac{\iiint n^2(\mathbf{r})|\mathbf{E}(\mathbf{r})|^2 \, d^3r}{n^2|E_{max}|^2} \tag{5.5}$$

In our structure, calculating the field in the WGM approximation, we obtain $V_{eff} \approx 20(\frac{\lambda}{n})^3$ and thus F$_p$ $\approx$ 38 for Q=10000. This would be the expected value for a single emitter optimally coupled to a mode. Experimentally, we are in the presence of many emitters, which are not spatially and spectrally optimally coupled to the optical mode. We have thus to average over this distribution [261]:

$$\overline{F_p} = \underbrace{\frac{1}{3}}_{\text{random dipole}} \overbrace{2}^{\text{2 modes}} \underbrace{\frac{1}{2}}_{\text{spatial averaging}} \overbrace{\frac{1}{2}}^{\text{spectral averaging}} F_p \tag{5.6}$$

In our structure the dipole is likely to be located in the plane. The factor $\frac{1}{3}$ should then perhaps be replaced by $\frac{1}{2}$. Anyway, as we are just interested in a rough estimation of the Purcell factor, it does not make a big difference. Thus one could hope an enhancement of the spontaneous emission up to 6 , which is experimentally accessible. We have realized preliminary experiments in order to figure out which experimental setup we would need to measure the effect (i.e. which is the required temporal resolution ?). In figure 5.5, we present TRPL performed on an unprocessed part of the sample. We see that the decay time is strongly dependent of the wavelength, due to the QCSE, but even for the wavelength range around 470 nm, where we measured the best quality factors, it is still around 2 ns. Thus in any case, we will have to work with the cavity dumper, in order to have access to a temporal window larger than 2 ns.

We have tried preliminary experiments in order to show the shortening of the decay times but so far these experiments were not successful. The main reason is that as we explained in the last part, in order to record a spectrum where a WGM shows up, one has to perform a very tricky step of optimization of the signal. In the TRPL setup, the only detector we have so far is a streak camera which has a poor efficiency compared to a CCD. Thus it is not possible to make a real time optimization, the way we did it in CW PL before running a long experiment in order to extract the decay time. We hope that in a near future we will have access to a setup which has both detectors (CCD for real time optimization + streak camera), in order to demonstrate the Purcell effect in these microdisks.

In this chapter, we have presented the characterization of GaN microdisks with embedded InGaN/GaN heterostructures. We have shown that thanks to a state of the art nanofabrication (performed in the EPFL), these microdisks can present whispering gallery modes with the best quality factors ever measured for nitride microdisks : up to 11000 for a diameter of 3 μm. This should open the way to the demonstration of the Purcell effect in these structures.

Chapter 6

Carrier and spin dynamics in polar GaN/AlN heterostructures

The aim of this chapter is to present studies performed during the last year of my work. It will be split in two parts : the study of nonradiative processes in c-plane GaN/AlN heterostructures and the study of the spin dynamics in c-plane GaN/AlN quantum dots. We gathered these studies in the same chapter because they are based on the same experimental technique, namely time resolved photoluminescence and because a prerequisite to understand the spin dynamics is to understand the carrier dynamics.

Contents

6.1 How and why study spin dynamics in the GaN/AlN system?

The study of the spin dynamics in semiconductors has recently attracted much interest, especially in quantum dots where the main spin scattering mechanisms which limit the spin lifetime in bulk or quantum wells are supposed to be frozen [8, 209, 274]. Having long spin relaxation times is indeed a prerequisite to implement spintonics or quantum information processing devices.

At the very beginning of this study, we thought about using resonant two photon excitation to study the spin dynamics in GaN/AlN quantum dots [275, 276]. In this kind of measurements, you excite the system in a dark state and looking at the time resolved luminescence, the rise time should give you informations about the spin flip processes between the dark and the bright states. But one requirement of such an experiment is to have undoped structure to ensure that you have indeed a dark state. When we started we had no guarantee that our structures were actually undoped and that is why we chose another experimental approach : the alignment of the exciton in quasi-resonant excitation [277–279]. The term alignment (resp. orientation) means the conservation of the linear (resp. circular) polarization of the excitation for the exciton recombination. The luminescence has thus the same polarization than the laser, and the decay time of the created degree of polarization gives informations about spin-flip mechanisms. You can thus probe the spin dynamics on a time scale which is set by the decay time of the exciton. The faster dynamics you can access is given by the resolution of your time resolved setup, typically not better than 10 ps for a streak camera or a photomultiplier/avalanche photodiode. To access faster time scales, one must use pump-probe techniques.

So far, very few experiments of exciton alignment/orientation have been performed in nanostructures made of III-N materials [280–283]. But these materials are very appealing because they are expected to present long spin lifetimes up to room temperature, contrary to III-As or II-VI materials. The main reasons invoked include their wide band gap and their small spin orbit coupling that should make the spin scattering mechanisms very inefficient and insensitive to the temperature. Nevertheless when studying these compounds in the wurtzite phase (which we recall is the most stable one), the excitation and relaxation mechanisms are likely to be different from the ones of traditional zinc blende compounds, especially due to the difference in the band structure. It could explain why very few studies have been reported up to now and none in wurtzite GaN/AlN heterostructures. Another possibility of III-N heterostructures comes from the QCSE which makes the radiative lifetimes potentially very long [14] allowing us theoretically to probe the spin on much larger time scale in an exciton alignment/orientation experiment.

Before focusing on the spin dynamics, we will present a detailed study of the carrier recombination in GaN/AlN heterostructures. In order to understand the spin dynamics, you indeed need first to have a clear understanding of the carrier recombination and especially its temperature dependence.

6.2 Nonradiative processes : quantum dots versus quantum wells

Due to the 3D electronic confinement, excitons trapped in quantum dots are expected to be much more insensitive to nonradiative recombinations than other semiconductor structures, such as quantum wells [284]. This difference should be particularly acute in semiconductors with high structural defects densities such as III-nitrides. But one can argue that the reduction of the nonradiative processes could be less effective in large GaN/AlN quantum dots due to very long radiative decay times [14]. In this section we will thus focus on the nonradiative processes in GaN/AlN quantum dots and wells of different thickness by means of temperature dependent photoluminescence.

6.2.1 Influence of the excitation power

Before carrying out temperature dependence of the luminescence one should check that one measures the intrinsic emission of the structures. Especially one should ensure that the internal electric field is not screened by photocarriers in the range of density of power used. The samples studied are superlattices of GaN/AlN quantum dots (40 periods, 8 nm thick spacer) grown by Plasma Assisted Molecular Beam Epitaxy (Eva Monroy) (see figure 6.4).

Figure 6.1(a) shows the power dependence of the luminescence spectrum recorded on GaN/AlN quantum dots luminescing around 3 eV. One sees that above a density around 1W.cm^{-2} the shape of the spectrum evolve as a consequence of the screening, starting from the low energy side where the influence of the field is the strongest. The densities of power needed to start to screen the electric field are in accordance with the value of ref. [119] for the GaN/AlN system. Thus one needs to work below this density in order to probe the intrinsic properties of the structures. One must nevertheless take care to the translation of these densities for the time resolved measurements. We checked that at low excitation powers we have no changes in both the

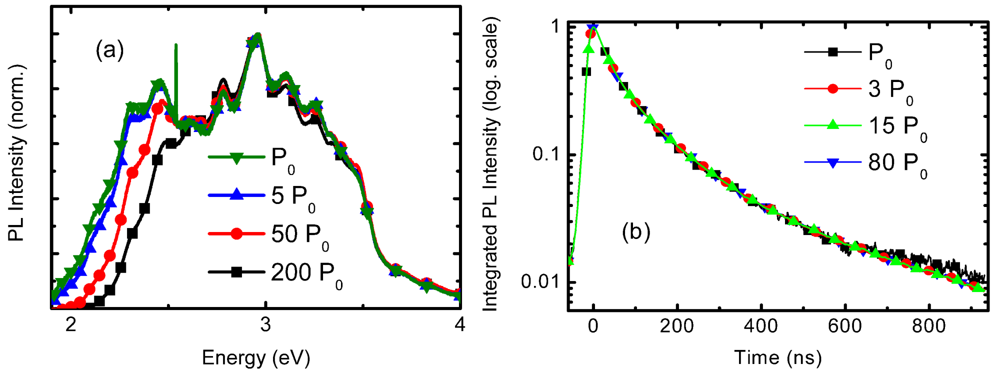

Figure 6.1: (a): continuous wave experiment (excitation at 244 nm) at low temperature illustrating the shape dependence of the spectrum as a consequence of a screening of the internal electric field. P_0 corresponds to a density around 100 mW.cm^{-2} (b): time resolved at low temperature (excitation around 270 nm) showing no dependence of the temporal trace with the excitation power. P_0 is an average density around 50 mW.cm^{-2} and the repetition rate is 580 kHz.

shape of the spectrum and its temporal trace. This is presented in figure 6.1(b) and 6.2(a). We conclude thus that in this range of excitation powers (i.e. average density and repetition rate, for instance 10 mW.cm^{-2} and 580 kHz) we are in the low pumping rate limit and no screening occurs.

6.2.2 Time resolved photoluminescence : energy dependence of the decay time

By ensuring that no screening occurs in time resolved experiments and also that the repetition rate is low enough (we typically chose a rate corresponding to at least 10 decay times), we can now study the dependence of the radiative decay on the energy/wavelength (in other words the height of the quantum dots). There is indeed some discrepancies in the literature especially for the high energy part [14, 85]. On the one hand Kako et al. [85] reported radiative decay times around 400 ps for small dots (luminescence around 4 eV). On the other hand Bretagnon et al. [14] argued that even for these small dots the radiative decay time is more than 2 ns. This is actually not an irrelevant debate because what is at stake is the flat band value of the decay rate. The dependence of the temporal traces on the energy is illustrated in figure 6.2(b). One sees that by selecting a small energy window,

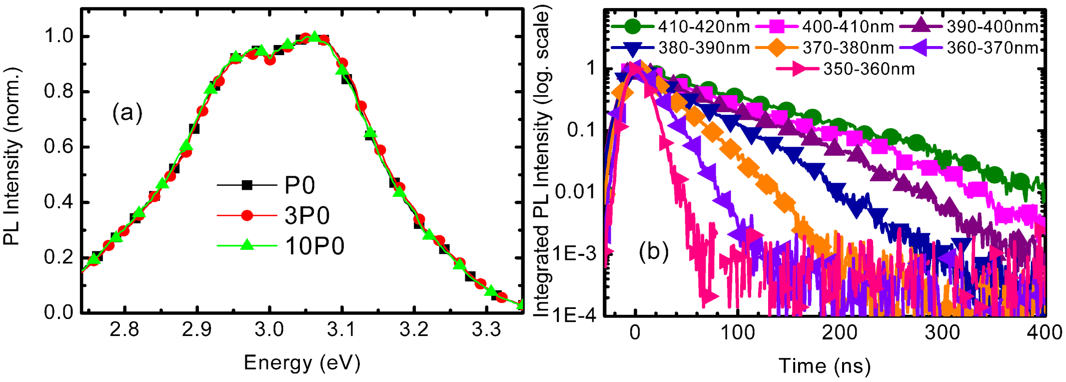

Figure 6.2: (a): low temperature measurements with a pulsed laser (excitation around 270 nm) showing no dependence of the shape on the excitation power. P_0 is an average density around 200 mW.cm^{-2} and the repetition rate is 580 kHz. (b): illustration of the dependence of the decay time on the energy. Measurements at low temperature.

the decays are purely monoexponential. It means that the radiative decay time is dominated by the electron-hole overlap along the growth axis and that the dispersion in lateral dimensions from dot to dot is weak. In figure 6.3, we present thus the measured decay times for small dots luminescing around 4 eV up to larger dots luminescing around 2.7 eV. The comparison with the literature leads us to the conclusion that our measurements are in accordance with the ones of Kako et al. [85]. We indeed measure decay times around 300 ps at 4 eV. On the other side of the graph, one sees that at 450 nm (2.75 eV), we measured decay times around 500 ns. For this long lived quantum dots, one may thus at this point wonder about the importance of the nonradiative processes.

6.2.3 Influence of the temperature

Time resolved measurements

We have probed the evolution of the decay times of both quantum dots and quantum wells as a function of the temperature. To have access to the whole range of decay times we have studied samples (dots and wells) of various thicknesses. This is illustrated in figure 6.4, where we show TEM images of a sample of small and large dots. In figure 6.5, we present the

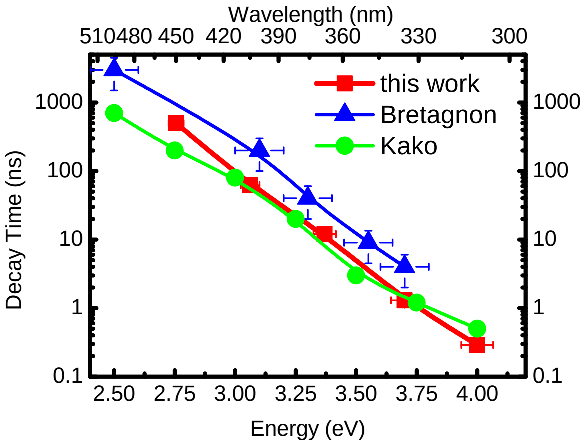

Figure 6.3: Measured radiative decay time at low temperature for dots luminescing from 2.7 eV to 4 eV. The solid line is a guide for the eyes. Comparison with data available in the literature : Kako et al. [85] and Bretagnon at al. [14].

comparison of the evolution of quantum dots and quantum wells. The most striking feature is seen in figure 6.5(a), where one notices that for quantum dots whatever the lifetime at low temperature, it is nearly constant up to room temperature. This is further illustrated in figure 6.6(a), where one compares the decay curves at low temperature and room temperature. They are actually the same, within the accuracy of the experiment. On the other hand for quantum wells, the decay time starts to decrease above 50 K for all samples, as illustrated in figure 6.5(b). It looses at least one order of magnitude at room temperature, as clearly illustrated in figure 6.6(b).

One can thus conclude that the nonradiative processes are very efficient in quantum wells, as expected from the high density of dislocations in these structures. Also, as it is widely admitted that low temperature localization occurs in such structure [110, 124], one can nevertheless assume that the interface are clean enough so that these structures are really 2D like at least above 50 K and fairly different from quantum dots. Let us notice that on one sample, we even measured an increase of the decay time at low temperature (see figure 6.7(a)). This is actually what is expected for a 2D exciton in which excited states with a lower oscillator strength are thermally populated. It could mean that these quantum wells are really 2D like, in the sense that the localization induced by interface fluctuation is small, even below 50 K.

Concerning the quantum dots, one can conclude that the nonradiative processes are efficiently suppressed even for radiative decay times in the μs

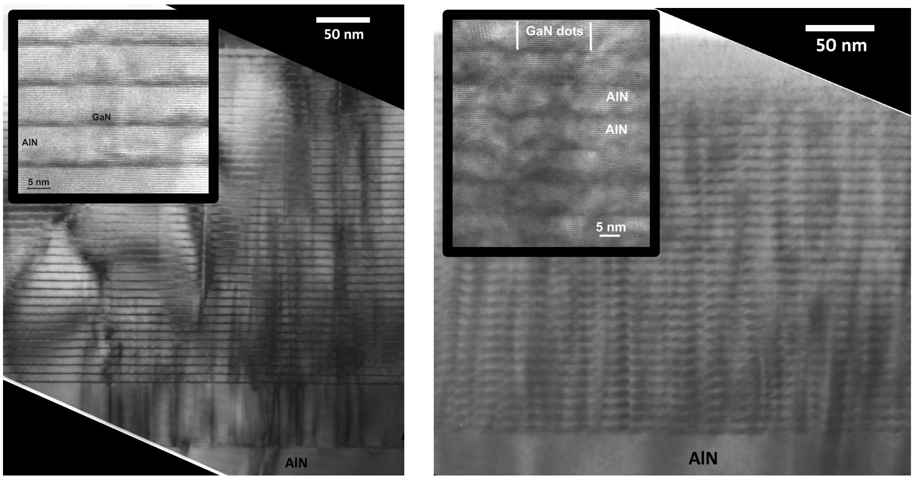

Figure 6.4: Illustration of two samples of superlattices of GaN/AlN quantum dots studied. On the left, a TEM image (courtesy of Ph. Komninou) of small dots, grown under N-rich conditions (Eva Monroy) and on the right is for large dots grown under Ga-rich conditions. In both case, the inset is a zoom which shows the dots on a smaller scale.

range. The measured data allow us to deduce that the change in the decay time between 4 K and room temperature is smaller than 10% (i.e. the resolution of the setup in the configuration used). We conclude thus that for these structures the nonradiative decay times are longer than 10 μs at room temperature.

Let us now make some comments on the nonradiative processes in quantum wells (see figure 6.5(b)). One sees that the decay times at room temperature seems to depend on the radiative decay time (i.e. the decay time at low temperature). To account for this feature, one should invoke that the nonradiative recombination rates depend on the radiative ones. In other word it would mean that there is a relationship between nonradiative and radiative recombinations. It could be explained by the fact that nonradiative processes involve two particles processes and are thus sensitive to the electron-hole overlap that on the other hand sets the radiative recombination rate. Although for some processes there are indeed some relationship between radiative and nonradiative rate in semiconductors [50], there are very few experiments showing this effect, especially in heterostructures.

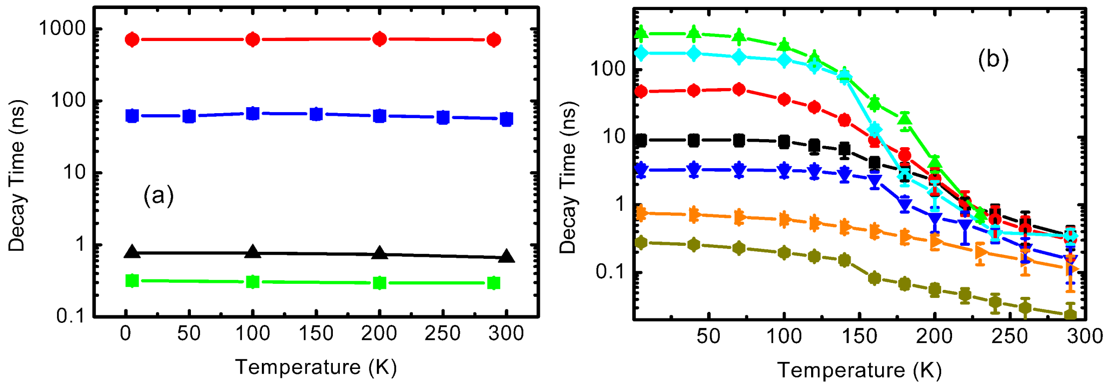

Figure 6.5: Evolution of the decay time (1/e) with the temperature for quantum dots (a) and quantum wells (b). Each curve stems for one sample.

Continuous wave measurements

The fact that the nonradiative processes are not efficient in GaN/AlN quantum dots should somehow appear in a continuous wave measurement as a function of the temperature. In figure 6.7(b), we studied the integrated intensity of the luminescence as a function of the temperature and compare dots to wells. The difference is impressive : the ratio of the room temperature integrated intensity to the low temperature one is around 0.65 for quantum dots and only 0.002 for quantum wells. This illustrates once again the strong disparity between the two systems.

6.2.4 Discussion

At this point one may wonder why the room temperature luminescence is "only" 65% of its value at low temperature, considering that the lifetime does not evolve (see part 2.2.2 for more details about the relationship between both). If the mechanism that explains the decrease of the luminescence is not related to the decay time, one should then look in more details to the other mechanisms responsible for the measured intensity in a photoluminescence experiment. They are detailled in equation 2.3. We have now established that the radiative efficiency (η_{rad}) does not depend significantly on the temperature. Thus the explanation should come from the two remaining terms, namely the absorption (resp. relaxation) efficiency η_{abs} (resp. η_{relax}).

To probe the relaxation efficiency, one can try to tune the excitation en-

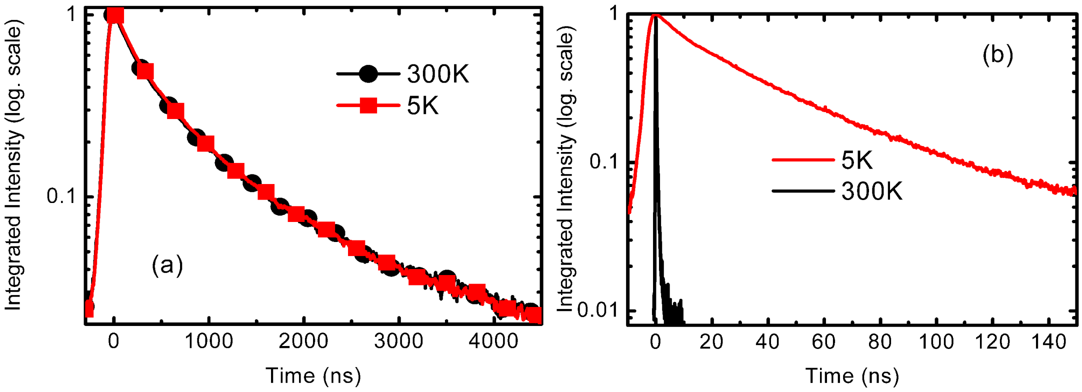

Figure 6.6: (a) illustrates that even for dots presenting a decay around 700 ns at low temperature, the decay is constant up to room temperature. On the other hand (b), the quenching is significant for quantum wells.

ergy because it can depend on the energy difference between the excitation and the luminescence. If the carriers are injected at higher energy, they are indeed more likely to find an escape channel before reaching the ground state of the quantum dots. In figure 6.8(a), one sees that exciting at lower energy (i.e. closer to the quantum dots ground state) increases significantly the ratio of the room temperature intensity to the low temperature one. One now reaches almost 90%. It would thus be very tempting to conclude that all the losses seen when excited at 244 nm occur during the relaxation. Eventually, one could hope that exciting closer to the quantum dots ground state (the experiment of figure 6.8(a) is still for an excitation 800 meV above the ground state) would lead to the same intensity a low and room temperature. But one has to stress that a clean experiment should follow the temperature induced luminescence shift with the excitation. In other words, the energy difference between the excitation and the luminescence should remain constant. This is actually very important for GaN/AlN quantum dots as illustrated in figure 6.8(b). The photoluminescence excitation shows that the absorption is strongly energy dependent, as a consequence of a strong reduction of the oscillator strength of the states for λ above 300 nm. Thus changing slightly the excitation energy changes significantly the number of photocreated electron-hole pairs. In figure 6.9(a), we thus studied the temperature dependence of the integrated intensity for various excitation wavelengths. But the excitation follows now a Varshni law (with the parameters from [16]) and it results in a shift of roughly 70 meV between low and room temperature. The situ-

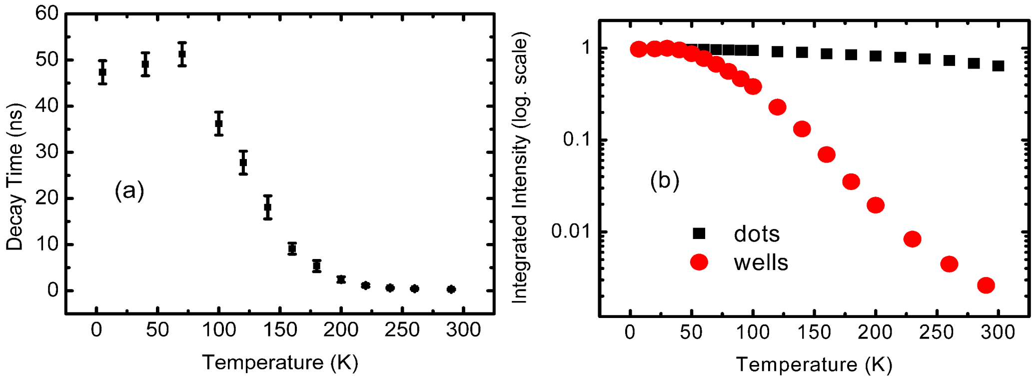

Figure 6.7: (a) illustrates the temperature dependence of the 1/e decay time in a sample of quantum wells. One sees an increase at low temperature (see text). (b) : temperature dependence of the integrated photoluminescence for quantum dots (luminescence around 410 nm) and quantum wells (luminescence around 440 nm). The excitation is at 244 nm (5.1 eV).

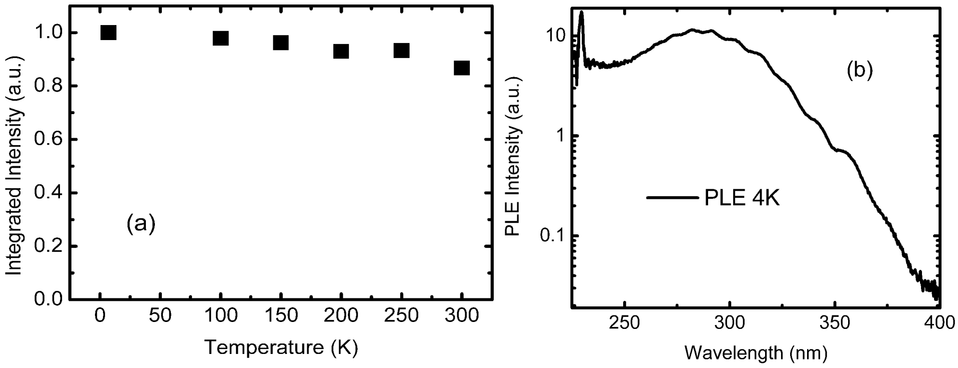

Figure 6.8: (a) shows the temperature dependence of the integrated luminescence for quantum dots luminescing around 440 nm and excited at 340 nm. (b) : photoluminescence excitation at low temperature. The detection is set at 460 nm. Note by the way the huge decrease of the signal for λ above 300 nm as a direct consequence of the reduction of the oscillator strength.

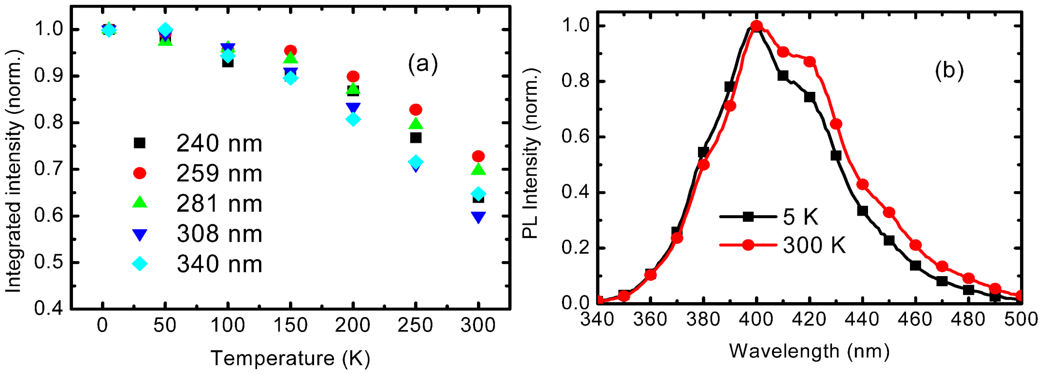

Figure 6.9: (a) shows the temperature dependence of the integrated luminescence for quantum dots luminescing around 410 for various excitation wavelength at low temperature and evolving with a Varshni law ([16]). (b) : normalized spectra at low and room temperature.

ation becomes not so clear and the ratio $\frac{I_{RT}}{I_{4K}}$ varies from 60 to 75 % but not monotonically with the excitation wavelength. We argue that it comes from a deviation from the Varshni law we used. But chosing the right parameters for the quantum dots we study is not an easy task as illustrated in figure 6.9(b). The band gap shift is indeed hidden by the Fabry-Perot interference and only a small shift of the luminescence peak (15 meV) is seen between low and room temperature.

To conclude this part, we will give evidences to show that although the experiments presented so far do not allow to draw a definitive conclusion due to the uncertainty on the band gap shift, there is an effect of the excitation energy on the variation of the relaxation efficiency. This comes from the comparison of the photoluminescence excitation spectra of figure 6.10. One sees in figure 6.10(b) that the shape of the photoluminescence excitation spectrum evolve with the temperature. If there was only an effect of the band gap shift, one should see a shift (which exists as seen in the inset) of the photoluminescence excitation and not a change in the shape. Thus the fact that the ratio $\frac{I(\lambda_1)}{I(\lambda_2)}$ (where λ is the excitation wavelength) depends on the temperature shows that the relaxation efficiency depends on both wavelength and temperature. Furthermore figure 6.10(a) shows that the two effects (band gap shift and wavelength dependence of the relaxation efficiency) have to be taken into account. The band gap shift is clearly evidenced in the right part, where the spectrum at room temperature is above the one at low tem-

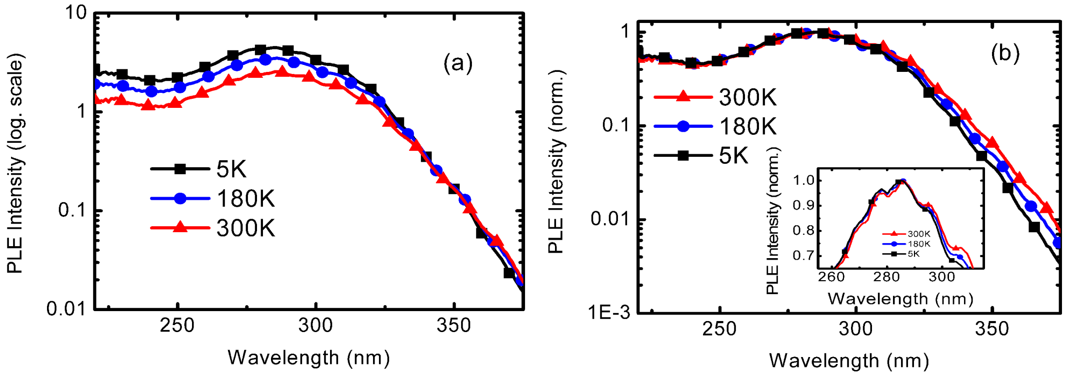

Figure 6.10: (a) variation of the photoluminescence excitation spectra with the temperature. The detection follows a Varshni law (b) : same spectra but normalized to their maximum. The inset is a zoom around 300 nm.

perature. The fact that there is more luminescence at room temperature than at low temperature for the same excitation wavelength shows indeed that the absorption is larger at room temperature at a given wavelength as a consequence of this band gap shift. But at higher energy, there is thus more luminescence at low temperature as a proof of a temperature dependence of the relaxation efficiency.

Coming back to the initial problem, one can say that the fact that the integrated intensity at room temperature is smaller than the one at low temperature when exciting at 244 nm is partly related to losses during the relaxation process. Further experiments (for instance dependence of the transmission in order to probe the absorption efficiency) will hopefully help to clarify the remaining issues.

6.3 Optical alignment of the exciton spin in GaN/AlN quantum dots

In this section, we will present preliminary results that seem to show evidence for spin alignment of the exciton in GaN/AlN quantum dots up to room temperature. Before focusing on the experiments, we will give both theoretical and experimental background about the topic.

6.3.1 Theoretical background : spin relaxation mechanisms in semiconductors

There are several mechanisms responsible for spin relaxation in semiconductors [285]. The dominant one depends on the dimensionality of the system. Generally, one can describe a mechanism in terms of an effective magnetic field.

Elliot Yafet (EF) mechanism

It comes from the scattering by phonons or charged impurities (due to the electric field they create). In this mechanism, there is a spin-flip when the carrier is scattered and the spin relaxation time is thus correlated to the scattering time. It is the generally the dominant mechanism in bulk materials.

Dyakanov-Perel (DP) mechanism

It occurs when there is a spin-splitting, whatever its origin. This is often the dominant mechanism in quantum wells. Due to the splitting, the carriers are thus subject to an effective Hamiltonian [285, 286]:

$$\mathrm{H} \sim \hbar \mathbf{\Omega}(\mathbf{p}).\mathbf{S} \tag{6.1}$$

where $\mathbf{S}$ is the pseudo-spin vector operator (in terms of Pauli Matrix) and $\mathbf{\Omega}(\mathbf{p})$ an effective Larmor vector, which depends on the momentum $\mathbf{p}$ and its amplitude is linked to the spin-splitting. Due to the momentum scattering, the precession turns out to be random and one generally writes the relaxation time of the spin along i $\tau_{s,i}$:

$$\frac{1}{\tau_{s,i}} = \left\langle \Omega_{\perp}^{2} \right\rangle \tau_{p}^{*} \tag{6.2}$$

where $\Omega_{\perp}$ is the precession vector in the plane perpendicular to i and τ_{p}^{*} is the relaxation time of the momentum.

Ω (in other words the spin-splitting) can have several origins but requires a spin-orbit coupling and an inversion asymmetry. The Dresselhaus or Bulk Inversion Asymmetry is responsible for a term which is often written Ω_{BIA} and produces terms proportional to k^3 (resp. k and k^3) in the Zinc Blende structure (resp. Wurtzite) [287]. The field induced spin splitting or Structural Inversion asymmetry (Ω_{SIA}, Rashba effect) comes from an asymmetry in the potential in the quantum wells. It can be created by an electric field

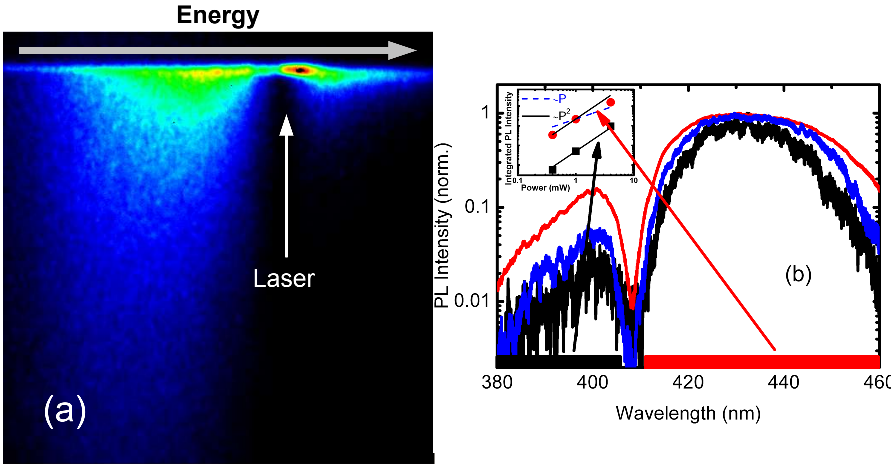

Figure 6.11: (a) : evidence for luminescence above the energy of the laser on a sample of quantum dots luminescing around 410 nm. The laser is set at 406 nm. The vertical scale is 1 μs and the horizontal one 85 nm. (b) : evidence for two photon absorption. The luminescence above the laser is quadratic and the luminescence below is neither linear nor quadratic due to the fact that the two processes (linear excitation and two photon absorption) contribute to it. The hole in the spectrum comes from the use of a notch filter to prevent the blindness of the detector by scattered laser light.

(internal or externally applied) [288]. The Natural Interface Asymmetry (Ω_{NIA}) is linked to the interface bounds.

This DP mechanism strongly depends on the orientation of the quantum well. For instance in (110) zinc blende quantum wells, due to the (110) direction, one ends up with $\Omega_{\perp}$=0 for the z (110) direction and thus this mechanism is suppressed for this component of the spin [289]. Also it is possible to tune the Dresselhaus and Rashba terms in order that they compensate each other and in this case the relaxation is strongly suppressed [290].

Hyperfine Interaction

When all the interactions mentioned above, that do require a spin-orbit coupling, are frozen, one has to take into account the interaction with the spins of the nucleus. This is the case in quantum dots [8].

6.3.2 Experimental background

The experiment

The idea of the experiment relies on creating an alignment of the spin of the exciton thanks to a linearly polarized excitation. In quantum dots, when there is no additional charge (which we will assume in this discussion), the eigenstates of the neutral exciton are indeed linearly polarized because of the anisotropy of the exchange interaction [200]. The two eigenstates are usually named $|X\rangle$ and $|Y\rangle$ referring to two orthogonal directions. These directions are often linked to some crystallographic directions but sometimes the situation is more complicated and the directions can vary from one dot to another [291]. In wurtzite III-N quantum dots, the situation is not well understood. Very few experiments report polarization measurements on the single dot level but recent works seem to indicate the possibility that the eigenstates vary from one dot to another [222, 223].

Experimental issues

Following the experiments carried out on zinc blende quantum dots [8, 281], the idea is to excite the luminescence of the ensemble of dots as close as possible (spectrally speaking) from the region studied. The aim is to reduce the losses of the polarization during the relaxation process by minimizing the number of emitted phonons. The excitation is generally a pulsed laser in order to have access to the dynamics. If one works in a basis (i.e. the polarization of the laser) that matches the one of the eigenstates, one can hope to detect a luminescence which is significantly polarized. One of the major problem of such an experiment comes from the scattered light at the surface of the sample. Also in our case, if we want to excite in a quasi-resonant manner large quantum dots luminescing below the GaN band gap, the problem is further enhanced. These quantum dots have indeed a very low oscillator strength (see for instance the photoluminescence excitation spectrum of figure 6.10) and we need to work at high excitation power (typically around 100 W.cm^{-2}) to get a reasonnable luminescence signal. Another difficulty comes from the fact that the samples are grown on a transparent substrate. Thus the optical quality of the back side has a great importance. To reduce the scattered light, we thus carefully polished this side and then deposited a metallic layer in order to realize a mirror. We managed to have an intensity scattered on the back side similar to what is scattered on the front side (epitaxied side), which is the best we could reasonably hope for. Anyway, the front side could not be improved and thus improving further the back side would not have had a significant effect. To conclude this part on the scattering let us stress that even with all these steps, the scattered light was still significant and we thus had to use a set of interference filters when working on the large dots. It limits the wavelength range where we can work : the excitation has to be situated between 400 and 410 nm.

As we said, we have to work at high excitation density for the large dots. But we noticed that when exciting strongly, we could detect luminescence above the energy of the laser, as illustrated in figure 6.11(a). The luminescence being far above the laser, processes assisted by phonon can be ruled out. Looking at the power dependence of this emission (see figure 6.11(b)), we conclude that it was actually due to two photon absorption. Furthermore it looks like this process is a resonant one. When exciting exactly in the same conditions (405 nm, same excitation power) a sample of smaller dots, luminescing around 350 nm, we did indeed see almost no luminescence. To the best of our knowledge, there is no report of this phenomenon (namely exciton enhanced non linear absorption with the excitation energy matching the one of the ground state) in GaN/AlN nanostructures in the literature. It has been demonstrated only for bulk GaN [292].

Thus if one wants to study the spin alignement in large quantum dots, one has to take care that the density of excitation power used does not induce significant non linear processes. If an important amount of electrons and holes are indeed created by a non linear process, the alignement will be lost during the relaxation towards the ground state.

6.3.3 Evidence for exciton spin alignment

We began the experiments by working on self assembled quantum dots. But so far, for both small (luminescence around 300 nm) and large dots (luminescence around 400 nm) we could not evidence any alignment of the spin of the exciton. We have only performed the experiments in the basis ($[11\bar{2}0]$,$[1\bar{1}00]$), which was the basis where spin alignment was evidenced in InGaN/GaN quantum dots [283]. Several explanations could account for the fact that these experiments did not succeed so far. If the basis of the eigenstates is not the one we used, the expected degree of polarization can be very weak and eventually vanish if the basis is at 45°. But most likely it could come from the fact that the basis of eigenstates changes from one dot to another, as we already mentioned [222, 223]. In this case, no alignment of the spin of the exciton can be realized on an ensemble of dots.

We also tried the experiments on thin GaN/AlN dots (luminescence around 300 nm) embedded in GaN nanowires (see figure 6.12(a)). In this case, the basis chosen for the excitation has a-priori no links to any crystallographic orientation. We will nevertheless call this basis of two orthogonal

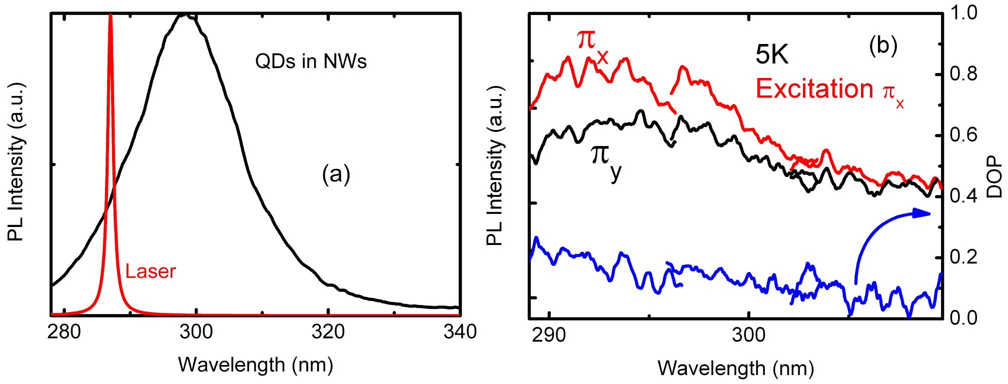

Figure 6.12: (a) : principle of the experiment. The spectrum of luminescence presented is recorded under non resonant excitation. (b) : low temperature photoluminescence spectra under quasi-resonant linearly polarized excitation at 287 nm. The degree of polarization (DOP) and its energy dependence evidence the optical alignment.

directions ($|X\rangle$,$|Y\rangle$) in what follows. As seen in figure 6.12(b), we could evidence the alignment of the spin of the exciton in this system. One clearly see in figure 6.12(b) that the luminescence is polarized in the same direction than the excitation (Π_X). We define the degree of polarization :

$$\frac{I_{||laser} - I_{\perp laser}}{I_{||laser} + I_{\perp laser}} \tag{6.3}$$

The energy dependence of the degree of polarization is a first clue to support the attribution to an alignment (and rules out an artifact). In figure 6.13(a), one sees furthermore that this degree of polarization is stable over the exciton decay time. It implies that the spin relaxation is slower than several ns. In figure 6.13(b), we present the exact same experiment but the excitation occurs now along Π_Y. The maximum of the luminescence is in this case detected along the Y-direction. This is another strong evidence of a spin alignment. When rising the temperature in figure 6.14(a), one sees that the effect is still observable. We conclude thus that the spin relaxation time is longer than several ns in this system even at room temperature.

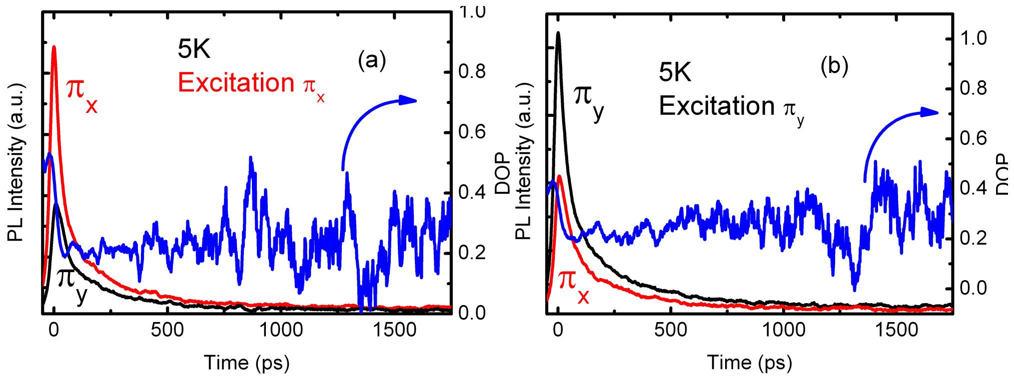

Figure 6.13: (a) and (b) : temporal dependence of the degree of polarization (DOP) under quasi-resonant excitation at low temperature.

6.3.4 Prospects

These preliminary results and the demonstration of the feasibility of the experiment have open the path to an in depth investigation of the spin dynamics in wurtzite GaN/AlN nanostructures. First, if it is confirmed, one needs to understand the difference between self organized quantum dots and quantum dots embedded in nanowires. The fact that alignment could be observed in the latter could indicate that the fine structure of an exciton is significantly different from what it is in self organized quantum dots. In particular, one can argue that due to strain relaxation the quantum dots embedded in nanowires are more symmetric than their self assembled counterpart so that less dispersion in terms of eigenstates basis exists. For the large dots, it will be interesting to probe the possibility of spin orientation (i.e. circular excitation) in both systems. Due to the electron-hole separation, it is indeed possible that the anisotropy of the exchange interaction vanishes and that the eigenstates turns out to be the eigenstates of the projection of the total momentum of the exciton J_z : $|1\rangle$ and $|-1\rangle$.

Studies in a magnetic field could give very valuable informations about the $|X\rangle$-$|Y\rangle$ splitting of the neutral exciton. When the eigen states are back to $|1\rangle$ and $|-1\rangle$ thanks to the application of a magnetic along the z-axis (one should now observe orientation instead of alignment), it means that the Zeeman splitting is larger than the $|X\rangle$-$|Y\rangle$ splitting. Studying the evolution from linear to circular polarization is thus an indirect way to estimate this splitting.

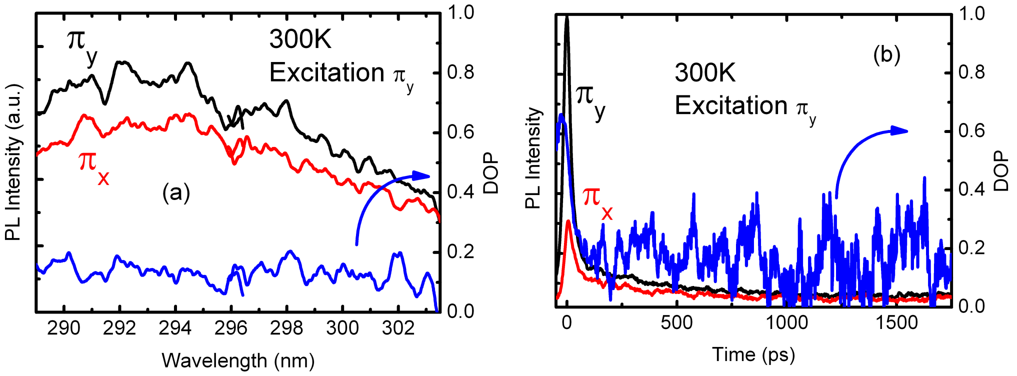

Figure 6.14: (a) : room temperature photoluminescence spectra under quasi-resonant linearly polarized excitation at 287 nm. The luminescence is polarized as illustrated with the degree of polarization (DOP). (b) : temporal dependence of the DOP.

Another interesting issue will be to study charged exciton. In our case, it will be X^- excitons and we will thus have access to the spin dynamics of the hole.

Thanks to time resolved luminescence, we have evidenced that non radiative processes are suppressed in polar quantum dots up to room temperature, even for radiative lifetimes reaching the microsecond. The behavior of quantum wells is very different and non radiative processes appear to influence the recombination dynamics above 50 K. We argue that the main mechanism responsible for the losses in photoluminescence intensity when rising the temperature is related to the relaxation mechanisms between the excitation and the ground state. Exciton alignment experiments performed on ensemble of quantum dots embedded in nanowires under quasi-resonnnant linearly polarized excitation show that spin relaxations mechanisms are efficiently suppressed in these structures. We could indeed observe no depolarization over the exciton lifetime up to room temperature.

Conclusion

My thesis work was mainly focused on the optical study of III-N nanostructures. Various systems were studied and original effects have been demonstrated.

Regarding non polar nanostructures, we evidenced the strong reduction of the quantum confined Stark effect in m-plane quantum dots. We were also able to probe the optical anisotropy down to the single dot level and showed that the optical polarization anisotropy is similar to the one of the bulk material. On the other hand, for a-plane quantum wells grown on SiC we have shown that strains modify significantly the selection rules. The luminescence turns to be polarized along the c-axis for the thicker quantum wells, which is opposite to the bulk behavior.

GaN nanowires grown by molecular beam epitaxy have shown interesting properties in themselves and also as a building block for the characterization of single GaN quantum dots. On the ensemble of nanowires level, we have performed polarization resolved experiments that show that the interplay between the electromagnetic anisotropy and the electronic anisotropy has important effects. Capping the GaN nanowires with AlN seems to have a significant role in terms of elastic and plastic relaxation of strains. Above a AlN shell thickness of a few nm, dislocations appear in the AlN shell. This effect has been evidenced thanks to Raman measurements and a simulation of the elastic strain relaxation. When inserting heterostructures in these nanowires, it seems that the quantum confined Stark effect is reduced compared to two dimensional structures. This effect appears clearly when studying the energy of the luminescence as a function of the thickness of the quantum dots. The red shift is indeed clearly reduced for insertions above 3 nm compared to two dimensional structures. We attributed this reduction to a strain relaxation which occurs thanks to the nanowire geometry.

GaN nanowires appear also as a very interesting system to perform the spectroscopy of single quantum dots, which are defined as a slice of a nanowire. The isolation of the luminescence of a single quantum dot is indeed much easier than for traditional self-assembled quantum dots. It allowed us to identify the luminescence of exciton and biexciton thanks to power dependence measurements. Concerning photon correlation experiments, we have presented a discussion based on Monte-Carlo simulations describing the excitation decay mechanism. Following these considerations, we have presented continuous wave experiments to measure the second order autocorrelation function and shown an antibunching with a $g_2(0)$ limited by the setup resolution. This experiment fully demonstrates that these emitters are indeed quantum dots.

We have studied the quality factors of GaN microdisks with embedded InGaN quantum wells. We have reported quality factors reaching 11000 for microdisks having a diameter of 3 μm. Such quality factors should lead to a strong Purcell effect. A reduction of the decay times up to 6 is expected and will hopefully be measured soon.

Finally, the carrier and spin dynamics in GaN/AlN heterostructures were investigated. The decay times of the luminescence of quantum dots do not evolve when rising the temperature even for decay times around 1 μs. This is on contrast with quantum wells and shows that non radiative processes are very inefficient in quantum dots. A discussion to understand the small decrease of the integrated intensity between low and room temperature was presented. These quantum dots are also very efficient to suppress the spin relaxation of the exciton as evidenced by experiments of alignment of the exciton spin. On small quantum dots embedded in nanowires, we could show that there is no decay of the induced polarization on the lifetime of the exciton up to room temperature. We could then conclude that spin relaxation is larger than the ns in this system up to room temperature. This is a strong improvement in comparison with non nitride semiconductor quantum dots.

Appendix A

The three and four indexes notations

In the hexagonal system, one generally uses the four index notation to label the planes and directions. A direction labeled [hkil] (we recall that h+k+i=0) in the four index notation would be [h'k'l'] in the three index notation following :

$$\begin{aligned} h' &= 2h + k \\ k' &= 2k + h \\ l' &= l \end{aligned} \tag{A.1}$$

or the other way around :

$$\begin{aligned} h &= \frac{1}{3}(2h' - k') \\ k &= \frac{1}{3}(2k' - h') \\ i &= -(h + k) = -\frac{1}{3}(h' + k') \\ l &= l' \end{aligned} \tag{A.2}$$

For the planes the relationships simply read :

$$(hkil) \rightarrow (hkl) \qquad \text{or}(hkl) \rightarrow (hk - (h + k)l).$$

Let us stress that in general a plane (hkil) is not perpendicular to the direction [hkil]. This is true for polar and non polar directions but not for semi-polar. The plane (hkil) is indeed perpendicular to the direction [hki($\frac{3a^2}{2c^2}$l)].

Appendix B

Photoluminescence setup and polarization resolved photoluminescence

The complete microphotoluminescence setup is presented in figure B.1. The laser light is focused thanks to a refractive microscope objective of numerical aperture 0.4 (LMU-20X-λ from OFR). The spectrometer (focal length 550 mm) has 3 gratings with various groove densities : 600, 1200 or 1800 g/mm. The resolution can reach 0.02 nm with the 1800 g/mm grating and entrance slits around 20 μm.

For polarization resolved measurements, two elements have to be inserted in the collection path. A $\lambda/2$ (resp. $\lambda/4$) wave plate and a polarizer. By rotating the $\lambda/2$ (resp. $\lambda/4$) wave plate, one can then analyze the linear (resp. circular) components of the luminescence. The direction of the polarizer is set depending on the grating in order to maximize the signal. The $\lambda/2$ (or $\lambda/4$) wave plate is made by a Berek rotator (New Focus) which is a very versatile component providing any retardation for wavelengths between 200 and 1600 nm. There is nevertheless a small beam deviation when rotating the component. The polarizers are calcite Glan Taylor polarizers purchased from Halbo Optics which do transmit the UV light down to 220 nm.

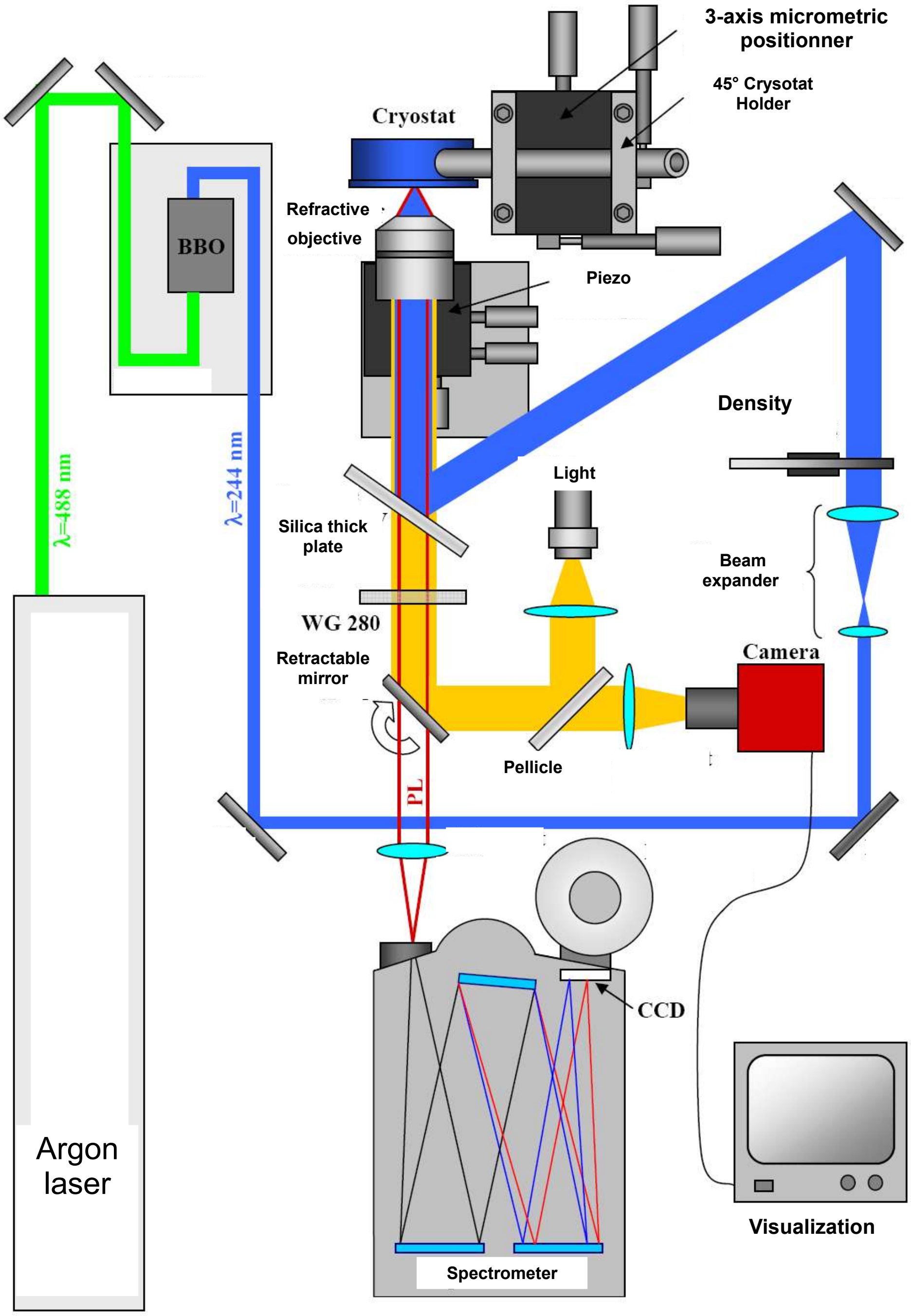

Figure B.1: Microphotoluminescence setup (after [125]).

Appendix C

Time resolved photoluminescence setup

The excitation of the time resolved setup consists of pulsed Ti-Sa laser (Mira from Coherent) pumped by a doubled YAG laser (5W Verdi from Coherent). The pulse width is either 200 fs or 2 ps but the laser is less stable in the picosecond mode. The repetition rate of the pulsed laser is tunable. The standard cavity gives a rate of 76 MHz but adding a cavity dumper, the rate is adjustable and depends on the division factor chosen. The pulse is frequency doubled or tripled depending on the wavelength needed.

The detection is made by a streak camera (Hamamatsu) as illustrated in figure C.1. In the synchroscan mode the best resolution achievable is around 5 ps. When working with the cavity dumper, the resolution is essentially limited by the jitter introduced by the delay generator (DG635 from Stanford). When the resolution is not limited by the pixelization on the streak camera, it can be down to around 150 ps.

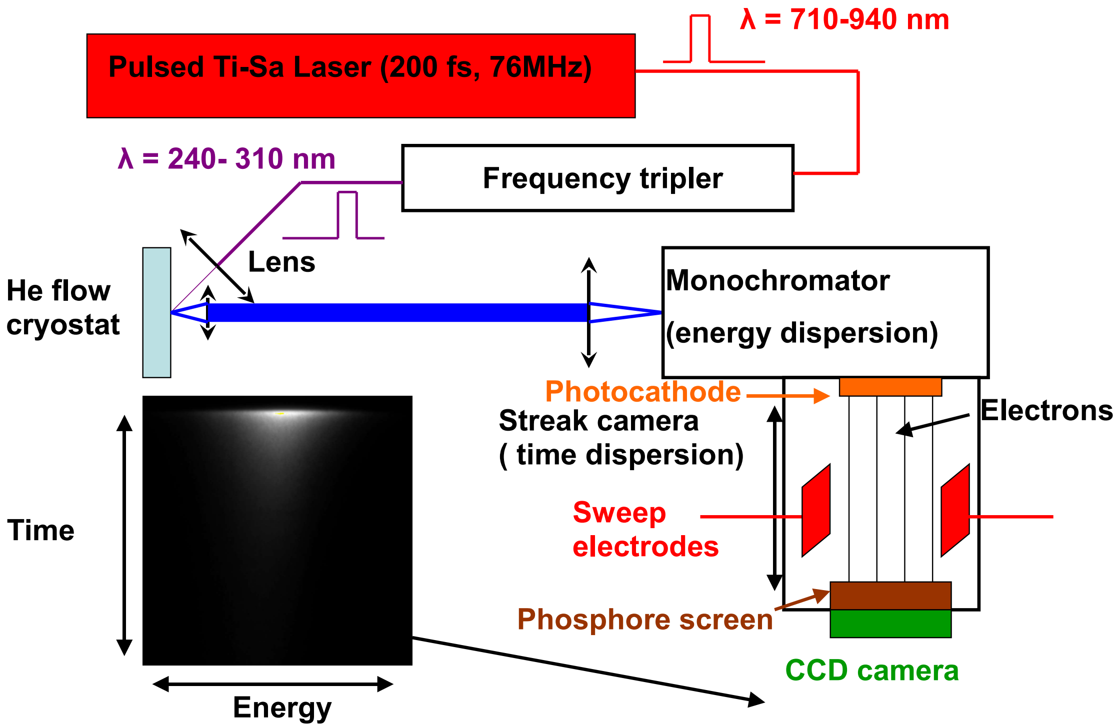

Figure C.1: Time resolved setup.

Appendix D

Reflectivity and excitation of the photoluminescence setup

For reflectivity and photoluminescence excitation (PLE), we used the same excitation light, namely a 400 W Xe lamp coupled to two 1800 g/mm gratings. The output is coupled to a fiber. The resolution, i.e. the spectral width of the light, is set by the slits of the spectrometer and can theoretically go down to less than 0.1 nm. But the signal is then very low and we thus generally performed the experiments with a resolution not better than 0.1 nm. In order to suppress the effects of chromaticity when performing experiments on a broad range of wavelengths, the light is directed and focused onto the sample thanks to Al parabolic mirrors. The collection is also made by parabolic mirrors and the light is then directed to the same monochromator that is used for the microphotoluminescence experiments. When performing PLE or near band edge reflectivity, the collection is made by lenses.

The detection is made with a single channel detector : a Hamamatsu photomultiplier (ref. 8249-102). For reflectivity, we simply used the gratings at the 0-order. We generally used a lock-in detection in both experiments (reflectivity and PLE). For near band edge reflectivity (or PLE) experiments, a part of the excited light is sent to a photodiode and is used to normalized (after the lock in detection) the signal sent by the photomultiplier in order to enhance the signal to noise ratio. The complete setup is presented in figure D.1.

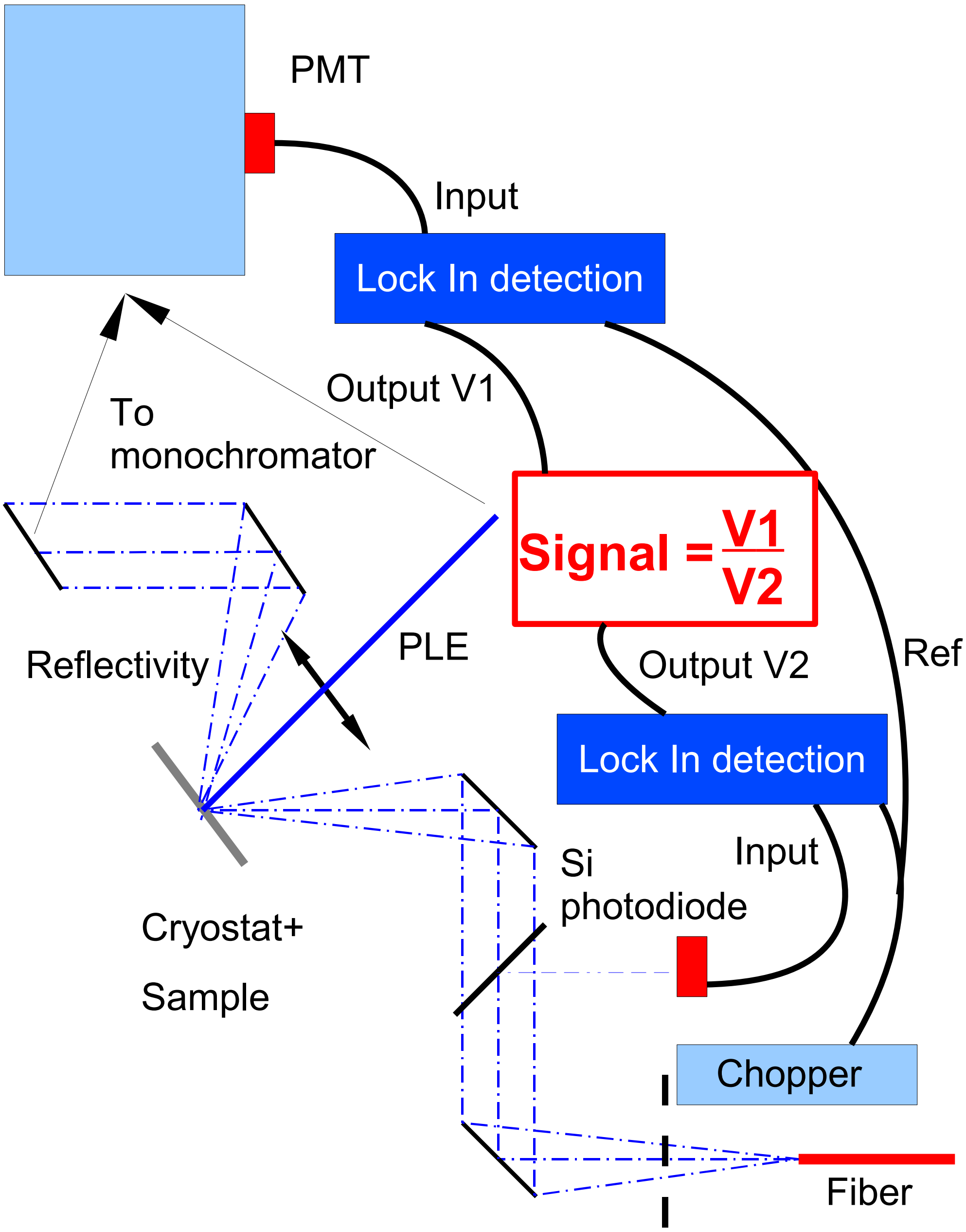

Figure D.1: PLE and reflectivity setup.

Appendix E

Correlation setup

The correlation setup is part of the microphotoluminescence (see appendix B). One just needs to split the collection and send each beam to two different monochromators E.1. The single channel detection is then performed by two photomultiplier (PMH100 from Becker and Hickl). They provide pulses with a width of 1.5 ns and an amplitude around 300 mV. The jitter limits the resolution to about 250 ps for one detector. The counting and the building of the correlation function is made by a TimeHarp correlation card from Picoquant.

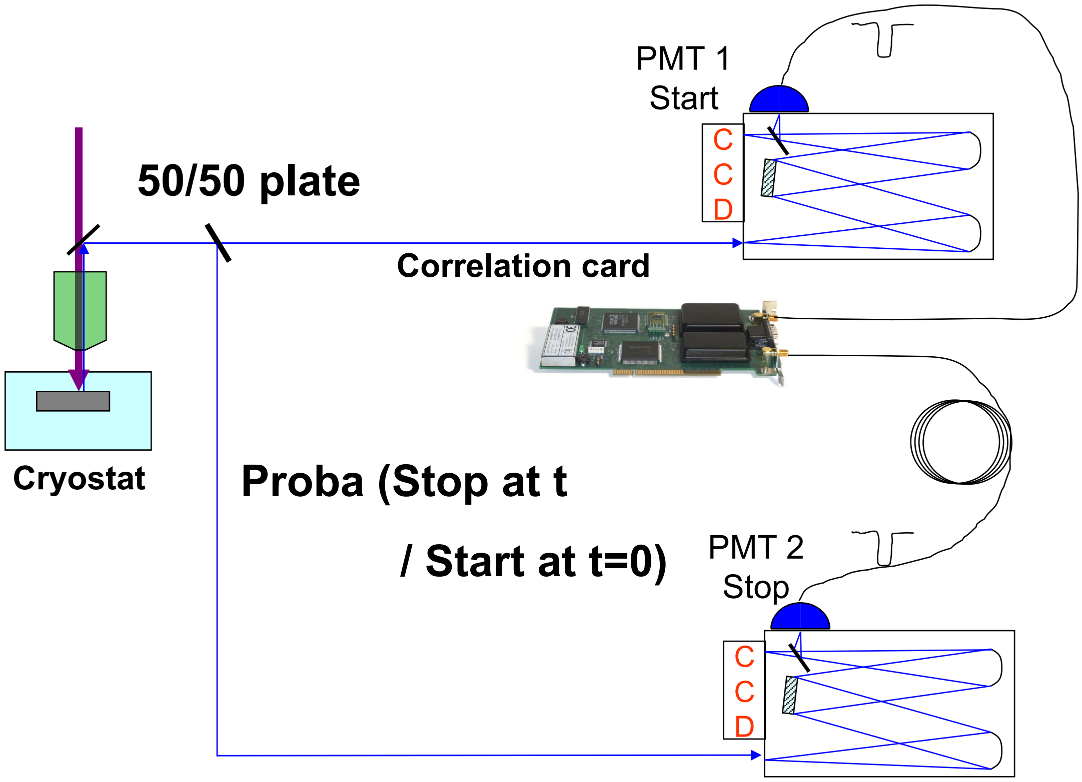

Figure E.1: Correlation setup.

Appendix F

Details about the MBE growth conditions

F.1 Polar samples

The polar samples were grown by Eva Monroy. They were generally grown on AlN on sapphire substrates (Dowa). The active nitrogen was supplied by a rf plasma cell (HD-25 from Oxford applied research). The quantum dots superlattices studied in chapter 6 are grown at a substrate temperature of 720°C. The small dots samples (luminescence up to 360 nm) are grown under N-rich conditions while the large ones are grown under Ga-rich conditions followed by a growth interruption. The quantum wells superlattices studied in chapter 6 are grown at a substrate temperature of 720°C under Ga-rich conditions without growth interruptions. In both cases the AlN barriers are grown in Al-rich regime and followed by a growth interruption.

F.2 Semipolar samples

The $(11\bar{2}2)$ samples were grown by Lise Lahourcade [59]. The substrates used were m-plane sapphire (Kyocera). The chamber was the same that for the polar samples. The isolation of the $(11\bar{2}2)$ phase requires to grow the AlN under slightly N-rich conditions ($\frac{\Phi_{III}}{\Phi_V} \approx 0.9$). The substrate temperature was around 720°C. $(11\bar{2}2)$ GaN can be isolated only if an AlN buffer is grown prior to the GaN growth (made under Ga-rich conditions at the accumulation limit).

F.3 m-plane samples

The m-plane samples were grown by Benoît Amstatt [116] on m-plane 6H-SiC substrates (Novasic). The active nitrogen was supplied by a rf plasma cell (EPI). The nanostructures studied in chapter 2 were grown at 730 °C under metal-rich conditions with $\frac{\Phi_{III}}{\Phi_V} \approx 1.2$.

F.4 a-plane samples

The a-plane samples were grown by Sebastien Founta [141] on a-plane 6H-SiC substrates (Novasic). The chamber used was the same that for m-plane samples. The quantum wells studied in part 2.4 were grown at a substrate temperature of 750°C under N-rich regime. The flux ratio was indeed $\frac{\Phi_{III}}{\Phi_V} \approx 0.6$.

F.5 Nanowires samples

For the detail of the growth of nanowires, see chapter 3.

Résumé en français

Introduction

Les hétérostructures semiconductrices se sont révélées être très intéressantes en terme d'applications mais également à des fins plus fondamentales. Par exemple, depuis leurs premières caractérisations optiques dans les années 80 [1–4], les boites quantiques ont été largement étudiées et ont démontré des phénomènes physiques intéressants. Du fait de la quantification des niveaux d'énergies, des effets originaux ont pu être observés par des moyens optiques ou électriques. On peut par exemple citer : l'émission de photons uniques [5], le bloquage de Coulomb et la manipulation de charge au niveau de l'électron unique [6], la robustesse du spin ainsi que sa manipulation [7–9]. D'un autre côté, l'introduction des hétérostructures semiconductrices dans les dispositifs a permis d'améliorer significativement les performances, par exemple le courant de seuil pour un laser contenant des puits quantiques [10].

Les semiconducteurs III-N ont attiré l'attention plus tard que les autres semiconducteurs en terme d'application, particulièrement les arsenures, mais depuis le développement du premier dispositif optoélectronique à base de semiconducteurs III-N [11, 12], l'interêt qu'ils suscietent reste important. D'un point de vue dispositif, ils sont supposés apporter de nouvelles possibilités, par exemple en ce qui concerne de longueur d'ondes pour les dispositifs optiques et les fréquences atteignables dans les dispositifs électroniques. Les particularités des composés III-N, une large bande interdite et une structure wurtzite, ont aussi conduit à des nouveaux phénomènes physiques. Par exemple, le large décalage de bandes augmente la stabilité thermique de l'émission des boites quantiques et a permis la démonstration de l'émission de photons uniques à 200 K [13]. Le fort champ éléctrique qui apparait dans les héterostructures crues selon l'axe polaire a pour conséquences une séparation de l'électron et du trou ce qui entraine un fort décalage vers le rouge de la luminescence ainsi qu'une réduction de la force d'oscillateur. Des temps de vie radiatifs atteignant la microseconde ont été mesurés [14].

Les nanofils sont un autre type de structure semiconductrice qui a récemment été trés étudiée. Leurs avantages attendus viennent en partie de leur surface libre qui devrait permettre une relaxation facilitée des contraintes et ainsi diminuer la densité de défauts dans les hétérostructures. Pour les nitrures, qui présentent des très fortes densités de défauts, les améliorations potentielles sont très importantes.

Dans ce contexte, le but de cette thèse ést d'étudier les propriétés optiques de diverses sortes d'hétérostructures faites à base de nitrures et de démontrer de nouveaux comportements.

Le manuscrit est organisé de la façon suivante : des considérations générales sur les semiconducteurs et hétérostructures III-N sont présentées dans le premier chapitre. Le second chapitre est dédié aux propriétés des nanostructures non polaires. Nous montrons qu'au delà de la forte réduction du champ éléctrique, qui est très intéréssante en vue d'applications, ces structures ont un comportement original en ce qui concerne la polarisation de la luminescence.

Dans le chapitre trois, nous mettons en évidence les nouvelles possibilités offertes par les nanofils GaN comparés aux structures 2D. Les nanofils présentent en effet une forte anisotropie optique du fait de l'anisotropie de l'indice de réfraction . Nous montrons que le champ éléctrique est réduit pour des hétérostructures insérées dans des nanofils, si on le compare à des hétérostructures 2D. Cette réduction est attribuée à une diminution de la contribution piezoelectrique.

L'étude de boites quantiques uniques insérées dans des nanofils est présentée au chapitre 4. Nous mettons en évidence l'émission d'excitons et biexcitons. Finalement, nous montrons que ces structures sont bien des boites quantiques, i.e. que les niveaux d'énergies sont discrétisés, grâce à une expérience de corrélation de photons.

Dans le chapitre 5, nous étudions des structures dans lesquelles un émetteur de lumière est couplé à un mode optique, i.e. des microcavités. Nous présentons des résultats obtenus sur des microdisques en GaN avec des puits quantiques en InGaN. Nous montrons des spectres de photoluminescence sur lesquels des facteurs de qualité atteignant 11000 sont mesurés. Ce sont les meilleurs facteurs de qualité reportés pour des microcavités nitrures.

La dynamique des porteurs et de leurs spins est étudiée dans le chapitre 6. Des expériences résolues en temps montre que lorsqu'ils sont confinés dans des boites quantiques, les excitons sont insensibles aux recombinations non radiatives et à la relaxation de spin. Nous montrons que les déclins non radiatifs sont supérieurs à quelques μs à température ambiante. La relaxation de spin est quant à elle plus longue que la ns jusqu'à température ambiante.

Chapitre 1 : Propriétés générales des matériaux nitrures

Dans ce chapitre, nous présentons les particularités des semiconducteurs III-N qui sont nécessaires pour comprendre leur propriétés optiques. Leur structure wurtzite leur confère un comportement unique et nous montrons que du fait de la polarisation spontanée et de la polarisation piezoelectrique, les héterostructures crues selon l'axe c présentent un fort effet Stark confiné quantique. Le champ électrique peut en effet atteindre 10 MV/cm. Nous montrons que le champ électrique peut être supprimé dans les puits quantiques non polaires. Pour les boites quantiques, la situation est plus compliquée mais une modélisation simple nous permet de conclure qu'il doit être fortement réduit.

Chapitre 2 : Particularités des nanostructures non polaires : étude résolues en temps et en polarisation

Dans ce chapitre, nous montrons que les hétérostructures GaN/AlN non polaires ont plusieurs particularités comparées aux hétérostructures polaires. La forte réduction de l'effet Stark confiné quantique est démontrée. Nous présentons une étude détaillée des processus non radiatifs dans les deux types de structures qui peuvent être crus sur un substrat plan m de SiC : des boites et des fils quantiques. Nous montrons que malgré le confinement et la contrainte, la polarisation de la luminescence des nanostructures plan m est comparable au massif : un maximum perpendiculaire à l'axe c. Nous avons réussi à accomplir une telle étude jusqu'à l'échelle de la nanostructure unique. La polarisation de la luminescence est aussi étudiée pour des puits quantiques plan a. Nous montrons que dans ce cas la variation de contrainte avec l'épaisseur du puit conduit à un phénomène original. Pour le puit le plus épais, l'état fondamental est polarisé selon l'axe c. Mais lorsque l'on réduit la taille et par la même augmente la contrainte, il y a un changement de polarisation et la polarisation de la photoluminescence redevient comparable à celle du massif.

Chapitre 3 : Propriétés optiques d'hétérostructures à base de nanofils GaN

Dans ce chapitre, nous présentons les propriétés optiques d'ensemble de nanofils en GaN. En plus des spectres de photoluminescence, nous présentons des spectres de réfléctivité et d'excitation de la photoluminescence. Ces deux méthodes nous permettent d'identifier précisément la position des excitons libres. L'étude de la polarisation de la photoluminescence, réalisée dans un plan contenant l'axe c, montre que les anisotropies électroniques et électromagnétiques jouent toutes les deux un rôle important. Un comportement original dans la luminescence du bord de bande est observé comme conséquence de cette interaction. La présence de l'effet Stark confiné quantique pour des nanofils contenant des héterostructures est démontrée, à la fois pour des fils GaN et AlN et ceci grâce à la démonstration de luminescence bien au dessous du bord de bande de GaN. Cet effet Stark confiné quantique semble néanmoins être réduit comparé à des hétérostructures 2D pour des insertions d'épaisseur supérieure à 3 nm. Les boites quantiques insérées dans les nanofils apparaissent également peu sensibles aux défauts non radiatifs, ce qui est démontré par une étude de photoluminescence en fonction de la température. Enfin, nous montrons que les propriétés optiques de nanofils uniques dispersés sur un substrat présentent une forte dispersion et que l'étude de nanofils suspendus serait plus à même de fournir des informations sur les caractéristiques intrinsèques de ces nanofils.

Chapitre 4 : Spectroscopie de boites quantiques uniques insérées dans des nanofils GaN

Dans ce chapitre, nous étudions les propriétés optiques de boites quantiques uniques insérées dans des nanofils. La diffusion spectrale semble être présente dans ces structures comme dans les boites quantiques auto-organisées. Des études en fonctions de la puissance ont été utilisées pour identifier l'exciton et le biexciton. L'énergie de liaison du biexciton apparait bien supérieure à celle mesurée dans des boites auto-organisées, suggérant une différence dans le potentiel de confinement. Des considérations générales sur les expériences de corrélation sont présentées grâce à des simulations Monte Carlo. La force d'oscillateur dans ces structures est comparable à celle des boites auto-organisées, avec un temps de 300 ps autour de 4 eV. La discrétisation des niveaux d'energie dans ces structures est démontrée par une expérience d'autocorrélation réalisée sous excitation continue. $g_2(0)$ est limité par la résolution comme le démontrent les simulations Monte Carlo.

Chapitre 5 : Etude des facteurs de qualités de microdisques GaN

Dans ce chapitre, nous présentons la caractérisation de microdisques GaN contenant des hétérostructures InGaN/GaN. Nous montrons que grâce à une nanofabrication à l'état de l'art (réalisée à l'EPFL), ces microdisques peuvent présenter des modes de galleries avec les meilleurs facteurs de qualité jamais mesurés pour des microdisques nitrures : jusqu'à 11000 pour un diamètre de 3 μm. Cela devrait ouvrir la voie à la démonstration de l'effet Purcell dans ces structures.

Chapitre 6 : Dynamique de spin et des porteurs dans les hétérostructures GaN/AlN polaires

Grâce à des études de photoluminescence résolue en temps, nous montrons que les processus non radiatifs sont supprimés dans les boites quantiques jusqu'à température ambiante, même pour des temps de vie de l'ordre de la microseconde. Le comportement des puits quantiques est très différent et les processus non radiatifs influencent la recombinaisons au-delà de 50 K. Nous supposons que le mécanisme principal responsable des pertes d'intensité de photoluminescence quand la température est augmentée est lié aux mécanismes de relaxation entre l'excitation et l'état fondamental. Des expériences d'alignement d'excitons réalisées sur des ensembles de boites quantiques insérées dans des nanofils sous excitation quasi résonnante polarisée linéairement montrent que les mécanismes de relaxation de spin sont efficacement supprimés dans ces structures. Nous n'observons en effet aucune dépolarisation sur le temps de vie de l'exciton jusqu'à température ambiante.

Conclusion

Mon travail de thèse s'est focalisé sur l'étude optique de nanostructures III-N. Divers systèmes ont été étudiés et des effets originaux ont été démontrés.

Nous avons démontré la forte réduction de l'effet Stark confiné quantique dans les boites quantiques plan m. Nous avons étudié l'anisotropie optique jusqu'au niveau de la nanostructure unique et montré que l'anisotropie de polarisation optique est comparable à celle du matériau massif. Pour des puits quantiques plan-a crus sur SiC, nous avons démontré que les contraintes et le confinement modifient significativement les règles de selection. Quand celles-ci sont dominées par la contrainte, la luminescence est polarisée le long de l'axe c, i.e. a l'opposé au comportement du massif.

Les nanofils GaN crus par épitaxie par jet moléculaire présentent des propriétés intéressantes en eux-mêmes,mais également en tant que bloc élémentaire pour la caractérisation de boites quantiques uniques. Au niveau des ensembles de nanofils, nous avons réalisé des expériences résolues en polarisation qui montrent que l'interaction entre l'anisotropie électromagnétique et l'anisotropie électronique a des effets importants. Recouvrir des nanofils GaN par de l'AlN semble avoir un rôle important en terme de relaxation plastique et élastique des contraintes. Au-delà d'une coquille d'AlN de seulement quelques nm, des dislocations apparaissent dans la coquille d'AlN. Cet effet a été démontré grâce à des mesures Raman et à une simulation de la relaxation élastique des contraintes. Lorsque l'on insère des héterostructures dans ces nanofils, il semble que l'effet Stark confiné quantique est réduit en comparaison à des stuctures 2D. Cet effet apparaît clairement en étudiant l'énergie de luminescence en fonction de l'épaisseur des boites quantiques. Le décalage vers le rouge est en effet ralenti pour des insertions plus épaisses que 3 nm. Nous attribuons ce ralentissement à une relaxation des contraintes qui intervient grâce à la géométrie nanofil.

Les nanofils en GaN sont également un système très intéressant pour réaliser la spectroscopie de boites quantiques uniques qui sont définis comme tranches de nanofils. Isoler la luminescence d'une boite quantique unique est en effet beaucoup plus simple que pour les boites quantiques traditionnelles. Cela nous a permis d'identifier l'exciton et le biexciton grâce à des mesures en fonction de la puissance. Nous avons présenté les résultats attendu lors des expériences de corrélations grâce à des simulations de Monte Carlo. Nous avons également présenté une mesure de la fonction d'autocorélation du second ordre et montré un dégroupement de photons avec un $g_2(0)$ limité par la résolution expérimentale. Cette expérience est la preuve décisive que ces émetteurs sont bien des boites quantiques.

Nous avons étudié les facteurs de qualité de microdisques GaN avec des puits quantiques InGaN. Nous avons reportés des facteurs de qualités atteignant 11000 pour des microdisques de 3 μm. De tels facteurs de qualité devraient permettre d'observer l'effet Purcell et des accélérations des temps de déclin jusqu'à 6 sont attendues.

Enfin, la dynamique des porteurs et du spin dans les hétérostructures GaN/AlN a été étudiée. Les temps de déclin de la luminescence des boites quantiques n'évoluent pas lorsqu'on augmente la température même pour des temps de déclin autour de la microseconde. Par contre ce n'est pas le cas pour les puits quantiques et ceci montre que les processus non radiatifs sont inefficaces dans les boites quantiques. Nous avons présenté une discussion pour comprendre les pertes d'intensité observées lors d' expériences de photoluminescence en fonction de la température. Ces boites quantiques sont aussi très efficaces pour supprimer la relaxation de spin de l'exciton comme démontré par des expériences d'alignement. Nous avons conclu que pour des petites boites quantiques insérées dans des nanofils, la relaxation de spin est plus longue que la ns et ce jusqu'à température ambiante. C'est une amélioration importante comparé aux boites quantiques semiconductrices faites à partir de matériaux autres que des nitrures.

Bibliography

[1] L. Goldstein, F. Glas, J. Y. Marzin, M. N. Charasse, and G. L. Roux, *Appl. Phys. Lett.* **47**, 1099 (1985).

[2] J. Cibert, P. M. Petroff, G. J. Dolan, S. J. Pearton, A. C. Gossard, and J. H. English, *Appl. Phys. Lett.* **49**, 1275 (1986).

[3] K. Brunner, U. Bockelmann, G. Abstreiter, M. Walther, G. Böhm, G. Tränkle, and G. Weimann, *Phys. Rev. Lett.* **69**, 3216 (1992).

[4] J. Y. Marzin, J. M. Gérard, A. Izraël, D. Barrier, and G. Bastard, *Phys. Rev. Lett.* **73**, 716 (1994).

[5] P. Michler, A. Kiraz, C. Becher, W. Schoenfeld, P. Petroff, L. Zhang, E. Hu, and A. Imamoglu, *Science* **290**, 2282 (2000).

[6] B. Meurer, D. Heitmann, and K. Ploog, *Phys. Rev. Lett.* **68**, 1371 (1992).

[7] D. Gammon, E. S. Snow, B. V. Shanabrook, D. S. Katzer, and D. Park, *Science* **273**, 87 (1996).

[8] M. Paillard, X. Marie, P. Renucci, T. Amand, A. Jbeli, and J. M. Gérard, *Phys. Rev. Lett.* **86**, 1634 (2001).

[9] M. Kroutvar, Y. Ducommun, D. Heiss, M. Bichler, D. Schuh, G. Abstreiter, and J. Finley, *Nature* **432**, 81 (2004).

[10] Y. Arakawa and H. Sakaki, *Appl. Phys. Lett.* **40**, 939 (1982).

[11] S. Nakamura, T. Mukai, and M. Senoh, *Appl. Phys. Lett.* **64**, 1687 (1994).

[12] S. Nakamura, M. Senoh, S. ichi Nagahama, N. Iwasa, T. Yamada, T. Matsushita, H. Kiyoku, and Y. Sugimoto, *Japanese J. Appl. Phys.* **35**, L74 (1996).

[13] S. Kako, C. Santori, K. Hoshino, S. Gotzinger, Y. Yamamoto, and Y. Arakawa, *Nature Mater.* **5**, 887 (2006).

[14] T. Bretagnon, P. Lefebvre, P. Valvin, R. Bardoux, T. Guillet, T. Taliercio, B. Gil, N. Grandjean, F. Semond, B. Damilano, et al., *Phys. Rev. B* **73**, 113304 (2006).

[15] R. Enderlein and N. J. Horing, *Fundamentals of semiconductor physics and devices* (Singapore River Edge, N.J. , World Scientific, 1997).

[16] I. Vurgaftman and J. R. Meyer, *J. Appl. Phys.* **94**, 3675 (2003).

[17] J. F. Nye, *Physical properties of crystals* (Oxford Univ. Press, Oxford, 1985).

[18] F. Bernardini, V. Fiorentini, and D. Vanderbilt, *Phys. Rev. B* **56**, R10024 (1997).

[19] F. Bernardini and V. Fiorentini, *Phys. Rev. B* **64**, 085207 (2001).

[20] F. Bernardini and V. Fiorentini, *Phys. Rev. B* **65**, 129903 (2002).

[21] S. de Gironcoli, S. Baroni, and R. Resta, *Phys. Rev. Lett.* **62**, 2853 (1989).

[22] F. Bernardini and V. Fiorentini, *Appl. Phys. Lett.* **80**, 4145 (2002).

[23] I. L. Guy, S. Muensit, and E. M. Goldys, *Appl. Phys. Lett.* **75**, 4133 (1999).

[24] A. D. Bykhovski, V. V. Kaminski, M. S. Shur, Q. C. Chen, and M. A. Khan, *Appl. Phys. Lett.* **68**, 818 (1996).

[25] G. Bu, D. Ciplys, M. Shur, L. J. Schowalter, S. Schujman, and R. Gaska, *Appl. Phys. Lett.* **84**, 4611 (2004).

[26] K. Kim, W. R. L. Lambrecht, and B. Segall, *Phys. Rev. B* **53**, 16310 (1996).

[27] C. F. Klingshirn, *Semiconductor optics* (Springer, 2006).

[28] G. F. Koster, *Properties of the thirty-two point groups* (MIT, Cambridge, 1963).

[29] D. Curie, *Champ cristallin et luminescence* (Gauthier-Villars, 1968).

[30] M. Balkanski and J. des Cloizeaux, *J. Phys. Radium* **21**, 825 (1996).

[31] K. Cho, *Phys. Rev. B* **14**, 4463 (1976).

[32] S. L. Chuang and C. S. Chang, *Phys. Rev. B* **54**, 2491 (1996).

[33] I. Vurgaftman, J. R. Meyer, and L. R. Ram-Mohan, *J. Appl. Phys.* **89**, 5815 (2001).

[34] P. Ramvall, S. Tanaka, S. Nomura, P. Riblet, and Y. Aoyagi, *Appl. Phys. Lett.* **73**, 1104 (1998).

[35] E. Silveira, J. A. Freitas, O. J. Glembocki, G. A. Slack, and L. J. Schowalter, *Phys. Rev. B* **71**, 041201 (2005).

[36] G. Pikus, *Zh. Eksp. Teor. Fiz.* **54**, 1507 (1961) (Sov. Phys. JETP **14**, 1075 (1962)).

[37] G. L. Bir and G. E. Pikus, *Symmetry and strain induced effects in semiconductors* (Wiley, New York, 1974).

[38] S. Ghosh, P. Waltereit, O. Brandt, H. T. Grahn, and K. H. Ploog, *Phys. Rev. B* **65**, 075202 (2002).

[39] Y. M. Sirenko, J. B. Jeon, B. C. Lee, K. W. Kim, M. A. Littlejohn, M. A. Stroscio, and G. J. Iafrate, *Phys. Rev. B* **55**, 4360 (1997).

[40] B. Gil, F. Hamdani, and H. Morkoç, *Phys. Rev. B* **54**, 7678 (1996).

[41] B. Gil and A. Alemu, *Phys. Rev. B* **56**, 12446 (1997).

[42] A. Shikanai, T. Azuhata, T. Sota, S. Chichibu, A. Kuramata, K. Horino, and S. Nakamura, *J. Appl. Phys.* **81**, 417 (1997).

[43] A. Alemu, B. Gil, M. Julier, and S. Nakamura, *Phys. Rev. B* **57**, 3761 (1998).

[44] P. Misra, Ph.D. thesis, Mathematisch-Naturwissenschaftlichen Fakultät I Humboldt-Universität zu Berlin, Berlin, Germany (2005).

[45] B. Gil, O. Briot, and R.-L. Aulombard, *Phys. Rev. B* **52**, R17028 (1995).

[46] J.-M. Wagner and F. Bechstedt, *Phys. Rev. B* **66**, 115202 (2002).

[47] W. Shan, R. J. Hauenstein, A. J. Fischer, J. J. Song, W. G. Perry, M. D. Bremser, R. F. Davis, and B. Goldenberg, *Phys. Rev. B* **54**, 13460 (1996).

[48] Suzuki and T. Uenoyama, *Jpn. J. Appl. Phys., Part 1* **35**, 1420 (1996).

[49] H. Y. Peng, M. D. McCluskey, Y. M. Gupta, M. Kneissl, and N. M. Johnson, *Phys. Rev. B* **71**, 115207 (2005).

[50] A. M. Stoneham, *Philos. Mag.* **36**, 983 (1977).

[51] J. J. Hopfield, *Phys. Rev.* **112**, 1555 (1958).

[52] P. Y.Yu and M. Cardona, *Fundamentals of semiconductors* (Springer, 2001).

[53] R. Stępniewski, K. P. Korona, A. Wysmołek, J. M. Baranowski, K. Pakuła, M. Potemski, G. Martinez, I. Grzegory, and S. Porowski, *Phys. Rev. B* **56**, 15151 (1997).

[54] A. V. Rodina, M. Dietrich, A. Göldner, L. Eckey, A. Hoffmann, A. L. Efros, M. Rosen, and B. K. Meyer, *Phys. Rev. B* **64**, 115204 (2001).

[55] P. P. Paskov, T. Paskova, P. O. Holtz, and B. Monemar, *Phys. Rev. B* **70**, 035210 (2004).

[56] J. R. Haynes, *Phys. Rev. Lett.* **4**, 361 (1960).

[57] K. Kornitzer, T. Ebner, K. Thonke, R. Sauer, C. Kirchner, V. Schwegler, M. Kamp, M. Leszczynski, I. Grzegory, and S. Porowski, *Phys. Rev. B* **60**, 1471 (1999).

[58] H. Teisseyre, P. Perlin, T. Suski, I. Grzegory, S. Porowski, J. Jun, A. Pietraszko, and T. D. Moustakas, *J. Appl. Phys.* **76**, 2429 (1994).

[59] L. Lahourcade, Ph.D. thesis, Institut National Polytechnique de Grenoble, Grenoble, France (2009).

[60] L. Lahourcade, J. Renard, B. Gayral, E. Monroy, M. P. Chauvat, and P. Ruterana, *J. Appl. Phys.* **103**, 093514 (2008).

[61] M. Leroux, N. Grandjean, B. Beaumont, G. Nataf, F. Semond, J. Massies, and P. Gibart, *J. Appl. Phys.* **86**, 3721 (1999).

[62] M. A. Reshchikov and H. Morkoç, *J. Appl. Phys.* **97**, 061301 (2005).

[63] R. Liu, A. Bell, F. A. Ponce, C. Q. Chen, J. W. Yang, and M. A. Khan, *Appl. Phys. Lett.* **86**, 021908 (2005).

[64] P. P. Paskov, R. Schifano, B. Monemar, T. Paskova, S. Figge, and D. Hommel, *J. Appl. Phys.* **98**, 093519 (2005).

[65] P. Paskov, T. Paskova, B. Monemar, S. Figge, D. Hommel, B. Haskell, P. Fini, J. Speck, and S. Nakamura, *Superlattices and Microstructures* **40**, 253 (2006).

[66] L. Eckey, J.-C. Holst, P. Maxim, R. Heitz, A. Hoffmann, I. Broser, B. K. Meyer, C. Wetzel, E. N. Mokhov, and P. G. Baranov, *Appl. Phys. Lett.* **68**, 415 (1996).

[67] G. Bastard, *Wave Mechanics Applied to Semiconductor Heterostructures* (Wiley-Interscience, 1991).

[68] O. Ambacher, *J. Phys. D* **31**, 2653 (1998).

[69] R. André, Ph.D. thesis, Université Joseph Fourier, Grenoble, France (1994).

[70] J. Simon, N. T. Pelekanos, C. Adelmann, E. Martinez-Guerrero, R. André, B. Daudin, L. S. Dang, and H. Mariette, *Phys. Rev. B* **68**, 035312 (2003).

[71] P. Lefebvre, S. Anceau, P. Valvin, T. Taliercio, L. Konczewicz, T. Suski, S. P. Łepkowski, H. Teisseyre, H. Hirayama, and Y. Aoyagi, *Phys. Rev. B* **66**, 195330 (2002).

[72] P. Waltereit, O. Brandt, A. Trampert, H. T. Grahn, J. Menniger, M. Ramsteiner, M. Reiche, and K. H. Ploog, *Nature* **406**, 865 (2000).

[73] Y. E. Kitaev and P. Tronc, *Phys. Rev. B* **64**, 205312 (2001).

[74] P. Tronc and P. Vennéguès, *Phys. Rev. B* **77**, 075336 (2008).

[75] A. D. Andreev and E. P. O'Reilly, *Phys. Rev. B* **62**, 15851 (2000).

[76] D. P. Williams, A. D. Andreev, E. P. O'Reilly, and D. A. Faux, *Phys. Rev. B* **72**, 235318 (2005).

[77] S. Schulz, A. Berube, and E. P. O'Reilly, *Phys. Rev. B* **79**, 081401 (2009).

[78] A. Cros, J. A. Budagosky, A. García-Cristóbal, N. Garro, A. Cantarero, S. Founta, H. Mariette, and B. Daudin, *Phys. Status Solidi B* **243**, 1499 (2006).

[79] D. P. Williams, A. D. Andreev, and E. P. O'Reilly, *Phys. Rev. B* **73**, 241301 (2006).

[80] N. Gogneau, D. Jalabert, E. Monroy, E. Sarigiannidou, J. L. Rouvière, T. Shibata, M. Tanaka, J. M. Gerard, and B. Daudin, *J. Appl. Phys.* **96**, 1104 (2004).

[81] S. Founta, C. Bougerol, H. Mariette, B. Daudin, and P. Vennéguès, *J. Appl. Phys.* **102**, 074304 (2007).

[82] D. Jalabert, J. Coraux, H. Renevier, B. Daudin, M.-H. Cho, K. B. Chung, D. W. Moon, J. M. Llorens, N. Garro, A. Cros, et al., *Phys. Rev. B* **72**, 115301 (2005).

[83] F. Widmann, J. Simon, B. Daudin, G. Feuillet, J. L. Rouvière, N. T. Pelekanos, and G. Fishman, *Phys. Rev. B* **58**, R15989 (1998).

[84] B. Damilano, N. Grandjean, F. Semond, J. Massies, and M. Leroux, *Appl. Phys. Lett.* **75**, 962 (1999).

[85] S. Kako, M. Miyamura, K. Tachibana, K. Hoshino, and Y. Arakawa, *Appl. Phys. Lett.* **83**, 984 (2003).

[86] P. Lefebvre, A. Morel, M. Gallart, T. Taliercio, J. Allègre, B. Gil, H. Mathieu, B. Damilano, N. Grandjean, and J. Massies, *Appl. Phys. Lett.* **78**, 1252 (2001).

[87] T. Kuroda and A. Tackeuchi, *J. Appl. Phys.* **92**, 3071 (2002).

[88] B. Daudin, G. Feuillet, J. Hübner, Y. Samson, F. Widmann, A. Philippe, C. Bru-Chevallier, G. Guillot, E. Bustarret, G. Bentoumi, et al., *J. Appl. Phys.* **84**, 2295 (1998).

[89] H. Yang, L. X. Zheng, J. B. Li, X. J. Wang, D. P. Xu, Y. T. Wang, X. W. Hu, and P. D. Han, *Appl. Phys. Lett.* **74**, 2498 (1999).

[90] S. V. Novikov, N. M. Stanton, R. P. Campion, R. D. Morris, H. L. Geen, C. T. Foxon, and A. J. Kent, *Semicond. Sci. Technol.* **23**, 015018 (2008).

[91] E. Martinez-Guerrero, C. Adelmann, F. Chabuel, J. Simon, N. T. Pelekanos, G. Mula, B. Daudin, G. Feuillet, and H. Mariette, *Appl. Phys. Lett.* **77**, 809 (2000).

[92] C. Chen, V. Adivarahan, J. Yang, M. Shatalov, E. Kuokstis, and M. A. Khan, *Japanese J. Appl. Phys.* **42**, L1039 (2003).

[93] M. C. Schmidt, K.-C. Kim, R. M. Farrell, D. F. Feezell, D. A. Cohen, M. Saito, K. Fujito, J. S. Speck, S. P. DenBaars, and S. Nakamura, *Japanese J. Appl. Phys.* **46**, L190 (2007).

[94] D. F. Feezell, M. C. Schmidt, R. M. Farrell, K.-C. Kim, M. Saito, K. Fujito, D. A. Cohen, J. S. Speck, S. P. DenBaars, and S. Nakamura, *Japanese J. Appl. Phys.* **46**, L284 (2007).

[95] J. P. Liu, J. B. Limb, J.-H. Ryou, D. Yoo, C. A. Horne, R. D. Dupuis, Z. H. Wu, A. M. Fischer, F. A. Ponce, A. D. Hanser, et al., *Appl. Phys. Lett.* **92**, 011123 (2008).

[96] T. Detchprohm, M. Zhu, Y. Li, Y. Xia, C. Wetzel, E. A. Preble, L. Liu, T. Paskova, and D. Hanser, *Appl. Phys. Lett.* **92**, 241109 (2008).

[97] Y. Tsuda, M. Ohta, P. O. Vaccaro, S. Ito, S. Hirukawa, Y. Kawaguchi, Y. Fujishiro, Y. Takahira, Y. Ueta, T. Takakura, et al., *Applied Physics Express* **1**, 011104 (2008).

[98] O.-H. Nam, M. D. Bremser, T. S. Zheleva, and R. F. Davis, *Appl. Phys. Lett.* **71**, 2638 (1997).

[99] K. Hiramatsu, K. Nishiyama, M. Onishi, H. Mizutani, M. Narukawa, A. Motogaito, H. Miyake, Y. Iyechika, and T. Maeda, *J. Cryst. Growth* **221**, 316 (2000).

[100] P. Gibart, *Rep. Prog. Phys.* **67**, 667 (2004).

[101] A. Denis, G. Goglio, and G. Demazeau, *Mater. Sci. Eng., R* **50**, 167 (2006).

[102] D. Hanser, L. Liu, E. Preble, K. Udwary, T. Paskova, and K. Evans, *J. Cryst. Growth* **310**, 3953 (2008).

[103] A. Bhattacharyya, I. Friel, S. Iyer, T. C. Chen, W. Li, J. Cabalu, Y. Fedyunin, K. F. Ludwig, T. D. Moustakas, H. P. Maruska, et al., *J. Cryst. Growth* **251**, 487 (2003).

[104] T. Koida, S. F. Chichibu, T. Sota, M. D. Craven, B. A. Haskell, J. S. Speck, S. P. DenBaars, and S. Nakamura, *Appl. Phys. Lett.* **84**, 3768 (2004).

[105] M. D. Craven, P. Waltereit, J. S. Speck, and S. P. DenBaars, *Appl. Phys. Lett.* **84**, 496 (2004).

[106] H. Teisseyre, C. Skierbiszewski, B. Łucznik, G. Kamler, A. Feduniewicz, M. Siekacz, T. Suski, P. Perlin, I. Grzegory, and S. Porowski, *Appl. Phys. Lett.* **86**, 162112 (2005).

[107] N. Akopian, G. Bahir, D. Gershoni, M. D. Craven, J. S. Speck, and S. P. DenBaars, *Appl. Phys. Lett.* **86**, 202104 (2005).

[108] S. Founta, F. Rol, E. Bellet-Amalric, J. Bleuse, B. Daudin, B. Gayral, H. Mariette, and C. Moisson, *Appl. Phys. Lett.* **86**, 171901 (2005).

[109] N. Garro, A. Cros, J. A. Budagosky, A. Cantarero, A. Vinattieri, M. Gurioli, S. Founta, H. Mariette, and B. Daudin, *Appl. Phys. Lett.* **87**, 011101 (2005).

[110] F. Rol, S. Founta, H. Mariette, B. Daudin, L. S. Dang, J. Bleuse, D. Peyrade, J.-M. Gerard, and B. Gayral, *Phys. Rev. B* **75**, 125306 (2007).

[111] B. Amstatt, J. Renard, C. Bougerol, E. Bellet-Amalric, B. Gayral, and B. Daudin, *J. Appl. Phys.* **102**, 074913 (2007).

[112] J. Renard, B. Amstatt, C. Bougerol, E. Bellet-Amalric, B. Daudin, and B. Gayral, *J. Appl. Phys.* **104**, 103528 (2008).

[113] B. Rau, P. Waltereit, O. Brandt, M. Ramsteiner, K. H. Ploog, J. Puls, and F. Henneberger, *Appl. Phys. Lett.* **77**, 3343 (2000).

[114] Y. J. Sun, O. Brandt, M. Ramsteiner, H. T. Grahn, and K. H. Ploog, *Appl. Phys. Lett.* **82**, 3850 (2003).

[115] M. Ueda, M. Funato, K. Kojima, Y. Kawakami, Y. Narukawa, and T. Mukai, *Phys. Rev. B* **78**, 233303 (2008).

[116] B. Amstatt, Ph.D. thesis, Université Joseph Fourier, Grenoble, France (2008).

[117] B. Amstatt, O. Landré, V. F. Nicolin, M. G. Proietti, E. Bellet-Amalric, C. Bougerol, H. Renevier, and B. Daudin, *J. Appl. Phys.* **104**, 063521 (2008).

[118] B. Amstatt, J. Renard, C. Bougerol, E. Bellet-Amalric, B. Gayral, and B. Daudin, *Phys. Rev. B* **79**, 035313 (2009).

[119] S. Kalliakos, T. Bretagnon, P. Lefebvre, T. Taliercio, B. Gil, N. Grandjean, B. Damilano, A. Dussaigne, and J. Massies, *J. Appl. Phys.* **96**, 180 (2004).

[120] P. Misra, O. Brandt, H. T. Grahn, H. Teisseyre, M. Siekacz, C. Skierbiszewski, and B. Łucznik, *Appl. Phys. Lett.* **91**, 141903 (2007).

[121] K. Kojima, M. Ueda, M. Funato, and Y. Kawakami, *Phys. Status Solidi B* **244**, 1853 (2007).

[122] M. Gurioli, A. Vinattieri, M. Colocci, C. Deparis, J. Massies, G. Neu, A. Bosacchi, and S. Franchi, *Phys. Rev. B* **44**, 3115 (1991).

[123] M. Gurioli, J. Martinez-Pastor, M. Colocci, C. Deparis, B. Chastaingt, and J. Massies, *Phys. Rev. B* **46**, 6922 (1992).

[124] P. Lefebvre, J. Allègre, B. Gil, A. Kavokine, H. Mathieu, W. Kim, A. Salvador, A. Botchkarev, and H. Morko, *Phys. Rev. B* **57**, R9447 (1998).

[125] F. Rol, Ph.D. thesis, Université Joseph Fourier, Grenoble, France (2007).

[126] R. Bardoux, T. Guillet, P. Lefebvre, T. Taliercio, T. Bretagnon, S. Rousset, B. Gil, and F. Semond, *Phys. Rev. B* **74**, 195319 (2006).

[127] J. H. Rice, J. W. Robinson, A. Jarjour, R. A. Taylor, R. A. Oliver, G. A. D. Briggs, M. J. Kappers, and C. J. Humphreys, *Appl. Phys. Lett.* **84**, 4110 (2004).

[128] H. Kamada and T. Kutsuwa, *Phys. Rev. B* **78**, 155324 (2008).

[129] M. Abbarchi, F. Troiani, C. Mastrandrea, G. Goldoni, T. Kuroda, T. Mano, K. Sakoda, N. Koguchi, S. Sanguinetti, A. Vinattieri, et al., *Appl. Phys. Lett.* **93**, 162101 (2008).

[130] L. Besombes, Ph.D. thesis, Université Joseph Fourier, Grenoble, France (2001).

[131] J. Seufert, R. Weigand, G. Bacher, T. Kümmell, A. Forchel, K. Leonardi, and D. Hommel, *Appl. Phys. Lett.* **76**, 1872 (2000).

[132] V. Türck, S. Rodt, O. Stier, R. Heitz, U. Pohl, R. Engelhardt, and D. Bimberg, *Journal of Luminescence* **87-89**, 337 (2000).

[133] V. Türck, S. Rodt, R. Heitz, O. Stier, M. Straßburg, U. W. Pohl, and D. Bimberg, *Physica E (Amsterdam)* **13**, 269 (2002).

[134] S. A. Empedocles and M. G. Bawendi, *Science* **278**, 2114 (1997).

[135] R. G. Neuhauser, K. T. Shimizu, W. K. Woo, S. A. Empedocles, and M. G. Bawendi, *Phys. Rev. Lett.* **85**, 3301 (2000).

[136] L. Coolen, X. Brokmann, P. Spinicelli, and J.-P. Hermier, *Phys. Rev. Lett.* **100**, 027403 (2008).

[137] P. Frantsuzov, M. Kuno, B. Janko, and R. A. Marcus, *Nat Phys* **4**, 519 (2008).

[138] M. Sugisaki, H.-W. Ren, K. Nishi, and Y. Masumoto, *Phys. Rev. Lett.* **86**, 4883 (2001).

[139] I. Chung and M. G. Bawendi, *Phys. Rev. B* **70**, 165304 (2004).

[140] R. G. Banal, M. Funato, and Y. Kawakami, *Phys. Rev. B* **79**, 121308 (2009).

[141] S. Founta, Ph.D. thesis, Université Joseph Fourier, Grenoble, France (2007).

[142] M. Arlery, J. L. Rouvière, F. Widmann, B. Daudin, G. Feuillet, and H. Mariette, *Appl. Phys. Lett.* **74**, 3287 (1999).

[143] H. Harima, *J. Phys. , Condens. Matter* **14**, R967 (2002).

[144] V. Darakchieva, T. Paskova, M. Schubert, H. Arwin, P. P. Paskov, B. Monemar, D. Hommel, M. Heuken, J. Off, F. Scholz, et al., *Phys. Rev. B* **75**, 195217 (2007).

[145] S. L. Chuang and C. S. Chang, *Semiconductor Science and Technology* **12**, 252 (1997).

[146] M. A. Sanchez-Garcia, E. Calleja, E. Monroy, F. J. Sanchez, F. Calle, E. Muñoz, and R. Beresford, *J. Cryst. Growth* **183**, 23 (1998).

[147] E. Calleja, M. A. Sánchez-García, F. J. Sánchez, F. Calle, F. B. Naranjo, E. Muñoz, U. Jahn, and K. Ploog, *Phys. Rev. B* **62**, 16826 (2000).

[148] F. Glas, *Phys. Rev. B* **74**, 121302 (2006).

[149] S. Raychaudhuri and E. T. Yu, *J. Appl. Phys.* **99**, 114308 (2006).

[150] A. David, H. Benisty, and C. Weisbuch, *J. Display Technol.* **3**, 133 (2007).

[151] O. Landré, Ph.D. thesis, Université Joseph Fourier, Grenoble, France (2009).

[152] S. Ishizawa, K. Kishino, and A. Kikuchi, *Applied Physics Express* **1**, 015006 (2008).

[153] K. Kishino, T. Hoshino, S. Ishizawa, and A. Kikuchi, *Electronics Letters* **44**, 819 (2008).

[154] K. Kishino, H. Sekiguchi, and A. Kikuchi, *J. Cryst. Growth* **311**, 2063 (2009).

[155] C. Foxon, S. Novikov, J. Hall, R. Campion, D. Cherns, I. Griffiths, and S. Khongphetsak, *J. Cryst. Growth* **311**, 3423 (2009).

[156] R. K. Debnath, R. Meijers, T. Richter, T. Stoica, R. Calarco, and H. Lüth, *Appl. Phys. Lett.* **90**, 123117 (2007).

[157] R. Songmuang, O. Landré, and B. Daudin, *Appl. Phys. Lett.* **91**, 251902 (2007).

[158] O. Landré, R. Songmuang, J. Renard, E. Bellet-Amalric, H. Renevier, and B. Daudin, *Appl. Phys. Lett.* **93**, 183109 (2008).

[159] L. Largeau, D. L. Dheeraj, M. Tchernycheva, G. E. Cirlin, and J. C. Harmand, *Nanotechnology* **19**, 155704 (2008).

[160] L. Lymperakis and J. Neugebauer, *Phys. Rev. B* **79**, 241308 (2009).

[161] O. Landre, C. Bougerol, H. Renevier, and B. Daudin, *submitted* (2009).

[162] T. Stoica, E. Sutter, R. J. Meijers, R. K. Debnath, R. Calarco, H. Lüth, and D. Grützmacher, *Small* **4** (2008).

[163] J. Ristic, E. Calleja, S. Fernandez-Garrido, L. Cerutti, A. Trampert, U. Jahn, and K. H. Ploog, *J. Cryst. Growth* **310** (2008).

[164] N. Thillosen, K. Sebald, H. Hardtdegen, R. Meijers, R. Calarco, S. Montanari, N. Kaluza, J. Gutowski, and H. Luth, *Nano Lett.* **6**, 704 (2006).

[165] H. Sekiguchi, T. Nakazato, A. Kikuchi, and K. Kishino, *J. Cryst. Growth* **300** (2007).

[166] L. H. Robins, K. A. Bertness, J. M. Barker, N. A. Sanford, and J. B. Schlager, *J. Appl. Phys.* **101**, 113505 (2007).

[167] F. Furtmayr, M. Vielemeyer, M. Stutzmann, A. Laufer, B. K. Meyer, and M. Eickhoff, *J. Appl. Phys.* **104**, 074309 (2008).

[168] J. Sánchez-Páramo, J. M. Calleja, M. A. Sánchez-García, E.Calleja, and U.Jahn, *Physica E (Amsterdam)* **13** (2002).

[169] P. Corfdir, P. Lefebvre, J. Ristić, P. Valvin, E. Calleja, A. Trampert, J.-D. Ganière, and B. Deveaud-Plédran, *J. Appl. Phys.* **105**, 013113 (2009).

[170] J. B. Schlager, K. A. Bertness, P. T. Blanchard, L. H. Robins, A. Roshko, and N. A. Sanford, *J. Appl. Phys.* **103**, 124309 (2008).

[171] H.-Y. Chen, H.-W. Lin, C.-Y. Wu, W.-C. Chen, J.-S. Chen, and S. Gwo, *Opt. Express* **16**, 8106 (2008).

[172] H.-Y. Chen, Y.-C. Yang, H.-W. Lin, S.-C. Chang, and S. Gwo, *Opt. Express* **16**, 13465 (2008).

[173] S. Shokhovets, O. Ambacher, B. K. Meyer, and G. Gobsch, *Phys. Rev. B* **78**, 035207 (2008).

[174] J. B. Schlager, N. A. Sanford, K. A. Bertness, J. M. Barker, A. Roshko, and P. T. Blanchard, *Appl. Phys. Lett.* **88**, 213106 (2006).

[175] H. E. Ruda and A. Shik, *J. Appl. Phys.* **100**, 024314 (2006).

[176] V. V. Ursaki, I. M. Tiginyanu, V. V. Zalamai, S. M. Hubbard, and D. Pavlidis, *J. Appl. Phys.* **94**, 4813 (2003).

[177] P. N. Keating, *Phys. Rev.* **145**, 637 (1966).

[178] M. Borgstrom, V. Zwiller, E. Muller, and A. Imamoglu, *Nano Lett.* **5**, 1439 (2005).

[179] A. Tribu, G. Sallen, T. Aichele, R. Andre, J.-P. Poizat, C. Bougerol, S. Tatarenko, and K. Kheng, *Nano Lett.* **8**, 4326 (2008).

[180] M. H. M. van Weert, N. Akopian, U. Perinetti, M. P. van Kouwen, R. E. Algra, M. A. Verheijen, E. P. A. M. Bakkers, L. P. Kouwenhoven, and V. Zwiller, *Nano Lett.* **9**, 1989 (2009).

[181] Y. Kawakami, S. Suzuki, A. Kaneta, M. Funato, A. Kikuchi, and K. Kishino, *Appl. Phys. Lett.* **89**, 163124 (2006).

[182] C.-Y. Wang, L.-Y. Chen, C.-P. Chen, Y.-W. Cheng, M.-Y. Ke, M.-Y. Hsieh, H.-M. Wu, L.-H. Peng, and J. Huang, *Opt. Express* **16**, 10549 (2008).

[183] J. Ristić, E. Calleja, M. A. Sánchez-García, J. M. Ulloa, J. Sánchez-Páramo, J. M. Calleja, U. Jahn, A. Trampert, and K. H. Ploog, *Phys. Rev. B* **68**, 125305 (2003).

[184] J. Ristić, C. Rivera, E. Calleja, S. Fernández-Garrido, M. Povoloskyi, and A. Di Carlo, *Phys. Rev. B* **72**, 085330 (2005).

[185] C. Rivera, U. Jahn, T. Flissikowski, J. L. Pau, E. M. noz, and H. T. Grahn, *Phys. Rev. B* **75**, 045316 (2007).

[186] C. Bougerol, R. Songmuang, D. Camacho, Y. M. Niquet, R. Mata, A. Cros, and B. Daudin, *Nanotechnology* **20**, 295706 (2009).

[187] T. Aschenbrenner, C. Kruse, G. Kunert, S. Figge, K. Sebald, J. Kalden, T. Voss, J. Gutowski, and D. Hommel, *Nanotechnology* **20**, 075604 (5pp) (2009).

[188] A. Wysmolek, K. P. Korona, R. Stępniewski, J. M. Baranowski, J. Błoniarz, M. Potemski, R. L. Jones, D. C. Look, J. Kuhl, S. S. Park, et al., *Phys. Rev. B* **66**, 245317 (2002).

[189] A. W. ek, R. Stepniewski, M. Potemski, B. Chwalisz-Pietka, K. P. a, J. M. Baranowski, D. C. Look, S. S. Park, and K. Y. Lee, *Phys. Rev. B* **74**, 195205 (2006).

[190] G. Sallen, Ph.D. thesis, Université Joseph Fourier, Grenoble, France (2009).

[191] L. Coolen, Ph.D. thesis, Université Paris VII, Paris, France (2006).

[192] M. O. Manasreh, *Phys. Rev. B* **53**, 16425 (1996).

[193] J. Wang, M. Gudiksen, X. Duan, Y. Cui, and C. Lieber, *Science* **293** (2001).

[194] H. E. Ruda and A. Shik, *Phys. Rev. B* **72**, 115308 (2005).

[195] K. Brunner, G. Abstreiter, G. Böhm, G. Tränkle, and G. Weimann, *Phys. Rev. Lett.* **73**, 1138 (1994).

[196] A. Chavez-Pirson, J. Temmyo, H. Kamada, H. Gotoh, and H. Ando, *Appl. Phys. Lett.* **72**, 3494 (1998).

[197] E. Dekel, D. Gershoni, E. Ehrenfreund, D. Spektor, J. M. Garcia, and P. M. Petroff, *Phys. Rev. Lett.* **80**, 4991 (1998).

[198] L. Besombes, K. Kheng, L. Marsal, and H. Mariette, *Phys. Rev. B* **65**, 121314 (2002).

[199] S. Kako, K. Hoshino, S. Iwamoto, S. Ishida, and Y. Arakawa, *Appl. Phys. Lett.* **85**, 64 (2004).

[200] G. Cassabois, Habilitation à diriger des recherches, Université Paris VI, Paris, France (2006).

[201] M. Nirmal, D. J. Norris, M. Kuno, M. G. Bawendi, A. L. Efros, and M. Rosen, *Phys. Rev. Lett.* **75**, 3728 (1995).

[202] A. Franceschetti, L. W. Wang, H. Fu, and A. Zunger, *Phys. Rev. B* **58**, R13367 (1998).

[203] M. Bayer, G. Ortner, O. Stern, A. Kuther, A. A. Gorbunov, A. Forchel, P. Hawrylak, S. Fafard, K. Hinzer, T. L. Reinecke, et al., *Phys. Rev. B* **65**, 195315 (2002).

[204] N. Le Thomas, E. Herz, O. Schöps, U. Woggon, and M. V. Artemyev, *Phys. Rev. Lett.* **94**, 016803 (2005).

[205] J. Shumway, A. Franceschetti, and A. Zunger, *Phys. Rev. B* **63**, 155316 (2001).

[206] S. Rodt, R. Heitz, A. Schliwa, R. L. Sellin, F. Guffarth, and D. Bimberg, *Phys. Rev. B* **68**, 035331 (2003).

[207] S. Rodt, A. Schliwa, K. Pötschke, F. Guffarth, and D. Bimberg, *Phys. Rev. B* **71**, 155325 (2005).

[208] G. A. Narvaez, G. Bester, and A. Zunger, *Phys. Rev. B* **72**, 245318 (2005).

[209] M. Chamarro, C. Gourdon, P. Lavallard, O. Lublinskaya, and A. I. Ekimov, *Phys. Rev. B* **53**, 1336 (1996).

[210] J. W. Luo, A. Franceschetti, and A. Zunger, *Phys. Rev. B* **79**, 201301 (2009).

[211] R. Stępniewski, M. Potemski, A. Wysmołek, K. Pakuła, J. M. Baranowski, J. Łusakowski, I. Grzegory, S. Porowski, G. Martinez, and P. Wyder, *Phys. Rev. B* **60**, 4438 (1999).

[212] U. Woggon, K. Hild, F. Gindele, W. Langbein, M. Hetterich, M. Grün, and C. Klingshirn, *Phys. Rev. B* **61**, 12632 (2000).

[213] V. Ranjan, G. Allan, C. Priester, and C. Delerue, *Phys. Rev. B* **68**, 115305 (2003).

[214] D. Simeonov, A. Dussaigne, R. Butté, and N. Grandjean, *Phys. Rev. B* **77**, 075306 (2008).

[215] A. Kiraz, Ph.D. thesis, University of California Santa Barbara, Santa Barbara, USA (2002).

[216] M. Grundmann and D. Bimberg, *Phys. Rev. B* **55**, 9740 (1997).

[217] A. Kiraz, S. Fälth, C. Becher, B. Gayral, W. V. Schoenfeld, P. M. Petroff, L. Zhang, E. Hu, and A. Imamoğlu, *Phys. Rev. B* **65**, 161303 (2002).

[218] C. Becher, A. Kiraz, P. Michler, A. Imamoğlu, W. V. Schoenfeld, P. M. Petroff, L. Zhang, and E. Hu, *Phys. Rev. B* **63**, 121312 (2001).

[219] A. Beveratos, R. Brouri, T. Gacoin, J.-P. Poizat, and P. Grangier, *Phys. Rev. A* **64**, 061802 (2001).

[220] C. Santori, S. Gotzinger, Y. Yamamoto, S. Kako, K. Hoshino, and Y. Arakawa, *Appl. Phys. Lett.* **87**, 051916 (2005).

[221] R. Bardoux, A. Kaneta, M. Funato, Y. Kawakami, A. Kikuchi, and K. Kishino, *Phys. Rev. B* **79**, 155307 (2009).

[222] R. Bardoux, T. Guillet, B. Gil, P. Lefebvre, T. Bretagnon, T. Taliercio, S. Rousset, and F. Semond, *Phys. Rev. B* **77**, 235315 (2008).

[223] C. Kindel, S. Kako, T. Kawano, H. Oishi, and Y. Arakawa, *Japanese J. Appl. Phys.* **48**, 04C116 (2009).

[224] E. Purcell, *Phys. Rev.* **69**, 681 (1946).

[225] P. Goy, J. M. Raimond, M. Gross, and S. Haroche, *Phys. Rev. Lett.* **50**, 1903 (1983).

[226] R. G. Hulet, E. S. Hilfer, and D. Kleppner, *Phys. Rev. Lett.* **55**, 2137 (1985).

[227] E. Yablonovitch, *Phys. Rev. Lett.* **58**, 2059 (1987).

[228] C. Weisbuch, M. Nishioka, A. Ishikawa, and Y. Arakawa, *Phys. Rev. Lett.* **69**, 3314 (1992).

[229] T. Someya and Y. Arakawa, *Appl. Phys. Lett.* **73**, 3653 (1998).

[230] T. Someya, R. Werner, A. Forchel, M. Catalano, R. Cingolani, and Y. Arakawa, *Science* **285**, 1905 (1999).

[231] H. M. Ng, T. D. Moustakas, and S. N. G. Chu, *Appl. Phys. Lett.* **76**, 2818 (2000).

[232] G. S. Huang, T. C. Lu, H. H. Yao, H. C. Kuo, S. C. Wang, C.-W. Lin, and L. Chang, *Appl. Phys. Lett.* **88**, 061904 (2006).

[233] T.-C. Lu, C.-C. Kao, H.-C. Kuo, G.-S. Huang, and S.-C. Wang, *Appl. Phys. Lett.* **92**, 141102 (2008).

[234] N. Antoine-Vincent, F. Natali, D. Byrne, A. Vasson, P. Disseix, J. Leymarie, M. Leroux, F. Semond, and J. Massies, *Phys. Rev. B* **68**, 153313 (2003).

[235] R. Butté, G. Christmann, E. Feltin, J.-F. Carlin, M. Mosca, M. Ilegems, and N. Grandjean, *Phys. Rev. B* **73**, 033315 (2006).

[236] T. Tawara, H. Gotoh, T. Akasaka, N. Kobayashi, and T. Saitoh, *Phys. Rev. Lett.* **92**, 256402 (2004).

[237] R. Thielsch, A. Gatto, J. Heber, and N. Kaiser, *Thin Solid Films* **410**, 86 (2002).

[238] V. Pervak, F. Krausz, and A. Apolonski, *Optics Letters* **32**, 1183 (2007).

[239] J.-F. Carlin and M. Ilegems, *Appl. Phys. Lett.* **83**, 668 (2003).

[240] J.-F. Carlin, J. Dorsaz, E. Feltin, R. Butté, N. Grandjean, M. Ilegems, and M. Laügt, *Appl. Phys. Lett.* **86**, 031107 (2005).

[241] R. Butte, J.-F. Carlin, E. Feltin, M. Gonschorek, S. Nicolay, G. Christmann, D. Simeonov, A. Castiglia, J. Dorsaz, H. J. Buehlmann, et al., *J. Phys. D, Appl. Phys.* **40**, 6328 (2007).

[242] I. R. Sellers, F. Semond, M. Leroux, J. Massies, M. Zamfirescu, F. Stokker-Cheregi, M. Gurioli, A. Vinattieri, M. Colocci, A. Tahraoui, et al., *Phys. Rev. B* **74**, 193308 (2006).

[243] E. Feltin, G. Christmann, R. Butté, J.-F. Carlin, M. Mosca, and N. Grandjean, *Appl. Phys. Lett.* **89**, 071107 (2006).

[244] G. Christmann, R. Butté, E. Feltin, A. Mouti, P. A. Stadelmann, A. Castiglia, J.-F. Carlin, and N. Grandjean, *Phys. Rev. B* **77**, 085310 (2008).

[245] S. Christopoulos, G. B. H. von Högersthal, A. J. D. Grundy, P. G. Lagoudakis, A. V. Kavokin, J. J. Baumberg, G. Christmann, R. Butté, E. Feltin, J.-F. Carlin, et al., *Phys. Rev. Lett.* **98**, 126405 (2007).

[246] G. Christmann, R. Butté, E. Feltin, J.-F. Carlin, and N. Grandjean, *Appl. Phys. Lett.* **93**, 051102 (2008).

[247] J. J. Baumberg, A. V. Kavokin, S. Christopoulos, A. J. D. Grundy, R. Butté, G. Christmann, D. D. Solnyshkov, G. Malpuech, G. B. H. von Högersthal, E. Feltin, et al., *Phys. Rev. Lett.* **101**, 136409 (2008).

[248] K. Busch, G. von Freymann, S. Linden, S. Mingaleev, L. Tkeshelashvili, and M. Wegener, *Physics Reports* **444**, 101 (2007).

[249] R. P. Stanley, R. Houdré, U. Oesterle, M. Ilegems, and C. Weisbuch, *Phys. Rev. A* **48**, 2246 (1993).

[250] S. Noda, M. Fujita, and T. Asano, *Nature photonics* **1**, 449 (2007).

[251] A. Badolato, K. Hennessy, M. Atature, J. Dreiser, E. Hu, P. Petroff, and A. Imamoglu, *Science* **308**, 1158 (2005).

[252] K. Hennessy, A. Badolato, M. Winger, D. Gerace, M. Atatuere, S. Gulde, S. Faelt, E. L. Hu, and A. Imamoglu, *Nature* **445**, 896 (2007).

[253] D. Englund, A. Faraon, I. Fushman, N. Stoltz, P. Petroff, and J. Vuckovic, *Nature* **450**, 857 (2007).

[254] K. Aoki, D. Guimard, M. Nishioka, M. Nomura, S. Iwamoto, and Y. Arakawa, *Nature Photonics* **2**, 688 (2008).

[255] T. N. Oder, K. H. Kim, J. Y. Lin, and H. X. Jiang, *Appl. Phys. Lett.* **84**, 466 (2004).

[256] J. J. Wierer, Jr., A. David, and M. M. Megens, *Nature Photonics* **3**, 163 (2009).

[257] H. Matsubara, S. Yoshimoto, H. Saito, J. Yue, Y. Tanaka, and S. Noda, *Science* **319**, 445 (2008).

[258] T.-C. Lu, S.-W. Chen, L.-F. Lin, T.-T. Kao, C.-C. Kao, P. Yu, H.-C. Kuo, S.-C. Wang, and S. Fan, *Appl. Phys. Lett.* **92**, 011129 (2008).

[259] M. Arita, S. Ishida, S. Kako, S. Iwamoto, and Y. Arakawa, *Appl. Phys. Lett.* **91**, 051106 (2007).

[260] S. L. McCall, A. F. J. Levi, R. E. Slusher, S. J. Pearton, and R. A. Logan, *Appl. Phys. Lett.* **60**, 289 (1992).

[261] B. Gayral, *Ann. Phys. Fr.* **26**, N.2 (2001).

[262] K. Srinivasan, M. Borselli, T. J. Johnson, P. E. Barclay, O. Painter, A. Stintz, and S. Krishna, *Appl. Phys. Lett.* **86**, 151106 (2005).

[263] P. Michler, A. Kiraz, L. Zhang, C. Becher, E. Hu, and A. Imamoglu, *Appl. Phys. Lett.* **77**, 184 (2000).

[264] B. Gayral, J. M. Gérard, A. Lemaître, C. Dupuis, L. Manin, and J. L. Pelouard, *Appl. Phys. Lett.* **75**, 1908 (1999).

[265] B. Gayral, J.-M. Gérard, B. Sermage, A. Lemaître, and C. Dupuis, *Appl. Phys. Lett.* **78**, 2828 (2001).

[266] E. D. Haberer, R. Sharma, C. Meier, A. R. Stonas, S. Nakamura, S. P. DenBaars, and E. L. Hu, *Appl. Phys. Lett.* **85**, 5179 (2004).

[267] A. C. Tamboli, E. D. Haberer, R. Sharma, K. H. Lee, S. Nakamura, and E. L. Hu, *Nature Photonics* **1**, 61 (2007).

[268] D. Simeonov, E. Feltin, H.-J. Bühlmann, T. Zhu, A. Castiglia, M. Mosca, J.-F. Carlin, R. Butté, and N. Grandjean, *Appl. Phys. Lett.* **90**, 061106 (2007).

[269] D. Simeonov, E. Feltin, A. Altoukhov, A. Castiglia, J.-F. Carlin, R. Butté, and N. Grandjean, *Appl. Phys. Lett.* **92**, 171102 (2008).

[270] J. Dorsaz, H.-J. Bühlmann, J.-F. Carlin, N. Grandjean, and M. Ilegems, *Appl. Phys. Lett.* **87**, 072102 (2005).

[271] B. Gayral and J. M. Gérard, *Phys. Rev. B* **78**, 235306 (2008).

[272] E. Peter, A. Dousse, P. Voisin, A. Lemaître, D. Martrou, A. Cavanna, J. Bloch, and P. Senellart, *Appl. Phys. Lett.* **91**, 151103 (2007).

[273] R. E. Slusher, A. F. J. Levi, U. Mohideen, S. L. McCall, S. J. Pearton, and R. A. Logan, *Appl. Phys. Lett.* **63**, 1310 (1993).

[274] X. Marie, B. Urbaszek, O. Krebs, and T. Amand, *Exciton spin dynamics in semiconductor quantum dots, in Spin Physics in Semiconductors* (M.I. Dyakonov, 2008).

[275] D. W. Snoke, W. W. Rühle, K. Köhler, and K. Ploog, *Phys. Rev. B* **55**, 13789 (1997).

[276] D. W. Snoke, J. Hübner, W. W. Rühle, and M. Zundel, *Phys. Rev. B* **70**, 115329 (2004).

[277] G. Pikus and E. L. Ivchenko, *Optical orientation and polarized luminescence of excitons in semiconductors, in Excitons* (E.I. Rashba and M.D. Sturge, 1982).

[278] R. Planel and C. B. à la Guillaume, *Optical orientation of excitons, in Optical Orientation* (F. Meier and B.P. Zakharrchenya, 1984).

[279] E. Ivchenko, *Pure and Appl. Chem.* **67**, 463 (1995).

[280] S. Nagahara, M. Arita, and Y. Arakawa, *Appl. Phys. Lett.* **88**, 083101 (2006).

[281] D. Lagarde, A. Balocchi, H. Carrère, P. Renucci, T. Amand, X. Marie, S. Founta, and H. Mariette, *Phys. Rev. B* **77**, 041304 (2008).

[282] J. Brown, J.-P. R. Wells, D. O. Kundys, A. M. Fox, T. Wang, P. J. Parbrook, D. J. Mowbray, and M. S. Skolnick, *J. Appl. Phys.* **104**, 053523 (2008).

[283] M. Sénès, D. Lagarde, K. L. Smith, A. Balocchi, S. E. Hooper, T. Amand, J. Heffernan, and X. Marie, *Appl. Phys. Lett.* **94**, 223114 (2009).

[284] J. M. Gérard, O. Cabrol, and B. Sermage, *Appl. Phys. Lett.* **68**, 3123 (1996).

[285] M. Dyakonov, *Basics of Semiconductor and spin physics, in Spin Physics in Semiconductors* (M.I. Dyakonov, 2008).

[286] R. Harley, *Spin dynamics of Free Carriers in Quantum Wells, in Spin Physics in Semiconductors* (M.I. Dyakonov, 2008).

[287] W.-T. Wang, C. L. Wu, S. F. Tsay, M. H. Gau, I. Lo, H. F. Kao, D. J. Jang, J.-C. Chiang, M.-E. Lee, Y.-C. Chang, et al., *Appl. Phys. Lett.* **91**, 082110 (2007).

[288] P. S. Eldridge, W. J. H. Leyland, P. G. Lagoudakis, O. Z. Karimov, M. Henini, D. Taylor, R. T. Phillips, and R. T. Harley, *Phys. Rev. B* **77**, 125344 (2008).

[289] Y. Ohno, R. Terauchi, T. Adachi, F. Matsukura, and H. Ohno, *Phys. Rev. Lett.* **83**, 4196 (1999).

[290] J. D. Koralek, C. P. Weber, J. Orenstein, B. A. Bernevig, S.-C. Zhanga, S. Mack, and D. D. Awschalom, *Nature* **458**, 610 (2009).

[291] Y. Léger, Ph.D. thesis, Université Joseph Fourier, Grenoble, France (2007).

[292] K.-H. Lin, G.-W. Chern, Y.-C. Huang, S. Keller, S. P. DenBaars, and C.-K. Sun, *Appl. Phys. Lett.* **83**, 3087 (2003).

Abstract

We studied the optical properties of wurtzite III-N heterostructures by means of various photoluminescence methods. Polarization resolved photoluminescence experiments allowed us to probe the combined effects of strain and confinement on the band structure of an heterostructure. We managed to perform the study of single GaN/AlN quantum dots on an original system: a quantum dot as a slice of a nanowire. This new system allowed us to identify the exciton and biexciton recombination. We also demonstrated that this structure behave as a single photon source thanks to a correlation experiment performed in the UV. We also studied the optical properties of III-N microdisks and measured quality factors up to 11000, which is promising to demonstrate the Purcell effect. Finally, we studied the carrier and spin dynamics in GaN/AlN heterostructures. The quantum dots are very efficient to inhibit the non radiative recombinations. The decay times are indeed not sensitive to temperature, even for lifetimes in the microsecond range. The quantum dots seem also to be very effective to reduce the spin scattering mechanisms for a localized exciton. Optical alignment experiments, performed under quasiresonnant excitation, allowed us to show that the induced polarization was conserved on the lifetime of the exciton up to room temperature.

Résumé

Nous avons étudié par diverses techniques de photoluminescence les propriétés optiques d'hétérostructures à base de composés III-N de structure wurtzite. Des expériences de photoluminescence résolues en polarisation nous ont permis de mettre en évidence l'influence des contraintes et du confinement sur la structure de bande d'une hétérostructure. L'étude de boites quantiques uniques GaN/AlN a pu être réalisée sur un système original : une boite quantique comme tranche d'un nanofil. Ce nouveau système nous a ainsi permis d'identifier les émissions de l'exciton et du biexciton. Nous avons également démontré le caractère d'émetteur de photon unique d'une boite quantique insérée dans un nanofil grâce à une expérience de corrélation de photon fonctionnant dans l'ultraviolet. Nous nous sommes également intéressés aux propriétés optiques de microdisques III-N et avons mesuré des facteurs de qualité atteignant 11000, ouvrant la porte à l'étude de l'effet Purcell dans ces structures. Finalement nous nous sommes penchés sur la dynamique des porteurs et du spin dans les hétérostructures GaN/AlN. Les boites quantiques se révèlent extrêmement efficaces pour éviter les recombinaisons non radiatives, les temps de déclin de la luminescence étant indépendants de la température même pour des boites présentant des déclins de l'ordre de la microseconde. Les boites quantiques semblent aussi être très efficientes pour supprimer les effets de diffusion sur le spin d'un exciton localisé. En effet des expériences d'alignement optique en pompage quasi résonnant nous ont permis de montrer que la polarisation induite était conservée sur la durée de vie de l'exciton et ce jusqu'à température ambiante.